Cancer characterization using quantitative ultrasound and light backscattering spectroscopy

Cyril Malinet

▶ **To cite this version:**

Cyril Malinet. Cancer characterization using quantitative ultrasound and light backscattering spectroscopy. Bioengineering. Université Claude Bernard Lyon 1 (UCBL), 2023. English. NNT : . tel-04501275

HAL Id: tel-04501275
https://hal.science/tel-04501275

Submitted on 12 Mar 2024

HAL is a multi-disciplinary open access archive for the deposit and dissemination of scientific research documents, whether they are published or not. The documents may come from teaching and research institutions in France or abroad, or from public or private research centers.

L'archive ouverte pluridisciplinaire **HAL**, est destinée au dépôt et à la diffusion de documents scientifiques de niveau recherche, publiés ou non, émanant des établissements d'enseignement et de recherche français ou étrangers, des laboratoires publics ou privés.

Université Claude Bernard Lyon 1

THESE de DOCTORAT DE
L'UNIVERSITE CLAUDE BERNARD LYON 1

Ecole Doctorale N° 162
Mécanique, Énergétique, Génie civil, Acoustique

Discipline : Ingénierie pour le vivant

Soutenue publiquement le 19/12/2023, par :

Cyril MALINET

Cancer characterization using quantitative ultrasound and light backscattering spectroscopy

---

Devant le jury composé de :

BOSSY Emmanuel *Professeur des universités, Université Grenoble Alpes*	Président
FRANCESCHINI Emilie *Directrice de recherche, CNRS*	Rapporteure
BACKMAN Vadim *Professor, NorthWestern University*	Rapporteur
BOCOUM Maïmouna *Chargée de recherche, Institut Langevin*	Examinatrice
MAMOU Jonathan *Associate professor, Weill Cornell Medicine*	Examinateur
SAINTIGNY Pierre *Professeur des universités – Praticien hospitalier, Université Claude Bernard Lyon 1*	Examinateur
LIEBGOTT Hervé *Professeur des universités, Université Claude Bernard Lyon 1*	Directeur de thèse
MULEKI-SEYA Pauline *Chargée de recherche, CNRS*	Co-encadrante de thèse
DUTOUR Aurélie *Chercheure, Centre Léon Bérard – Centre de Recherche en Cancérologie de Lyon*	Invitée
MONTCEL Bruno *Professeur des universités, Université Claude Bernard Lyon 1*	Co-encadrant de thèse

Université Claude Bernard - Lyon 1

Président de l'Université	M. Frédéric FLEURY
Président du Conseil Académique	M. Hamda BEN HADID
Vice-Président du Conseil d'Administration	M. Didier REVEL
Vice-Président du Conseil des Études et de la Vie Universitaire	M. Philippe CHEVALIER
Vice-Président de la Commission de Recherche	M. Jean-François MORNEX
Directeur Général des Services	M. Pierre ROLLAND

Composantes Santé

Département de Formation et Centre de Recherche en Biologie Humaine	Directrice : Mme Anne-Marie SCHOTT
Faculté d'Odontologie	Doyenne : Mme Dominique SEUX
Faculté de Médecine et Maïeutique Lyon Sud-Charles Mérieux	Doyenne : Mme Carole BURILLON
Faculté de Médecine Lyon-Est	Doyen : M. Gilles RODE
Institut des Sciences et Techniques de la Réadaptation (ISTR)	Directeur : M. Xavier PERROT
Institut des Sciences Pharmaceutiques et Biologiques (ISBP)	Directrice : Mme Christine VINCIGUERRA

Composantes & Départements de Sciences & Technologie

Département Génie Électrique et des Procédés (GEP)	Directrice : Mme Rosaria FERRIGNO
Département Informatique	Directeur : M. Behzad SHARIAT
Département Mécanique	Directeur M. Marc BUFFAT
École Supérieure de Chimie, Physique, Électronique (CPE Lyon)	Directeur : Gérard PIGNAULT
Institut de Science Financière et d'Assurances (ISFA)	Directeur : M. Nicolas LEBOISNE
Institut National du Professorat et de l'Éducation	Administrateur Provisoire : M. Pierre CHAREYRON
Institut Universitaire de Technologie de Lyon 1	Directeur : M. Christophe VITON
Observatoire de Lyon	Directrice : Mme Isabelle DANIEL
Polytech Lyon	Directeur : Emmanuel PERRIN
UFR Biosciences	Administratrice provisoire : Mme Kathrin GIESELER
UFR des Sciences et Techniques des Activités Physiques et Sportives (STAPS)	Directeur : M. Yannick VANPOULLE
UFR Faculté des Sciences	Directeur : M. Bruno ANDRIOLETTI

Funding

This work was supported by the LABEX PRIMES (ANR-11-LABX-0063) of Université de Lyon, within the program "Investissements d'Avenir" (ANR-11-IDEX-0007) operated by the French National Research Agency (ANR).

A Oncle Philippe

Acknowledgements

Tout d'abord, je tiens à remercier mes encadrants Pauline, Hervé et Bruno. Merci Pauline de m'avoir fait confiance pour prendre part à ton projet de recherche sur la caractérisation de la microstructure. Merci de m'avoir suivi au plus près. Merci de ta patience et de ta disponibilité. Merci Hervé pour tes conseils avisés, ton encadrement humain dans lequel je suis toujours senti écouté et soutenu. Merci Bruno pour ta perspicacité, chacun de tes conseils m'ont toujours permis d'avancer de façon significative vers les résultats finaux.

Mes remerciements vont également à Aurélie et Iveta, qui m'ont fait découvrir l'univers passionnant de la biologie (et ses aléas). Merci d'avoir donné du poids à mes travaux grâce à votre expertise sur les modèles animaux.

Merci Jonathan M. de m'avoir accueilli à New York. Merci de m'avoir appris tant de choses. Merci de m'avoir fait vivre NY à travers les inombrables restaurants, bières, burgers ainsi que la course de la pride, où une erreur de chrono a sûrement dû atténuer ma performance olympique.

I would also like to thank the jury members Mrs Franceschini, M. Backman, Mrs Bocoum, M. Saintigny and M. Bossy. It is an honor for me to have your feedback and your great expertise.

Merci aux équipes ultim et optique (tip top) pour l'environnement de qualité, la disponibilité et l'expertise de chacun des membres.

Merci Celia pour ta contribution considérable au chapitre 7. C'était un plaisir de travailler avec toi.

Mes remerciements vont également aux collègues Nicolas Pinon, Pierre Rougé, Maylis, Benoît, Nathan, Juliette, Robin, Valentin M., qui m'ont plus ou moins expliqué le machine learning ainsi que la commande qsub. On se revoit vite dans l'espace latent.

Merci à mes co-bureaux de l'office 21, Mehdi, Samaneh, Alexandre, Axel d'avoir accompagné mes moments d'égarements dans le bureau.

Je remercie Arthur Gautheron que j'ai un peu considéré comme mon grand oncle de Supopopop avec mes 10000 questions.

Merci à mon Franky de la protéine, pour ses encouragements incessants (« on défonce tout mon gars ») et pour ses entrées fracassantes dans le bureau à 16h pétante pour l'appel de l'immanquable goûter. Je te souhaite le meilleur et de devenir parisien.

Merci à Sophie, avec moi du premier jour jusque dans les heures tardive de rédaction de la smart 4a. Merci de tes inombrables attentions et de ta bienveillance infinie. C'était très drôle le jour où tu avais supprimé ton .tex devant moi. J'en rigole encore.

Un merci à la Louisasse Friaud—-Jiroud, d'avoir écouté les lamentations de Cyril en 2ème année en quête de résultats, d'avoir suivi mes quarts d'heure carte blanche. Merci pour tous ces rires.

Un grand merci à mes frérots Vincent et Axel, mes amis de toujours. Merci à toi, Jennifer, d'être un soutien sans faille de longue date. Merci mon cher Ambroise d'être une oreille présente et attentive.

Merci à mes amis Rachel, Jérôme, Mattéo, Mathieu, Nicolas, Alice, Alexis, Thomas, Agnès, Grégoire, Laetitia, Solène, Coco, Marius, Elise, Léo, Mazzo, d'avoir continué de me cotoyer malgré mon départ pour la province.

Thanks Eshaan for making my three months experience in New York that crazy.

Merci Louise Sinegre, Coline et Quentin avec qui j'ai fait mes premiers pas dans Lyon en plein covid.

Merci Pauline Ogrine, d'avoir vécu ces années à Lyon avec moi, de nos rendez-vous

immanquables dans les salons de thés cosy. I genuinely wish you the best in Boston (mdr t'as pas compris genuinely je suis sûr).

Merci mon petit Valoche, d'avoir tenu avec moi notre belle demeure rue de Flesselles. Plus d'un souvenir restera dans ma mémoire : les blagues sur Claudine, les imitations de Burnos au téléphone, nos assiettes de cheval, ton émerveillement constant pour la finition de la salle de bain et j'en passe. Le bruit de la sauce samouraï se déversant dans ta semoule hante encore mes oreilles.

Je tiens à remercier Maman, Papa, Hugues et Pauline pour leur soutien. En particulier, merci de m'avoir offert un cadre optimal pour mes études.

Pour finir, merci Juliette (baby chat), d'avoir suivi un doctorant à distance en dernière année. Merci d'avoir été présente et attentionnée jusque dans les heures les plus difficiles de la thèse. Merci de m'avoir supporté lors de la rédaction du manuscrit. Maintenant, je souhaite écrire l'avenir avec toi. A noter pour briller en société : ton copain n'est plus un étudiant.

Abstract

Cancer development is characterized by complex processes that occur in different stages, involving tissue changes at various scales. In a clinical context, cancer characterization aims to identify the hallmark features of cancer to establish the patient's diagnosis. The initial diagnosis is typically made following a biopsy and histological examinations, which are inherently invasive and resource-intensive. Thus, a minimally invasive tool able to quickly extract diagnostic information could address these limitations.

As a starting point toward this solution, quantitative ultrasound techniques and light backscattering techniques were combined. These techniques aim to extract quantitative estimates that reflect the tissue's underlying microstructure. Associating these methods could probe the cancer-related changes previously mentioned with a certain complementarity. Indeed, ultrasound and light waves can experience scattering when they encounter variations of acoustic impedance and refractive index respectively. Additionally, medical ultrasound wavelengths are substantially higher than optical visible wavelengths. Therefore, ultrasound and light waves may interact with different cellular components of various sizes, leading to more comprehensive tissue assessment.

Firstly, our bimodal approach was validated on three tissue-mimicking phantoms composed of different microparticle sizes. Combining Backscattering Coefficient (BSC) parametrization and light Enhanced Backscattering Spectroscopy (EBS) allowed to differentiate each phantom following a qualitative approach. Each technique showed a different sensitivity regarding the scatterer sizes.

Secondly, an ex vivo study on animal models was conducted. In addition to BSC parametrization and EBS, ultrasound Envelope Statistics (ES) and Light Scattering Spectroscopy (LSS) were combined to characterize two sarcoma subtypes: chondrosarcoma and osteosarcoma. Histological analyses were conducted to serve as references. Three ultrasound parameters and the EBS parameter showed significant differences between chondrosarcomas and osteosarcomas at the 5% level. BSC parametrization identified the mean size of chondrosarcoma cells and nuclei with relative errors of about 22% and 9% respectively. LSS correctly estimated the nucleus and the cell size distributions for chondrosarcomas and osteosarcomas ($R^2 = 0.80$ and $R^2 = 0.73$ respectively).

Thirdly, we investigated the extent to which our bimodal approach could serve as a solution to monitor the tumor response over time when chemotherapeutic treatments are administered. To do so, we applied the four techniques mentioned above to the same sarcoma subtypes over weeks, injecting a chemotherapeutic drug twice a week into certain rodents and saline solutions to others. Relative tumor volumes, taken as measurements of reference, revealed that all tumors were likely to be non-responders. Several scattering parameters appeared sensitive to the effects of injections of treatment during the first days of treatment. Convergences were then observed between treated and control tumors after the final treatment. Consequently, scattering parameters may have reflected the mechanism of chemotherapy resistance.

Fourthly, the structural effects of ultrasound scattering that can be found in biological tissues were investigated in a phantom study. To do so, a novel experimental approach was introduced. The phantom was composed of magnetic particles that had their spatial organization modified by a surrounding magnetic field. The physical meanings of the ultrasound parameters and their concordance were observed in three distinct experiments.

The results reported in this thesis showed that the association of ultrasound and light scattering is valuable for cancer characterization. Promising results could be obtained in future studies.

Résumé

Le développement du cancer se caractérise par des processus complexes se déroulant à différents stades et impliquant des modifications tissulaires à plusieurs échelles. Dans un contexte clinique, la caractérisation du cancer vise à identifier les traits caractéristiques du cancer afin d'établir le diagnostic du patient. Le diagnostic initial est généralement établi à la suite d'une biopsie et d'examens histologiques, qui sont invasifs par nature et nécessitent des ressources importantes. Un outil relativement peu invasif capable d'extraire rapidement des informations diagnostiques pourrait remédier à ces limitations.

Comme point de départ de cette solution, des techniques quantitatives d'échographie ultrasonores et des techniques de spectrales de rétrodiffusion de la lumière ont été combinées. Ces méthodes visent à extraire des paramètres quantitatifs qui reflètent la microstructure sous-jacente du tissu sondé. L'association de ces méthodes pourrait permettre de sonder les changements liés au cancer mentionnés précédemment avec une certaine complémentarité. En effet, les ondes ultrasonores et optiques pourraient interagir avec différents composants cellulaires, ce qui permettrait une évaluation plus complète des tissus.

Premièrement, notre approche bimodale a été validée sur trois fantômes composés de microparticules de différentes tailles. La combinaison de la paramétrisation du coefficient de rétrodiffusion (BSC) et de la spectroscopie de rétrodiffusion augmentée par la lumière (EBS) a permis de différencier chaque fantôme en suivant une approche qualitative.

Deuxièmement, une étude ex vivo sur des modèles animaux a été réalisée. En plus de la paramétrisation du BSC et de EBS, les statistiques d'enveloppe ultrasonore (ES) et la spectroscopie de lumière diffusée (LSS) ont été combinées pour caractériser deux sous-types de sarcomes : le chondrosarcome et l'ostéosarcome. Des analyses histologiques ont été réalisées pour servir de référence. La paramétrisation du BSC a permis d'identifier la taille moyenne des cellules et des noyaux des chondrosarcomes avec des erreurs relatives d'environ 22% et 9% respectivement. LSS a correctement estimé les distributions de taille des noyaux et des cellules pour les chondrosarcomes et les ostéosarcomes ($R^2 = 0{,}80$ et $R^2 = 0{,}73$ respectively).

Troisièmement, nous avons étudié les performances de notre approche bimodale pour évaluer la réponse d'une tumeur au fil du temps lorsque des traitements chimiothérapeutiques sont administrés. Pour ce faire, nous avons appliqué les quatre techniques mentionnées ci-dessus aux mêmes sous-types de sarcomes pendant plusieurs semaines, en injectant un médicament chimiothérapeutique deux fois par semaine à certains rongeurs et de la solution saline à d'autres. Les volumes tumoraux relatifs, considérés comme références, ont révélé que toutes les tumeurs étaient susceptibles d'être non répondeuses. Plusieurs paramètres ultrasonores et optiques sont apparus sensibles aux effets des injections de traitement pendant les premiers jours de traitement. Des convergences ont ensuite été observées entre les tumeurs traitées et témoins après le traitement final. Par conséquent, certains paramètres de diffusion pourraient avoir reflété le mécanisme de résistance à la chimiothérapie.

Quatrièmement, les effets structurels sur la diffusion ultrasonore que l'on peut trouver dans les tissus biologiques ont été étudiés dans le cadre d'une analyse sur fantôme. Pour ce faire, une nouvelle approche expérimentale a été introduite. Le fantôme était composé de particules magnétiques dont l'organisation spatiale était modifiée par un champ magnétique environnant. Les significations physiques des paramètres ultrasonores et leur concordance ont été constatées dans trois expériences distinctes.

Les résultats rapportés dans cette thèse ont montré que l'association de techniques ultrasonores et optique est pertinente pour la caractérisation du cancer.

Contents

List of abbreviations

BCS Breast-conserving surgery

BSC Backscatter coefficient

B-mode Brightness mode

CBS Coherent backscattering spectroscopy

CCD Charge-coupled device

CE Coded excitation

CMUT Capacitive micromachined ultrasonic transducers

C-CLASS Coherent confocal light absorption and scattering spectroscopy

CT Computed Tomography

DOP Degree of polarization

EAC Effective acoustic concentration

EBS Enhanced backscattering spectroscopy

ES Envelope statistics

ESD Effective scatterer diameter

FFSM Fluid-filled sphere model

FM Faran model

FNCLCC Fédération nationale des centres de lutte contre le cancer

FWHM Full width half maximum

H and E Hematoxylin and Eosin

HGD High grade dysplasia

HK Homodyned-K

LGD Low grade dysplasia

LEBS Low enhanced backscattering spectroscopy

LF Lizzi-Feleppa

LSS Light scattering spectroscopy

MC Monte Carlo

MRI Magnetic Resonance Imaging

NDB Non-dysplastic biopsy

NoTTT No treatment

PDF Probability density function

PI Polydisperse I

PII Polydisperse II

PTTT Post treatment

QUS Quantitative ultrasound

REC Resolution enhancement compression

RF Radiofrequency

RMSE Root mean squared error

ROI Region of interest

RTV Relative tumor volume

SGM Spherical Gaussian model

SNR Signal-to-noise ratio

ROC Receiver operating characteristic

SFM Structure factor model

a/LSS Angularly resolved light scattering spectroscopy

Ch Chondrosarcoma

Os Osteosarcoma

Chapter 1

Introduction

The development of cancer manifests as a multifaceted phenomenon occurring across different stages and affecting the tissues at diverse spatial and temporal scales [1]. At an early stage, cancer-induced morphological alterations, known as dysplasia, can occur at the cellular and nuclear scales. As cancer progresses, the malignant tissues can exhibit highly atypical cells in shape and size, often following an abnormal spatial organization. At a later stage, cell death, or necrosis, can be observed. In the case where chemotherapy is chosen as a treatment option, necrosis can be induced by the drug exposure. The chemotherapeutic drugs penetrate the malignant cells and aim to inhibit cancer progression [2]. However, tumors may not respond positively and can develop chemotherapy resistance during the course of treatment. All these mechanisms of malignancy can result from a complex interplay of genetic and molecular changes.

In clinical settings, cancer characterization aims to identify the hallmark features of cancer previously mentioned to establish the patient's diagnosis. The initial diagnosis is made after histological examinations. At this stage, the cancer characterization involves the process of determining the cancer type and its key features, such as the grade. The grade reflects the tumor aggressiveness and is assigned based on various criteria, including the cell and the nucleus morphologies [3]. The cancer diagnosis is of crucial importance for the patient outcome as the medical board decides the treatment options accordingly. Cancer characterization may take place at other phases using conventional imaging modalities, spanning from cancer screening to the ongoing monitoring of therapy effectiveness. For these two specific applications, early detection of cancer and prompt identification of ineffective drugs are of great importance respectively, as time also plays a critical role in the patient outcome.

Conventional ultrasound imaging primarily provides anatomical information through gray-scale images, termed as B-mode images. However, the diagnosis based on B-mode images may be subject to inter-observer and intra-observer variabilities [4]. To enhance the reproducibility of diagnosis, the use of quantitative estimates appears as a relevant solution. Quantitative ultrasound (QUS) techniques aim to provide quantitative measurements that can be used for diagnostic purposes. Indeed, valuable information regarding the microstructures of the underlying tissue can be obtained by analyzing the spectral content analysis and the statistics of the envelope of the radiofrequency (RF) signals used to generate ultrasound scans. These two approaches are referred to as the Backscattering Coefficient (BSC) parametrization and Envelope Statistics (ES). Interestingly, BSC parametrization and ES can be conducted on the same RF signals and provide different ultrasound scattering parameters that reflect the tissue microstructures. Indeed, ultrasound waves are scattered if they experience variations of impedance contrast. Thus, cells or nuclei may be considered as ultrasound scatterers surrounded by extracellular matrix and cytoplasm respectively at sufficiently high frequencies [5]. The scatterer diameter can be estimated by conducting BSC parametrization on a tissue sample for instance. All the changes induced by the development of cancer mentioned in the first paragraph may impact ultrasound scattering parameters.

Interestingly, light waves can also be scattered if they encounter variations of refractive index. Similarly, the spectral analysis of the backscattered light waves can lead to scattering parameters that carry information about the tissue microstructure. Enhanced Backscattering Spectroscopy (EBS) and Light Scattering Spectroscopy (LSS) are two light-based techniques that can be performed using a similar experimental setup to characterize biological tissues through quantitative estimates [6, 7]. Notably, LSS can also involve the estimation of the scatterer diameter [8]. Recent papers reported successful applications for cancer characterizations [9, 10].

Visible light wavelengths are about one hundred times smaller than the ultrasound wavelengths used for medical imaging. Therefore, one can expect that the scattering process would arise from different cellular structures of varying sizes given the distinct wavelength ranges when light and ultrasound are combined. Consequently, analyzing ultrasound and optical scattered waves may provide complementary information regarding the tissue microstructure. This association may potentially lead to a more comprehensive tissue assessment. The research works presented in this thesis focus on a bimodal approach that was motivated by this hypothesis.

Combining ultrasound and light through BSC parametrization, ES, EBS and LSS offers multiple advantages. Indeed, the resulting association can remain:

- Minimally-invasive, as no tissue excision is required.
- Non-ionising, as visible light can be used.
- Point-of-care, as all the necessary materials can be integrated on a trolley.

- Relatively low-cost, in comparison to some conventional imaging tools such as Magnetic Resonance Imaging (MRI) or Computed Tomography (CT) scanners (approximately less than 60k$).
- Real-time, as the methods employed here are compatible with intra-operative applications.

Given that the inner mechanisms of our methods probe microstructural alterations that are characteristics of cancerous tissues, our bimodal approach could potentially be applied to all types of cancers.

The association of these quantitative ultrasound and light backscattering techniques is motivated by all the rationales aforementioned. This thesis aims to investigate the use of a bimodal approach for cancer characterization.

It is important to note that our objective is not to outperform or substitute the established gold standard methods in clinical procedures. Instead, our intention is to develop the premises of a tool that could support clinician decision-making by providing complementary information alongside conventional methods. More importantly, a bimodal tool that combines all the qualities mentioned above has also the potential to bring diagnostic information in clinical cases where no tool is currently employed routinely (*e.g.* therapy monitoring for certain cancer types).

The thesis is organized as follows: Chapter 2 describes the clinical context. The background in ultrasound and optical scattering for tissue characterization is then reviewed through successful applications. In Chapter 3, the ultrasound theoretical framework is detailed along with the method to conduct BSC parametrization and to estimate Envelope parameters. In Chapter 4, the methods for Enhanced Backscattering Spectroscopy and Light Scattering Spectroscopy are explained after describing the insight of optical scattering. Chapter 5 entails the validation of our bimodal approach using tissue-mimicking phantoms. The subsequent two chapters present the application of our method on biological samples. In Chapter 6, we use animal models to characterize two distinct histological subtypes of bone tumors *ex vivo*. In Chapter 7, a longitudinal study is performed on the same tumor models, aiming to demonstrate the potential sensitivity of our method for therapy monitoring. Chapter 8 introduces a novel phantom method for studying ultrasound scattering in structured media. Finally, chapter 9 gives the perspectives and the conclusions.

Chapter 2

Context

This chapter aims to expose the clinical context that motivates the research work. Then, the QUS techniques for tissue characterization are reviewed through their successful implementations. Last, two light backscattering spectroscopy methods are also presented through their successful applications for tissue diagnostics.

2.1 Clinical context

This thesis aims to validate the association of quantitative ultrasound and light backscattering spectroscopy methods for characterizing cancerous tissues. The working principle of both techniques is the same: analyzing the backscattered waves that have interacted with the cellular components of the probed tissue. Before delving into the potential clinical applications of such a minimally invasive tool, insights into malignancy mechanisms at the cellular scale are described.

2.1.1 Cancerous physiological changes

Carcinogenesis refers to the process by which normal cells transform into cancer cells. It involves a series of changes at multiple scales that result in the uncontrolled growth and proliferation of cells that can aggregate into a macroscale tumor. Before leading to the development of a primary tumor, the cancerous cells undergo distinct states.

Early changes

Two subcategories refer to pre-cancerous conditions:

Histological normal tissue Field carcinogenesis is the earliest stage of cancer progression and can lead to a "fertile" environment [10]. The latter results from multiple ultrastructural (*i.e.* smaller than the optical diffraction limit) tissue alterations, such as chromatin condensation in the nuclei or collagen fibers cross-link in the extracellular matrix. A number of stochastic genetic mutations then lead to cells with an abnormal histological appearance.

Histological abnormal tissue Dysplasia typically occurs in precancerous tissues. Dysplastic sites exhibit tissue alterations at the nuclear and cellular scales. Indeed, these regions manifest enlarged nuclei and present a disordered spatial arrangement of cells characterized by diverse morphologies (Figure 2.1). Dysplasia can commonly occur in the superficial epithelial tissues (*i.e.* lining of organs) of the respiratory tract, the gastrointestinal tract or skin. More than 85% of all cancers originate in epithelial tissues [11].

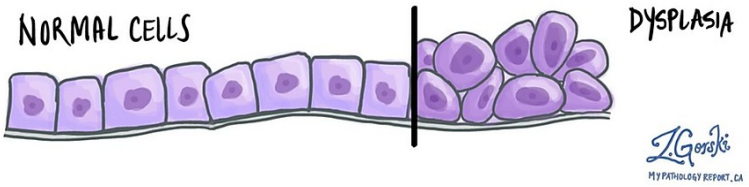

Figure 2.1: Scheme representing an illustrative example of dysplasia. Reproduced from mypathologyreport.ca [12]

Cancerous tumors

The cells exhibiting dysplasia may lead to the formation of a compact tumor, referred to as a primary tumor. These cells can exhibit various characteristics that contrast with healthy cells, often being classified as undifferentiated (as shown in Figure 2.2), unlike the differentiated normal cells. Cancerous tumors may also contain highly abnormal-looking cancer cells, referred to as anaplastic cells, which exhibit atypical shapes and sizes. Additionally, a high density of mitotic figures is commonly observed in cancerous tissues. Mitotic figures are cellular structures visible during cell divisions. Besides, cellularity, or cell density, may be abnormal and can reflect cell proliferation or a specific histological subtype (*i.e.* tumor type). Necrosis can also be observed in compact tumors. Necrosis refers to the process of cell death caused by external factors, unlike apoptosis, which is a programmed cell death. For example, exposure of the tumor to chemotherapeutic drugs can lead to necrosis, resulting in the rupture of the cellular membrane and the release of cellular debris. As cancer progresses, cancerous cells from the primary tumors may then migrate to form metastases in other regions of the human body.

In summary, the development of malignancy is characterized by complex mechanisms

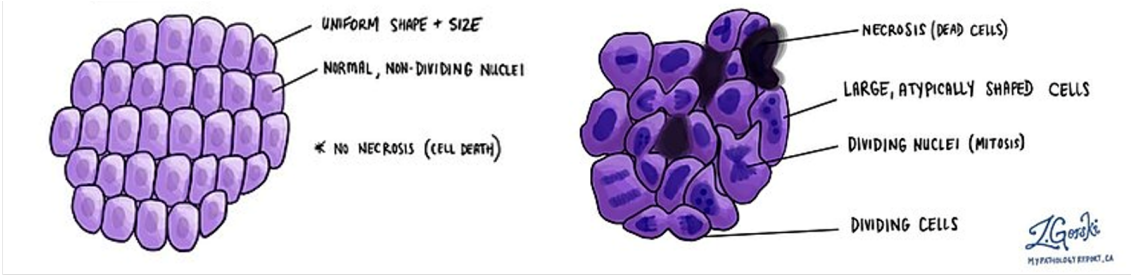

Figure 2.2: (a) Schemes of healthy cells. (b) Schemes of cancerous cells with their characteristic features. Adapted from mypathologyreport.ca [13]

that occur in different stages, involving tissue changes at various scales. In a clinical context, cancer characterization aims to identify these hallmark features to establish the patient's diagnosis. Interestingly, the ultrasound and the light waves that have traveled into the probed tissue may carry complementary information about the underlying microstructure that could reflect these cancer-related changes.

2.1.2 Cancer characterization in clinical settings

This subsection exposes the potential clinical applications of our bimodal method that combines QUS and light scattering techniques. For each application, the theoretical feasibility of the use of a such bimodal tool is briefly shown by citing past related studies. To understand these potential clinical applications, brief practical characteristics of this tool are described. Broader descriptions will be detailed in Chapter 3 and 4. In this section, each medical application is then introduced following a typical chronology of the cancer care workflow.

Our bimodal approach

This thesis project aims to develop the premises of a tool that could provide a near-real-time tumor characterization from quantitative measurements without conducting biopsies. The corresponding estimates reflect the tissue microstructure and may carry relevant diagnosis information. What "characterization" refers to is detailed below for each potential clinical application.

Quantitative ultrasound and light backscattering spectroscopy techniques can be non-ionizing and point-of-care. To avoid acoustic impedance mismatches, gentle probe/tissue contact would be necessary. As order-of-magnitudes, the depth selectivity of our technique would reach hundreds of microns in optics and a few centimeters in ultrasound. These considerations can be further discussed depending on the frequency used. The probed tissue surface would be about 2 mm^2 in optics. Varying lateral field-of-view can be obtained in QUS imaging depending on the transducer used.

Ultrasound and optical techniques are compatible with endoscopic applications for minimally-invasive procedures [14, 15]. Additionally, endoscopic scanning systems were reported [9, 16] and could therefore be designed in the case of spatially extended samples.

Cancer screening

A medical consensus exists about the fact that early cancer detection improves the patient outcome [7, 17]. Cancer screening appears as one of the first practical solutions for this purpose. This procedure entails a first analysis that can be applied to a large-scale population. Thus, the associated tool needs to be low-cost, fast and causes minimal discomfort to patients. Mutyal et al. [18] reported an optical endoscopic probe to detect early colon carcinogenesis, that is not visible during routine endoscopy. Their application is introduced as an affordable pre-screen test for a large population that is part of a two-step approach for risk stratification. The patients with positive results would then need to undergo a conventional cancer screening test.

Similarly, the bimodal solution that we aim to develop in this thesis could meet the requirements needed for cancer screening/pre-screening in the case of shallow tissue alterations. Indeed, early cancerous conditions such as dysplasia may alter the quantitative scattering parameters in comparison to healthy tissues. Larger cells or nuclei may impact the estimated effective scatterer size for instance. Thus, relevant scattering parameters could be compared to threshold reference values validated after clinical trials to classify the probed tissue as healthy or suspicious.

Initial cancer diagnostics

The initial cancer diagnostics is of crucial importance for the patient's prognosis since it will guide the clinicians toward the right treatment options. Following a positive screening test or suspicious symptoms, a biopsy can be indicated.

Biopsy The biopsy entails in extracting a sample of tissue from the patient. Biopsies are typically performed by radiologists. The sampled tissue then undergoes histo-pathological analyses conducted by an anatomopathologist, who establishes the patient diagnosis. However, the biopsy is inherently invasive. More importantly, the sampled sections may not include the most aggressive cancerous regions due to tumor heterogeneities [19]. Thus, the sampling bias could lead to inaccurate diagnostics.

The number of biopsies needs to be minimized for their resource-intensive nature, their impact on patient's anxiety and also because of the risk of dissemination. Indeed, when a clinician extracts the sampled tissue from the patient, cancerous cells may migrate and spread to other tissues in the vicinity of the tumor. If dissemination is suspected, surgery can then be indicated to remove the tissues that have been in contact with the biopsied sample.

To address these drawbacks, numerous studies investigated non-invasive optical biopsy techniques to target tissue alterations in various tissue types [14, 20]. As an example, Qiu et al. [9] reported an optical endoscopic fiber probe able to scan the esophagus to detect dysplastic sites. Similarly to the screening application mentioned above, they aimed to reveal tissue alterations that are invisible to routine endoscopy, namely dysplasia. Their objective was also to reduce the number of invalid biopsies and sampling errors. Likewise, an endoscopic version of the bimodal tool that we aim to develop may guide the biopsy toward the most suspicious regions in a minimally invasive fashion. This could potentially reduce the number of biopsies required and therefore mitigate all the drawbacks of the tissue excision that were mentioned. Similarly to cancer screening, the biopsy guidance could be based on a simple classification procedure of the scattering parameters, involving a reference threshold for a specific scattering parameter.

Quantitative pathology Histo-cytopathology serves as a gold standard for diagnosing cancers. The histological classification of a biopsied sample relies on cellular morphological measurements and is traditionally determined by microscopic examination. The analyses conducted by anatomopathologists are subject to inter-observer and intra-observer variabilities [3, 7]. Two quantities can be affected: the cancer grade and the histological subtype.

The cancer grade describes only the intrinsic quality of the primary tumour [1]. It reflects the cancer aggressiveness behavior of a malignant tissue based on histological features. The degree of cellular differentiation is described through a number that typically varies between I (similar to normal tissue) and IV (anaplastic). One could note that multiple grading systems exist. They aim to describe accurately the patient prognosis for specific tumor types. Therefore, the histological subtype also needs to be determined and is associated with the grade. Some features are common to most of the grading systems, namely the nuclear-cytoplasmic ratio (nucleus to cell volume ratio), the cell density, the hyperchromasia (nuclear staining), the concentration of mitoses, and the percentage of necrosis area. For example, in the FNCLCC (*Fédération Nationale des Centres de Lutte Contre le Cancer*) grading system, which is the most used grading system for soft tissue sarcomas [1], the grade depends on the percentage of necrosis following a semi-quantitative criteria (score 1 if < 50 % of tumor necrosis, score 2 is $\geq 50\%$ and 0 if no necrosis).

Interestingly, the cellular characteristics mentioned above could probably be estimated using the bimodal approach developed in this thesis. Firstly, the nucleus and the cell sizes could be measured independently to compute the corresponding ratio using LSS and QUS techniques respectively. Secondly, the volume fraction is a common parameter in ultrasound theoretical scattering models and could therefore be experimentally estimated to reflect the cell density. Finally, multiple QUS applications reported high sensitivity to cell death [4], making the detection of necrosis possible through quantitative estimates. All these arguments will be supported by successful applications described in the following sections.

It is noteworthy that our objective is not to outperform histo-cytopathology. At best, our bimodal tool could come as an additional device for the anatomopathologist to estimate/validate the cancer grade. This application remains a long-term objective. However, it is important to point out the numerous parameters of interest observed in histo-cytopathology that could be estimated using quantitative ultrasound and light scattering techniques.

Therapy monitoring

Based on cancer diagnostics, clinicians indicate the most adapted cancer treatments such as chemotherapy, radiation therapy, immunotherapy, hormone therapy or surgery for instance. The tumor progression can be inhibited if the patient positively responds to the chosen treatment. However, tumors can also develop resistance mechanisms that make a treatment ineffective.

For example, chemotherapeutic solutions can be selected in the case of bone sarcomas. In this case, to our knowledge, there is no established standard procedure for evaluating tumor response between the initial drug treatment and the follow-up surgery, typically occurring 8 weeks after. As a result, clinicians are unable to adjust treatment strategies for non-responsive tumors during this interval. Responsive or resistant tumor cells may exhibit different characteristic mechanisms at the molecular and cellular scales. Thus, ultrasound and optical scattering parameters may reflect the corresponding changes. Multiple quantitative ultrasound studies reported successful therapy monitoring applications [4]. Similarly, our bimodal technique could be applied by comparing estimated scattering parameters to reference thresholds to classify tumors as responders or not. Its penetration depth may limit the measurements to shallow tumors. This clinical application is investigated in Chapter 7.

These considerations focused on bone sarcomas. However, we can reasonably infer that similar challenges might arise in other types of therapy directed at different tumor types. Thus, our bimodal tool has the potential to bring diagnostic information in clinical cases where no tool is currently employed routinely.

Intra-operative resection margin assessment

Resection surgery involves the removal of a tumor and a margin of surrounding healthy tissue. The latter is known as the resection margin. If cancer cells are found in the resection margins (*i.e.* positive margins), more tissues need to be removed from the patient to prevent a cancer recurrence.

In the case of breast cancer, the percentage of patients who need to undergo a second surgery after a breast-conserving surgery (BCS) is estimated between 15% and 35% [21]. Leiloglou et al. [22] reported the use of an optical fluorescence imaging device to assist the surgeon in BCS to reduce the risk of incomplete surgical resection. Dutour et al. [23] conducted a similar approach for bone sarcomas.

Likewise, our bimodal technique would guide the surgeons toward suspicious regions non-invasively, following a semi-quantitative analysis of estimated scattering parameters. Interestingly, the depth selectivity of our methods is not limiting in this open-surgery application.

In summary, cancer characterization is a key component of numerous standard medical procedures. Thus, detecting cancer-related changes at the cellular scale with all the qualities mentioned in the paragraph 2.1.2 (minimally-invasive, non-ionizing and so forth) is relevant for multiple medical applications. The following explains why quantitative ultrasound and light scattering techniques can be used for this purpose. Indeed, most of the potential clinical applications mentioned above are based on successful applications of quantitative ultrasound and light backscattering spectroscopy techniques. The next two sections describe them successively.

2.2 Quantitative ultrasound techniques

Quantitative ultrasound techniques encompass a broad range of methods that involve the estimation of tissue properties [24], including Backscatter Coefficient (BSC) parametrization and Envelope Statistics (ES). BSC parametrization and ES can be performed using conventional ultrasound imaging systems, increasing the likelihood of their clinical acceptance. Additionally, BSC parametrization and ES are compatible with *in vivo* applications and they can be performed using the same backscattered RF signals to extract complementary scatterer properties. This section aims to trace the historical development of these two quantitative ultrasound (QUS) techniques by highlighting their key breakthroughs for cancer applications. The BSC analysis was of prime interest for this thesis project and was the first technique implemented in this project. Thus, deeper insights about this method will be given.

2.2.1 Backscatter coefficient parametrization

The BSC quantifies the tissue's ability to backscatter the acoustic energy as a function of the frequency. The BSC reflects the underlying tissue microstructure and can be seen as the spectral signature of the probed sample. In tissue characterization applications, the primary challenge lies in accurately estimating the BSC (*c.f.* section 3.2.4). The following step is the BSC parametrization, which eventually extracts the scattering parameters through inversion procedures. To achieve this, theoretical analytical scattering models are fitted to the measured BSCs. Multiple analytical models were developed and improved. The performances of different models for tissue characterization are described below. More specifically, their capacity to determine the size of cellular components through the estimated scatterer size is emphasized.

The Lizzi-Feleppa parameters

A first approach involves modeling the BSC as a linear function [25]. This simple procedure leads to three ultrasound parameters known as the Lizzi-Feleppa (LF) coefficients: the LF intercept, the LF midband value and the LF slope. A typical implementation of the linear model can be found in Mamou et al. [26], who reported significant statistical differences in the intercept and the slope values between normal and metastatic resected lymph nodes (Figure 2.3, b).

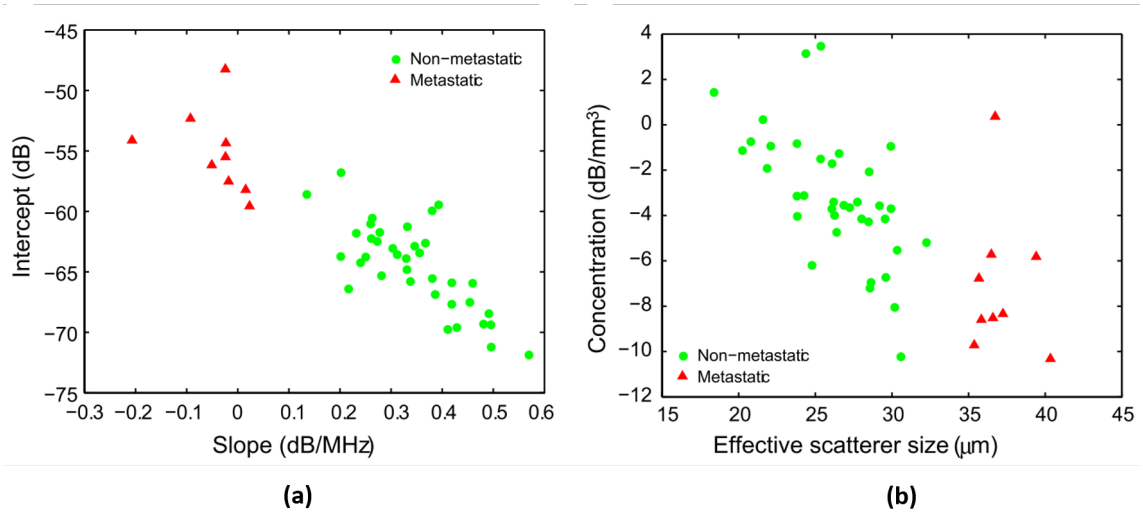

Figure 2.3: Scatter plots of estimates by model. One dot corresponds to a resected lymph node. (a) Intercept and slope (straight-line model). (b) Effective scatterer size and acoustic concentration (Gaussian form factor). Reproduced from Mamou et al. [26]

The physical interpretation of these parameters was investigated multiple times. First, the LF intercept and midband were reported as indicators of the backscattering intensity, and the LF slope was associated with the scatterer's size [27]. More recently, Muleki-Seya et al. [28] studied the theoretical relations between the LF and other QUS-derived parameters in diluted media (*i.e.* relatively few scatterers per unit volume). The analytical analyses were then compared to BSC measurements on *ex vivo* mouse livers. The expected correlation between the LF slope and the Effective Scatterer Diameter (ESD) was validated experimentally. Similarly, the LF midband was correlated to the Effective Acoustic Concentration (EAC). LF midband and EAC were reported as the best biomarkers for liver fat percentage estimation in this study. The ESD and the EAC are defined below.

The Spherical Gaussian model

The ESD and EAC parametrize the Spherical Gaussian model and invite us to introduce a heavily used BSC theoretical model developed by Lizzi et al. [25]. The Spherical

Gaussian Model (SGM) considers continuous impedance fluctuations in the media [29]. ESD and EAC can be used in the same fashion as the LF parameters for tumor classification [26] (Figure 2.3, a). The EAC (expressed in $dB.mm^{-3}$) reflects the product of the scatterer concentration with the square of the impedance mismatch with the surrounding medium. Its physical interpretation is more limited than the ESD (expressed in µm) that can be related to scattering structures. Thus, multiple studies investigated the identification of the main scattering structures through the ESD [24]. Insana et al. [30] reported the scattering of glomeruli ($\approx$ 200 µm) and the efferent arterioles ($\approx$ 50 µm) in the low (1 - 5 MHz) and the high (5 - 15 MHz) frequency range respectively in *in vitro* dog kidney parenchyma. In this study, the product of the wavenumber k with the scatterer radius a was approximately unity ($ka \approx 1$). A few years after, Oelze et al. [31] identified the glandular acini (100 µm) as the main scattering structures in fibroadenoma ($ka \approx 0.5$) and the cell nuclei in mammary carcinoma ($ka \approx 1$) in a *in vivo* rodent study. Conventional B-mode images can map the ESD values through a color overlay that encodes the average scatterer diameter for each ROI (Figure 2.4). The carcinomas were found to have a more uniform scatterer size than the fibroadenoma. One should note that despite the over-

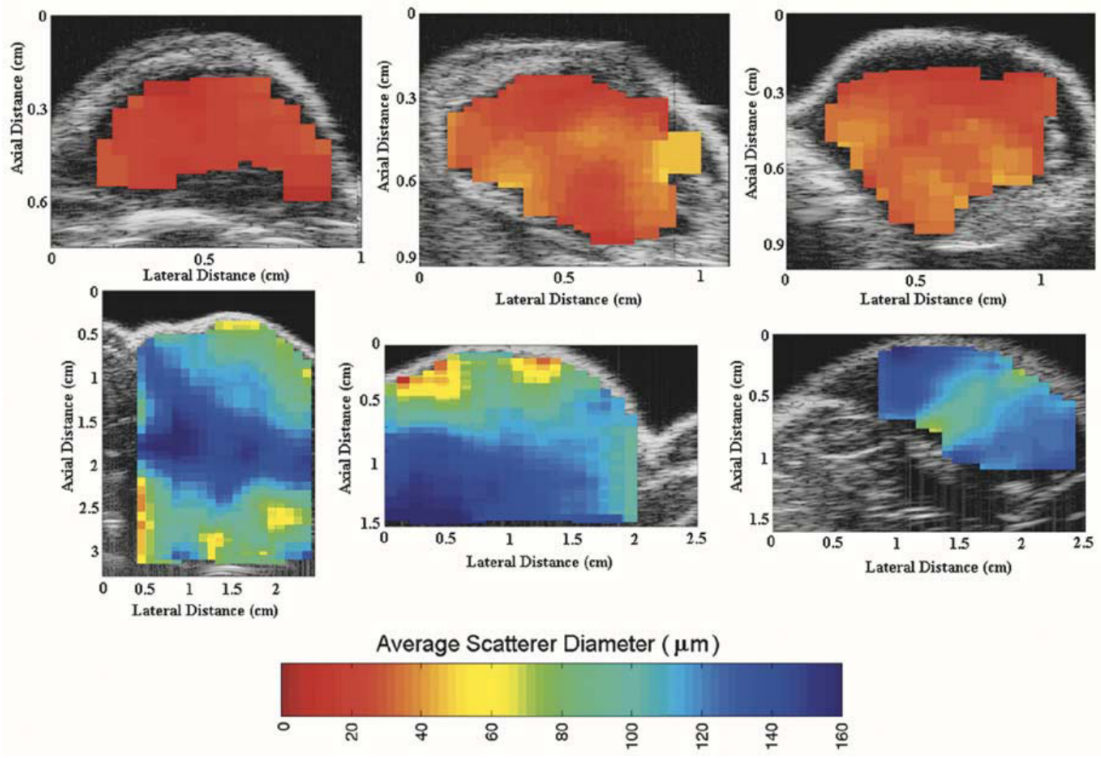

Figure 2.4: QUS images of mouse carcinomas (top panel) achieved at 20 MHz and rat fibroadenomas (middle panel, 8.5 MHz) using the mean ESD. The color bar shows the relation between the color encoding and the ESD. Reproduced from Oelze et al. [31]

simplified geometries implied in this model, the SGM remains widely utilized, probably due to its ease of computation [4]. Indeed, recent investigations have reported successful implementations of the SGM, even when compared to more recent and sophisticated mod-

els [29].
The physical meaning behind the SGM parameters comes at the expense of multiple approximations such as Born, far-field, incident plane wave and isotropic medium with randomly and independently distributed scatterers [29] (see Chapter 3). Although these assumptions may appear restrictive, these hypotheses are commonly applied in BSC parametrization and ES. All the models that will be introduced below rely on these approximations as well.

The Fluid-Filled Sphere model

In parallel, successful applications of another model were reported to describe the scattering from biological structures. One of the first appearances of the analytical expression of the Fluid-filled sphere model (FFSM) was given by Bracewell et al. [32]. It models the scattering from a fluid sphere in a homogeneous medium under the same hypotheses as mentioned above. The FFSM is also parametrized by the scatterer radius and the acoustic concentration in the monodisperse case. Muleki-Seya et al. [5] reported an estimation of the nuclei size with relative errors less than 7% in canine livers through the FFSM. In this case, the measured BSC was modeled as the incoherent contribution of individual scatterers. This implies the measured BSC to be linearly proportional to the scatterer density. However, the use of the FFSM appeared unsuccessful in concentrated media. Oelze et al. [33] illustrated this point using a hypercellular model of mammary cancer (carcinoma 4T): the FFSM extracted a nucleus size equal to 47 µm while the expected cell size was 13 µm. This overestimation suggested that the ultrasound backscattering signals from dense media such as tumors might not be modeled by incoherent spectra only [34].

The Concentric Fluid Sphere model

In the early 2010s, McNew et al. [35] derived the analytic expression that describes scattering from two concentric fluid spheres randomly spatially distributed. They approximated the cell geometry with one inner sphere and one outer sphere that represent the nucleus and its cell respectively. The concentric model is parametrized by nine coefficients: the radius of each sphere, the mass density, the sound speed of each sphere with the surrounding medium and the scatterer number density. One year later, Teisseire et al. [36] obtained decent approximations of both the nucleus and the cell radius using this model on Chinese hamster ovary (CHO) cell pellet biophantoms with volume fractions up to 3%. They used two mono-element transducers with center frequencies at 40 MHz and 80 MHz to estimate the BSC across the 25 - 100 MHz frequency range. The concentric model led to nuclear radii between 0 and 6 µm (histology 2 - 4.6 µm) and cell radii between 6 and 7 µm (histology 5.7 - 8.3 µm). A follow-up study from the same group investigated the performances of the concentric model using dense CHO cell pellet biophantoms with volume

fractions up to 63% [37]. Figure 2.5 summarizes the results of their inversion procedures and shows the extracted values for the six independent parameters.

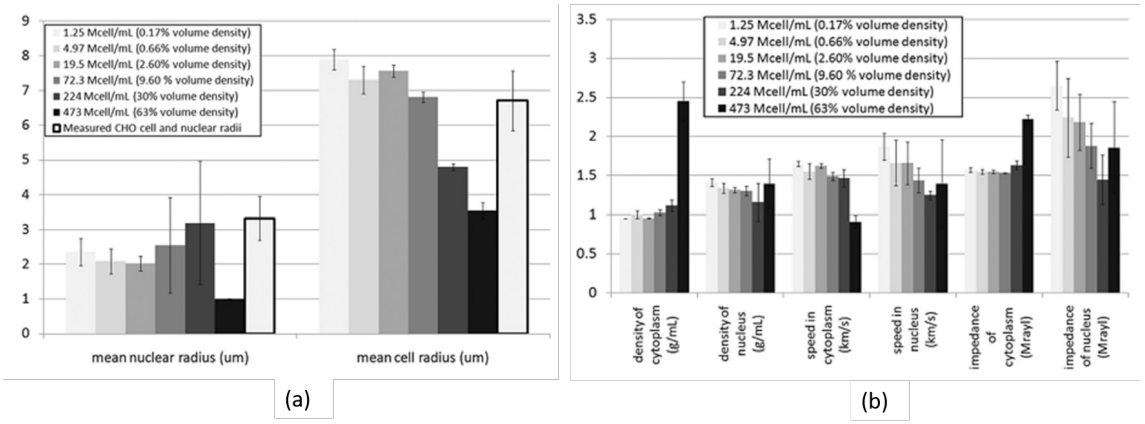

Figure 2.5: Estimated parameters extracted by the concentric sphere model. (a) Estimated versus reference nuclear and cell radii. (b) Estimated acoustic properties of the nucleus and cytoplasm. Reproduced from Han et al. [37]

The impedances are computed as the product between densities and sound speeds. The nucleus and the cell radii are compared to histological analyses. The low cell concentrations yielded correct nucleus and cell sizes while it turned out to be more difficult for concentrated biophantoms (Figure 2.5, a). The critical threshold suggested in this paper is between 10% and 30%. Coherent scattering is cited as one of the most likely reasons to explain this breakdown of the concentric model. Indeed, the assumption of random cell positions becomes less valid as cells get closer to each other. Moreover, the authors reported discrepancies between acoustic impedances in their previous study. Indeed, the extracted acoustic impedance of the nucleus for the lower concentrations ranges between 1.9 and 2.6 MRayl in this study versus $\approx$ 1.6 MRayl in Teisseire et al. [36]. Among other reasons, they argue that the concentric model might be less sensitive to sound speed and density than to cell and nucleus sizes, making this tool potentially unsuited for determining these coefficients. In summary, the concentric model is a nine-parameter BSC model that leverages the *a priori* known geometry of a cell and its nuclei. It appears more relevant in determining the nucleus and cell size at low concentrations.

The Structure Factor models

The previous models do not cover the case of dense media. Indeed, it can be assumed that the scatterer position correlation increases with their concentration [38]. When the scatterers are not randomly spatially distributed, structural effects affect the ultrasound backscattering and the BSC is no longer the incoherent sum of the contributions of each scatterers. To take this concentration and coherence effects into account, the incoherent BSC signal can be modulated by a structure factor. In quantitative ultrasound, the use of

	Cell line	Frequency bandwidth	Models	$\bar{r}^* \pm \mu^*(\mu m)$	$\lvert \gamma_z^* \rvert$	Normalized errors
1	K562	10–42 MHz	FFSM	4.48 ± 0.00	0.112	0.116
2	K562	10–42 MHz	PM	4.03 ± 1.15	0.137	0.053
3	K562	10–42 MHz	SFM	6.40 ± 1.44	0.051	0.029
4	CHO	26–105 MHz	FFSM	5.04 ± 1.18	0.073	0.108
5	CHO	26–105 MHz	PM	4.02 ± 1.67	0.101	0.183
6	CHO	26–105 MHz	SFM	5.47 ± 1.07	0.068	0.077
7	CHO	26–56 MHz	FFSM	3.83 ± 1.39	0.094	0.196
8	CHO	26–56 MHz	PM	3.67 ± 1.56	0.124	0.069
9	CHO	26–56 MHz	SFM	6.04 ± 1.11	0.057	0.054

Table 2.1: Estimated parameters given by the FFSM, PM, and SFM in the polydisperse case. The actual mean nucleus and cell radii were found to be equal to 4.18 ± 0.43 and 6.34 ± 0.94 µm, respectively for the K562 cells. The actual radii of nuclear and CHO cells are 3.32 ± 0.63 and 6.71 ± 0.86µm, respectively. Reproduced from Franceschini et al. [40]

a structure factor was initially investigated for blood characterization. Indeed, the degree of red blood cell aggregation can indicate inflammatory or abnormal circulatory conditions [4]. While extensive literature can be found on this topic [4, 24, 34], our focus will be on the applications of the structure factor in dense solid media, excluding cell suspensions. Franceschini et al. [39] reported the first use of a Structure Factor Model (SFM) to extract the scatterer concentration in concentrated tissue-mimicking phantoms composed of monodisperse microspheres. Firstly, the SFM outperformed other incoherent models such as the SGM to describe the BSC magnitudes at concentrations spanning from 1% to 25%. Secondly, the SFM led to the best estimations (relative errors less than 38%) of volume fractions at actual concentrations ranging from 10% to 25%. However, this satisfying result was obtained through the combination of another quantitative parameter, highlighting the limitations of the SFM to differentiate between low and high concentration cases when used independently. A follow-up study from the same group investigated the SFM's capability to describe the BSCs from concentrated cell pellet biophantoms [40]. In this study, they accounted for the cell size polydispersity in all models. Once again they reported the superiority of the SFM over the FFSM and the Particle Model (PM) in fitting the measured BSC and extracting both the scatterer size and the relative impedance contrast. Table 2.1 shows that SFM minimized the normalized error between the measured and the fitted BSCs for each case. This study also showed that the cells can be identified as isolated scatterers while numerous studies reported the cell nuclei as main scattering structures [34].

Two years later, Franceschini et al. [41] conducted a similar study and compared the performances of FFSM, SGM with SFM on cell pellet biophantoms composed of human leukemia K562 cells. They designed biophantoms with multiple cell volume fractions. They reported the superiority of the SFM in terms of quality of data fitting and agreement with the true values for both sparse and concentrated phantoms (from 0.006 to 0.30).

The same year, Muleki-Seya et al. reported one of the first applications of structure factor models on excised tumors. QUS estimates extracted from the 12 - 40 MHz frequency range from the SGM, FFSM and the SFM in the monodisperse case [5]. In canine livers, the scatterer radius extracted from the three models showed good agreement with the nucleus sizes estimated by histological analyses (relative errors less than 7%). The authors argue that the liver could be modeled as a sparse medium to explain the successful applications of incoherent BSC models. Thus, nuclei may be the predominant scatterers in this case. Muleki-Seya et al. also carried out the same protocol over homogeneous xenograft mouse tumors that contain HT29 cells. The scatterer radius estimated with the SFM matches the histological results with relative errors of less than 15%. Conversely, the SGM and the FFSM led to inconsistent estimates. The authors suggest that densely packed HT29 cells may be the main scatterers in this case.

More recently, Franceschini et al. applied QUS techniques to characterize *ex vivo* rabbit liver fibrosis [29]. Higher ESD values were reported in fibrotic livers when compared to healthy livers for the two working frequency ranges (10 - 20 MHz and 10 - 40 MHz). They also observed that EAC decreased with increasing fibrosis grade. Interestingly, the SGM outperformed the SFM model for the specific task of grading. Indeed, even sophisticated scattering models such as the polydisperse structure factor model did not describe the measured BSCs.
One should note that the SFM was employed as a generic term to refer to BSC theoretical models that are modulated by structure factors. Indeed, Francheschini et al. used the Faran model (suited for elastic scatterers) in the phantom study [39] while the FFSM was used in the cell pellet study [40]. Similarly, the SFM analytical expression can be derived in the size monodisperse or polydisperse case [41].

Size polydispersity and structure factors

One year later, Han et al. [38] investigated the effect of size polydispersity over the structure factor. They applied an ingenious technique to isolate the experimental structure factors from BSC measurements. To do so, they designed one concentrated cell pellet biophantom and its sparse equivalent, composed of the same cells. The structural effects caused by the spatial arrangement of the scatterers were extracted by computing the quotient of the BSC of the first phantom with its corresponding incoherent BSC measured on the sparse phantom. Figure 2.6 (a) shows the experimental setup used in this study. A single-element transducer insonified the cell pellet biophantoms over the 11 - 105 MHz frequency range. They fitted their structure factor measurements with new analytical models, namely the polydisperse I (PI) and the polydisperse II (PII) models. In the PI model, the scatterers are assumed to be polydisperse in size but monodisperse in scattering amplitudes while they are both polydisperse in the PII model. Polydisperse I describes an unrealistic model but is considered as a valuable approximation for ease of computation. Using the polydisperse models, Han et al. extracted the scatterer mean radius and the

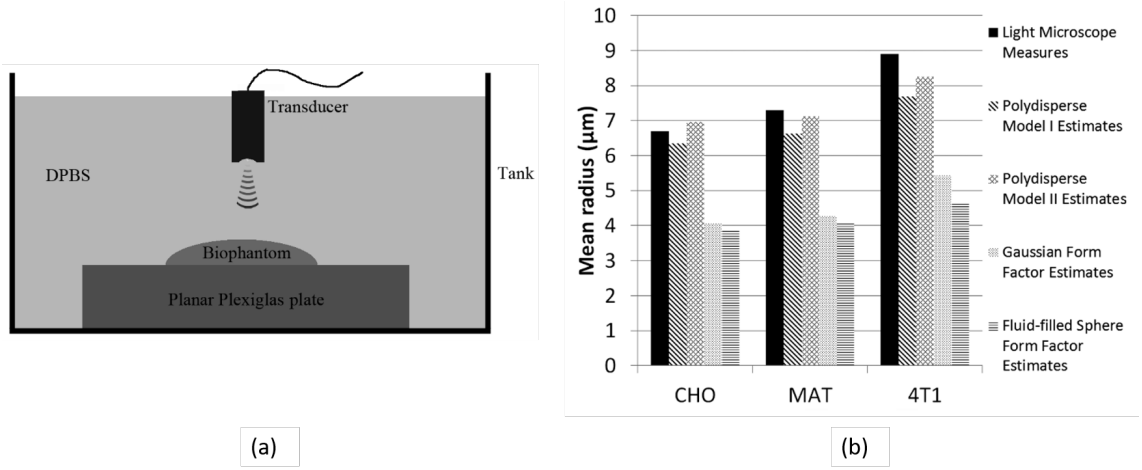

Figure 2.6: (a) Diagram of the experimental setup for BSC measurements. (b) Comparison between the estimated effective scatterer radius using SGM, the FFSM and the estimated mean cell radius from two polydisperse structure functions models PI and PII. Light Microscope measures give reference cell sizes. Reproduced from Han et al. [38]

Schulz width factor (somewhat the sharpness of the size distribution). They use the volume fraction as *a priori* known parameter to facilitate the inversion procedures. The estimated scatterer radius from the SGM and the FFSM are shown in Figure 2.6 (b). One should keep in mind that PI and PII estimates were extracted on experimental structure factors while the other radii came from conventional BSC measurements. The two polydisperse models led to more accurate inversions compared to the BSC models. The authors emphasized that the BSC-related coefficients may potentially reflect the size of the cell nuclei. Conversely, the estimated scatterer size can be related to cells with less doubts because PI and PII take into account the spatial position scatterers, which are affected by cells and not the nuclei [38].

This elegant way of measuring the structure factor with two biophantoms of different concentrations was useful for studying the effect of polydispersity. However, the protocol in this paper cannot be conducted in clinical applications. Nonetheless, Han et al. [38] provided a structure factor expression to model the ultrasound backscattering of polydisperse scatterers in concentrated media. The latter can be combined with the Fluid-Filled sphere form factor to fully model the BSC in dense polydisperse media. In this case, the BSC becomes a function of the following parameters of interest: the scatterer mean radius, the Schulz width factor, the volume fraction and the impedance contrast.

2.2.2 Envelope statistics

While the BSC parametrization extracts spectral-based parameters, Envelope Statistics (ES) entails in estimating the shape and attributes of the envelope of the ultrasound backscattering signals, leading to additional scattering parameters. To do so, the Probabil-

ity Density Function (PDF) of the measured envelope can be fitted to known distributions such as Nakagami distributions.

Physical interpretations of envelope parameters

The physical interpretation of the envelope parameters is not as straightforward as the BSC-related parameters mentioned above. In a simulation study, Saha and Kolios [42] suggested that the shape of an envelope histogram depends on the spatial organization of scatterers and the bandwidth of the ultrasound pulse. Indeed, they observed that constructive or destructive interferences resulting from the periodicity in the scatterer arrangements may impact the ultrasound backscattering echoes. Multiple envelope models were extensively studied to describe the backscattering echo in ultrasound imaging [4]: the Rayleigh distribution, the Rician distribution, the K-distributions to name just a few. However, the physical meaning of the associated envelope parameters could be limited in some cases, such as the vanishing of the incoherent signal [43]. Conversely, the Homodyned-K (HK) distribution is parametrized by coefficients that hold their physical meaning in various configurations, making the interpretation of its estimates more reliable. The Nakagami distribution is another model that can be seen as an approximation of the Homodyned-K distribution [24]. These two distributions are the most commonly used models for ultrasound signal envelopes [44]. In the Nakagami distribution, the scaling factor Ω_{nak} and the Nakagami parameter α_{nak} represent the mean backscattered intensity and a measurement of the number of scatterers per resolution cell (i.e. the smallest resolvable volume by the probe) respectively [44]. The HK distribution can also lead to estimates of the scatterer concentration through the parameters μ_{hk} and can additionally provide measurements of the coherent-to-diffuse signal ratio k_{hk} [45]. The latter can describe the degree of scatterer spatial arrangements within a Region-of-Interest (ROI). The HK μ_{hk} parameter successfully characterizes sparse media (typically less than 10 scatterers per unit volume) [44]. However, its physical interpretation can be discussed at higher volume fractions. Cristea et al. [44] reported a simulation and a phantom study to investigate the extent to which the parameters α_{nak} and μ_{hk} could reflect the number of scatterers per resolution cell. They observed that μ_{hk} is more sensitive to the volume fraction and saturates less quickly than α_{nak} when the number of scatterers per resolution cell is increasing. Thus, the HK parameter μ_{hk} may outperform its Nakagami equivalent in concentrated media.

Illustrative application

Recently, Zhou et al. [46] investigated the sensitivity of the envelope parameters μ_{hk} and α_{nak} to the severity of hepatic steatosis. Using a linear array with a center frequency equal to 7 MHz, they estimated these QUS estimates over 66 steatotic rat livers. B-mode images were color-encoded to create parametric images for each grade (Figure 2.7, a and b). Both the HK and the Nakagami parameters increase with the severity and showed correlations with the steatosis grade ($R^2 = 0.68$ and 0.76 respectively, Figure 2.7, c and d).

In summary, Envelope Statistics provide quantitative parameters that can successfully characterize tissue microstructure. Envelope parameters can be extracted from the same ROI as other BSC-related estimates but are sensitive to different features such as the scatterer spatial organization. In the next section, we will see that QUS studies that combine all the previous parameters can lead to enhanced tissue assessments

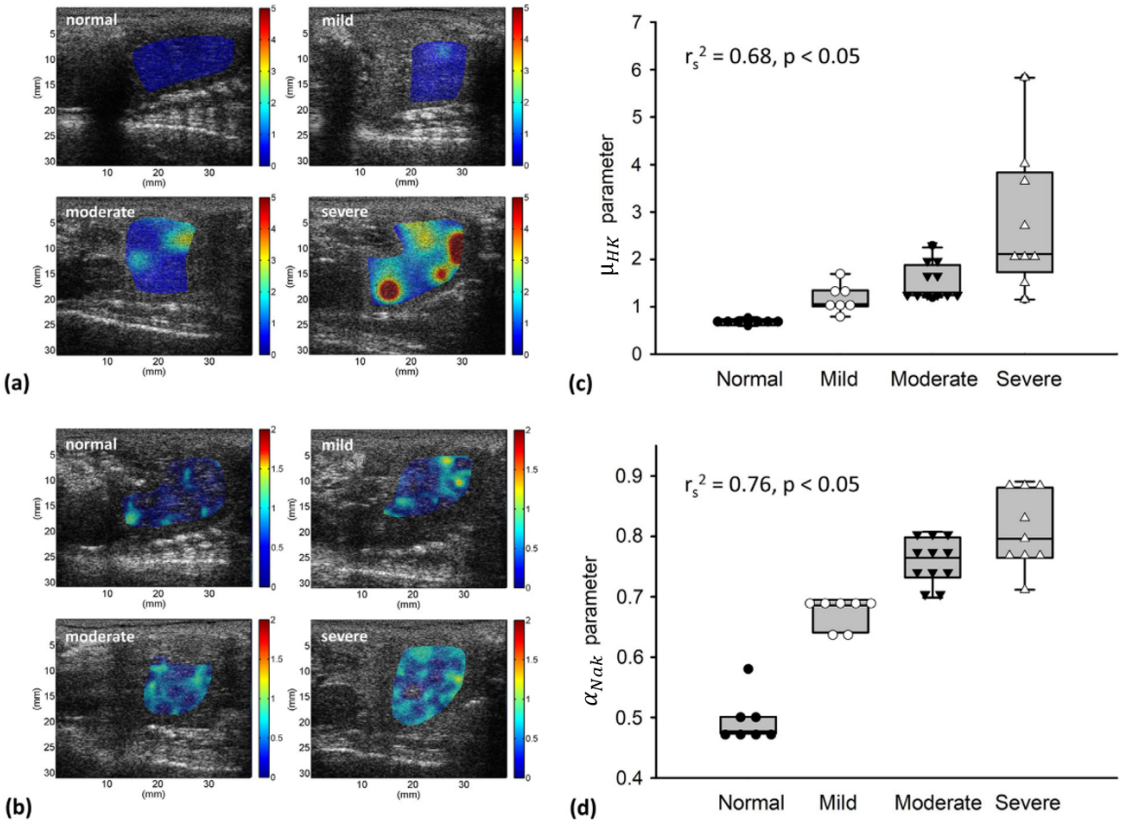

Figure 2.7: (a)–(b) The μ_{hk} and α_{nak} parametric images at different stages of hepatic steatosis: normal, mild, moderate, severe. (c)–(d) Box plots of the μ_{hk} and α_{nak} parameters, respectively. Adapted from Zhou et al. [46]

2.2.3 Successful applications

Cancer characterization

One of the first QUS applications for cancer characterization was reported in the 80s. Feleppa et al. [47] observed the increase in the scatterer size in cancerous tumors and used the ESD as a biomarker of malignancy. One year later, the EAC was used to discriminate ambiguous cases of cancerous conditions [27]. In a multiparametric study, Oelze et al. [48] combined BSC-related and envelope-related parameters to classify three kinds of rodent models of mammary cancers using a singe-element transducer with a center frequency of 20 MHz. Figure 2.8 shows that the ESD, the scatterer clustering parameter μ

and the coherent-to-diffuse signal ratio k_{hk} they measured allowed them to identify three non-overlapping clusters in each tissue type, making these QUS parameters promising biomarkers for breast cancer characterization.

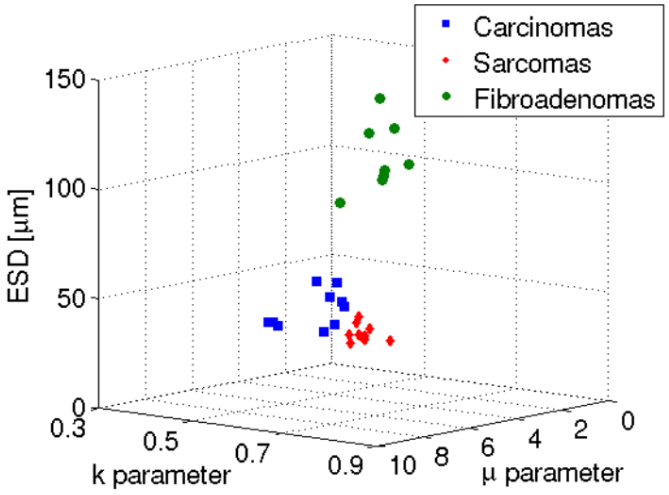

Figure 2.8: Feature analysis plot of the ESD versus μ_{hk} versus k_{hk} parameter. Reproduced from Oelze et al. [48]

A similar study conducted by the same group for thyroid cancer characterization was reported [49]. Measurements were performed on mice excised thyroids using a mono-element transducer with a center frequency of 40 MHz. Once again, the combinations of the QUS parameters ESD, EAC and μ_{hk} allowed them to observe statistical differences between two thyroid cancer types and healthy thyroids in the 25 - 45 MHz frequency range. However, the coherent-to-diffuse signal ratio k_{hk} did not appear as a relevant biomarker in this study. Additionally, although some correlations were observed, the estimated ESD does not correspond directly to the expected sizes of cellular structures.

Mamou et al. conducted multiple studies about lymph node characterization for the detection of micrometastases. Indeed, the cancer staging directly reflects the cancer spread and is of critical importance for proper diagnosis. Firstly, 46 excised lymph nodes from colorectal cancer patients were 3D-scanned using a mono-element transducer with a center frequency of 25.6-MHz [26]. Histological analyses were conducted for reference. The ESD, EAC, the LF slope and intercept were estimated on the measured BSCs. Fully metastatic nodes were perfectly discriminated based on the ESD and the LF slope (Figure 2.3). Metastatic nodes led to an average ESD significantly higher ($p < 0.05$) than the normal lymph nodes. Once again, an increase in the scatterer size due to cancerous conditions was reported. One year later, measurements over 112 lymph nodes were conducted using the same experimental protocol. Envelope parameters were also estimated. Multiple combinations of the four QUS parameters were tested to classify them. The best one appeared to be the combination of ESD with the coherent-to-diffuse signal ratio k_{hk}. The latter brought an area under the ROC curve of 0.996 with specificity and sensitivity

of 95%, thus showing the power of QUS multi-parametric studies for detecting malignant lymph nodes. These promising results led to the development of a graphical user interface, called *Lymph Explorer* [50], to guide pathologists towards suspicious regions. This study also reported excellent classification over 250 excised lymph nodes. Similarly, the same QUS estimates were combined to estimate the degree of malignancy. The areas under the ROC curves exceeded 0.95 for gastrointestinal nodes and 0.85 for nodes of breast cancer patients. An example of *Lymph Explorer* screenshot shows the cancer probabilities (Figure 2.9) computed from QUS estimates and a microphotograph of the histological slice of the corresponding lymph node.
Lymph Explorer showed an example of how QUS techniques could be routinely used in clinics for *ex vivo* applications. However, the previous results rely on high frequency analyses, which may impact the acceptance in clinical settings. Recently, Hoerig et al. addressed this issue and reported the first *in vivo* classification of metastatic lymph nodes at clinical frequencies [51]. The same QUS estimates were extracted after ultrasound measurements from 19 patients using a 10-MHz linear probe and were used to train Machine Learning classifiers. ESD and EAC were reported as the most effective biomarkers to detect malignant lymph nodes (area under the ROC curve 0.94)

These lymph node studies can be considered as illustrative examples of the performances of QUS techniques for cancer characterization. Interestingly, the classification results reported in these studies rely on the combinations of a few QUS estimates. Furthermore, it could be noted that most of the parameters are extracted from models with simple analytical expressions, thereby limiting the computational time for inversion procedures. Hence, it is important to keep in mind that the the high classification performances reported in these studies rely on overall low computational complexities.

Therapy monitoring

The non-invasive nature of BSC parametrization techniques makes them suitable for therapy monitoring applications [24]. Indeed, QUS estimates can be mapped over conventional B-mode images to assess the tumor responsiveness, and thus, help clinicians in their decisions related to treatments at the early stage of a therapy. The first experimental QUS applications for longitudinal studies were reported in the early 2000s [52, 53]. Kolios et al. [53] estimated the Lizzi Feleppa parameters and the ESDs from BSCs measured on cell pellets exposed to chemotherapeutics from 22 - 47 MHz to monitor apoptosis. They reported an increase in the LF slope and the LF midband value with time after drug exposure, while the ESD was decreasing. A few years later, Banihashemi et al. [54] reported the first *in vivo* application of QUS to detect apoptosis in melanoma tumors undergoing photodynamic therapy. They observed a strong correlation over time between variations in the LF slope with changes in the cell nucleus size measured by histological analyses. More recently, Sannachi et al. [55] conducted a clinical study that aimed at predicting the

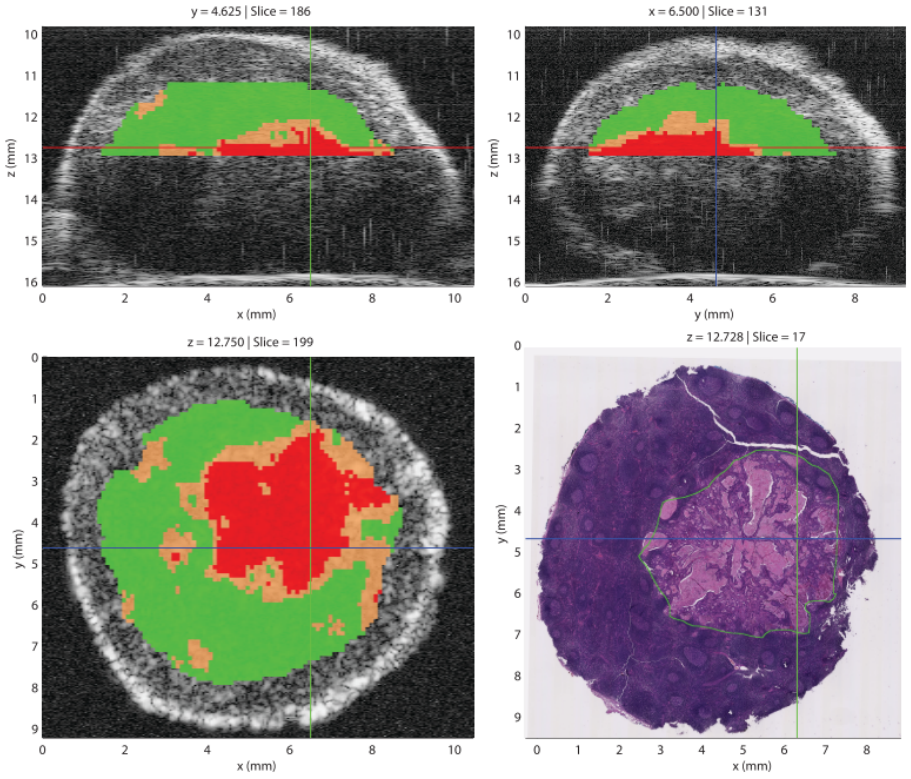

Figure 2.9: Illustrative Lymph Explorer screen capture providing visual representations of cancer probabilities. These results were derived from a lymph node affected by colorectal cancer, demonstrating partial metastasis. Within the three QUS images, areas marked in red signify cancer probabilities exceeding 75%, while those in green represent probabilities under 25%, and those in orange depict probabilities falling between 25% and 75%. In the histology image, the green outline demarcates the metastatic region. Reproduced from Mamou et al. [50]

early response of 30 breast cancer patients to chemotherapy. To do so, they estimated the ESD and EAC on BSCs measurements performed with a clinical imaging system operating from 4.5 to 9 MHz. QUS estimates were reported at different weeks after the beginning of chemotherapy and just before surgery. Significant variations in the EAC values were observed in patients responding to therapy, contrasting with non-responding patients (Figure 2.10, a). Significant variations were only observed at week 8 for ESD values (Figure 2.10, b).

Thus, QUS estimates can probe cellular death mechanisms non-invasively, making QUS techniques powerful for treatment monitoring applications

In recent years, there has been a growing interest in the applications of machine learning techniques in multi-parametric QUS studies, including lymph node classification [51], prostate cancer imaging [56] or fatty liver diagnosis [56]. Taleghamar et al. [57] reported the use of an unsupervised learning method to predict breast cancer response to chemotherapy prior to the start of treatment using the ESD, EAC, LF midband value and LF intercept,

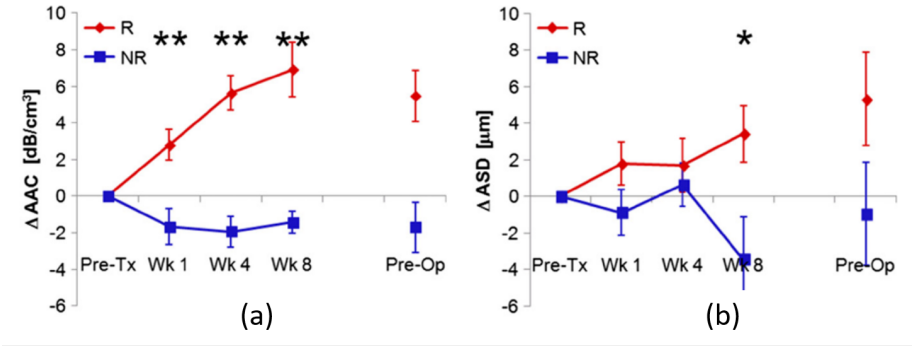

Figure 2.10: EAC (a) and ESD (b) parameters measured in treatment responders and non-responders over during the course of the treatment. Error bars represent the mean ± one standard error.** ($p < 0.005$) and * ($p < 0.05$) represent the significant difference between responders and non-responders based on ANOVA test. R: Responder; NR: Non-Responder; Pre-Tx: Pretreatment; Pre-Op: Preoperation. Reproduced from Sannachi et al. [55]

extending the previous study mentioned above [55]. They observed that the biomarkers derived from the entire tumor core may predict the treatment response of patients with an accuracy of 74.5% with an area under the ROC curve of 0.79. For comparison, conventional clinical features led to an accuracy of 69.1% and an area under the ROC curve of 0.6. One year later, Taleghamar et al. [58] improved the performances using a deep learning technique for the same application, using the same four QUS estimates. They obtained a response prediction with an accuracy of 88% and an area under the ROC curve of 0.86.

In summary, we described theoretical BSC scattering models of various complexity that successfully characterized different tissue types. Remarkable agreements were also reported between the ESDs and the actual size of cellular components, showing that a physical interpretation can be attributed to this parameter. Therefore, the increase in the cell and the nucleus sizes associated with dysplasia may be detected using this parameter.

The volume fraction of BSC models, the Nakagami parameter α_{nak} and the scatterer clustering parameter μ_{hk} can carry interesting physical meanings since they can reflect the scatterer density. It is noteworthy that cancerous tissue can be characterized by an abnormal cell density and could potentially be detected using these parameters.

The BSC structure factor and the coherent-to-diffuse signal ratio k_{hk} are sensitive to the scatterer spatial organization. Notably, a chaotic cell organization can be characteristic of undifferentiated tissues and that could be therefore detected using these parameters.

Additionally, other BSC and envelope parameters may act as robust biomarkers of malignancy. Thus, the BSC parametrization and ES appear as relevant techniques for cancer characterization. Their implementations are described in the next chapter.

2.3 Light scattering for tissue diagnosis

This section aims to provide an overview of the light scattering methods for cancer diagnosis. A vast literature exists on this topic. Thus, the following part will focus on the *in vivo* studies or the applications that have the potential of being employed in living tissues, excluding microscopy applications. After introducing the key principles of different optical methods, the different implementations of light backscattering spectroscopy will be analyzed chronologically.

2.3.1 Pioneer studies in Light Scattering Spectroscopy (LSS)

The identification of the main scattering structures in biological samples represents a fundamental issue in biophotonics. In the 90s, mitochondria were reported as predominant scatterers in the liver [59] and in fibroblasts [60]. Other papers studied the extent to which cell nuclei could be identified as scatterers [61,62]. However, none of these methods provided size measurements of the probed organelles [63]. Moreover, they could not be applied in living tissues. The first studies about the size estimations of organelles and the refractive index measurements were reported in the late 90s [64,65].

Perelman et al. [64] described an elegant way to estimate the nuclear size distribution from unpolarized reflectance measurements using the Fourier transform. In this study, an optical probe composed of one excitation fiber and six collection fibers detected the tissue backscattered light in the visible range (Figure 2.11). The probe tip sampled tissue over a circular spot of approximately 1 mm^2 in area. The single scattered component of

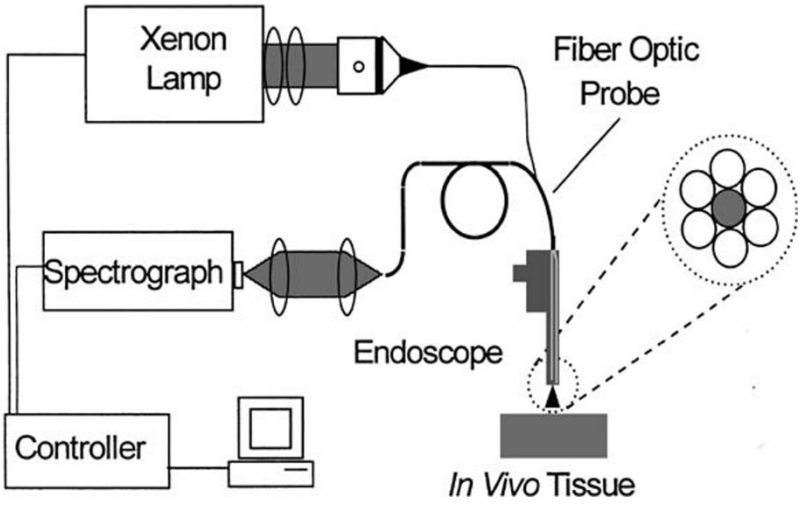

Figure 2.11: Schematic diagram of the LSS system used by Perelman et al. [64] and Wallace et al. [66]. This instrument allowed endoscopic applications.

light was extracted after model-based diffusive background removal. Thus, assumptions about the hemoglobin absorption and the scattering properties from the underlying tissues were needed. The periodicity of the resulting spectra presented fine oscillations that were then related to nucleus diameters under the Van de Hulst approximation [64]. Using Mie

Theory, the nuclear size distributions of normal and cancerous colon cells were successfully extracted at the expense of assumptions about the nucleus-to-cytoplasm relative refractive index and the cytoplasm refractive index values. This approach is termed as Fourier transform-based analysis

Another analytical procedure referred to as Mie Theory-based analysis can also lead to the nuclear size distribution. Backman et al. [65] estimated the nuclear size distribution of intestinal malignant and normal cells using a bench-top instrument with bulk optics and a spectrometer *in situ*. Healthy cells present uniform and circular shapes while cancerous cells are enlarged and show more variations in size (Figure 2.12, a). In this study, a polarized discrimination technique was used to isolate the single scattered component of the probed tissue. The predictions of Mie Theory were then fitted to the experimental data, resulting in the estimations of three parameters: the mean scatterer radius, the standard deviation in size (assuming a Gaussian distribution) and the relative refractive index. The size-related parameters were extracted with an accuracy of about 0.1 µm (Figure 2.12, b). One thousand to ten thousand cells were approximately probed in a single LSS measurement [65]. Contrary to the previous study, the background removal technique used here does not rely on assumptions about the probed tissue, making this approach theory-independent and applicable to different kinds of tissues. However, the successful inversion procedures achieved in this study came at the expense of the assumed Gaussian size distribution of the nuclei while the Fourier transform-based analysis does not require such approximation. A few years later, Backman et al. [67] introduced LSS imaging, which adds

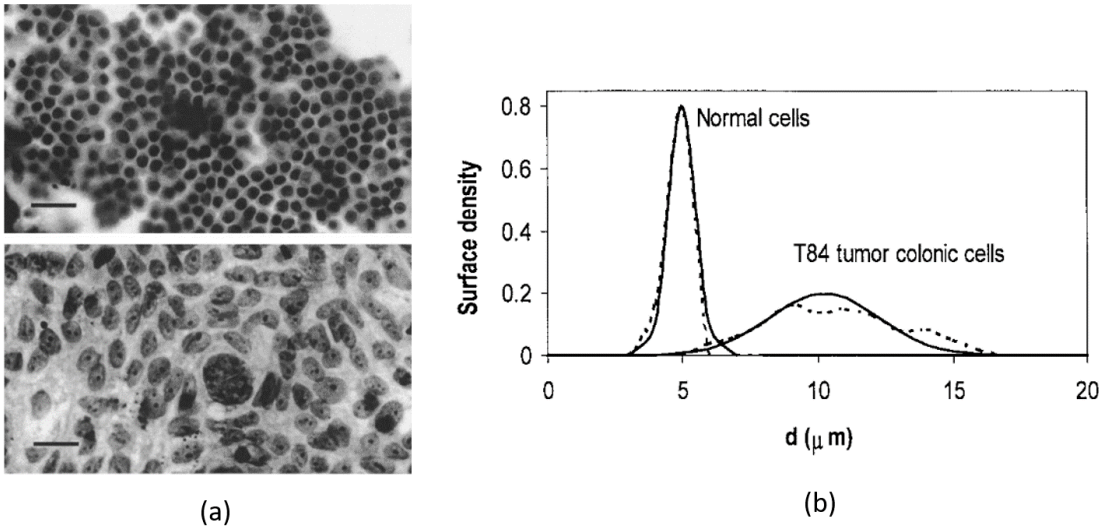

Figure 2.12: (a) Microphotographs of normal intestinal epithelial cells (top) and intestinal malignant cell line T84 (bottom). Scaling bars: 20 µm. (b) Nucleus size distributions for T84 intestinal malignant cells and normal intestinal cells. In each case, the solid line represents the distribution extracted from the light scattering technique and the dashed line is the reference distribution measured using light microscopy. Adapted from Backman et al. [65]

spatial dimensions to the LSS spectrum by replacing the spectrograph with a CCD camera. In this study, the LSS image of a cell monolayer showed morphometric measurements of the nuclear size with excellent agreement when compared to the corresponding light microscope measurement over a field of view of 125x275 µm. This study also introduced the scattering angle-sensitive LSS (a/LSS), which can be considered as a precursor to Low Enhanced Backscattering Spectroscopy (LEBS) discussed in detail in subsection 2.3.3. The purpose of a/LSS was to measure subcellular structures at submicron scales. Wallace et al. [66] reported one of the first clinical applications of LSS for *in vivo* detection of dysplasia associated with Barrett's esophagus. In this study, the authors collected and analyzed 76 reflectance spectra from 13 patients with suspected adenocarcinoma, following a methodology similar to that employed by Perelman et al. [64]. The endoscope was brought into contact with the patient's esophageal mucosas. They built a diagnostic algorithm that classified samples into 4 histologic categories: nondysplastic Barrett's, indefinite for dysplasia, low-grade dysplasia (LGD) and high-grade dysplasia (HGD). They obtained a 90% sensitivity and 90% specificity for detecting LGD and HGD. These pioneer studies showed that LSS has the potential to detect cancerous epithelial cells at an early stage without tissue resection, thus making the technique minimally invasive.

2.3.2 Toward real-time LSS diagnosis

The next challenge was to make the LSS *in vivo* size measurements real-time for intra-operative applications using a resource-efficient instrument. Qiu et al. [9] developed an endoscopic scanning LSS instrument that was able to diagnose the precancerous dysplasia of the esophageal mucosas in near real-time (Figure 2.13, a). This study aimed to provide biopsy guidance to address the low probability of detection of Barrett's esophagus using standard methods. Previous LSS instruments were able to probe a small part of tissue (1 mm^2). Here, the system was able to collect a significant amount of data for a 2-cm segment of Barrett's esophagus in less than one minute [9] (Figure 2.13, b). They used the polarization subtraction technique mentioned in section 2.3.1 to extract the single scattered component of light, thus probing the superficial epithelial layer. The resulting differential polarization signals were then analyzed using an approach somewhat similar to the Mie Theory-based analysis. Qiu et al. [9] followed the analytical procedure described by Fang et al. [68]. This method, initially developed to estimate the sizes of submicron organelles, was used here to measure the nuclear changes induced by dysplasia. The Mie LSS spectra were precomputed for a wide range of scatterer radii by setting the relative refractive index nucleus/cytoplasm to a fixed assumed value. An inversion procedure was then applied to extract the scatterer size distribution from the experimental LSS spectra using a non-negativity constraint (*i.e.* no Gaussian distribution assumed contrary to Backman et al. [65]). To further reduce the computational time, a diagnostic parameter was used to discriminate normal and dysplastic sites. This diagnostic parameter is simply the squared difference between the spectra of the probed sites with the mean of all measured spectra.

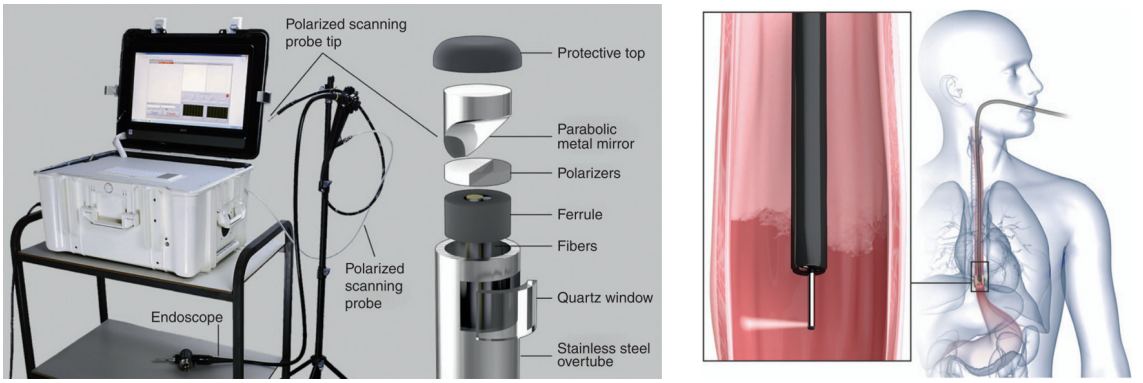

Figure 2.13: (a) Endoscopic scanning LSS instrument developed by Qiu et al. [9]. The photograph on the left shows the point-of-care system on a cart with its scanning probe inserted into a commercialized endoscope. The schematic on the right shows the exploded view of the probe tip with the polarizer and the analyzer combined in a single optical component. (b) Clinical procedure. The LSS instrument performs fast rotational and longitudinal scans of the suspected Barrett's esophagus area. Figures reproduced from Qiu et al. [9]

This approach is based on the fact that the spectra of normal sites are dominant. Thus, the diagnostic parameter takes low values when a healthy area is probed. Conversely, the larger dysplastic nuclei strongly affect the LSS spectrum of cancerous regions, thus increasing the diagnostic parameters values. Hence, threshold values can be set to quantify the degree of malignancy of Barret's esophagus segment. The diagnostic parameters are mapped along the azimuthal angle and the distance from the front teeth in the upper jaw in Figure 2.14 (a). Examples of estimated nucleus size distributions and light microscope measurements are shown in 2.14 (c) and (d). An excellent agreement is found between histological reference measurements and LSS estimations. The diagnostic algorithm built in this study diagnosed correctly 55 out of 57 patients, making this tool relevant for biopsy guidance. More recently, Pleskow et al. [69] reported an *in vivo* detection of bile duct pre-cancer with an endoscopic LSS instrument similar to the one used by Wallace et al. [66] (Figure 2.11). In this study, they combined diffuse reflectance microscopy and LSS with a diagnostic parameter. Malignant transformations was detected with 97% accuracy over 29 patients.

One should note that LSS applications can also be found in confocal microscopy [70,71]. The first study reported the use of an incoherent light source to detect the sizes of two different organelle types in aqueous solutions, following a post-processing procedure close to the one described by Fang et al. [68]. A few years later, Qiu et al. [72] demonstrated the superiority of coherent confocal light absorption and scattering spectroscopic (termed as C-CLASS) over its incoherent version. The C-CLASS technique recently led them to characterize microstructures beyond the diffraction limit [73]. They additionally evaluated the sensitivity of the C-CLASS technique to the degrees of aggressiveness exhibited by two

distinct cancer cell types. This evaluation aimed to identify the different cancer grades in excised tumors without the need for labeling agents.

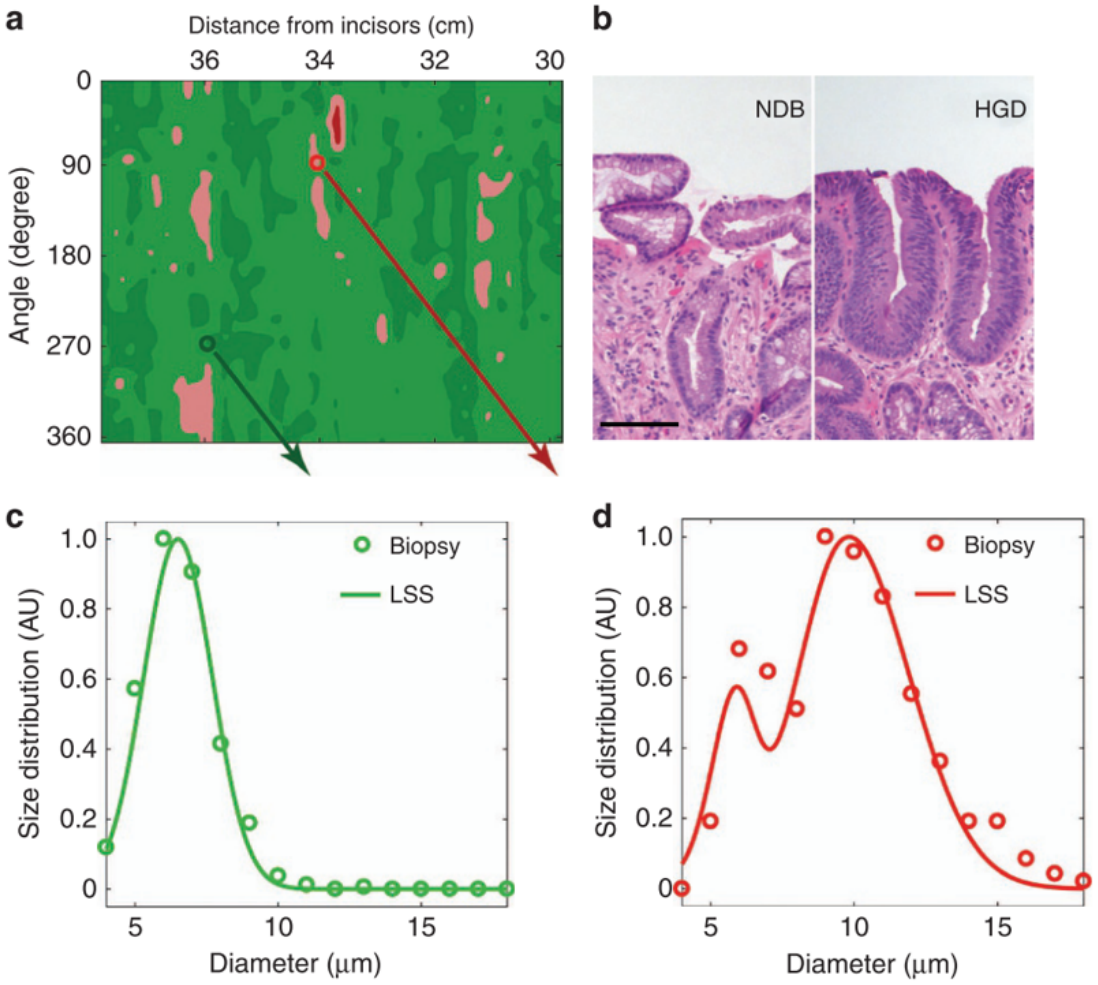

Figure 2.14: (a) Nucleus size distributions for one dysplastic and one non-dysplastic site in Barrett's esophagus. (a) The map highlights regions with potential dysplasia in red and pink based on nuclear size distributions extracted from backscattering spectra at individual spatial locations. Diagnostic parameter values below 0.05 are represented in dark green, 0.05–0.10 in light green, 0.10–0.15 in pink, and values above 0.15 in red. Two biopsy sites, histologically diagnosed as non-dysplastic biopsy (NDB) and high-grade dysplasia (HGD), are indicated by green and red circles, respectively. (b) Histology images corresponding to the marked biopsy locations are displayed, with NDB on the left and HGD on the right (scale bar: 100 µm). Comparison of nucleus size distributions obtained from light microscopy measurements (circles) of biopsies presented in panel (b) and those reconstructed from *in vivo* LSS data (solid lines) collected at the same NDB (c) and HGD (d) locations. Figures reproduced from Qiu et al. [9]

2.3.3 Low Enhanced Backscattering Spectroscopy (LEBS)

Coherent Backscattering Spectroscopy (CBS) is a non-invasive optical technique used to probe the scattering properties of various materials. Several CBS applications were

reported in the 80s [74], including material sciences [75] for instance. Nevertheless, the investigation of the coherent backscattering phenomenon in biological applications has been limited, primarily due to the technical challenges associated with its observation. Indeed, the CBS peak can be extremely narrow in biological tissue, reaching as low as 0.001°. Moreover, the presence of speckles can mask the signal, making CBS measurement even more challenging. However, after extensive studies of the LSS incoherent spectrum, the early 2000s witnessed the emergence of a new optical method that takes benefits from the light spatial coherence for tissue characterization. Kim et al. [74, 76] reported one of the first modified versions of CBS applied for biological tissues, termed Low Enhanced Backscattering Spectroscopy (LEBS). LEBS involves the analysis of both the spectrum and the angle of the coherent intensity peak that occurs in the backscattering direction. This peak results from the constructive interferences between pairs of multiple scattered photons that propagate along a scattering light path and its time-reversed path, thus accumulating an equal phase. The attributes of the coherent peak can be related to the scattering properties of the sample such as its mean free path or its anisotropy coefficient. In their studies, Kim et al. investigated the capability of LEBS to detect early cancerous alterations in the superficial tissue layer, such as the colon epithelia. These investigations build upon previous research on LSS in the search for a minimally invasive tool able to detect precancerous conditions. Using an experimental setup similar to the LSS benchtop instrument used by Backman et al. [67], Kim et al. [74, 76] broaden the CBS peak using a low-spatial-coherent light source and remove the speckle using a broadband illumination combined with a low-temporal-coherence detection. They reported significant changes in the LEBS spectral slopes in rat colonic tissues 2, 4 and 6 weeks after the initiation of colon carcinogenesis compared to control rat [76] as shown in Figure 2.15 (b). These variations reflect the proliferation of epithelial cells in the lower compartment of crypts in the colon mucosa (Figure 2.15, a). Then, they underscored the depth selectivity of LEBS by probing the cells from the upper compartment which undergo apoptosis. Different variations in the spectral slope were then observed (Figure 2.15, c). The finesse of depth selectivity achieved by LEBS was emphasized in comparison to the limited depth selectivity observed in previous LSS studies, which were unable to differentiate between epithelial and stromal layers effectively. A few years later, several applications reported the use of fiber optic LEBS instruments [77, 78], turning the LEBS technique into a point-of-care tool. These studies concluded that LEBS is sensitive to sub-cellular structures, making this technique suitable for early cancer detection [18]. LEBS was initially presented as a tool capable of providing new biomarkers that could precede the expression of conventional histological biomarkers in the early detection of cancer. However, no existing model provided a comprehensive understanding of the underlying tissue microstructure in relation to the LEBS signatures at that time [76, 79].

A couple of years later, Turzhitsky et al. reported the use of Monte Carlo algorithms to relate LEBS signatures with the scatterer phase functions (**i.e.** the probability of scattering at a given angle) [6]. The Monte Carlo (MC) method provides a solution to the

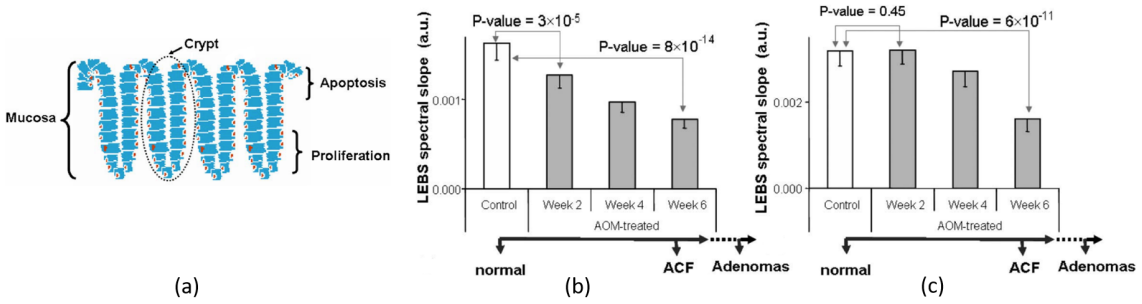

Figure 2.15: (a) Crypt of a colonic mucosa. The depth of a colonic crypt is about 70 µm. LEBS spectral slopes per week after the initiation of colon carcinogenesis in the lower compartment (70 µm deep, b) and the upper compartment (40 µm deep, c). Figures adapted from Kim et al. [76]

radiative transfer equation by taking into account the statistical nature of light propagation. MC simulations are often used as a gold standard to validate light transport models. The simulated LEBS were validated with the experimental measurements performed on aqueous solutions of suspended microspheres using the Mie phase function. They demonstrated the remarkable sensitivity of the Fourier transform of the two-dimensional (2D) LEBS signal, called the radial point spread function, to changes in the phase function. They illustrated the potential of LEBS to detect precancerous tissues by identifying alterations at small length scales in the radial point spread functions between normal and precancerous rat epithelial tissues. One year after, Turzhitsky et al. [80] reported a similar work using a phase function based on the Whittle–Matérn refractive index correlation function. Indeed, the Mie theory can be helpful to describe the scattering properties from suspended microparticles [81] but tissue complexities can make its application difficult for biological samples. As opposed to discrete spherical scatterers in a surrounding medium, another approach models tissues as continuous random media. Thus, the refractive index is no longer discontinuous and follows fluctuations that can be statistically described. Under this assumption, a versatile model that is based on the Whittle–Matérn function to describe the refractive index excess autocorrelation function can be used. Thus, MC simulations enabled a better understanding of the LEBS signature with the sample optical properties, answering the questions raised in the first LEBS studies. However, one should note that Turzhitsky et al. [80] did not take into account polarization effects in this study despite the fact that light polarization properties alter the spatial reflectance profile [10]. Thus, a polarized Monte Carlo algorithm would allow a comprehensive understanding of the dependencies between the peak shape and the tissue structural composition.

Radosevich et al. [82] reported a post-processing technique that allows to reconstruct the shape of a wide range of experimentally measured LEBS peaks from the experimental measurement of one LEBS peak taken with a certain value of the light source spatial coherence length. The LEBS reconstruction could only be carried out for spatial coherence length shorter than the experimentally measured one. In other words, the depth selec-

tivity of LEBS can be adjusted during post-processing, provided that the desired depth does not exceed the maximum depth achievable by the unique LEBS measurement. Consequently, the higher the light source spatial coherence is, the more tissue information can be reconstructed from a single measurement. Enhanced Backscattering Spectroscopy (EBS, another terminology for Coherent Backscattering Spectroscopy) that uses a highly coherent light source (such as broadband lasers) is advantageous in terms of data quantity compared to LEBS. Indeed EBS should be preferred wherever possible. However, the use of the LEBS is more advantageous for practical instrumentation reasons [83]. For instance, EBS requires expensive materials such as broadband lasers and extremely sensitive cameras. This could impact its acceptance in clinical settings. Furthermore, stationary samples generate speckles that could mask the coherent peak when illuminated with a highly coherent source. Samples are usually rotated to average away this noisy component but this can be technically impossible for certain clinical applications. Conversely, LEBS can get rid of the speckle even for stationary samples.

2.3.4 Enhanced Backscattering Spectroscopy (EBS)

The early 2010s marked the renaissance of EBS (formerly CBS) for tissue characterization. Radosevich et al. [83] explored the effects of polarization on the EBS signals using an aqueous suspension of latex microspheres and underscored the sensitivity of the EBS peak to the shape of the scattering phase function. The performances obtained by Turzhitsky et al. [6] with LEBS were reproduced with EBS [10,83]. An open-source polarized Monte Carlo algorithm was released by Radosevich et al. [84]. This program enables computation of the EBS signals in media that can be modeled using the Whittle-Matérn formalism or Mie Theory. This work provided a powerful tool to investigate the dependencies between the shape of the coherent peak and the underlying tissue microstructure. The computational times were optimized using a semi-analytical approach and multiple parallel computing nodes. This program paved the way to fitting procedures.

Radosevich et al. [10] used this tool and reported successful applications of EBS to detect pre-invasive cells in colorectal and pancreatic cancers, thus expanding the previous LEBS studies on these tissues. Radosevich et al. identified significant differences at small length scales in the reflectance profiles between precancerous and normal pancreatic cancers (Figure 2.16, a and b), reflecting different tissue structural compositions in the superficial layer. The normalized intensity evaluated at the optimal exit radius exhibited significant statistical differences (Figure 2.16, c).

For colorectal cancer, the collected biopsies were classified into four categories by a pathologist (diminutive adenomas (DA), healthy control with no adenomatous adenomas (A) and advanced adenomas (AA)). The optical properties were extracted after EBS measurement and fitting procedures using the polarized MC algorithm [83]. Figure 2.17 (a), (b) and (c) shows the transport mean free path, the anisotropy coefficient and the ultrastructural parameters that determine the shape of the Whittle-Matérn functions respectively.

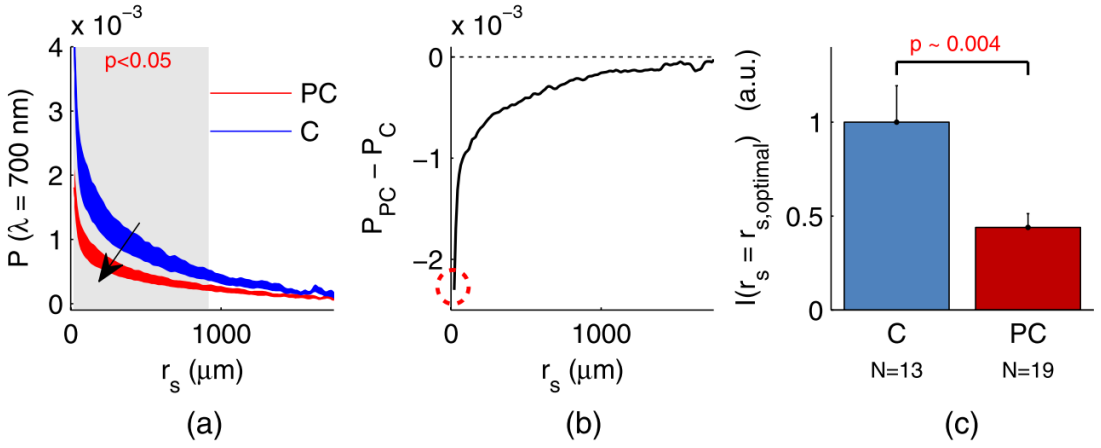

Figure 2.16: Pancreatic cancer (PC) field carcinogenesis alterations measured in the shape of reflectance profiles P from biopsies. (a) Comparison between reflectance profiles P for PC and control (C). The shaded region indicates the values of exit radius r_s for which the curves are significantly different. (b) Difference of reflectance profiles PC - C. The dotted circle indicates the optimal exit radius value for which the statistical differences are the most pronounced. (c) Normalized intensity of reflectance profiles at the optimal exit radius value for PC and control groups. Figures adapted from Radosevich et al. [10]

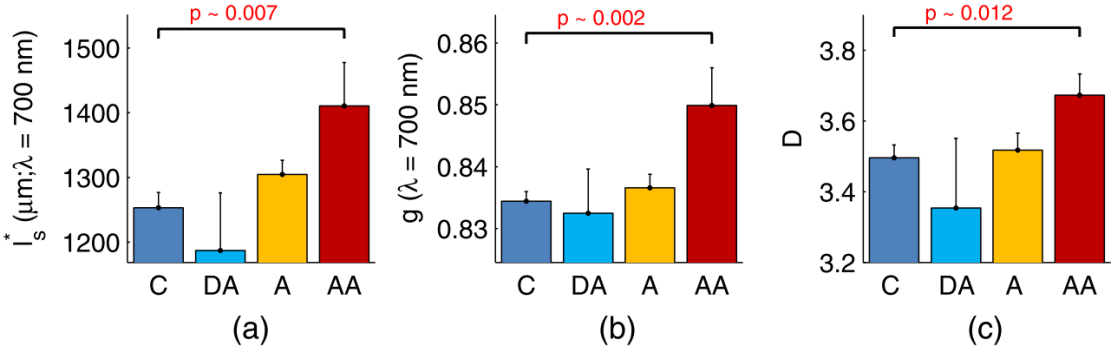

Figure 2.17: Optical properties of rectal biopsies in a colorectal study. (a) Transport mean free paths with its mean standard error. (b) Anisotropy g coefficient at 700 nm. (c) Shape parameter D of the Whittle-Matérn model. 43 controls (C), 6 diminutive adenomas (DA), 25 adenomas (A), 19 advanced adenomas (AA) were used. Figures adapted from Radosevich et al. [10]

Radosevich et al. [85] provided a Matlab routine to perform inversion procedures from experimental reflectance profiles to extract the Whittle-Matérn or the Mie parameters with microvascular properties. Look-up tables built using the polarized MC algorithms allowed the fitting of experimental reflectance profiles with nearly analytical speed and accuracy. This procedure was illustrated with ex-vivo rat tissue samples and allowed a thorough tissue characterization through the estimations of the three Whittle-Matérn parameters and three absorption-related parameters. Given that the Whittle-Matérn coefficients parametrize the refractive index excess autocorrelation function, random repre-

sentations of the medium refractive index can be deduced from their computation. The corresponding representations of the spatial distribution of the excess of refractive index for three tissue types are given in Figure 2.18. Details about the generation of such representations are given in the section 4.2.4. More recently, Pinkert et al. [86] designed a

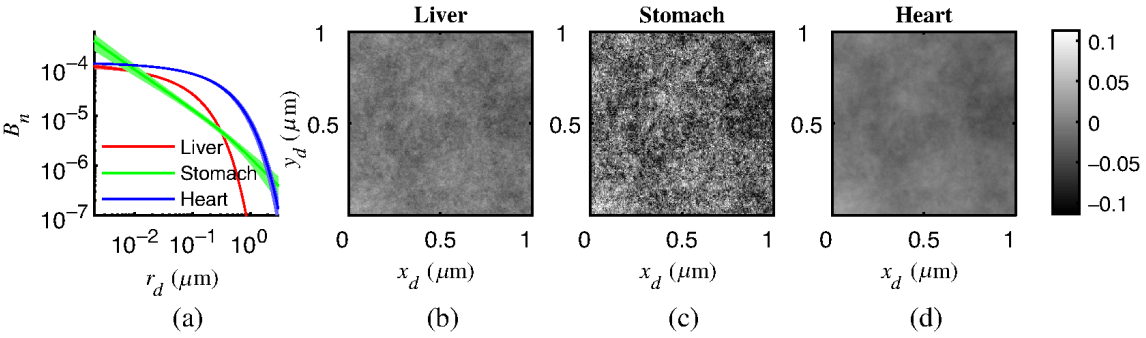

Figure 2.18: (a) Extracted refractive index autocorrelation functions B_n for liver, stomach, and heart tissues. The thickness of each curve corresponds to the standard error. The corresponding random media representations of (b) liver, (c) stomach, and (d) heart. The color map represents the excess refractive index value. Reproduced from Radosevich et al. [85]

multiscale imaging platform with sensitivity ranging from the cellular to the macro scale. They combined ultrasound imaging, Second Harmonic Generation Microscopy, Multiphoton Microscopy, Optical Coherence Tomography, and Enhanced Backscattering on a rabbit eye. They reported the first multimodal application that included EBS. They also implemented EBS into a microscopic application to allow direct comparison with the optical imaging modalities. EBS brought valuable information that relate to the scattering tissue properties that completed the anatomical information brought by the other imaging techniques.

In summary, LSS appears as a relevant tool to estimate the nucleus size distributions that may be impacted by dysplasia. The backscattered spectra need to be spectrally resolved to apply this technique.

EBS appears as another robust option to characterize cancerous tissues. It requires angularly resolved spectra, and can also be achieved at multiple wavelengths. EBS showed an interesting sensitivity at small length scales and probed fine tissue alterations. Interestingly, the Whittle-Matérn model does not need any assumption regarding the scatterer geometry and can result in a representation of the excess of refractive indices, that may carry interesting physical interpretations.

Thus, LSS and EBS appear as relevant techniques for cancer characterization. They may bring complementary diagnostic information with quantitative ultrasound techniques. Their implementations are described in the Chapter 4.

Chapter 3

Quantitative ultrasound: theories and methods

This chapter aims to describe the theoretical background of two quantitative ultrasound (QUS) techniques used in this thesis: the BSC parametrization and Envelope Statistics (ES). These two techniques can provide a variety of quantitative estimates that reflect the underlying tissue microstructure from the same ultrasound acquisition. Therefore, it is interesting to combine them for cancer characterization. Numerous theoretical backscattering models were reported in the literature for each technique [4, 24]. Thus, the theoretical framework presented in this thesis is restricted to the analytical expressions and hypotheses used in the following chapters. Firstly, all the physical quantities required for QUS analyses are introduced. Secondly, the scattering theoretical models are presented, followed by the detailed workflow that leads to BSC estimations and the associated QUS estimates. Thirdly, the ES theoretical framework is described. The estimation of envelope parameters is then presented. In this thesis, the BSC analysis was of prime interest for our application and was the first technique implemented in this project. Thus, deeper insights about this method will be given.

3.1 Ultrasound basics

Before introducing the BSC and the envelope parameters, some essential ultrasound principles and concepts are presented in this section. Ultrasound imaging is based on the propagation of acoustic waves in tissues. They experience several mechanisms that are explained below.

3.1.1 Wave and tissue interactions

Ultrasound is a disturbance of a pressure field. In most of medical imaging applications, the acoustic wave in tissues is a longitudinal wave that propagates linearly at the sound speed c, after being emitted by a transducer. The sound speed is commonly assumed to be constant in homogeneous tissues (typically $c = 1540$ m/s). Its wavelength λ is linked to the excitation frequency of the transducer f through the sound speed such as $c = \lambda f$.

Specular reflection occurs when the ultrasound wave meets an object of a characteristic size larger than the wavelength (Figure 3.1, a). This object can be modeled by a spatial variation in the acoustic impedance Z, defined under certain conditions as the product of the local density ρ by the sound speed c such as $Z = \rho c$. In practice, specular reflection occurs when ultrasound waves propagate through muscle/fat or muscle/bone interfaces for instance. Part of the ultrasound wave returns to the ultrasound probe in case of normal incidence and is referred to as echoes. If the object is smaller than the incident wavelength

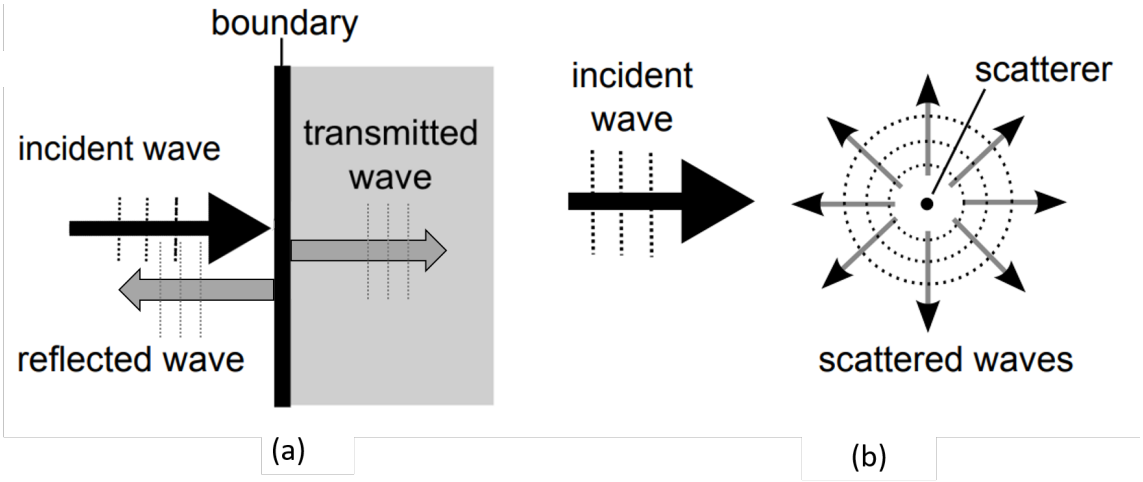

Figure 3.1: (a) Specular scattering occurs when the structure is much larger than the ultrasound wavelength. The ultrasound wave can be reflected or transmitted at the interface between the two media. (b) Diffuse scattering occurs when the structure is much smaller than the ultrasound wavelength. Adapted from Mercado et al. [87]

(*e.g.* cellular structures at clinical frequencies), the ultrasound wave is scattered in all directions (diffuse scattering, Figure 3.1, b). The signal that is scattered at 180° with respect to the propagation direction of the incident wave is detected by the ultrasound probe and is referred to as the diffuse backscattered echoes. The strength of this backscattered echo is proportional to the impedance contrast γ_z defined as $\gamma_z = \frac{Z-Z_0}{Z_0}$, with Z being the scatterer acoustic impedance and Z_0 the acoustic impedance of the surrounding medium. The diffuse backscattering is the phenomenon of interest when estimating the BSC and the envelope parameters in biological tissues.

3.1.2 Attenuation

As mentioned above, ultrasound waves undergo scattering in biological tissues. They also experience absorption due to viscous and thermal losses. Indeed, as the ultrasound waves propagate through the tissue, microscopic deformations leading to local frictions and energy dissipations occur. Both scattering and absorption lead to a reduction in wave intensity. Tissue attenuation refers to these two mechanisms and affects the backscattered signal of interest. When estimating QUS estimates, the effect of attenuation needs to be mitigated. The attenuation $\alpha(f)$ in tissue can be modeled as a function of the frequency such that $\alpha(f) = \alpha_0 f^m$, α_0 being the tissue attenuation coefficient, expressed in dB/(mm.MHz^m) and m, the attenuation exponent which usually varies from 1 to 2 [88]. Thus, at a given depth, higher frequency waves undergo more attenuation than low frequency waves. In other words, low frequency waves have deeper penetration depth in comparison to high frequency waves. In biological tissues, m is generally assumed to be unity [89]. The attenuation is then a linear function of the frequency. To give some order of magnitudes, the attenuation at 1 MHz is typically 0.16 dB/mm in muscles, 0.02 dB/mm in blood, 0.8 dB/mm in skull bone and 0.002 dB/mm in water [88].

3.1.3 Principle of ultrasound imaging

Now that the key mechanisms of wave and tissue interactions were introduced, the principle of ultrasound imaging can be presented. Image generation is part of the workflow when estimating the QUS parameters of a biological sample.

After the pulse emission, the time of return of the ultrasound wave to the transducer allows for object localization. Indeed the transducer-object distance d can be estimated using the back-and-forth traveling time Δt as follows: $d = \frac{c\Delta t}{2}$. This property is the key principle for ultrasound image generation. Amplitude Mode (A-mode) refers to the measurement of the amplitude of the backscattered signal envelope. A-mode was the first implementation of medical ultrasound historically and can be achieved using a single-element transducer. To obtain a two-dimensional (2D) signal (*i.e.* an image), the mono-element transducer can be moved to scan the region of interest. Alternatively, arrays of elements can acquire the backscattered signals simultaneously. In the second case, the radiofrequency signals generated by each element need to be beamformed to generate an interpretable image [90]. Anatomical information about the probed tissue then appears by turning the detected amplitude of the beamformed signals into gray levels. This process leads to the conventional Brightness mode (B-mode) images.

3.1.4 Diffraction

To understand the estimation of the QUS parameters detailed below, the diffraction effect needs to be introduced. It also impacts the process of image generation from the backscattered ultrasound signals.

The ultrasound wave is emitted by a piezo-electric transducer that has an extended spatial dimension. Thus, it can be considered that each point on the aperture generates a spherical wave (Huygens Principle). The pressure field near the transducer is affected by constructive and destructive interferences because of the coherence of these ultrasound waves. This area is known as the Fresnel zone and presents numerous fluctuations, which makes this zone difficult to use for imaging (Figure 3.2).

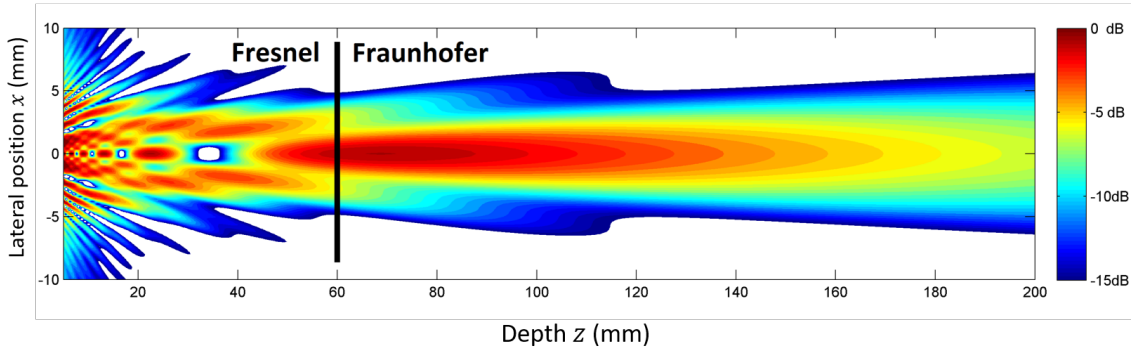

Figure 3.2: Example of the pressure field intensity from a circular ultrasound transducer (diameter 10 mm, center frequency 4 MHz). Adapted from Jain et al. [91]

The far-field presents a relatively more uniform pressure field and is referred to as the Fraunhofer zone. In this area, the beam spread can be quantified through the divergence angle. The beam divergence results from the transducer dimension and its shape (circular, rectangular). All these phenomena are termed as diffraction effects. The diffraction pattern can be expressed by analytical expressions in the Fresnel and in the Fraunhofer zone. However, these equations are difficult to calculate and come at the expense of approximations such as on-axis configuration.

3.1.5 Transducer properties

Now that we have discussed the principles of ultrasound imaging, we can now proceed to introduce the fundamental concept of resolution. This notion is useful in imaging and is also part of the physical interpretation of QUS parameters.

In most imaging medical applications, ultrasound transducers emit short pulses with a broad frequency content. The center frequency of the transducer is one of its main properties and it can be defined using the zero-crossing of the pulse (*i.e.* points at which the ultrasound signal crosses zero-amplitude level). The pulse length affects the axial resolution R_{ax} (*i.e.* the capability of the transducer to separate two scatterers along the propagation direction of incident waves). For a single-element circular transducer, $R_{ax} = \frac{c}{2B}$ with B being the bandwidth defined as the frequency range at -6 dB. The lateral resolution R_{lat} (*i.e.* same as the axial resolution but in the orthogonal direction) is defined as the product of the wavelength and the F-number F such as $R_{lat} = \lambda F = \lambda \frac{d_f}{A}$, were d_f represents the focal distance and A the aperture of the transducer. The

axial and the lateral resolutions can be combined to define the resolution cell, which represents the smallest volume resolvable by the probe. Although this might be true for circular single transducers with fixed geometries, these formulas no longer hold for arrays. First, one should note that focused or steered wavefronts can be generated with arrays using the time delay between the elements. The resolution cell then depends on the probe characteristics (elements width, distance between elements, center frequency) but also on acquisition parameters such as the pulse sequence. Additionally, post-processing procedures required for proper ultrasound image generation such as beamforming and compounding can further affect the resolution cell. Thus, quantifying the volume of the resolution cell is not straightforward. In practice, software simulations (*e.g.* SIMUS [92], CREANUIS [93]) or standardized phantoms can lead to estimations of the resolution cell in the chosen experimental configuration.

3.1.6 Ultrasound speckle

In a typical medical ultrasound image, specular echoes and diffuse scattering can be observed through different textures. The second mechanism is of prime interest in QUS analysis. In this subsection, we present how this phenomenon manifests in ultrasound images and introduce the different types of scattering.

Speckle refers to the granular patterns visible in ultrasound images. It results from interferences of ultrasound waves that are backscattered by scatterers within a resolution cell in the diffuse regime. In some medical imaging applications, ultrasound speckle is considered as a noisy component that can mask underlying structures of interest (Figure 3.3). Thus, speckle removal techniques were extensively studied to enhance ultrasound images [94]. However, speckle patterns are indicators of tissue properties. Speckle anal-

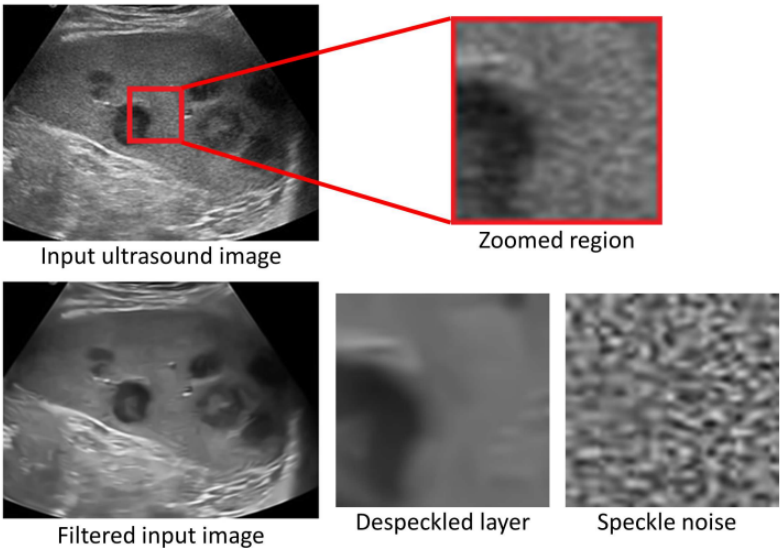

Figure 3.3: (Top) A typical clinical ultrasound image corrupted with speckles. (Bottom) The despeckled and speckle noise layers were recovered by a low-rank non-local filtering method. Reproduced from Zhu et al. [95]

ysis can be conducted by analyzing the spectral content of the ultrasound signals or by estimating the statistical attributes of the signal envelope. In the first case, we refer to BSC-related techniques and to ES in the second. These two techniques aim to estimate quantitative parameters that reflect the underlying microstructures. Thus, speckle analysis can provide valuable information for tissue diagnostics.

One may choose the adapted ultrasound frequency range to induce scattering from the object of interest. The different scattering regimes are summed up in Figure 3.4. Geometric scattering refers to the specular reflection mentioned above. For a given ultrasound wavelength, Mie scattering is a diffuse scattering regime that occurs when the object of interest has a characteristic size between $\lambda/10$ and λ. In this scattering regime, the backscattering cross-section exhibits important variations when the incident frequency is varying. These fluctuations are characteristics of the particle geometries. When the object is smaller than $\lambda/10$, Rayleigh scattering occurs. In this regime, the backscattering cross section presents a characteristic decay in $1/\lambda^4$ and no longer depends on the shape of the particle. The scattering regime is commonly given by the product of the wavenumber associated with the center frequency with the scatterer radius ka. For instance, the Mie regime corresponds to $ka \sim 1$, the Rayleigh scattering to $ka \ll 1$ and the geometrical scattering to $ka \gg 1$) . Thus, to observe characteristic oscillations from small structures, the frequency needs to be sufficiently high to hold the Mie scattering region by maintaining $ka \sim 1$. In practice, one should note that the scattering regimes can overlap because of the broad frequency content of the ultrasound incident pulse. Consequently, the experimental identification of the scattering regime is not a straightforward task but orders of magnitude should be kept in mind.

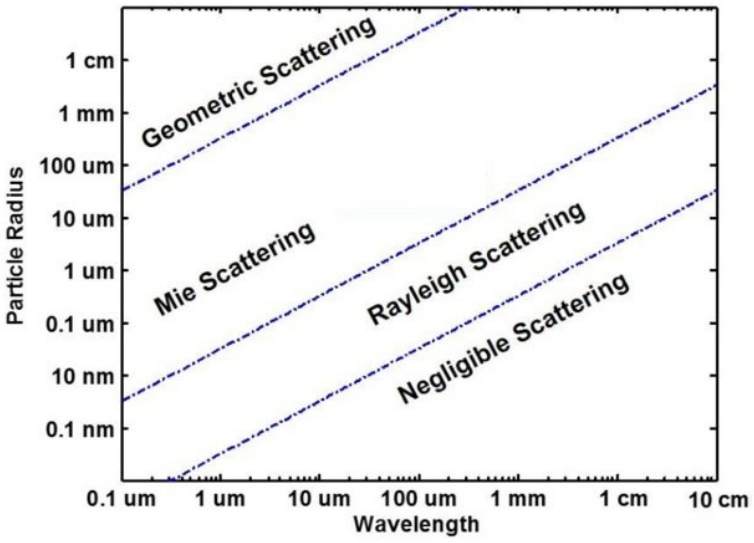

Figure 3.4: The scattering regimes for a given wavelength and particle size. Adapted from Zhao et al. [96]

3.1.7 Born approximation

As mentioned above, diffuse scattering occurs when an ultrasound wave travels through a medium that contains small scatterers. When the relative impedance contrast is low (typically $\gamma_z < 0.15$), the incident ultrasound waves undergo minor changes in amplitude and phase as they interact with the scatterers. The scattered field is then negligible in comparison to the incident ultrasound field. This configuration is known as weak scattering and refers to the Born approximation. The Born approximation is commonly used in ultrasound medical applications and serves as a basis in numerous imaging applications. Indeed, the main consequence of this approximation is that multiple scattering becomes negligible. Thus, the detected backscattered ultrasound waves are single-scattered and bear information about the microstructure they interacted with. Thus, a unique sound speed can be defined to characterize the propagation of the ultrasound waves and the time of flight directly dictates the position of the scatterers. This hypothesis is also of prime importance for quantitative ultrasound studies. Indeed, the estimates extracted from the ultrasound signals can be associated with the tissue underlying microstructure at the precise location of the Region of Interest. Conversely, the single scatterer signatures would be lost in multiple scattering.

As an example, the relative impedance contrast between plasma and red blood cells is about 13% [97], making blood a suitable medium for the Born approximation. No consensus values are known for impedance contrasts of cells and nuclei, as they may vary depending on the tissue type. However, the Born approximation is implicit in most quantitative ultrasound studies that aim to characterize tissues. This approximation will be adopted in the framework of our study.

Interestingly, tissue characterization can still be conducted independently of the hypothesis of weak scattering. Indeed, Muller et al. [98] leveraged multiple scattering in lungs and successfully characterized pulmonary fibrosis and edema *in vivo* in rodents. Indeed, the Born approximation no longer holds in this highly diffusive medium due to the high impedance contrast of the alveoli filled with air.

One could note that alternative solutions exist to the simple Born approximation. For instance, Huang et al. [99] reported a modified version of the "doubly distorted Born approximation". They obtained improved scattering results for both weak and strong scattering inclusions.

3.2 Backscatter coefficient

3.2.1 Definition

The Backscatter Coefficient (BSC) describes the sample's ability to backscatter the acoustic energy as a function of the frequency, independently of the tissue attenuation or the instrumentation effects [100]. The BSC is defined as the scattered intensity in the backward direction per unit solid angle per unit volume normalized by the incident

intensity ($mm^{-1}.sr^{-1}$) [24]. In the far field, it is defined as [4] :

$$BSC(k) = \frac{R^2}{V}\frac{I_{sc}}{I_{inc}} \tag{3.1}$$

where V is the scattering volume of interest, R the distance between the observation point and the scattering volume, I_{sc} the scattered field, and I_{inc} the incident ultrasound field. Analytical expressions describe the BSC in different configurations. Once estimated, the experimental BSC can be fitted to the adapted theoretical model to lead to quantitative estimates through inversion procedures. This procedure is referred to as the BSC parametrization.

3.2.2 Discrete model

In this paragraph, a brief analytical framework is presented to understand the BSC estimation techniques explained in the next paragraphs. The stochastic nature of the BSC is demonstrated using a simple discrete model [24]. In the configuration where an ultrasound transducer insonifies a medium composed of discrete and sub-resolvable scatterers under the Born approximation, let $o(t)$ be the collected signal over time t such as:

$$o(t) = p(t) * a(t) * s'(t) \tag{3.2}$$

where p is the transducer response and accounts for the diffraction in the beam pattern, the transmitted pulse, and transducer filtering. The sample attenuation is represented by $a(t)$. The function $s'(t)$ is the scattering function of interest that characterizes the probed tissue. Given that N scatterers are randomly located, the scattered signals received by the probe are delayed by different times t_i, $i \in [|1, N|]$ because of different times of flights such as:

$$o(t) = p(t) * a(t) * \sum_{i=1}^{N} s'_i(t - t_i) \tag{3.3}$$

The Fourier transform of the previous equation leads to:

$$O(f) = P(f)A(f)\sum_{i=1}^{N} S'_i(f)e^{2\pi j f t_i} \tag{3.4}$$

With f being the frequency. In the case of identical scatterers with a characteristic scattering function $S'(f)$:

$$O(f) = P(f)A(f)S'(f)\sum_{i=1}^{N} e^{2\pi j f t_i} \tag{3.5}$$

The power spectrum is then obtained by taking the magnitude squared of $O(f)$:

$$|O(f)|^2 = |P(f)A(f)\ S'(f)|^2 \left|\sum_{i=1}^{N} e^{-2\pi j f t_i}\right|^2 \tag{3.6}$$

or

$$|O(f)|^2 = |P(f)A(f)S'(f)|^2 \left(\sum_{i=1}^{N} e^{-2\pi j f t_i} \right) \left(\sum_{i=1}^{N} e^{2\pi j f t_i} \right) \tag{3.7}$$

which gives,

$$|O(f)|^2 = |P(f)A(f)S'(f)|^2 \left[N + 2 \sum_{i>m=1}^{N} cos(2\pi f(t_i - t_m)) \right] \tag{3.8}$$

The first term in the bracket accounts for the incoherent scattering. Incoherent scattering is then only the product of the characteristic squared magnitude of the scattering function $|S'(f)|^2$ with the number of probed scatterers N. The second term in the bracket represents the coherent scattering. It depends on the scattering function but also on the scatterer's spatial positions through the different time delays. We will refer to Equation 3.8 to explain the BSC estimation technique.

One should note that each physical quantity employed here can be equivalently written as a function of the wavenumber k, such as $k = 2\pi f/c$, where c is the medium sound speed

3.2.3 Theoretical scattering models

Incoherent BSC

Equation 3.1 gives a theoretical definition of the BSC that is not used for the experimental BSC parametrization. In this subsection, we introduce the equations used in this procedure.

In biological media with a sparse distribution of identical scatterers randomly and independently located, the incoherent theoretical BSC can be expressed as the product of the BSC in the Rayleigh limit and a backscatter form factor FF (detailed below) as follows:

$$BSC_{in,mono}(k) = n\sigma_b(k) = n\frac{k^4 V_s(a)^2 \gamma_z^2}{4\pi^2} FF(k,a) \tag{3.9}$$

with n being the number of scatterers per unit volume, k the wavenumber, $\sigma_b(k)$ the differential backscattering cross section defined as $\sigma_b(k) = \pi a^2 |S'(k)|^2$ for a sphere of radius a and $V_s(a)$ the scatterer volume. In the case of polydisperse size distribution, an integral sums incoherently the contribution of each scatterer and weights it with a probability density function D:

$$BSC_{in,poly}(k) = n \int_0^\infty \frac{k^4 V_s(x)^2 \gamma_z^2}{4\pi^2} FF(k,x) D(x) dx \tag{3.10}$$

where x represents the varying sphere radius.

The Faran model Faran et al. [101] provided the exact analytical solution for the acoustic scattering of a plane wave by an isotropic solid sphere in a fluid surrounding medium. The expression of the resulting scattered pressure field in the backscattering direction can be multiplied by the scatterer number density to obtain the incoherent BSC from identical solid spheres [39]:

$$BSC_{Faran}(k) = n\sigma_{b,Faran}(k,a) \tag{3.11}$$

The analytical computation of $\sigma_{b,Faran}(k,a)$ is not straightforward and can be found here [101]. The solution provided by Faran et al. relies on spherical Bessel functions of the first and second kind and takes into account shear waves and compressional waves in the solid scatterers. The authors argue that the acoustic waves that penetrate the scatterer can impact the scattered field and should therefore be considered.

Form Factors When considering a diluted scattering medium, the form factor FF describes the frequency dependence of the BSC in terms of size, shape and acoustic properties of the scatterers. In the incoherent case, the form factor FF represents the scatterer signatures in the measured BSC. The scatterer radii can be estimated by fitting the observed BSC and are of prime interest for tissue characterization. The analytical expressions of the form factors are obtained by assuming the spherical geometry of the scatterers and their random spatial distribution, modeled through their acoustic impedance. The three-dimensional (3D) spatial autocorrelation function then leads closed form solution [102]. Depending on the physical modelling of the scatterers, different form factors are adapted. Here, we will focus on the most common form factors and the ones that are used in this project. The following form factors are introduced in the configuration of a relatively low scatterer concentration (*i.e.* typically volume fraction $\phi < 0.03$) that are independently and randomly distributed.

The Gaussian form factor Using the Gaussian form factor, the medium is modeled through a continuous spatial impedance function. The spherical scatterers are represented by Gaussian decays of acoustic impedance. These assumptions lead to the following form factor [102]:

$$FF_{SG}(k,x) = e^{-0.827k^2x^2} \tag{3.12}$$

The fluid-filled sphere form factor This form factor models the scattering from a fluid-filled sphere in a homogeneous media and is commonly used to describe the cell scattering in biological samples [41]:

$$FF_{FS}(k,x) = \left[\frac{3}{2kx}j_1(2kx)\right]^2 \tag{3.13}$$

where j_1 is the spherical Bessel function of the first kind of order 1. In the case of monodisperse scatterers, the BSC is expressed as a function of the following parameters

of interest: the volume fraction $\phi = nV_s$, the scatterer radius a ($x = a$ in this case) and γ_z. Hereafter, the Fluid-Filled Sphere model (FFSM) will refer to the following analytical expression:

$$BSC_{FFSM}(k) = \frac{3\phi a k^2 \gamma_z^2}{4\pi} j_1^2(2ka) \tag{3.14}$$

Coherence effects

The previous BSC expressions do not cover the case of dense media. Indeed, it can be assumed that the scatterer position correlation increases with their concentration [38]. When the scatterers are not randomly spatially distributed, structural effects affect the ultrasound backscattering and the BSC is no longer the incoherent sum of the contributions of each scatterer. To take this concentration effect into account, the incoherent signal BSC_{in} can be modulated by a structure factor S:

$$BSC(k) = BSC_{in}(k)S(k) \tag{3.15}$$

The incoherent BSC_{in} can be replaced by any above expression. The analytical expression of $S(k)$ depends on the scatterer polydispersity in size. Therefore, two cases can be distinguished:

Monodispersity in the scatterer size In the case of non-overlapping identical scatterers, the scattering function $S'(k)$ can be factorized (Equation 3.5), and the structure function can be written:

$$S(\vec{k}) = \frac{1}{N}\left(\sum_{i=1}^{N} e^{-2j\vec{k}\cdot\vec{r_i}}\right)\left(\sum_{i=1}^{N} e^{2j\vec{k}\cdot\vec{r_i}}\right) \tag{3.16}$$

where $\vec{r_i}$ is the position vector of the ith scatterer. Its equivalent scalar frequency form appeared in Equation 3.7. The structure factor S denotes the effect of scatterer positions on the ultrasound scattering. When the scatterer's positions are not known (*i.e.* most of the tissue characterization application), a stochastic alternative can estimate the structure factor S [38, 39]:

$$S(\vec{K}) = 1 + n\int (g(\vec{r}) - 1)e^{-j\vec{K}\cdot\vec{r}}d\vec{r} \tag{3.17}$$

where $g(\vec{r})$ is the pair correlation function and $\vec{K}$ is the scattering vector. The pair correlation function g represents the probability of finding two scatterers separated by the distance $\vec{r}$. In the case of hard spheres that are randomly distributed, the pair correlation function can be expressed analytically following the equations given in Appendix A.1. Equation 3.17 can be seen as the 3D Fourier transform of the total correlation function $h(\vec{r}) = g(\vec{r}) - 1$.

Polydispersity in the scatterer size The analytical expression of $S(k)$ for polydisperse scatterers (Polydisperse II model) can be found in Han et al. [38]. In the Polydisperse

II model, the scatterer size distribution is assumed to follow a Γ-distribution:

$$D_z(x) = \frac{1}{z!}\left(\frac{z+1}{a}\right)^{z+1} x^z e^{-(z+1)\frac{x}{a}} \tag{3.18}$$

where D_z is the probability density function, a the mean scatterer radius, and z the Schulz width factor (the higher z is, the narrower the distribution). Han et al. [38] provided an expression to model the ultrasound backscattering of hard randomly distributed polydisperse scatterers in concentrated media based on a Fluid-Filled sphere form factor. Under these assumptions, the BSC is a function of the following parameters of interest: the scatterer mean radius a, the Schulz width factor z, the volume fraction ϕ and the relative impedance contrast γ_z. Hereafter, the PII model will refer to this BSC model:

$$BSC_{PII}(k) = BSC_{FFSM}(k) S_{PII}(k) \tag{3.19}$$

In this model, the scattering amplitude $S_i'(k)$ is based on the fluid-filled sphere form factor. The full expression of the structure factor $S_{PII}(k)$ can be found in Han et al. [38]. Some details about its computation are given in Appendix A.2.

The models described in this section will be used in the following chapters. The estimation of the BSC is described in the next section.

3.2.4 Backscatter coefficient estimation

The BSC reflects the underlying tissue microstructure independently of the attenuation and the instrument effects. Multiple sources of noise may affect the BSC measurements and make the experimental estimation of the BSC an arduous task. The complete workflow is described here, starting to the pulse sequence chosen for the acquisition of RF data to the estimation of QUS parameters. This subsection encompasses all the physical concepts introduced in the previous part of the fundamentals of ultrasound.

Pulse sequence

The different types of pulse sequences used to insonify the medium were studied to produce spectral-based QUS estimates. Focused waves are typically used in most QUS studies. However, more sophisticated options are also possible. Kanzler et al. [103] studied the benefits of coded excitations (CE) to improve the estimation bias of scatterer sizes in tissue-mimicking phantoms. They used a linear frequency-modulated chirp and a Wiener filter for pulse compression instead of conventional pulses. The penetration depth for a given accuracy in the scatterer radius estimate was increased up to 50%. A follow-up study reported excellent performances of the resolution enhancement compression (REC) technique in reducing the estimating bias of scatterer sizes. REC is a CE and a pulse compression technique that improves the -6 dB bandwidth of the ultrasound transducer [104].

A 71% reduction in the standard deviation of the average scatterer diameters was reported in tissue-mimicking phantoms compared to conventional excitation schemes.
Although these studies reported the potential superiority of CE over conventional pulse sequences using specific experimental setups, a limited number of studies have extended this research for QUS applications.

In ultrasound imaging, the 2010s saw the emergence of Ultrafast Imaging which commonly uses plane waves at multiple angles to insonify the media [105]. Each excitation angle generates RF data that are beamformed before being coherently compounded with other RF data acquired at other excitation angles. This technique leads to increased frame rates with limited loss in SNR compared to conventional focused imaging. This breakthrough impacted multiple ultrasound applications such as Doppler imaging (blood motion detection) or Shear wave Elastography (tissue motion detection). A few years after its introduction, the advantages of Ultrafast Imaging for QUS applications were reported by Salles et al. [106]. The authors estimated two BSC-related parameters (the BSC mid-band fit and intercept, detailed below in the subsection 3.2.5) using compound plane wave beamforming and conventional focused beamforming. They reported bias in the QUS parameters less than 2 dB for a given field of view, thus validating plane wave imaging for spectral-based analysis. One year later Garcia-Duitama et al. [100] extended this research to isotropic and anisotropic media (variations of QUS estimates depending on the angle of the incident excitation) and compared UI with conventional beamforming techniques. They estimated the effective scatterer sizes of tissue-mimicking phantoms and flowing porcine blood using UI. In the isotropic phantoms, errors were less than 0.26 ± 0.2 dB and 2.2 ± 0.8 for the blood experiment, which is known as an anisotropic medium. They concluded that Ultrafast Imaging can be used for BSC parametrization and anisotropy characterization.

Definition of a region of interest

Once, the RF data are acquired, the corresponding B-mode image can be used for segmentation. Indeed, the first task is to localize the areas of interest for tissue characterization. In a typical *ex vivo* QUS experiment such as the lymph node characterization conducted by Mamou et al. [26], the samples are immersed in a Phosphate-buffered saline (PBS) solution before being imaged. Mamou et al. reported the use of a semi-automatic segmentation algorithm to classify image regions as, PBS, fat or tissue of interest. The classification was based on the *a priori* known relative echogenicity of the three tissue types and used conventional image processing algorithms such as the Deriche filter. Although segmentation algorithms may improve the reproducibility of QUS analyses, manual segmentation seems to be conducted in most of the QUS studies, probably due to the relatively small datasets involved.

Once the areas of tissue of interest are determined in the B-mode images, the operator needs to define the Region-of-Interests (ROIs) where the BSC and the envelope amplitude

distribution will be computed to extract the corresponding QUS estimates. For 2D applications, the RF signals are time-gated in the depth direction and a certain number of RF lines are selected in the lateral direction for each ROI (Figure 3.5). In both directions, the sampling frequency and the transducer element pitch (or scanning step) impact the number of data points in the ROI for a given ROI length.

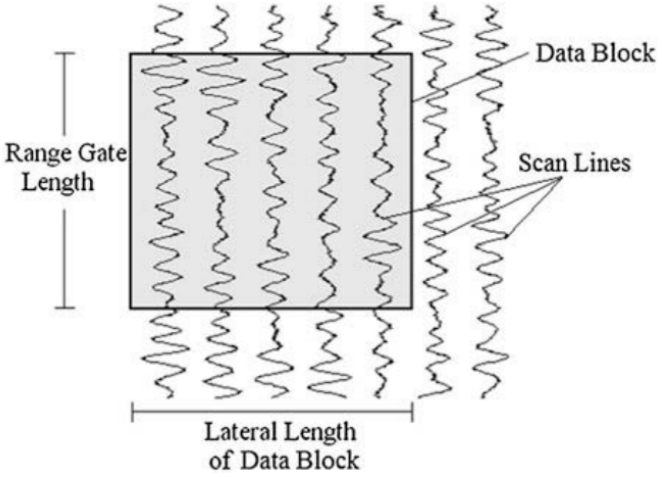

Figure 3.5: Diagram showing the time-gated RF lines contained within one ROI (data Block) Reproduced from Mamou et al. [24]

The Fourier transform is then applied to the time-domain signals. A mathematical window such as a Hann function can be applied to mitigate the effects of fast Fourier transform algorithms that are inherent to discrete numerical signals. Lizzi et al. [107] discussed the role of the windowing function in the estimations of the BSC-related parameters.

The power spectra are then computed by taking the squared magnitude of the frequency-domain signals. The power spectra of a ROI are then averaged to obtain a unique BSC per ROI. This BSC can then be parametrized. At the end of this processing, parametric images can show QUS estimates by color-encoding the B-mode images with overlays. The ROIs can be seen as "QUS pixels". Although the choice of the ROI size is often presented as arbitrary in QUS studies (typically a square of dimension 10-15λ [5,41,108]), its dimensions actually reflect a more subtle compromise:

The ROI needs to be as short as the *a priori* characteristic length scale of the tissue homogeneity for accurate QUS parameter estimations. Indeed, tissue homogeneity is implicitly assumed within one ROI since only one QUS estimate is extracted from a ROI. For instance, estimating the effective scatterer diameter would be of limited interest in a tissue region that exhibits a broad range of scattering structure sizes. Thus, the operator needs to mitigate the effects of potential tissue heterogeneities within the ROI over the backscattering signals by choosing it as small as possible.

However, the stochastic nature of the BSC signal limits the minimum ROI sizes. Equation 3.8 shows the stochastic nature of the backscattered signals. Indeed, since the exact positions of the scatterers (*i.e.* the time delays) cannot be known deterministically in

sparse media, the time difference that appears in the cosine can be modeled as a random variable that follows a uniform law. Interestingly, the expected value of the sum of cosines is zero, meaning that the coherent effect of random scatterer positions, considered as noise in a first time, can be mitigated by averaging a sufficient number of BSC estimates. This interesting property justifies why the squared magnitude value of the frequency signals (*i.e.* power spectra) are taken to estimate scatterer parameters, and not just the Fourier transform of the time domain signals. What "sufficient" is has been studied by Oelze et al. [109]. Simulations and phantom measurements showed that the best trade-off between a small ROI size and the accuracy and precision of scatterer property estimates occurred at 4 to 5 beamwidths laterally and 15 to 20 spatial pulse lengths axially. Although this study gives interesting orders of magnitudes, it is not straightforward to implement its conclusions in other experimental configurations, such as plane wave imaging. In this case, the beamwidth is not defined. Consequently, it is advisable to adjust the recommended ROI dimensions based on the lateral resolution, which is the closest comparable parameter.

The electrical noise that affects the BSC presents also a stochastic nature. To further reduce this and the coherent noise, the number of QUS estimates (*i.e.* number of ROIs) can be increased for a given B-mode image by choosing overlapping ROIs. The overlapping is typically about 50% in QUS studies. As a result, multiple QUS estimates correspond to one pixel in the B-mode image. Averaging the estimates for each pixel can then lead to smooth QUS parametric images with an apparent enhanced QUS estimate resolution. However, the QUS estimates are no longer independent since the same portion of the RF data served multiple times in the spectral analyses. The previous points are discussed in the case of sparse media with scatterers randomly distributed. However, one should note that when the scatterer positions are correlated, averaging the power spectrum estimates is not sufficient to mitigate the coherent signal. A structure factor should then be taken into account in the BSC parametrization.

Additionally, the ROI dimension should be large enough in the time axis (in terms of number of points) to produce a robust estimation of the Fourier transform. This constraint is purely a mathematical requirement due to the discrete Fourier transform.

Attenuation and sound speed estimation

The tissue attenuation affects the measured power spectra that lead to the BSC. To correct this unwanted effect, multiple attenuation estimation techniques were reported [24]. Our focus will be on the substitution technique [110]. It entails the determination of the characteristic attenuation coefficients α_0 and m using a planar reflector. The power spectrum is acquired without (P_1) and with (P_2) the sample on the reflector (Figure 3.6).

This leads to:

$$P_1(f) = \rho_1 P_0 e^{-2\alpha_{PBS}(f)L} \tag{3.20}$$

$$P_2(f) = \rho_2 \tau_1 \tau_2 P_0 e^{-2[\alpha_s(f)d - \alpha_{PBS}(f)(L-d)]} \tag{3.21}$$

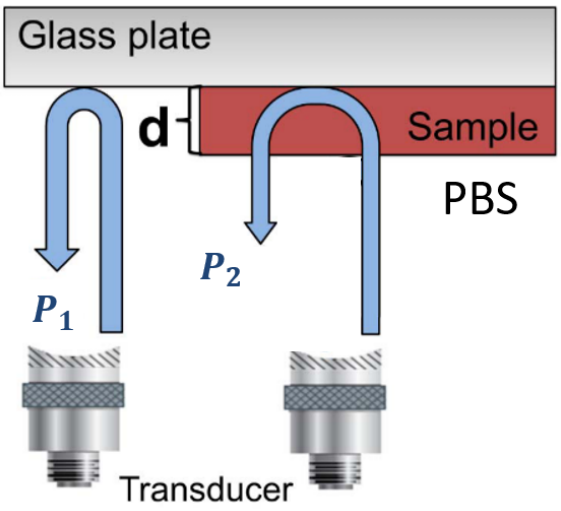

Figure 3.6: Attenuation substitution technique. The RF echo acquired from an acoustic reflector is referred to as the reference signal P_1. P_2 represents the reflection with the sample. d denotes the sample thickness. Reproduced from Rohrbach et al. [111]

where P_0 is the component of the power spectrum that accounts for the instrumentation effects,ρ_1 is the reflection coefficient at the PBS/reflector interface, ρ_2 is the reflection coefficient at the sample/reflector interface, L is the distance between the transducer and the reflector, d the sample thickness, $\alpha_{PBS}(f)$ the PBS attenuation, $\alpha_s(f)$ the sample attenuation, τ_1 and τ_2 are the transmission coefficients from PBS to the sample and from the sample to PBS respectively. Assuming that $\rho_1 \approx \rho_2$, the ratio is then:

$$\frac{P_1(f)}{P_2(f)} = \frac{1}{\tau_1\tau_2} e^{-2d[\alpha_{PBS}(f)-\alpha_s(f)]} \tag{3.22}$$

The sample spectral attenuation can then be expressed as follows:

$$\alpha_s(f) = \alpha_{PBS} + \frac{1}{2d} ln\left[\tau_1\tau_2 \frac{P_1(f)}{P_2(f)}\right] \tag{3.23}$$

The coefficients τ_1 and τ_2 are assumed to be unity as an approximation. The PBS attenuation is considered to be identical to water attenuation, where known values are reported in the literature. The sample thickness d can be estimated based on the B-mode image using the water sound speed. The sample attenuation α_s can then be computed. Once estimated, the sample attenuation can be modeled as a linear function of frequency assuming that m equals unity or to a power function. This fitting procedure finally leads to α_0 and m.

Interestingly, the sample sound speed c_s can also be estimated using the substitution technique using P_1 and P_2 [111]:

$$c_s = \left(\frac{1}{c_{PBS}} - \frac{\varphi}{4\pi f_{max} d}\right)^{-1} \tag{3.24}$$

where c_{PBS} is the sound speed in PBS, f_{max} is the maximum working frequency and φ is the unwrapped phase of the ratio $P_2(f)/P_1(f)$

This technique presents some inherent drawbacks. First, it estimates a global attenuation coefficient or sound speed and assumes homogeneity within the probed sample. This hypothesis can be discussed in certain tissue types. Moreover, the transducer has to be fixed between the reference and the phantom measurements. Slight displacements may corrupt the measurements, especially when working at high frequencies. Additionally, this technique is only suitable for *ex vivo* procedures.

BSC computation

The raw power spectra collected by an ultrasound transducer do not directly reflect the tissue BSC. Indeed, two experiment-dependent spectral quantities affect this signal. The instrumentation effect that accounts for the transmitted pulse, the transducer filtering, and the beam diffraction affect the backscattered signals. The tissue attenuation also impacts the backscattered waves. Thus, different methods were developed to isolate the sample scattering contribution from the instrument effects and the depth of Region of Interest (ROI):

Planar reference method This method is adapted for mono-element transducers [100, 112]. Although they are less expensive, their fixed geometry needs them to be optimally chosen depending on the specific application (*e.g.* F-number). Moreover, spatially extended samples need moving transducers to be scanned. This increases the acquisition time to generate an image. One advantage of this technique is that no beamforming procedures are needed to create an interpretable image. The power spectrum of a planar reflector is acquired as shown in Figure 3.6 and serves as a reference. The ratio of the sample power spectrum with the reference one is then corrected for the diffraction beam pattern. Attenuation correction needs to be performed independently.

Reference phantom method This method is adapted for arrays with any geometries [113]. The power spectra of a reference phantom $P_{ref}(f)$ with known scatterer size and acoustic properties are acquired exactly with the same acquisition parameters as the ones used for the sample measurements (*e.g.* voltage, insonification angle, pulse sequence). The sample BSC_s is then estimated as:

$$BSC_s(f) = \frac{P_s(f)e^{-4z[\alpha_{ref}(f)-\alpha_s(f)]}}{P_{ref}(f)} BSC_{th,ref} \tag{3.25}$$

where $P_s(f)$ and $P_{ref}(f)$ are the sample and the reference power spectra respectively, $BSC_{th,ref}$ the expected theoretical BSC of the reference phantom, $\alpha_s(f)$ and $\alpha_{ref}(f)$ the attenuation of the sample and the reference phantom respectively and z the ROI depth. The previous expression relies on the expression of each power spectrum as the product of

the instrument effects $P(f)$ with the attenuation effects $A(f)$ and the scattering function of interest such as:

$$P_s(f) = |P(f)A_s(f)|^2 BSC_s(f); \tag{3.26}$$

and

$$P_{ref}(f) = |P(f)A_{ref}(f)|^2 BSC_{ref}(f) \tag{3.27}$$

The effect of the diffraction beam pattern is then canceled out in Equation 3.25. The exponential term corrects for both the attenuation in the sample and in the phantom. In practice, the reference phantom can be composed of glass beads or polyamide microspheres in a setting agent such as agar gel at a very low concentration (volume fraction less than 1%). In this case, the theoretical $BSC_{th,ref}$ of the reference phantom can be computed using the Faran model.

3.2.5 Backscatter coefficient parametrization

Once the BSC is properly estimated, quantitative estimates can be extracted using fitting procedures

Lizzi-Feleppa approach

A first approach involves fitting the BSC expressed in dB as a linear function. This simple procedure leads to ultrasound parameters known as the Lizzi-Feleppa coefficients the intercept I (dB), the slope S (dB/MHz) and the midband value M (dB):

$$10log_{10}(BSC_s) \rightarrow Y_{LF}(f) = S \times f + I \,; M = Y_{LF}(f_{mid}) \tag{3.28}$$

where $Y_{LF}(f)$ is the resulting linear fit and f_{mid} the middle frequency. Only two out of the three Lizzi-Feleppa parameters are independent. In practice, the relative values of these parameters can be used to discriminate one tissue type from others. Indeed, their absolute values convey limited physical meanings. However, the Born approximation is not required to compute them.

Inversion using theoretical scattering models

The theoretical scattering models introduced in the subsection 3.2.3 can be fitted to the experimental BSC to extract more sophisticated parameters at the expense of multiple approximations such as Born, far-field, incident plane wave and isotropic medium. The output coefficients of the inversion procedure then correspond to the parameters that minimize the cost function C, defined as the Root Mean Square Error (RMSE) between the measured and the expected BSC:

$$C(\vec{X}) = \sqrt{\frac{1}{N_f}\sum_{i=1}^{N_f}[BSC_s(f_i) - BSC_{th}(f_i, \vec{X})]^2} \tag{3.29}$$

where N_f is the number of discrete frequencies f_i and $\vec{X}$ has as many components as scattering parameters in the chosen theoretical BSC model. For instance, when working with the Gaussian or the Fluid-Shpere Form factors in the monodisperse case, the inversion procedure leads to two independent parameters $\vec{X} = (a, n_z^*)$ where a is the scatterer radius and n_z^* is the acoustic concentration defined as $n_z^* = n\gamma_z^2$. The structure factor models bring one supplementary inversion coefficient and lead to three independent parameters: $\vec{X} = (a, \phi, \gamma_z)$. The polydisperse models add one extra parameter that describe the width of the scatterer size distribution (e.g. the Schulz width factor z of the Polydisperse II model).

One can note that multiple cost functions can be implemented [34] to give more or less weight to the differences observed in the high frequencies. In QUS studies, these inversion problems are often solved using the *Nelder-Mead simplex* algorithm implemented in Matlab through the routine function *fminsearch*. The *Interior Point* algorithm can also be used through the *fmincon* Matlab function. For instance, Muleki-Seya et al. [5] reported slightly higher values for the scatterer radii and the volume fractions using *fminsearch* than the ones brought by *fmincon*. Notable differences were observed between the two algorithms in the relative impedance contrast values. To my knowledge, there is currently no consensus on the choice of optimization algorithm in QUS applications. However, some works investigated these issues. Oelze et al. [114, 115] reported optimized inversion procedures to extract the effective scatterer diameters and the effective acoustic concentrations. Similarly, Lavarello et al. [116] studied the effect of three algorithms to estimate the effective scatterer sizes in polydisperse media.

The previous points underline the fact that the convergence of optimization algorithms must be taken with caution. Indeed, inversion procedures can lead to local minima of the cost function, that should not be confused with the desired global minimum to estimate accurate QUS parameters.

3.2.6 Discussion

Although the estimation of BSCs and the associated spectral QUS parameters result from numerous processing steps (ROI grid, power spectrum computation, reference phantom method, etc.), an interlaboratory study [117] showed that BSC parametrization can be instrument and operator-independent. To further mitigate the potential discrepancies in the QUS analyses, recent studies reported model-free and reference-free approaches [118]. *In situ* calibration using biocompatible titanium beads placed in the tissue of interest was also investigated by Nguyen et al. [119]. This technique was introduced as an alternative to the gold standard reference phantom method to estimate the BSCs.

3.3 Envelope Statistics

While the BSC parametrization extracts spectral-based parameters, Envelope Statistics (ES) entails in estimating the attributes of the envelope statistical distribution of the backscattered signals. This procedure leads to additional scattering parameters that can characterize the underlying tissue microstructure. The Probability Density Function (PDF) of the measured envelope can be fitted to statistical distributions such as the Gamma, the Rayleigh, or the Rice distributions to cite just a few. More than 10 statistical distributions are reported in the literature. However, some statistical distributions are approximations of others, making them not all independent. In this thesis, we will focus on the two most common envelope distributions found in QUS studies: the Nakagami and the Homodyned-K distributions. Brief insights into their theoretical framework are given in this section.

3.3.1 Theory

Mathematically, the ultrasound envelope $e(t)$ of a signal $RF(t)$ is defined as the magnitude of the corresponding analytic signal such as:

$$e(t) = \sqrt{RF(t)^2 + H(RF(t))^2} \tag{3.30}$$

where $H(t)$ represent the Hilbert transform. The extraction of QUS parameters based on ES relies on the Born approximation as well. Thus, the discrete model introduced in subsection 3.2.2 can be adopted as well to describe the stochastic nature of the ultrasound envelope. Given that the backscattered signal is the result of individual contributions from all scatterers [120], it can be modeled as a random walk due to the random phase and amplitude variations resulting from the random positions of the different scatterers [44].

3.3.2 Statistical distributions

The Nakagami distribution

The Nakagami distribution can be used to extract the scaling factor Ω_{nak} and the Nakagami parameter α_{nak}. The scaling factor Ω_{nak} is equivalent to the mean backscattered intensity [44] and α_{nak} can be used to quantify the effective number of scatterers per resolution cell [44, 45]. If A is a random variable that follows a Nakagami distribution, then:

$$D_{nak}(A) = \frac{2\alpha_{nak}^{\alpha_{nak}}}{\Gamma(\alpha_{nak})\Omega_{nak}^{\alpha_{nak}}} A^{2\alpha_{nak}-1} e^{-\alpha_{nak}A^2/\Omega_{nak}} \tag{3.31}$$

where Γ is the Euler gamma function. The parameters Ω_{nak} and α_{nak} can also be written as:

$$\Omega_{nak} = E[A^2] \tag{3.32}$$

$$\alpha_{nak} = \frac{E^2[A^2]}{Var[A^2]} \tag{3.33}$$

where E and Var represent the expected value and the variance respectively.

The Homodyned-K distribution

The expression of the Homodyned-K (HK) distribution is [45]:

$$D_{hk}(A) = A \int_0^\infty x J_0(s_{hk}x) J_0(Ax)(1 + \frac{x^2\sigma_{hk}^2}{2\mu_{hk}})^{-\mu_{hk}} dx \tag{3.34}$$

where J_0 is the 0^{th}-order Bessel function of the first kind, s_{hk}^2 the coherent signal energy, σ_{hk}^2 the diffuse signal energy and μ_{hk} is somewhat the analogous to the Nakagami parameter α_{nak}. Indeed, the effective number of scatterers per resolution cell can also be reflected through the parameter μ_{hk} [44]. The ratio $k_{hk} = s_{hk}/\sigma_{hk}$, termed as the coherent-to-diffuse signal ratio, can describe the degree of structure in the scatterer spatial position in the considered ROI.

The physical interpretation of the Nakagami and the HK parameters can be found in subsection 2.2.2.

3.3.3 Envelope parameter estimation

Envelope parameters are often combined with spectral-based parameters to fully exploit the backscattering signal from an area of interest in the tissues. Thus, the ampltitude histogram of the non-saturated envelope signals within an ROI is computed following Equation 3.30. This procedure leads to the estimated probability density function.

The scaling parameters Ω_{nak} and α_{nak} from the Nakagami distribution were obtained using a maximum-likelihood estimator with the built-in Matlab function *fitdist*.

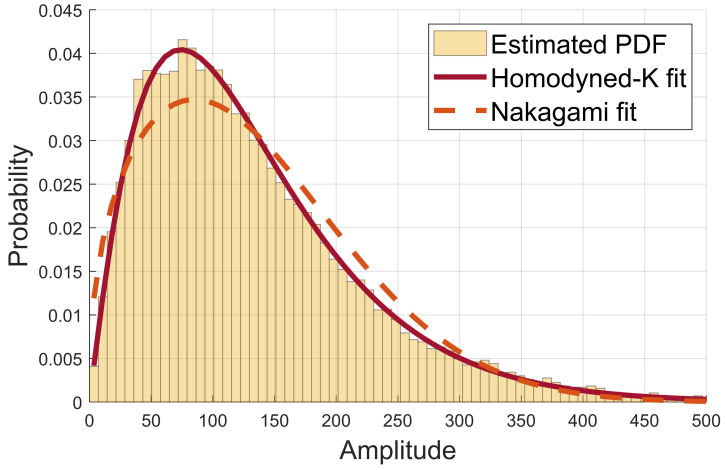

Figure 3.7: Example of an estimated PDF from a single ROI, its Homodyned-K fit ($R^2 = 0.99$) and its Nakagami fit ($R^2 = 0.96$). Reproduced from Malinet et al. [121]

Because no closed-form expression exists for D_{hk}, the estimation of the HK parameters is not straightforward. Different methods were reported in the literature for this specific task (*e.g.* using the first three even moments or moments of small orders [45]). In 2013, Destrempes et al. [122] introduced the XU estimator which extracts HK parameters based on the mean intensity and two log-moments. This technique is now widely accepted for its efficiency. Thus, the XU estimator was used in this thesis. Illustrative examples of fits with the Nakagami and the HK distributions are given in Figure 3.7.

3.3.4 Envelope parameter correction

The envelope parameters can be affected by the diffraction of the pressure field and the tissue attenuation, similarly to the spectral parameters previously described. The estimates Ω_{nak}, α_{nak} and μ_{hk} can be corrected post-processing for these undesired effects as suggested in Mamou et al. [45] (Eq. 9 and 10 in this article). The known geometry of the ultrasound transducer was used to assume the volume variations of the resolution cell across the field-of-view. The estimates α_{nak} and μ_{hk} that measure indirectly the scatterer density were then scaled by multiplicative factors to account for the expected changes in the resolution cell. Another factor based on the sample attenuation coefficients and the ROI depth was applied to each estimate of Ω_{nak}. These corrections allow the comparisons between the envelope parameters from ROI located at different positions within the field-of-view.

To our knowledge, relatively few studies reported the use of correction methods for the envelope parameters. A correction technique is suggested in section 6.2.2 and is applied in the chapters 6 and 7.

Chapter 4

Light Backscattering Spectroscopy: theories and methods

In this chapter, we present the two light backscattering techniques used in this thesis. After introducing some key optical quantities, the analytical formalism and the method of Enhanced Backscattering Spectroscopy (EBS) are exposed, followed by the theory and the method of Light Scattering Spectroscopy (LSS).

4.1 Optics basics

Despite their electromagnetic nature, numerous analogies can be made between light waves and mechanical ultrasound waves.

4.1.1 Propagation

Light propagates at the speed c with a wavelength λ in a homogeneous medium of refractive index n such as $c = \lambda\nu = c_0/n$ where ν is the optical frequency and c_0 the light speed in vacuum. In the visible range, the wavelengths range from 400 nm to 700 nm, and are substantially smaller than the ultrasound wavelengths found in clinical settings (*e.g.* $\lambda_{us} = 100$ µm at 15 MHz). Similarly to ultrasound, the concept of spatial and temporal coherence can be applied in optics. Therefore, light waves can experience interferences and form speckles as well. However, light presents an additional characteristic compared to ultrasound waves, namely its polarization. Polarization plays an important role in the description of light-matter interactions. Its analysis can even lead to biomedical applica-

tions for tissue diagnostics (*c.f.* Polarimetry [123]). The polarization refers to the spatial direction of the oscillation plane of the transverse fields that constitute light. In the case of linearly polarized light, the electric field is confined to a plane along the direction of light propagation. Unpolarized light refers to light waves in which the electric field oscillates in all possible directions perpendicular to the direction of propagation.

Similarly to ultrasound, specular reflection occurs when light interacts with an object in the geometric regime. Interestingly, the scattering regimes and their transitions are the same as the ones reported in ultrasound in subsection 3.1.6. Light waves experience scattering if they encounter variations of the refractive index in the medium, which is somewhat the equivalent of the acoustic impedance in optics.

4.1.2 Born approximation

The Born approximation is common in light scattering applications for tissue diagnostics, as it is in quantitative ultrasound studies. Its formulation is similar for ultrasound and light waves (c.f. subsection 3.1.7) and also results in the single scattering approximation [124]. However, a nuance can be added in EBS applications. Indeed, the Born approximation is not incompatible with a large volume of scatterers in which several scattering events can be subsequent [125]. The key is to be able to define a characteristic volume that represents the statistics of a single scattering event. If this requirement is met, the light transport in tissues can be accurately described numerically with Monte Carlo simulations. In continuous random media, the applicability of the Born approximation can be checked using analytical criteria based on refractive index-related parameters, as introduced in the next subsection. Interestingly, Radosevich et al. [85] simplified these previous points by arguing that the Born approximation is valid in all biological tissues where a scattering mean free path l_s' can be defined. This coefficient is analytically defined below (subsection 4.1.4). Thus, all the tissues commonly studied in biomedical optics may meet this criteria.

4.1.3 Phase functions

The phase functions describe the probability of scattering at a given angle θ for a single scattering event. It is defined as the normalized differential scattering cross section (sr^{-1}). Interestingly, the shape of the phase function can be related to the scatterer geometries or to tissue optical properties through analytical models. Thus, the phase function can be seen as the scatterer signature. For instance, the scattered spectrum from a single sphere in the Mie regime exhibits oscillations that directly reflect its radius. The estimation of the phase function parameters is a common objective in LSS for tissue characterization, as tissue optical properties can directly be derived from them. In this thesis, our focus will be on Mie Theory and the Whittle-Matérn model.

Mie theory

In purely scattering media, Mie Theory provides an exact analytical solution for the scattering of a plane wave by a discrete sphere of refractive index n_s surrounded by a medium of refractive index n_{env}. Interestingly, it can also provide a first-order description in the case of non-spherical scatterers [68]. The Mie phase function is parametrized by the scattering angle θ, the relative refractive index $n_{re} = n_s/n_{env}$ and the size parameter x defined as:

$$x = \frac{2\pi n_{env} a}{\lambda} \tag{4.1}$$

where a is the scatterer radius. The Mie phase function $p_{Mie}(\theta, n_{re}, x)$ does not have a closed form. Open-access algorithms such as the one provided by the Python module *miepython* [126] are optimized and widely accepted in the optical community to compute Mie spectra.

Whittle-Matérn model

As opposed to heterogeneous media composed of discrete spherical scatterers, biological samples can be considered as continuous random media to encompass their complexity. Indeed, cells and nuclei can exhibit a variety of shapes, and their sizes can range from a few microns to tens of microns. One scale below, organelles such as lysosomes, ribosomes or mitochondria are made of different molecular materials and their size spans from 0.2 nm to 30 nm. Other extracellular components such as collagen and elastin fibers also contribute to the tissue complexity through their different size [10]. In other words, the wide variety of cellular objects can lead to model the tissue as a continuous spatial function of the refractive index. An analogy can be made with the Gaussian model mentioned in the paragraph 3.2.3. Contrary to other discrete BSC models, this form factor also considers the tissue as a continuous function of acoustic impedance. One notable difference here is that tissue is optically modeled as random media following a statistical distribution approach, without assuming the spherical geometries of its scatterers.

Refractive autocorrelation function Light scattering results from relative variations in the refractive index. In the configuration of continuous media, it no longer depends on the unique relative refractive index n_{re} introduced in the discrete model but it can be described through the excess refractive index auto-correlation function B_n defined as:

$$B_n(r_d) = \int n_\Delta(r) n_\Delta(r - r_d) dr \tag{4.2}$$

where r_d represents the differential separation between two points, $n_\Delta(r)$ the excess refractive index defined as $n_\Delta(r) = n(r)/n_0 - 1$ with $n(r)$ being the fluctuating refractive index and n_0 the mean refractive index.

The scalar notation of r_d results from the approximation of statistically isotropic media, which is adopted hereafter.

Whittle-Matérn function A versatile model that is based on the three-parameter Whittle–Matérn function can describe the continuous function B_n [125]:

$$B_n(r_d) = A_n\Big(\frac{r_d}{L_n}\Big)^{(D-3)/2} K_{\frac{D-3}{2}}\Big(\frac{r_d}{L_n}\Big) \tag{4.3}$$

where A_n is the fluctuation strength, L_n the characteristic length of heterogeneity of refractive index (*i.e.* B_n decays exponentially for $r_d > L_n$), K_ν the ν-order modified Bessel function of the second kind and D the shape parameter which determines the shape of the distribution. For instance, when D tends to infinity, the autocorrelation function B_n approaches a Gaussian shape. The function B_n approaches a power law when $D < 3$, an exponential function when $D = 4$, the Henyey-Greenstein phase function when $D = 3$ and a Gaussian function when D tends to ∞. The parameter D makes the Whittle-Matérn model versatile since it can cover different refractive index autocorrelation functions that are likely to be encountered in biological tissues [10]. When $D < 3$, the medium can be regarded as a mass fractal, and in this context, the parameter D can be considered as the mass fractal dimension [125].

Normalization The parameter A_n has a limited physical interpretation and acts as a normalization factor in the expression of B_n. In this review of the Whittle-Matérn functions, Rogers et al. [125] exposed the different normalization options possible, along with their respective advantages and disadvantages. In this thesis, the normalization at a minimum length scale will be adopted. It entails: $B_n(r_{min}) = \sigma_n^2$ where r_{min} is the minimum length scale in the tissue and σ_n^2 is the refractive index variance. Therefore, we obtain [125]:

$$A_n = \sigma_n^2\Big(\frac{r_{min}}{L_n}\Big)^{(3-D)/2} \frac{1}{K_{\frac{(D-3)}{2}}\big(\frac{r_{min}}{L_n}\big)} \tag{4.4}$$

The advantage of this choice is that A_n is switched to σ_n^2 which carries more physical meaning. Therefore, the extraction of σ_n^2 is more relevant than A_n for tissue characterization. However, it introduces an additional parameter r_{min} that needs to be set *a priori*. The coefficient r_{min} represents the smallest elementary particles found in the biological tissues for which the definition of a refractive index still holds. In this thesis, r_{min} will be set to 2 nm as suggested in Radosevich et al. [85]. This value corresponds approximately to the typical size of DNA chains or macromolecules found in biological tissues such as lipids. For the sake of simplicity, A_n will be kept in the following equations.

Refractive index parameters and phase function Two more steps are required to express the scattering phase function using the Whittle-Matérn model.

First, the Wiener-Khinchin theorem is applied to link the power spectral density Ψ_n to B_n through the 3D Fourier transform [125]:

$$\Psi_n(\vec{k_s}) = \frac{1}{(2\pi)^3} \iiint B_n(\vec{r_d}) e^{-i\vec{k_s}.\vec{r_d}} d\vec{r_d} \tag{4.5}$$

With $\vec{k_s}$ is the scattering vector defined as $k_s = 2kn_0 sin(\theta/2)$ where k is the wavenumber and θ the polar angle of the scattering vector k_s. We can obtain [85]:

$$\Psi_n(k_s) = \frac{A_n L_n^3 \Gamma\left(\frac{D}{2}\right)}{\pi^{3/2} 2^{(5-D)/2} (1 + k_s^2 L_n^2)^{D/2}} \tag{4.6}$$

where Γ represents the mathematical Gamma function defined as $\Gamma(x) = \int_0^\infty t^{x-1} e^{-t} dt$ for $\Re(x) > 0$. The Born approximation is valid in continuous random media as long as $\sigma_n^2 (kL_n)^2 \ll 1$ according to finite-difference time-domain analysis [85]. Applying the Born approximation in the case of incident linear polarized plane waves, the unnormalized differential scattering cross section is [127]:

$$\sigma_{WM}(\theta, \phi) = 2\pi (kn_0)^4 [1 - sin^2(\theta) cos^2(\phi)] \Psi_n(k_s) \tag{4.7}$$

where ϕ is the azimuthal angle such as $\phi = 0$ in the direction of the linear polarization vector. The phase function $p_{WM}(\theta, \phi, \sigma_n^2, L_n, D)$ can be obtained by normalizing σ_{WM} such as the integral over all solid angles is equal to 1.

4.1.4 Optical properties

Photons undergo different mechanisms when traveling in the tissues. They are described by different coefficients referred to as the tissue optical properties introduced below.

Scattering in biological media can be described by the light scattering coefficient μ_s (cm^{-1}). The scattering coefficient μ_s can be computed from the differential cross-section per unit volume $\sigma(\theta, \phi)$ associated with Mie theory or the Whittle-Matérn model as defined above:

$$\mu_s = \int_{\phi=0}^{2\pi} \int_{\theta=0}^{\pi} \sigma(\theta, \phi)\, sin\theta \, d\theta d\phi \tag{4.8}$$

For instance, a photon that traveled a distance z in the tissue such as $z\mu_s = 1$ will undergo one scattering event on average [68].

The anisotropy coefficient g describes the amount of light scattered into the forward direction after a single scattering event. Analytically, g is the average cosine of the deflection angle θ:

$$g = \frac{\int_{\phi=0}^{2\pi} \int_{\theta=0}^{\pi} \sigma(\theta, \phi)\, cos\theta sin\theta \, d\theta d\phi}{\int_{\phi=0}^{2\pi} \int_{\theta=0}^{\pi} \sigma(\theta, \phi) sin\theta \, d\theta d\phi} \tag{4.9}$$

The coefficient μ_s and g define the reduced scattering coefficients $\mu'_s(\lambda)$ such as:

$$\mu'_s(\lambda) = \mu_s(1-g) \tag{4.10}$$

The length $l'_s = 1/\mu'_s$ represents the characteristic distance of travel for a photon to lose memory of its incident direction. This quantity is referred as the transport mean free path and typically varies from 300 to 2000 µm in biological tissues [74].

As the light wave propagates, energy is transferred to the tissue due to interactions with its molecules, such as hemoglobin or melanin. This phenomenon is referred to as absorption and is described by the absorption coefficient $\mu_a(\lambda)$ (cm^{-1}). This coefficient quantifies the exponential decay in intensity experienced by the light wave which propagates in the medium of interest through the Beer-Lambert law. In this thesis, absorption is not the mechanism of interest.

4.2 Enhanced Backscattering Spectroscopy

In this section, we present the theoretical framework of Enhanced Backscattering Spectroscopy (EBS). EBS entails extracting the sample reflectance profile p. Firstly, we introduce the EBS peak and its link with the tissue reflectance profile p. Then, we describe the method used for the experimental estimation of p, followed by its modeling using Monte Carlo simulations.

4.2.1 EBS peak

The EBS peak is a 2D angular intensity peak in the backscattering direction. Experimentally, a CCD camera can detect this angular intensity distribution. An example of an EBS peak is given in Figure 4.3. Figure 4.1 (a) shows an explanatory scheme of the

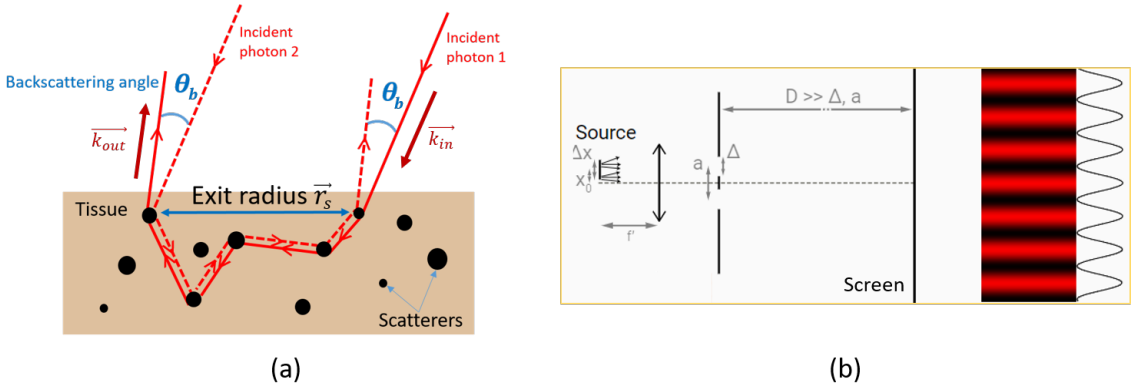

Figure 4.1: EBS phenomenon. (a) The time-reversed path-pairs photons exit the tissue with the same backscattering angle θ_b. (b) Equivalent of a Young's slits experience (using anim.institutoptique.fr, Xavier Delen, IOGS).

coherent phenomenon that gives rise to this peak. The sample is illuminated by plane waves. Let us introduce photon 1 which is multiply-scattered and exits the tissue with a backscattering angle θ_b. The reciprocity theorem guarantees the existence of a second photon traveling in the opposite direction following the exact same path [127]. The photon 2 finally exits the tissue with the same backscattering angle. As a result, the travel within the tissue does not increase the optical phase shift between the two photons. The two photons then pass through a Fourier lens which allows them to interfere onto a CCD camera (not depicted). The total phase shift $\Delta\varphi$ between the two photons can be written as:

$$\Delta\varphi = \Delta\varphi_{out} + \Delta\varphi_{in} = \Delta\varphi_{out} \tag{4.11}$$

where $\Delta\varphi_{out}$ denotes the phase shift due to travels outside the tissue, and $\Delta\varphi_{in}$ the phase shift inside the tissue that equals 0. In the reasonable configuration where the exit radius r_s is negligible in front of source-tissue distance, the phase shift between the two photons can then be expressed as [74]:

$$\Delta\varphi = (\vec{k}_{in} + \vec{k}_{out}) \cdot \vec{r_s} \tag{4.12}$$

Given that constructive interferences occur for $\Delta\varphi \approx 0$, two rationales can justify the angular intensity distribution observed in EBS:

First, for a given exit radius $\vec{r_s}$, backscattered rays with direction close to the exact backscattering direction (defined as 0°) are associated with $(\vec{k}_{in} + \vec{k}_{out}) \approx \vec{0}$. Thus, small backscattering directions contribute to constructive interferences. Similarly, the photons backscattered in other directions with relatively high values of θ_b will not contribute to the coherent phenomenon. This point justifies the fast intensity decay exhibited by the EBS peak when the backscattering angle is increasing.

Secondly, the weak exit radius values also contribute to the EBS peak. Interestingly, the exit radius r_s can be seen as an indicator of the photons' travel distance in the tissue. Thus, the tissues that exhibit long transport mean free paths l'_s are associated with long exit radii. If r_s is mostly held to relatively small values, high values of backscattering angles θ_b would still maintain $\Delta\varphi \approx 0$. As a result, low diffusive media show a broader EBS peak compared to highly diffusive media. Indeed, when using a coherent source, the full width at half maximum (FWHM) of the EBS peak is inversely proportional to the mean free path l'_s in the tissue [74].

An analogy with the Young's slits experience can be made (Figure 4.1, b) [82]. By thinking the exit points of the two rays as a double slit illuminated by a collimated beam, the EBS pattern is similar to the diffraction pattern observed on a screen in the far field in the Young's slit experience. In this case, the observed fluctuations in intensities can be described as being the Fourier transform of the two separated delta functions. The intensity angular distribution then appears as a cosine function. In a first scalar approximation, the EBS peak can be seen as the summed interference patterns of all time-reversed

path-pair photons. Summing all the cosine patterns in all directions results in a single halo in the center, corresponding to the EBS peak. The latter corresponds to the 2D Fourier transform of the reflectance profile in a tissue illuminated by an infinitely narrow pencil beam [124].

4.2.2 EBS peak and reflectance profile p

The intensity of multiply scattered photons exiting the tissue with a differential position (x_s, y_s) is denoted as I_{ms}, where x_s and y_s are the differential Cartesian coordinates. Single scattered photons $I_{ss}(x_s, y_s)$ cannot generate a time-reversed path and therefore do not contribute to the EBS peak. The EBS peak can be normalized by the incoherent baseline intensity which reflects all orders of scattering, such as [127]:

$$I_{EBS}(\theta_x, \theta_y) = \frac{\iint_{-\infty}^{+\infty} I_{ms}(x_s, y_s) e^{-ik[x_s sin(\theta_x)) + y_s sin(\theta_y)]} dx_s dy_s}{\iint_{-\infty}^{+\infty} [I_{ms}(x_s, y_s) + I_{ss}(x_s, y_s)] dx_s dy_s} \tag{4.13}$$

where θ_x and θ_y are the backscattering angles in the two Cartesian directions. Under the approximation of a semi-infinite medium irradiated by light plane waves, $p_{eff}(x_s, y_s)$ and the EBS peak are simply linked by the Fourier transform [81]:

$$I_{EBS}(\theta_x, \theta_y) = FT\{p_{eff}(x_s, y_s)\} \tag{4.14}$$

The effective reflectance profile $p_{eff}(x_s, y_s)$ represents the modulation of the tissue reflectance profile of interest $p(x_s, y_s)$ by other functions, such as [85]:

$$p_{eff}(x_s, y_s) = p(x_s, y_s) \cdot pc(x_s, y_s) \cdot s(x_s, y_s) \cdot c(x_s, y_s) \cdot mtf(x_s, y_s) \tag{4.15}$$

where FT denotes the 2D Fourier transform, pc the phase correlation function, s a modulation due to finite illumination spot size, c the spatial coherence function and mtf the imaging system's modulation transfer function. These functions are described below.

Sample reflectance profile

The sample reflectance profile is the quantity of interest in EBS. In practice, $p(x_s, y_s)$ can be radially averaged to mitigate experimental noise, such as:

$$p(r_s) = \int_0^{2\pi} p(x_s = r_s cos\phi, y_s = r_s sin\phi) d\phi \tag{4.16}$$

where r_s and ϕ represent the polar coordinates corresponding to the differential positions x_s and y_s. The tissue reflectance profile $p(r_s)$ can be seen as an optical tissue signature and is also known as the radial point spread function. Indeed, $p(r_s)$ is extremely sensitive to the phase function in the subdiffusion regime ($r < l'_s$, l'_s being the transport mean free

path) [81,85]. This can be explained by the fact that the photons that correspond to this regime have undergone few scattering events.

Phase correlation function pc

The phase correlation function pc represents the ability of forward and reversed photons to interfere. This function takes into account the vector wave nature of light, which is required to accurately describe the experimental EBS peak [81]. The coefficient can reflect the partial interference between rays when orthogonal polarization channels are used. However, in this thesis, EBS will be performed in the co-polarized channel (xx), where time-reversed path-pair photons can fully interfere [127]. Thus, this coefficient will be kept to unity hereafter.

Spatial coherence function c

The spatial coherence length of the source L_n is reflected through the function c. The length L_c is a measure of the maximum distance between two coherent wavefronts and gives the maximum size allowed for interference to occur.

Using a partial spatial coherence source, the reflectance profile is modulated by the function c which can be seen as a spatial filter. This configuration corresponds to an EBS-derived technique, known as Low Enhanced Backscattering Spectroscopy (LEBS). In LEBS, the inequality $L_c < l'_s$ is verified. In other words, the majority of path-pair photons have therefore traveled a distance l'_s greater than the coherence length. One photon of a given pair from this majority is then no longer able to interfere with the second photon: the photon pair is said to be incoherent. Long paths are thus rejected by the low coherence of the source. Assuming that longer paths reflect travel with deeper distances in the tissue, depth selectivity can be achieved by tuning the value of L_c.

In EBS, the coherence length of the source L_c is large in front of the transport mean free path of photons in the tissue $L_c \gg l'_s$. Thus, photons from the same pair are coherent. As a result, any pair of photons traveling in opposite directions in the tissue can form constructive interference. The function c is then taken to unity.

Finite illumination beam size s

In this thesis, the sample is illuminated by a laser beam, which therefore presents a finite spot diameter. Time-reversed path pair photons can only originate from rays that remain within the illumination spot. Thus, rays that exit outside this area do not contribute to the EBS peak. The experimental measurement of the reflectance profile then needs to be corrected for these rays, considered as losses. Let $A(x, y)$ be the top-hat function that describes the spatial intensity distribution of the illumination spot. Since the EBS signal depends on the relative distance of exits of rays r_s as opposed to the absolute position within the illumination spot, the function $s(x_s, y_s)$ can be computed as

the autocorrelation function of $A(x, y)$ such as:

$$s(x_s, y_s) = \frac{\iint_{-\infty}^{\infty} A(x, y)A(x_s - x, y_s - y)dxdy}{\iint_{-\infty}^{\infty} A(x, y)dxdy} = ACF[A(x, y)] \tag{4.17}$$

where ACF denotes the autocorrelation function.

4.2.3 Reflectance profile estimation

In this subsection, we present a typical EBS instrument and the associated data processing procedure to estimate the tissue reflectance profiles.

EBS instrumentation

The measurement of EBS peak can be conducted using different setups, including fiber optics-based instruments [78,128]. In this thesis, we used a benchtop configuration [127], as shown in Figure 4.2. A general description is given below. Additional details will be given for each implementation in the following chapters. A collimated beam from a broadband laser source irradiates the sample with plane waves. Then, an iris diaphragm shapes the beam into a circular spot. The polarizer forces the incident illumination into a vertical linear polarization. The analyzer is parallel to the polarizer to select the co-polarized channel. The hyperspectral camera then detects the angular intensity distribution thanks to the Fourier lens. The maximum backscattering angle and the angular resolution of the EBS measurement depend on the focal length of the Fourier lens, the pixel size and the sensor dimension.

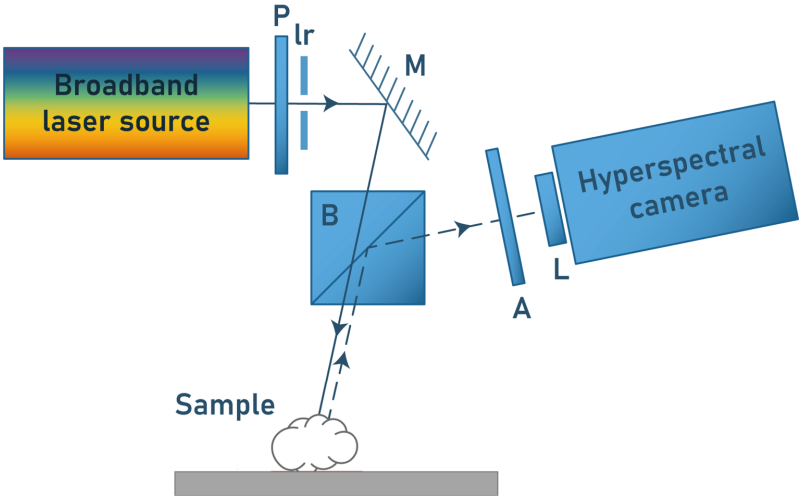

Figure 4.2: Example of EBS instrument. P: polarizer, Ir: iris diaphragm, M: mirror, B: 50:50 non-polarizing beamsplitter, A: analyzer, L: Fourier lens

Each optical component of the benchtop experimental setup needs to be aligned with

the laser source such as the exact backscattering direction corresponds to the center pixel of the camera.

Data collection

In this paragraph, we present the experimental protocol to measure the EBS peak, as outlined by Radosevich et al. [127].

- Firstly, the product of the imaging system's modulation transfer function mtf and the finite illumination beam size function s can be estimated simultaneously by placing a mirror at the sample position. The mirror is slightly moved and tilted until the reflection on the diaphragm matches the iris. Thus, the reflected beam passes back through the iris diaphragm in the reverse direction [129]. In this configuration, the position of laser spot confirms the position of the exact backscattering direction in the detected image. The exposition time is set such that the maximum intensity in the image reaches 80% of the saturation level for all measurements. Optical neutral densities (typically OD5) are placed before the polarizer to attenuate the laser power. The co-polarized channel is selected by orientating the axis of polarizer and the analyzer parallel. We refer to this acquisition as the mirror measurement mir.

- Secondly, the white standard acquisition is performed and is denoted as ws. To do so, the polarizers and the neutral densities are removed. A reflectance white standard is placed at the sample position, allowing to measure the total unpolarized incoherent intensity. The white standard is rotated to eliminate speckle noise using a motorized platform (150°/sec). An example of white standard measurement is given in Figure 4.3.

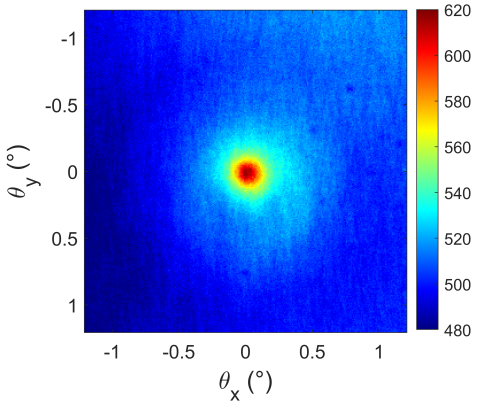

Figure 4.3: Example of white standard measurement ws_n in the co-polarized channel acquired at 700 nm.

- Thirdly, the background acquisition is conducted and is denoted as bg. To do so, the polarizers are replaced as initially. Then, a mirror is placed at the sample position and deviates the incident laser beam toward a beam dump.

- Finally, the sample acquisition is performed and is denoted as $sample$. To do so, the sample is gently rotated to eliminate speckle noise (80°/s). As a result, the tissue structural anisotropy is averaged away and is therefore not considered in this application. The sample can be submerged in an aqueous solution of glycerol with a refractive index close to the assumed tissue refractive index (typically n = 1.38) to assume refractive index matching.

These steps are repeated for each working wavelength if the EBS peak can be spectrally resolved (*i.e.* if a hyperspectral camera is used or if a monochrome camera is used with a filter wheel).

Data processing

In this paragraph, the post-processing steps to extract the reflectance profile from the EBS measurements are described, as outlined by Radosevich et al. [127]. These steps are conducted for all the spectral images if the EBS peak is spectrally resolved.

- Firstly, all the measurements are scaled by their exposition time. Background subtraction is then conducted pixel-wise using bg for the measurements mir, ws and $sample$. The normalized background-subtracted estimates mir_n, ws_n and $sample_n$ are then obtained.

- Secondly, the total unpolarized incoherent intensity is then estimated by integrating the signal of ws_n in the periphery of the EBS peak. This estimate is performed in a ring as far away as possible from the center (typically a ring spanning from 1° to 1.1°) to minimize the coherent signal. This procedure results in a scalar value for each wavelength. The known reflectivity of the white standard can be taken into account to mitigate its effect. The resulting spectrum is then used to correct each spectral sample image $sample_n$ for the spectral heterogeneities of the source. One could note that this spectrum also corresponds to the denominator in Equation 4.13. The resulting sample images can be denoted $sample'_n$.

- Thirdly, the incoherent baseline is removed. The incoherent signal in the sample image is considered as an artifact in EBS [80]. To mitigate its effect, the incoherent baseline can be estimated from a plane fit using $sample'_n$ from an annular ring in the periphery of the EBS peak. Then, the incoherent baseline modeled as a plane intensity distribution is subtracted from $sample'_n$. The corrected sample image $sample_c$ is then obtained.

- Fourthly, the 2D inverse Fourier transform of the corrected sample image $sample_c$ is taken. This procedure results in the 2D effective reflectance profile of the sample $p_{eff}(x_s, y_s)$. The same procedure can be conducted using the normalized mirror measurement mir_n to obtain the 2D product $mtf(x_s, y_s) \cdot s(x_s, y_s)$.

- Finally, the effective reflectance profile of the sample can be estimated by radial averaging (Equation 4.16) to obtain $p_{eff}(r_s)$. The same procedure can be applied to obtain the 1D product $mtf(r_s) \cdot s(r_s)$.
  The construction of the 1D vector r_s is detailed hereafter. The exit radius resolution δr can then be expressed as [124]:

$$\delta r(\lambda) = \frac{\lambda}{N \delta\theta} \tag{4.18}$$

  where N represents the number of pixels in the direction x or y and $\delta\theta$ the experimental angular resolution of the camera.

Based on Equation 4.18, the maximum "frequency" authorized by the Nyquist sampling criterion can be expressed as [81]:

$$r_{s,max} = \frac{\lambda_{min}}{2\delta\theta} \tag{4.19}$$

To ensure compliance with this criterion, the diaphragm diameter of the iris needs to be set to the $r_{s,max}$ value prior to acquisitions.

4.2.4 Monte Carlo simulations

Forward analysis

Now that we know that the EBS peak reflects the reflectance profile, its modeling is of prime interest for tissue characterization. A forward approach constitutes a first example of application. For instance, let us consider that the assumed optical properties for a tissue of interest can be associated to a theoretical reflectance profile. After being experimentally measured, the EBS peak can lead to the estimated reflectance profile that can be then compared with the expected one. This forward approach could validate the *a priori* known optical properties (Figure 4.4).

Up to this point, we have successfully established the connection between scatterer properties and their respective phase functions, as well as the relationship between the observable Enhanced Backscattering (EBS) peak and the reflectance profile. This subsection exposes the link between the scatterer phase function and the resulting reflectance profile.

Authors reported analytical expression that can provide a partial description of the EBS peak (*e.g.* under a scalar [130] or double-scattering approximation [131]) based

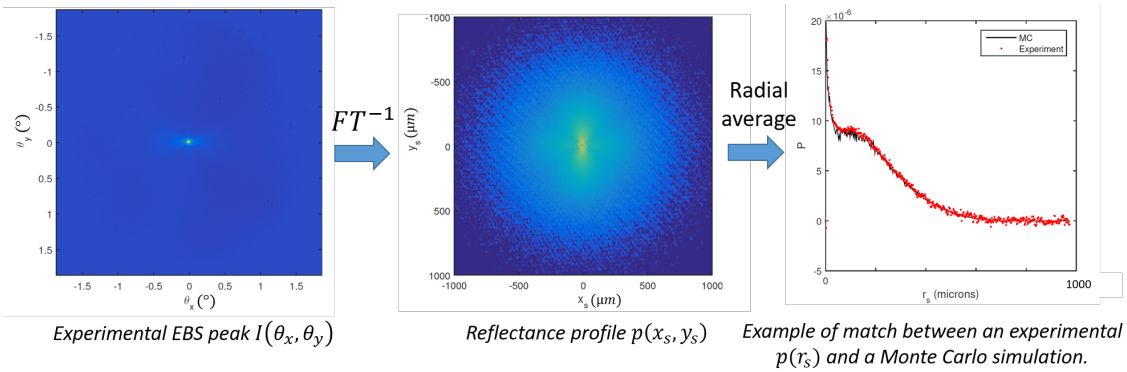

Figure 4.4: EBS workflow for forward studies. Adapted from *User Manual*, Andrew Radosevich [129]

on the tissue optical properties. Despite their computationally intensive nature, Monte Carlo (MC) simulations represent accurate methods to model light transport in biological tissues. Indeed, in the biomedical optics community, MC simulations are known as the gold standard to describe light transport in the tissues and are used as a reference to validate light transport models [132].

The main inputs in the MC simulations are the scattering phase function, the tissue geometry and the number of incident photons. If the two first inputs are accurate and the number of photons is sufficient to mitigate numerical noise (typically 1×10^7 photons), MC simulations provide an exact solution to the radiative transfer equation [80].

MC methods refer to stochastic approaches where an important amount of photon trajectories is computed in the tissue. Conceptually, every iteration can be thought of as the simultaneous launch of multiple photons in the sample of interest. Each photon packet then follows a random walk and is subject to partial absorption and/or scattering at each step. Between scattering events, the step sizes d_s follow a probability distribution defined the Beer-Lambert law such as [84]:

$$P(d_s) = (\mu_a + \mu_s)e^{-(\mu_a+\mu_s)d_s} \tag{4.20}$$

Similarly, for each scattering event, the deflecting angle is computed based on the probability distribution dictated by the phase functions. The photon's travel stops when the photon packet is fully absorbed or when it exits the tissues.

Radosevich et al. [84] provided an open-source MC algorithm that takes into account the vector nature of light and can then fully model the coherence phenomenon observed in EBS. To take into account, the interference between the time-reversed photon path-pairs, the program tracks the progression of the electric field using the Jones N-matrix formalism. In this algorithm, the user can choose between the Mie and the Whittle-Matérn phase functions. The tissue reflectance profile in the co-polarized channel is given as an algorithm output using a semi-analytical approach. This algorithm models the sample

with a single slab geometry and assumes refractive index matching at both boundaries. In practice, the sample can be placed in a refractive index-matching liquid to approximate this configuration.

Inverse analysis and refractive index representation

Inverse approaches can also be conducted using the estimated reflectance profiles to characterize the tissue of interest. Radosevich et al. [85] provided a Matlab routine able to perform inversion procedures from experimental reflectance profiles to extract refractive index-related properties from the Whittle-Matérn parameters L_n, σ_n and D. The computational inversion time is reduced thanks to a look-up table approach. Indeed, the reflectance profiles from multiple Monte Carlo simulations were pre-computed using the open software previously mentioned [84] for values of Whittle-Matérn parameters that are likely to be encountered in biological tissues. These reflectance profiles were then stored in look-up tables in a resource-efficient way to allow fast comparisons with experimental measurements.

The Whittle-Matérn parameters can be used to generate a spatial representation of the variations of refractive index. To do so, pure randomness can be convolved with the excess refractive index auto-correlation function B_n (Equation 4.3). This calculation is done in the Fourier domain. First, the power spectral density Ψ_n (*i.e.* Fourier transform of B_n) is computed (Equation 4.6). Second, an image of a Gaussian white noise of variance 1, denoted as GW, is calculated. The spatial representation of the excesses of the refractive index can then be obtained by taking the 2D inverse Fourier transform of the product $GW \cdot \Psi_n$.

4.3 Light Scattering Spectroscopy

Light Scattering Spectroscopy (LSS) aims to analyze the elastically single scattered photons to extract diagnostic information about the underlying tissue microstructure. In this paragraph, the scatterer size distribution is estimated using Mie theory by analyzing the incoherent component. Unlike EBS, which relies on both spatial and spectral resolutions for each measurement, the LSS method presented here only requires spectrally-resolved measurements. Interestingly, these measurements can be conducted using the same EBS instrument introduced in subsection 4.2.3. Furthermore, one can note that the similar nature of the analyzed signal and the extracted parameters makes LSS the optical equivalent of the ultrasound BSC parametrization technique in the incoherent case.

4.3.1 Experimental estimation of the single scattered component

The Born approximation is not required for the LSS method implemented in this thesis. Here, the contribution of multiply-scattered photons is mitigated using a diffuse background removal technique to isolate the single scattering component. Indeed, as light

propagates, photons interact with the tissue's microstructures and carry information about the scatterers. However, the scatterer properties cannot be directly extracted from the detected backscattered light in LSS. Two populations of photons can be distinguished: multiply-scattered photons which travel deeper distances on average and single-scattered photons, mostly emanating from shallow tissue layers [65]. Multiple scattering randomizes the scatterer information while single scattered photons are directly described by phase functions, which in turn reflect the scatterer properties.

To isolate the single scattering component, the polarization state of the detected backscattered light is leveraged. The polarization-gating technique is based on the key property that single scattering preserves the incident polarization at a relatively small backscattering angle in comparison to multiple scattering. Qiu et al. [9] reported the use of an endoscopic scanning fiber optic probe to perform LSS using the polarization-gating technique. This application will be used as an illustrative example (Figure 4.5). The incident white light passes through a linear polarizer before illuminating the sample. The backscattered intensities are then measured in the co-polarized channel (same polarizer) and in the cross-polarized channel using another linear polarizer orthogonally oriented.

In a scalar approximation, we define the backscattered intensities as $I_{\parallel}(\lambda)$ for the co-polarized channel and $I_{\perp}(\lambda)$ for the cross-polarized channel. Each intensity can be decomposed into two components:

$$I_{\parallel}(\lambda) = I_{\parallel}^{s}(\lambda) + I_{\parallel}^{d}(\lambda) \tag{4.21}$$

$$I_{\perp}(\lambda) = I_{\perp}^{s}(\lambda) + I_{\perp}^{d}(\lambda) \tag{4.22}$$

where the superscript s denotes the backscattered intensities associated with the shallow layer (i.e. single scattering) and the superscript d the deep tissue layers (i.e. multiple scattering). By subtracting the parallel and perpendicular signals, we obtain:

$$I_{\parallel}(\lambda) - I_{\perp}(\lambda) = I_{\parallel}^{s}(\lambda) + I_{\parallel}^{d}(\lambda) - I_{\perp}^{s}(\lambda) - I_{\perp}^{d}(\lambda) \tag{4.23}$$

Since the incident polarization is lost in multiple scattering, we can assume $I_{\parallel}^{d}(\lambda) \approx I_{\perp}^{d}(\lambda)$, we therefore obtain:

$$I_{\parallel}(\lambda) - I_{\perp}(\lambda) = I_{\parallel}^{s}(\lambda) - I_{\perp}^{s}(\lambda) \tag{4.24}$$

Since single scattering in shallow layers preserve the incident polarization, we have $I_{\parallel}^{s}(\lambda) \gg I_{\perp}^{s}(\lambda)$. The previous expression can further simplifies to:

$$\Delta I(\lambda) = I_{\parallel}(\lambda) - I_{\perp}(\lambda) = I_{\parallel}^{s}(\lambda) \tag{4.25}$$

where $\Delta I(\lambda)$ referred to the differential polarization signal. Hence, subtracting parallel and perpendicular signals cancels the multiple scattering contributions and isolates the scattering signal from superficial layers.

Experimentally, the polarization channel can be selected by setting the orientation

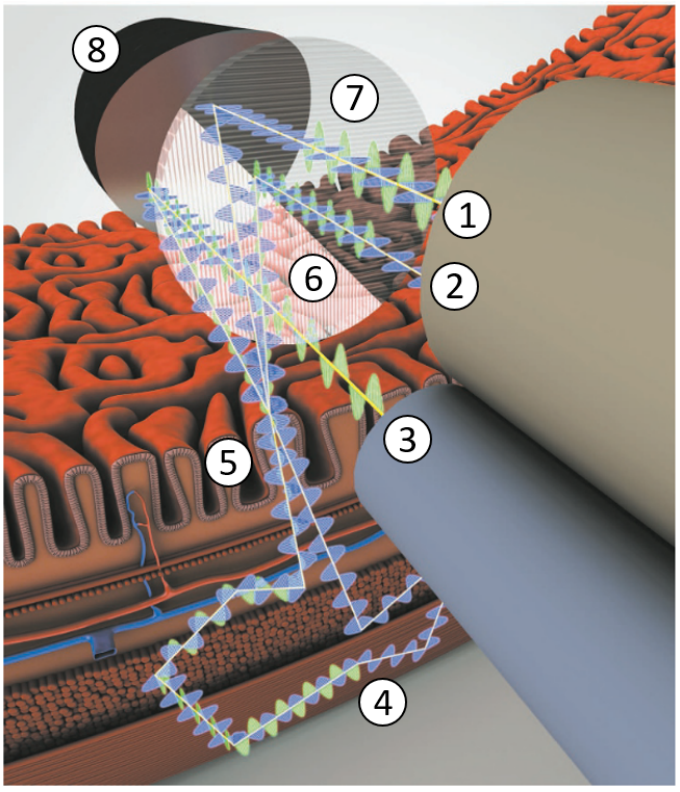

Figure 4.5: Implementation example of the polarization-gating technique using a polarized scanning fiber optic probe. Qiu et al. [9] developed this tool to detect pre-cancerous conditions in the esophagus. 1: Incident white light emitted by the delivery fiber. 2: Co-polarized detection by one collection fiber (not depicted in the diagram). 3: Cross-polarized detection by another collection fiber. 4: Depolarization in the deep tissue layers. 5: Epithelial tissue (*i.e.* shallow tissue layer of interest). 6: Linear polarizer in the perpendicular direction. 7: Linear polarizer in the parallel direction. 8: Parabolic mirror. Adapted from Qiu et al. [9]

of the analyzer. For each polarization channel, the raw co-polarized and cross-polarized intensities are background-subtracted and normalized using a white standard reference before leading to $\Delta I(\lambda)$:

$$I_{\parallel}(\lambda) = \frac{I_{\parallel}^{r}(\lambda) - I_{\parallel}^{bg}}{I_{\parallel}^{0}(\lambda)} \; ; \; I_{\perp}(\lambda) = \frac{I_{\perp}^{r}(\lambda) - I_{\perp}^{bg}}{I_{\perp}^{0}(\lambda)} \tag{4.26}$$

The superscript r denotes raw measurements, bg represents background measurements, and 0 corresponds to the white standard reference spectrum that corrects for the source heterogeneities.

One could note that model-based approaches [64, 65] and spatial-gating techniques [9] could alternatively serve as diffuse background removal procedures.

4.3.2 Single scattered light: theoretical expression

In this subsection, the theoretical expression of the differential polarization signal $\Delta I_{th}(\lambda)$ is given following the equations described in Backman et al. [63]. This expression will then be used in the inversion procedures described in the next section.

Let us consider a spherical particle illuminated by a light plane wave $\vec{E_i}(\vec{r}) = \vec{E_0}e^{j(\vec{k_i}\vec{r}-wt)}$ where E_0 is the wave amplitude, $\vec{k_i}$ the wavevector, $\vec{r}$ the position vector relatively to the center of the particle, ω the frequency and t the time.

The scattered wave $\vec{E_s}$ propagates along the direction of the scattering vector $\vec{k_s}(\theta, \phi)$, where θ and ϕ denote the polar angles in the spherical coordinate system. Let us set the corresponding coordinate system such that $\vec{z} \parallel \vec{k_i}$ and such that $\vec{x} \parallel \vec{E_0}$. The scattered field is a spherical wave that has a component parallel and a component orthogonal to the scattering plane (E_{s1} and E_{s2} respectively). They can be expressed from the corresponding components of the incident wave E_{i1} and E_{i2}. Given the radial symmetry of the scatterer geometry, we can write:

$$\begin{pmatrix} E_{s2} \\ E_{s1} \end{pmatrix} = \frac{e^{j(\vec{k}\vec{r}-wt)}}{jkr} \begin{pmatrix} S_2(\theta) & 0 \\ 0 & S_1(\theta) \end{pmatrix} \begin{pmatrix} E_{i2} \\ E_{i1} \end{pmatrix} \tag{4.27}$$

where $S_1(\theta)$ and $S_2(\theta)$ represent the scattering amplitudes and depend on the polar angle θ only. The scattering amplitudes do not have a closed form [133]. In this thesis, the module *miepython* [126] was used to compute them. The selection of the polarization channel mathematically corresponds to projections onto the $\vec{x}$ and the $\vec{y}$ axes. We therefore obtain the two components $E_{s,x}$ and $E_{s,y}$ such as:

$$\begin{pmatrix} E_{s,x} \\ E_{s,y} \end{pmatrix} = \frac{E_0 e^{j(\vec{k}\vec{r}-wt)}}{jkr} \begin{pmatrix} cos(\theta)cos(\phi) & -sin(\phi) \\ cos(\theta)sin(\phi) & cos(\phi) \end{pmatrix} \begin{pmatrix} S_2(\theta) & 0 \\ 0 & S_1(\theta) \end{pmatrix} \begin{pmatrix} cos(\phi) \\ sin(\phi) \end{pmatrix} \tag{4.28}$$

$$\begin{pmatrix} E_{s,x} \\ E_{s,y} \end{pmatrix} = \frac{E_0 e^{j(\vec{k}\vec{r}-wt)}}{jkr} \begin{pmatrix} S_2(\theta)cos(\theta)cos(\varphi)^2 - S_1(\theta)sin^2(\phi) \\ S_2(\theta)cos(\theta)cos(\phi)sin(\phi) + S_1(\theta)cos(\phi)sin(\phi) \end{pmatrix} \tag{4.29}$$

The corresponding intensities are computed by taking the square absolute value of the electric fields, such as:

$$I_{\parallel}(\lambda) - I_{\perp}(\lambda) = |E_{s,x}|^2 - |E_{s,y}|^2 \tag{4.30}$$

By substituting the equation 4.29 into the equation 4.30, we have:

$$\begin{aligned} I_{\parallel}(\lambda) - I_{\perp}(\lambda) = \frac{I_0}{k^2 r^2}\Big(& |S_2(\theta)|^2 cos^2(\theta)cos^2(\phi)[cos^2(\phi) - sin^2(\phi)] \\ & + |S_1|^2 sin^2(\phi)[sin^2(\phi) - cos^2(\phi)] - 4\Re(S_1(\theta)\overline{S_2}(\theta))cos(\theta)cos^2(\phi)sin^2(\phi)\Big) \end{aligned} \tag{4.31}$$

with $I_0 = |E_0|^2$ and $\Re$ the real part. Given that the incident light is collimated, the collected light $\Delta I_{th}(\lambda)$ is obtained by integrating the previous difference over the

backscattering angles θ_1 to θ_2 and over the azimuthal angle. We therefore obtain:

$$\Delta I_{th}(\lambda) = 2\pi \int_{\theta_1}^{\theta_2} \int_0^{2\pi} \Big(I_{\parallel}(\lambda) - I_{\perp}(\lambda)\Big) sin(\theta) d\theta d\phi \tag{4.32}$$

$$\begin{aligned}\Delta I_{th}(\lambda) = \frac{2\pi I_0}{k^2 r^2} \Bigg[& \int_{\theta_1}^{\theta_2} \Big[|S_2(\theta)|^2 cos^2(\theta) sin(\theta) \Big(\int_0^{2\pi} cos^4(\phi) d\phi - \int_0^{2\pi} cos^2(\phi) sin^2(\phi) d\phi \Big) \Big] d\theta \\ & + \int_{\theta_1}^{\theta_2} |S_1(\theta)|^2 sin(\theta) \Big[\int_0^{2\pi} sin^4(\phi) d\phi - \int_0^{2\pi} cos^2(\phi) sin^2(\phi) d\phi \Big] d\theta \\ & - 4 \int_{\theta_1}^{\theta_2} \Big(\Re(S_1(\theta) \overline{S_2}(\theta)) cos(\theta) sin(\theta) \int_0^{2\pi} cos^2(\phi) sin^2(\phi) d\phi \Big) d\theta \Bigg]\end{aligned} \tag{4.33}$$

which can be written as:

$$\begin{aligned}\Delta I_{th}(\lambda) = \frac{2\pi I_0}{k^2 r^2} \Bigg[& \int_{\theta_1}^{\theta_2} |S_2(\theta)|^2 cos^2(\theta) sin(\theta) \Big(\frac{3\pi}{4} - \frac{\pi}{4} \Big) d\theta \\ & + \int_{\theta_1}^{\theta_2} |S_1(\theta)|^2 sin(\theta) \Big(\frac{3\pi}{4} - \frac{\pi}{4} \Big) d\theta \\ & - 4 \int_{\theta_1}^{\theta_2} \Re(S_1(\theta) \overline{S_2}(\theta)) cos(\theta) sin(\theta) \frac{\pi}{4} d\theta \Bigg]\end{aligned} \tag{4.34}$$

$$\Delta I_{th}(\lambda) = \frac{\pi^2 I_0}{k^2 r^2} \int_{\theta_1}^{\theta_2} \Big[S_2(\theta)^2 cos(\theta)^2 + |S_1(\theta)|^2 - 2\Re(S_1(\theta) \overline{S_2(\theta)}) cos(\theta) \Big] sin(\theta) d\theta \tag{4.35}$$

Finally, we obtain:

$$\Delta I_{th}(\lambda) = \frac{\pi^2 I_0}{k^2 r^2} \int_{\theta_1}^{\theta_2} |S_2(\theta) cos(\theta) - S_1(\theta)|^2 sin(\theta) d\theta \tag{4.36}$$

The scattering amplitudes S_1 and S_2 depend not only on the backscattering angles but also on the scatterer radius r and the refractive indices n_{re} and n_{env} since they are computed using Mie theory. Therefore, the theoretical differential polarization signal $\Delta I_{th}(\lambda, r, \theta_1, \theta_2, n_{re}, n_{env})$ can be computed for different scatterer sizes and wavelengths by setting fixed values for the remaining parameters.

4.3.3 Extraction of the scatterer size distribution

Analysis of single scattered component

Once the single scattered spectrum has been estimated experimentally, its analysis can lead to scatterer properties. Indeed, the scatterer size distribution F can be estimated from the sample differential polarization signals $\Delta I(\lambda)$. In this subsection, the analytical treatment required to extract F is described.

LSS models the detected spectrum as the incoherent sum of the contributions of each scatterer [9].

$$\Delta I(\lambda) = \int_{r_{min}}^{r_{max}} \Delta I_{th}(\lambda, r) F(r)\, dr + \frac{C_R}{\lambda^4} + \epsilon(\lambda) \tag{4.37}$$

where λ is the wavelength, θ is the backscattering angle, n_{re} the relative refractive index between the scatterer and the surrounding medium n_{env}, $\Delta I_{th}(\lambda, r)$ the LSS spectrum of a single scatterer of radius r, r_{min} the radius threshold below which Rayleigh scattering is considered as dominant (typically 100 nm), C_R an unknown constant proportional to the number of Rayleigh scatterers, r_{max} the maximum scatterer radius, $F(r)$ the scatterer size distribution and $\epsilon(\lambda)$ the experimental noise.

Fang et al. [68] describes the analytic procedure to extract F. To mitigate the effect of Rayleigh scattering, equation 4.37 is multiplied by λ^4 prior to differentiation with respect to λ such as:

$$\Delta I(\lambda)\lambda^4 = \int_{r_{min}}^{r_{max}} \Delta I_{th}(\lambda, r) F(r) \lambda^4\, dr + C_R + \epsilon(\lambda)\lambda^4 \tag{4.38}$$

$$\frac{\partial[\Delta I(\lambda)\lambda^4]}{\partial\lambda} = \int_{r_{min}}^{r_{max}} \frac{\partial[\Delta I_{th}(\lambda, r)\lambda^4]}{\partial\lambda} F(r) dr + \frac{\partial[\epsilon(\lambda)\lambda^4]}{\partial\lambda} \tag{4.39}$$

By introducing $\hat{S}(\lambda) = \frac{\partial[\Delta I(\lambda)\lambda^4]}{\partial\lambda}$, $\hat{I}(\lambda) = \frac{\partial[\Delta I_{th}(\lambda,r)\lambda^4]}{\partial\lambda}$, $\hat{E}(\lambda) = \frac{\partial[\epsilon(\lambda)\lambda^4]}{\partial\lambda}$ and by discretizing the scatterer radius such as $\hat{F}(r) = F(r)dr$, we obtain:

$$\hat{S}(\lambda) = \sum_{r_{min}}^{r_{max}} \hat{I}(\lambda, r)\hat{F}(r) + \hat{E}(\lambda) \tag{4.40}$$

The previous equation can be formulated in the matrix format:

$$\hat{S} = \hat{I} \cdot \hat{F} + \hat{E} \tag{4.41}$$

Inverse problem

The spectrum $\hat{S}$ is measured experimentally. Its dimension depends on the number of wavelengths p at which the experimental spectrum $\Delta I(\lambda)$ is measured. The size distribution of interest F has a dimension q that depends on r_{min}, r_{max} and the scatterer radius resolution δr. These coefficients need to be set a priori and their value depends on the application. The intensity matrix $\hat{I}$ of dimension $p \times q$ can be pre-computed using Mie theory with the Python module *miepython*, following the equation 4.36. To do so, the relative refractive index n_{re} can be set to a fixed value. To target the nuclei/cytoplasm refractive index variation, $n_{re} = 1.06$ can be chosen for instance [65, 68]. Similarly, the surrounding medium refractive index was assumed to be 1.38 [85]. The backscattering angles θ_1 and θ_2 are fixed values that depend on the optical components chosen in the experimental setups (*e.g.* camera spatial resolution). The instrumentation used for LSS is detailed in the following chapters.

The size distribution F can be estimated by minimizing the following sum of squared

differences over the wavelengths:

$$F(r) = \arg\min_{F} \Big(\sum_{\lambda} \sqrt{(\hat{S} - \hat{I} \cdot \hat{F})^2} \Big) \tag{4.42}$$

To solve this equation, assumptions about the scatterer size distribution can be made. For instance, a Gaussian distribution would involve the determination of the mean scatterer size a and its standard deviation σ such as $F(a, \sigma)$ [65]. However, to take into account the variety of sizes of potential scatterers in biological tissues, a non-negativity constraint can be applied such as $F(r) > 0$ [68]. Then, the size distribution F can be estimated through an optimization problem because of the experimental noise $\hat{E}$. Equation (4.42) can be solved using a linear least squares algorithm [8]. One can note that the dimension q set by the operator conditions the problem: the problem is overdetermined if $p > q$ or underdetermined if $p < q$.

Discussion

Interestingly, the solving method mentioned above allows near real-time inversions of F since the intensity matrix $\hat{I}$ is pre-computed. Thus, this implementation of LSS is adapted for clinical applications. However, the short computation time observed here comes at the expense of *a priori* assumptions about experimental coefficients such as n_{re}. Fang et al. [68] argue that the relative refractive index weakly affects the shape of the measured spectra compared to the scatterer radius. Variations in the magnitude of the LSS spectra are reported when the parameter n_{re} varies. Thus, the approximation in the relative refractive index should not prevent the accurate estimation of the scatterer radii. The authors add that LSS can measure the refractive indices given that independent measurements of particle sizes and concentrations are available. Similarly, the experimental choice of the backscattering coefficient θ is of minor importance to extract the scatterer radius [68].

One could note that the LSS method introduced here involves the measurement of the incoherent spectrum associated with single scattered photons. This method is adapted for endoscopic polarized scanning spectroscopy [9]. In parallel, Qiu et al. [134] reported another LSS application termed confocal light absorption and scattering spectroscopic (CLASS) microscopy. In this case, the scatterer size distribution can be extracted from the incoherent (I-CLASS) or coherent signal (C-CLASS). Another analytical model is required to model the coherent signal. In this specific application, the C-CLASS technique outperformed the (I-CLASS) method in terms of SNR and particle sizing accuracy. Thus, follow-up studies using LSS for microscopy reported the use of C-CLASS technique [135, 136].

Chapter 5

Validation on tissue-mimicking phantoms

In the first chapter, successful applications of QUS and light backscattering techniques were described. These two modalities have the potential to address specific clinical needs related to cancer characterization and were, therefore, selected to provide complementary diagnostic information. Their methods were presented in the two previous chapters.

The study reported in this chapter aims to validate our bimodal approach using tissue-mimicking phantoms. To do so, three phantoms composed of different microparticles were characterized using Backscatter coefficient (BSC) estimations and Enhanced Backscattering Spectroscopy (EBS). This study represents an initial proof of concept for our innovative methodology.
The results presented in this chapter were published in a proceeding paper and were also orally presented at two international conferences and one national conference:

- Malinet, C., Montcel, B., Liebgott, H., Muleki-Seya, P., "Combined ultrasound and light backscattering spectroscopy for cancer characterization: a proof of concept." (proceeding), 2022 IEEE International Ultrasonics Symposium (IUS), Venice, Italy. [137]
- Artimino 2022 - Medical Ultrasound Technology, Boulder, Colorado, United States of America
- "Caractérisation du Cancer par Associations de Techniques Acoustiques et Optiques de Rétrodiffusion". Avril 2022, 16ème Congrès Français d'Acoustique, CFA2022, Marseille, France. [138]

We acknowledge A. Radosevich (Backman Biophotonics Laboratory, Northwestern

University, Illinois, United States of America) for publicly sharing the Matlab programs that were adapted for processing the EBS data in this study and in the following chapters [139].

5.1 Introduction

Cancerous cells can undergo dysplasia, during which tumor-type characteristic morphological alterations can be observed at both cellular and nuclear scales. More precisely, the nuclear-cytoplasmic ratio, denoting the proportion of nucleus size relative to cell size, may be notably affected. Typically, this quotient increases as the nuclei enlarge relatively to the cell. The nuclear-cytoplasmic ratio is a metric that can be used in cancerous grading systems [140, 141].

Combining an ultrasound method and an optical technique to estimate different cellular structure sizes appears as a potential non-invasive alternative to histological examinations. Given the magnitudes of the wavelengths in each modality, a certain complementarity in the sensitivity regarding the scatterer size can be expected. The BSC parametrization and EBS were chosen to provide a first experimental proof-of-concept in this chapter. As reported in section 2.2, numerous studies successfully extracted the sizes of cellular structures by parametrizing the BSC. On the other hand, EBS provides a measurement of the effective spatial reflectance profile. Previous papers have shown the extreme sensitivity of the reflectance profiles to the scattering phase function in the subdiffusion regime (*i.e.* lengthscales smaller than the transport mean free path) [85] (c.f. section 2.3.3). Under specific conditions, the scattering phase function can reflect the scatterer diameter. Hence, the sizes of cellular structures could be estimated in biological tissues based on their reflectance profile.

As a long-term objective, the local estimations of the nucleus sizes and cell sizes using BSC parametrization and EBS could successfully reflect the actual nuclear-cytoplasmic ratio of interest. However, in the framework of this thesis, this chapter aims firstly to provide a preliminary validation of the bimodal method on tissue-mimicking phantoms. The complementarity of the BSC parametrization and EBS are experimentally investigated. More specifically, the sensitivity regarding the scatterer size is studied for each technique using three phantoms with different microparticle sizes. To do so, contrasts between phantoms as well as agreements between experimental data and theoretical models are analyzed.

First, phantoms with consistent optical and acoustic properties are designed. Then, measured BSCs and reflectance profiles are compared to their expected theoretical models, following a forward approach. Last, the performances of each technique are discussed.

5.2 Methods

In this section, the design of the tissue-mimicking phantom characteristics is detailed, followed by a description of the BSC estimation method and the implementation of EBS.

5.2.1 Tissue-mimicking phantoms

The three tissue-mimicking phantoms were designed with chosen components and concentrations to obtain the most realistic ultrasound and optical scattering properties. Orgasol powders (Arkema, France) appear as a good candidate to meet the specifications that are detailed below:

The first challenge was to find particles with sizes similar to the nucleus and cell sizes that can be encountered in tissue. Orgasol powders are available in 10 µm (ref. 2002 EXD), 20 µm (ref. 2002 D) and 60 µm diameter (ref. 2002 ES6). To cite a few illustrative examples, the 10 µm particles present a diameter similar to the diameter of fibroblast nuclei, while the 20 µm and 60 µm particles are akin in size to glandular epithelial and osteoclast cells respectively. The powders consisted of transparent polyamide particles of spheroidal shape (Figure 5.1).

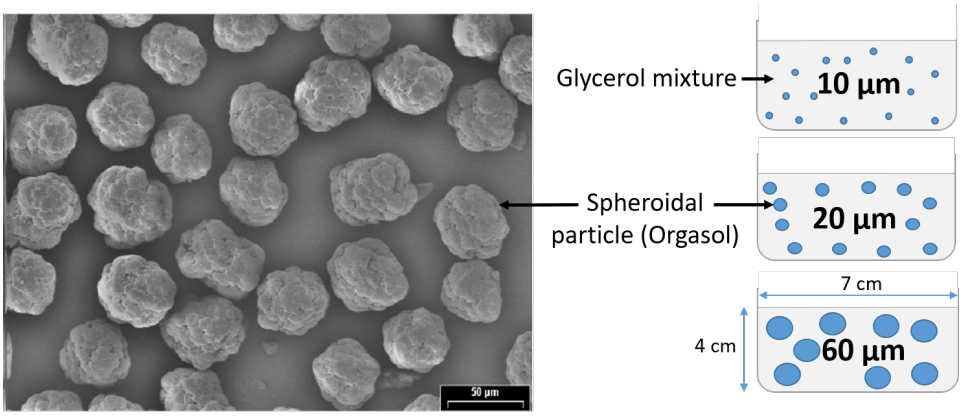

Figure 5.1: Illustrative example of microphotograph of Orgasol particles (2002 ES5) and schemes of phantom composition. The 10, 20 and 60 µm Orgasol powders used in this study present similar aspects to those observed in the microphotograph. The schemes are not drawn to scale. The microphotograph is reproduced from www.azelis.com [142]

The particles must also exhibit the capacity to scatter both optical and ultrasound waves, in a manner analogous to cellular structures. Orgasol particles exhibit a refractive index of $n_{org} = 1.52$ at 589 nm and a density of 1.03 g/cm^3 (supplier data). Taking the sound speed at 2300 m/s, Orgasol particles exhibit an acoustic impedance $Z_{org} = 2.4$ MRayl. The particles were suspended in a mix of water and glycerol to obtain more realistic scattering properties. Two to three droplets of surfactant were added (Syperonic, Sigma). Glycerol has the double effect of reducing the relative refractive index n_{re} and the impedance contrast γ_z between the scatterers and the surrounding medium. The

mass fraction of glycerol was set to 42% to approximate a surrounding media refractive index of $n_{env} = 1.38$ at 410 nm. [143]. Under the approximation that the refractive index dispersion is negligible, the relative refractive index n_{re} was then equal to $n_{re} = 1.10$ and is therefore similar to the cell nuclei relative to cytoplasm relative refractive index (n_{re} = 1.03 - 1.1 [65, 144]). Assuming that the sound speed in the mixture linearly increases with the glycerol concentration up to the sound speed reported in pure glycerol, the sound speed was taken to 1660 m/s. The density of the mixture (relative to water density) was calculated by weighting the densities of water and glycerol with the mass fractions of each component and is estimated equal to 1.06. The acoustic impedance of the mixture was then estimated at 1.8 MRayl, leading to a relative impedance contrast of $\gamma_z = 0.33$. The relative impedance contrast in biological tissues can vary greatly depending on the specific tissues. However, the estimated value of γ_z is not in contradiction with the order of magnitudes of relative impedance contrast in tissues reported in previous studies [5, 145]. Thus, the Born approximation was applied in this study.

The volume fractions of each phantom were chosen to obtain optical reduced scattering coefficients that are consistent with those encountered in human tissues ($\mu_s' = 7 - 15$ cm^{-1} at 700 nm [146]) except for the 60 µm phantom, as explained below. The μ_s' coefficients were computed with a forward model based on the Mie Theory [147]. The values for each phantom were provided in Table 5.1. The 60 µm phantom exhibits a low reduced scattering coefficient to allow a low volume fraction. Indeed, this particle size requires a high volume fraction ($\phi = 0.40$) to reach the lowest realistic μ_s' values. Thus, this trade-off was made to mitigate the strong acoustic attenuation of a highly concentrated phantom composed of 60 µm beads. In this phantom study, optical absorption was assumed negligible.

Each suspension filled a square box of dimension 7 x 7 x 4 cm^3. The smallest dimension of the phantom box was higher than the light scattering mean free paths l_s' ($60l_s'$ for the 10 µm phantom, $32l_s'$ for the 20 µm phantom and $4l_s'$ for the 60 µm phantom), thus allowing us to consider each phantom as a semi-infinite media.

In summary, three tissue-mimicking phantoms with consistent optical and acoustic scattering properties were designed. Hereafter, they will be referred to by the size of their constituent particles (*e.g.* 10 µm phantom). The BSCs and the reflectance profiles were then estimated on each phantom. The polyamide microsphere sound speed was taken at 2300m/s, the density at 1.03 and the Poisson's ratio at 0.43

Microspheres were suspended in water because of the practical difficulty of designing homogeneous phantoms at high concentrations ($\phi > 10\%$)

5.2.2 Backscatter coefficient

Acquisition parameters and data processing

Firstly, the ultrasound attenuations were experimentally estimated following the standard substitution method [110], detailed in the subsection 3.2.4. Secondly, BSC estimations were conducted. Each phantom was insonified with 13 tilted plane waves (between

Phantom	Volume fraction ϕ	Attenuation α_0 (dB/mm/MHz)	Reduced scattering coefficient μ_s' (cm^{-1})
Orgasol 10 µm	0.08	0.08	15
Orgasol 20 µm	0.11	0.14	8
Orgasol 60 µm	0.06	*0.20*	1

Table 5.1: Tissue mimicking phantom characteristics. The volume fractions ϕ were set, and the reduced scattering coefficients μ_s' were subsequently determined through calculation. The acoustic attenuations were experimentally estimated following standard substitution methods [110]. The measurement of the acoustic attenuation of the 60 µm phantom is inconclusive and is therefore empirically determined.

$-3°$ and $+3°$) using a linear probe centered at 15 MHz with a bandwidth extending from 8 to 22 MHz. (CMUT L228, ultrasound scanner Verasonics). As depicted in Figure 6.2, a magnet gently stired the phantoms to ensure their homogeneities during the acquisition. Two hundred fifty-six RF lines were acquired for each phantom. Corresponding B-mode images were then generated using a conventional Delay and Sum algorithm. Two rows of eleven Regions of Interest (ROI) that are 26λ long in the propagation direction and 22λ long in the lateral direction were delimited. The ROIs were located at a depth of 1 mm and 3.2 mm for the first and the second row respectively. This ROI size allowed to capture a sufficient number of uncorrelated RF lines for robust power spectrum estimations. The BSC for each ROI was estimated using the reference phantom method [113] that was detailed in subsection 3.2.4. The reference phantom had the same chemical composition as the others except that it has 5 µm Orgasol particles (ref. 2001 UD) with a volume fraction equal to 0.05. The Poisson coefficient was also taken equal to 0.43. Then, the 22 BSC estimations were averaged for each phantom to obtain the plotted curves in section 5.3.

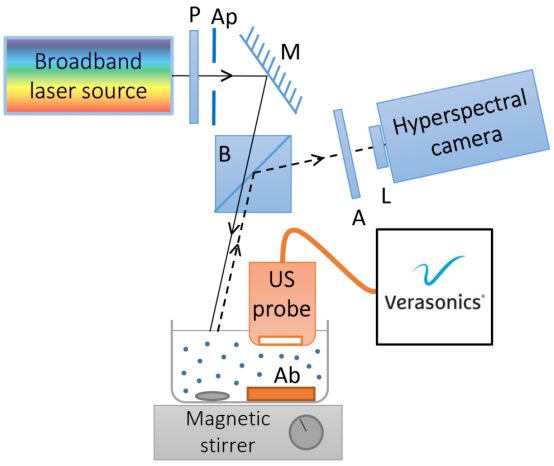

Figure 5.2: Experimental setup; P: polarizer, Ap: Aperture, M: mirror, B: beamsplitter, A: analyzer, L: Fourier lens, Ab: absorbing material.

Theoretical scattering models

Backscattering from randomly distributed solid spheres in a surrounding fluid medium can be modelled with the Faran Model (FM) under the Born approximation [39], as detailed by Equation 3.11 in Chapter 3. However, a frequency-dependent structure factor S should also be taken into account when considering a concentrated medium. For this case, Franceschini et al. [39] introduced the monodisperse Structure Factor Model (SFM):

$$BSC_{SFM}(k,a) = n\sigma_{b,Faran}(k,a)S(k,a) \tag{5.1}$$

where n being the number of scatterers per unit volume and $\sigma_{b,Faran}(k)$ the differential backscattering cross-section of the Faran model. The computation of S is detailed in Equation A.1 in Chapter 3. Here, the 10 µm and the 20 µm BSC measurements were compared with the SFM. However, the SFM showed irrealistic resonance peaks when plotted for the 60 µm phantom. The comparison was thereby made with a polydisperse Faran Model for this phantom. In this case, the BSC can be expressed as:

$$BSC_{Faran,poly}(k,a) = n\int_0^\infty \sigma_{b,Faran}(k,x)D(x)dx \tag{5.2}$$

where D is the probability density function of the scatterer radii denoted x. In this study, D was chosen to follow a Gaussian law of mean value 60 µm and a standard deviation of 3 µm to reproduce the particle size distribution specified by the supplier.

5.2.3 Enhanced Backscattering Spectroscopy

EBS measures the effective reflectance profile $p_{eff}(r)$, r being the exit radius of the backscattered photons. The EBS general method was detailed in section 4.2 in Chapter 4. This subsection provides the experimental implementation of EBS in this study.

Benchtop setup

Figure 6.2 illustrates the experimental setup used for EBS (blue components). A broadband laser source (WhiteLase micro Compact Supercontinuum, Fianium) illuminated the stirred phantom with plane waves. The aperture shaped the beam into a circular spot of 1.6 mm diameter in order to respect the Nyquist criterion. Indeed, according to Equation 4.18, the maximum beam radius is 1.7 mm. It is noteworthy that EBS entails in extracting the average scattering parameters from the illuminated region, somewhat making this area the optical equivalent of the concept ROI used in Quantitative Ultrasound. The polarizer then forced the incident illumination into a vertical linear polarization. The mirror aimed to minimize the overall bulk of the system. The beamsplitter has a 50 : 50 ratio and exhibits a limited impact on the light polarization. The analyzer was parallel to the polarizer to select the co-polarized backscattered light. The Fourier lens (focal distance of 25 mm)

focused the light onto the camera (HERA, Nireos) which acquired images at 702 nm. All the optical components are suitable for visible applications. The camera pixels are squares of dimension 5.3 µm. This configuration allowed an angular resolution of 0.01 °. Images were averaged five times to further reduce the speckles.

Implementation

EBS data processing is described in section 4.2.3. Its implementation is described here. The total unpolarized incoherent intensity was estimated on a white standard (SRT-99-050, Labsphere). by integrating the EBS image in a ring spanning from 0.90° to 0.96°, as noise was predominant above 1°. For each normalized sample image, a plane was then fitted to the intensity in the same ring and was substracted to the normalized sample image to remove the incoherent baseline. The resulting image is what is referred to as an EBS image in this study. The two-dimensional (2D) inverse Fourier transform was then taken before computing the radial average of the effective reflectance profile. A mirror measurement was achieved in the same conditions and led to an estimation of the functions that modulate the sample reflectance profile, namely the system mtf and the s function, related to the finite illumination beam size (*c.f.* subsection 4.2.2).

Simulations and theoretical data

Radosevich et al. [84] provides an open-source program to model the light backscattering in biological media through a Monte Carlo approach that takes into account the vectorial nature of light, as it was detailed in the subsection 4.2.4. The experimental effective reflectance profiles were compared to MC simulations. Each MC simulation was performed with one billion incident photons that were linearly polarized. The Mie scattering phase function was used along with the known properties of the phantoms mentioned. The simulation outputs led to the theoretical sample reflectance profile. This quantity was then modulated by the estimated mtf and s functions to obtain the expected effective reflectance profile. Indeed, the use of a laser and the co-polarized channel enabled us to consider the phase correlation function pc and the spatial coherence function $c \approx 1$ (Equation 4.15). Thus, the products of the simulated reflectance profile with mtf and s could then be compared directly with the experimental measurements of the effective reflectance profiles. One could note that the refractive index matching was assumed at the phantom surface in this tool.

5.3 Results

In the ultrasound and optical following experiments, the agreement between the measurement with the theoretical expected models is calculated using the coefficient of determination R^2. This metric will be used to assess the performances of each technique and is computed as follows:

$$R^2 = \frac{\left[\sum_{i=1}^{N}(x_i - \bar{x})(y_i - \bar{y})\right]^2}{\sum_{i=1}^{N}(x_i - \bar{x})^2 \sum_{i=1}^{N}(y_i - \bar{y})^2} \tag{5.3}$$

where N is the number of data points. The variables x_i and y_i denote the experimental and the expected theoretical data respectively. The variables $\bar{x}$ and $\bar{y}$ represent their average values.

5.3.1 Backscatter coefficient estimations

Phantom ultrasound attenuation coefficients are given in Table 5.1. The phantom attenuations follow a linear trend. The attenuation is then expressed as: $\alpha(f) = \alpha_0 f$, where f is the frequency and α_0 the attenuation coefficient. The coefficient α_0 of the 20 µm phantom exhibits a greater magnitude in comparison to the 10 µm phantom. The 60 µm phantom demonstrates even more pronounced attenuation effects. As a result, applying a substitution method is challenging and the estimation of its attenuation remains inconclusive due to the limited Signal-to-Noise ratio (SNR) of the reflector signal in the presence of the phantom. Consequently, the attenuation coefficient α_0 of the 60 µm phantom is estimated empirically. Its value is taken higher than the attenuation of the 20 µm phantom.

The B-mode images of each phantom with the positions of the ROIs are shown in Figure 5.3. The ROIs encompass uncorrelated speckle patterns. The intensity of the backscattered signals decreases as the particle diameter increases. The greater attenuation of the 60 µm phantom can be visualized on the B-mode image through the presence of darker regions at a deeper location.

Figure 5.4 gives the measured and the expected BSC versus the frequency for the 10 and the 20 µm phantoms. The SFM for the 10 µm phantom follows the trend of the corresponding BSC in the whole frequency range. The SFM for the 20 µm phantom shows discrepancies with the BSC of the 20 µm phantom up to 20 MHz and then predicts correctly the increase in the BSC. The root mean square error between the estimated and the expected BSCs of the 10 and the 20 µm phantoms are $3.9\times10^{-5}\text{mm}^{-1}.\text{sr}^{-1}$ and $1.5\times10^{-4}\text{mm}^{-1}.\text{sr}^{-1}$ respectively.

The coefficients of determination between the estimated BSC and the expected theoretical model are higher for the 10 and the 20 µm phantoms ($R^2 = 0.93$ and $R^2 = 0.84$ respectively) when compared to the one observed for the 60 µm phantom ($R^2 = 0.51$, Figure 5.5). The root mean square error between the estimated and the expected BSCs of the 60 µm phantom is $5.0\times10^{-3}\text{mm}^{-1}.\text{sr}^{-1}$. The polydisperse Faran model for the 60 µm

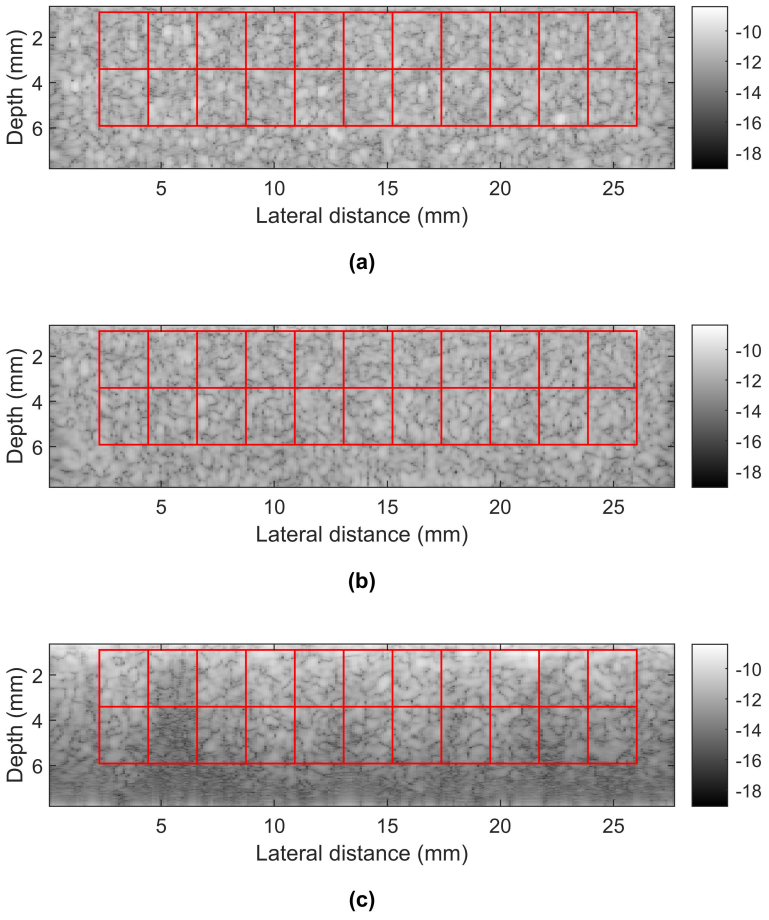

Figure 5.3: B-mode images of the 10 µm phantom (a), the 20 µm phantom (b) and the 60 µm phantom (c). The ROIs are depicted as red rectangles. The gray levels denote the intensity in dB.

phantom matches with the corresponding BSC up to 14 MHz. Above this frequency, discrepancies can be observed.

5.3.2 EBS measurements

The EBS peaks are shown in Figure 5.6. The coherent signal that represents the sample's signature lies in the center, corresponding to the exact backscattering direction. The intensity exhibits a fast decay as the backscattering angle increases for each phantom. The 60 µm phantom exhibits the sharpest and greatest peak (FWHM = 0.12°), followed by the 10 µm phantom (FWHM = 0.20°) and the 20 µm phantom (FWHM = 0.22°).

Theoretically, the reflectance profile computation is valid for low and high exit radii. In practice, the noise makes these r values unreliable [6]. Consequently, the lower limit of the exit radius was set to 60 µm. Similarly, the exit radius upper limit was taken at 1000 µm due to the decaying SNR in the region following this value. Experimental effective

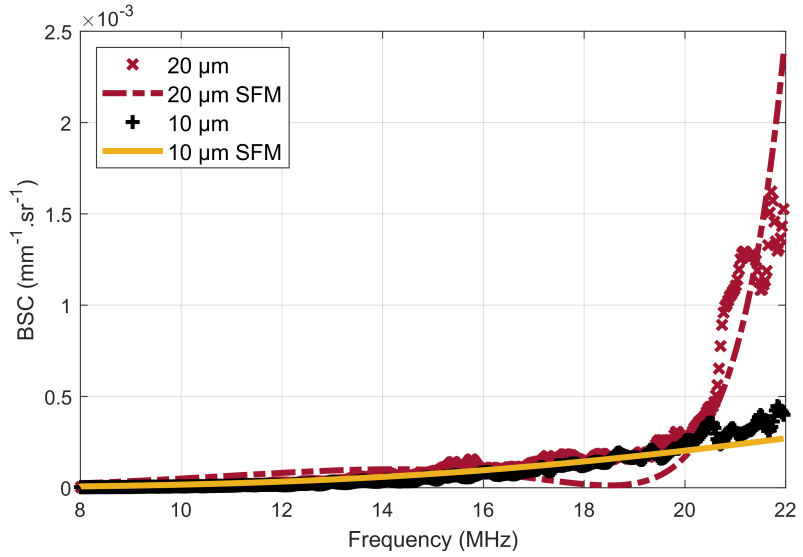

Figure 5.4: Backscatter coefficient measurements with Structure Factor Models (SFM) for the 10 µm and the 20 µm phantoms

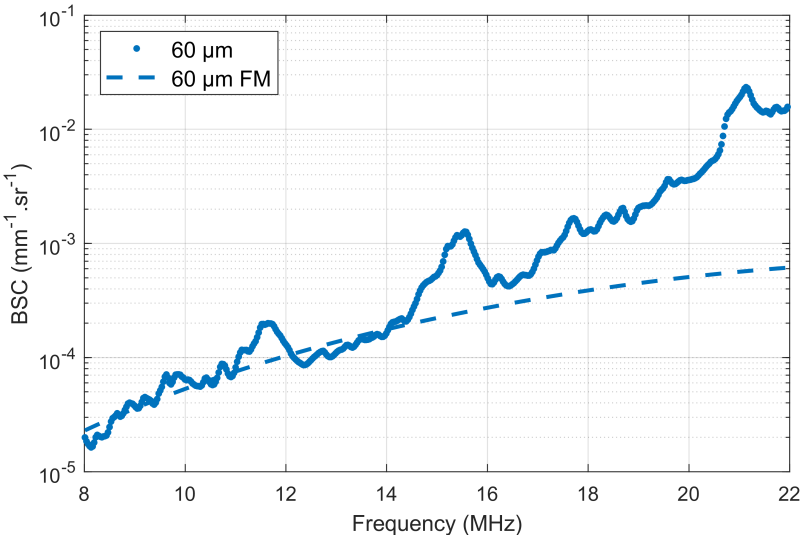

Figure 5.5: Backscatter coefficient measurement with the Faran Model (FM) for the 60 µm phantom

reflectance profiles $p_{eff}(r)$ and scaled simulated effective reflectance profiles are shown in Figure 5.7.

EBS analysis can be performed by comparing the relative shapes of the experimental and the simulated reflectance profiles [85]. This approach makes the measurements less sensitive to the temporal intensity fluctuations of the light source. Hence, the R^2 appears as a relevant metric since it compares the correlations between two vectors without being affected by the absolute values or the scaling factors. The agreements between the measured $p_{eff}(r)$ and MC simulations for the 10, 20 and 60 µm phantoms are $R^2 = 0.95$, $R^2 = 0.93$ and $R^2 = 0.97$ respectively.

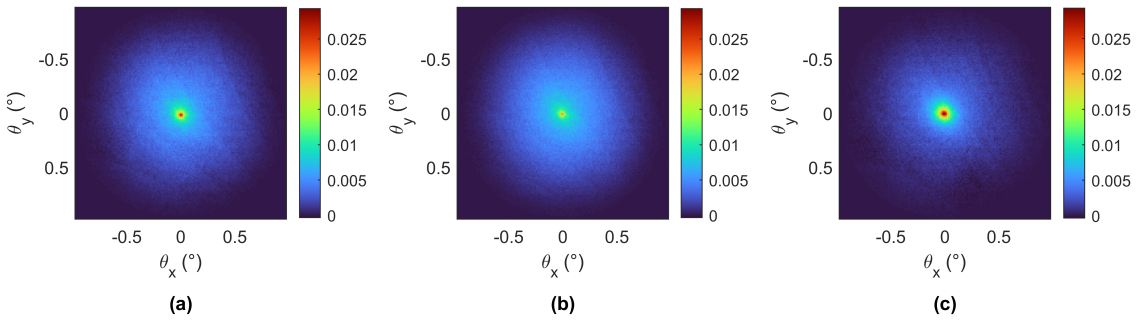

Figure 5.6: EBS images of the 10 µm phantom (a), the 20 µm phantom (b) and the 60 µm phantom (c). The colormap denotes the intensity in an arbitrary unit.

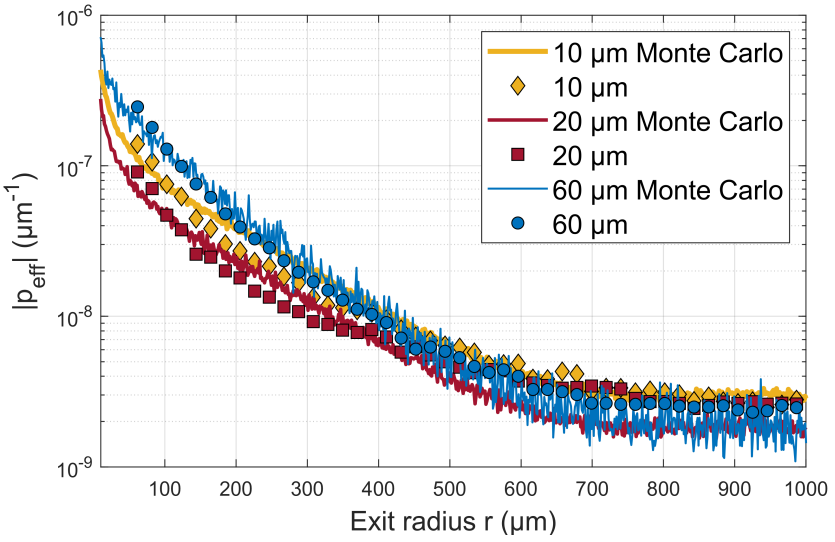

Figure 5.7: Effective reflectance profile measurements at 702 nm (co-polarized channel) and results from Monte Carlo simulations (MC). In each case, MC data have been scaled at $r = 123$ µm to obtain a match with experiment

5.4 Discussion

In this study, the combination of the BSC parametrization and EBS aims to characterize three tissue-mimicking phantoms through their scatterer size. This work serves as a preliminary validation of the experimental protocols carried out for the BSC estimation and EBS. After measuring the BSC and the reflectance profiles on each phantom, forward analyses were conducted by comparing BSC and EBS measurements with their corresponding theoretical scattering models.

The attenuation coefficients α_0 of the 10 and the 20 µm phantom are similar to the ones found in biological samples (about 0.12 dB/mm/MHz [148]). Given their characteristics summarized in Table 5.1, these two samples successfully reproduced the ultrasound and optical scattering properties of biological tissues.

The SFM successfully modeled the 10 and the 20 µm BSCs (Figure 5.4). A good over-

all agreement was also found between the estimated and the expected reflectance profiles (Figure 5.7) for these two phantoms. However, the simulated 10 µm and 20 µm reflectance profiles exhibit the same trend and are highly correlated ($R^2 = 0.99$). In the framework of an inversion study where the scatterer radius would be extracted using a fitting algorithm, it is reasonable to think that the accurate inversion of these reflectance profiles would be challenging due to their high degree of resemblance. Interestingly, the contrast between the BSCs of the 10 and the 20 µm phantoms allowed their clear distinction in the high-frequency area. Consequently, their successful inversion could be more likely, therefore potentially leading to an accurate estimation of the scatterer radius.

The Monte Carlo simulation provided the best predictions for the variations in the reflectance profile of the 60 µm phantom ($R^2 = 0.97$). Remarkably, it shows a lower correlation when compared to the simulated reflectance profiles of the 10 or the 20 µm phantom ($R^2 = 0.95$ in both cases). Thus, its successful inversion could potentially be more likely since the 60 µm phantom exhibits a more singular reflectance profile in comparison to the others. Similarly, this could lead to a proper estimation of the scatterer radius.

The BSC of the 60 µm phantom poorly matches with the theoretical scattering model (Figure 5.5). However, this BSC should be considered with caution, especially in the high frequency region. Indeed, the attenuation coefficients α_0 of the three phantoms were estimated in the same conditions. However, the implementation of the substitution method in this study did not allow the estimation of α_0 for the 60 µm phantom, due to its strong acoustic attenuation. To address this issue, this coefficient α_0 was empirically set. Consequently, the correction of the sample attenuation assuming a linear model may be limited for the 60 µm phantom. Interestingly, the low performance of the ultrasound approach reported in this study for the 60 µm phantom could be valued to discuss the complementarity with EBS. Indeed, as mentioned above, Mie theory successfully describes the reflectance profile of the 60 µm phantom. As a result, EBS could be a more practical solution to characterize media that present a high acoustic attenuation.

In summary, the ultrasound approach could successfully differentiate the 10 and the 20 µm phantom thanks to the notable contrast in their successfully modeled BSC. Although EBS predicts the variations of the reflectance profiles of these phantoms, their signatures could be too close for a proper estimation of these scatterer radii. However, conducting an inversion study on the reflectance profile of the 60 µm phantom could lead to an accurate characterization, where the application of the BSC method failed because of the strong acoustic attenuation. Thus, the three tissue-mimicking phantoms could be characterized by combining the ultrasound approach and the optical method. This observation suggests that these two modalities should have complementary sensitivities regarding the scatterer size.

The main purpose of this study was to validate the experimental protocols for estimating BSCs and reflectance profiles. The control over the acoustic and the optical properties of the suspensions conducted us to use tissue-mimicking phantoms. Thus, theoretical models suited for suspensions of solid spheres have been used (*i.e.* Faran model and Mie

theory). For further studies involving biological samples, other models adapted for soft tissues will be used such as the Fluid Sphere model for the BSC parametrization [5] or the Whittle Matérn model for EBS [85]).

5.4.1 Limitations

The observations from section 5.3 should be discussed with the following points:

One can notice that the 20 µm BSC does not follow the shape of the expected BSC in the low frequencies. This can be explained by the particle-size distribution of the microspheres used in the phantoms. Indeed, resonance peaks and fine variations in the BSC occur for perfectly monodisperse scatterers. However, they are difficult to obtain experimentally due to the size polydispersity of the scatterers. To verify this hypothesis, granulometric studies with a particle size analyzer (Partica LA-960, Horiba) were conducted. The latter revealed that the 20 µm microsphere powder has a variation coefficient (std/mean) estimated up to 22% (supplier: up to 10%). The use of a polydisperse model could then result in a better match with the experimental data at the expense of a higher computational complexity.

Given the simulated values of μ_s' given in Table 5.1, the reflectance profile of the 20 µm phantom was expected to be broader than the 10 µm phantom (*i.e.* sharper EBS peak). However, the 10 µm phantom exhibited a broader reflectance profile. The actual size polydispersity mentioned above may have also contributed to discrepancies between the simulated and the actual optical properties.

The magnetic stirrer creates a circular flow and can induce shear in the suspension. This can create an anisotropic microstructure that could affect the ultrasonic backscattering of the phantom. Indeed, Lombard et al. [149] showed that the structure factor differs for an isotropic microstructure or a shear-induced anisotropic microstructure. However, the SFM used in the present paper only models the isotropic case, which could be obtained by mixing the suspensions in an irregular fashion. Thus, further phantom studies should prefer random agitations when dealing with suspensions to avoid structural effects.

Finally, one should note that the results of this study are specific to the three phantoms and to the working frequency range used (8-22 MHz ultrasonic excitation and EBS spectral image acquired at 702 nm). Indeed, this study must be considered as a proof of concept which validates the experimental protocols and the potential complementarity between an ultrasound and a light-based technique. For instance, experiments with a larger ultrasound frequency range and other optical wavelengths should reveal more information about the probed sample. Likewise, the use of tissue-mimicking phantoms composed of other scatterer sizes (*e.g.* 15 µm, 30 µm and 40 µm) would have allowed a more thorough assessment of the sensitivity of each technique.

5.5 Conclusion

To conclude, EBS and the BSC parametrization offered a solution to model and to discriminate three different tissue-mimicking phantoms when combined. These encouraging results led us to carry out an experiment on rodent excised tumors from two tumor models. Complementarities in the two techniques are expected to characterize each cancer subtype. Histological analyses will be used as ground truth.

Chapter 6

Characterization of sarcoma subtypes: an *ex vivo* study on animal models

In the previous chapter, our experimental setups for EBS and BSC parametrization were validated on three tissue-mimicking phantoms which consisted of suspended microparticles of different sizes. Complementarities in terms of sensitivity to the scatterer sizes were observed. These interesting results led us to carry out an *ex vivo* animal study to further investigate the performances of a bimodal approach. In this chapter, quantitative ultrasound and light backscattering spectroscopy techniques were combined to characterize two different bone tumor types from animal models at the cellular and nuclear scales.

The findings presented in this chapter were disseminated through a peer-reviewed journal article and were also shared at three international conferences:

- Malinet, C., Montcel, B., Dutour, A., Fajnorova, I., Liebgott, H., Muleki-Seya, P., "Cancer characterization using light backscattering spectroscopy and quantitative ultrasound: an ex vivo study on sarcoma subtypes." Scientific Report 13, 16650 (2023), DOI: 10.1038/s41598-023-43322-4 [150].

- Best student poster award, ECBO 2023, Münich. "Toward cancer characterization using light backscattering spectroscopy and quantitative ultrasound". Conference SPIE 12629, Paper 12629-28.
  This poster was also presented by H. Liebgott at IUS 2023, Montreal.

- Oral presentation and proceeding paper at Photonics West 2023 [121], San Francisco, "Toward cancer characterization using light backscattering spectroscopy and quanti-

tative ultrasound", Proceeding SPIE 12379, Photons Plus Ultrasound: Imaging and Sensing.

We acknowledge J. Mamou and C. Hoerig (Department of Radiology of Weill Cornell Medicine, NYC, New York, United States of America) for providing the envelope statistic algorithms in this study and the following chapters.

6.1 Introduction

In clinical settings, the process of cancer characterization involves the determination of the tumor histological subtype and the cancer grade [1]. Determining these characteristics plays a crucial role in establishing the patient's diagnosis. This histological classification relies on cellular morphological measurements and is traditionally determined through histological analyses. Although histo-cytopathology serves as a gold standard for diagnosing cancers, this technique requires a biopsy and is therefore inherently invasive and resource-intensive. Additionally, it is subject to inter-observer and intra-observer variabilities [3]. For instance, the sampled sections may not include the most aggressive cancerous regions due to tumor heterogeneities. Thus, the sampling bias could lead to inaccurate diagnostics that ultimately worsen the patient's prognosis. Consequently, guiding the biopsy toward the most suspicious regions using a non-invasive quantitative tool would be of great benefit and could subsequently improve patient outcomes.

As a starting point toward this objective, the two optical and two ultrasound quantitative techniques introduced in the first three chapters of this thesis have been combined on a benchtop to lead to a thorough tissue assessment. Indeed, the BSC parametrization and ES can extract different tissue scattering properties from the same acquisition. Likewise, EBS and LSS can be performed using a similar experimental setup to characterize biological tissues. By combining light and ultrasound, one can expect that the scattering process would arise from cellular structures of varying sizes given the distinct wavelength ranges associated with each modality. Thus, this bimodal technique should have the potential to bring complementary information about the microstructures in the probed tissue.

As detailed in the section 2.2, successful applications of BSC parametrization and ES provided cancer type classification [4] and cancerous lymph node characterization [26, 45] for example. BSC inversions can also identify nuclear structures as scatterers in biological media [5]. Similarly, the cell size distribution can also be extracted in dense media [38].

In biomedical optics, numerous studies have investigated the ability of EBS to detect ultrastructural alterations in the field carcinogenesis [6, 81] as described in the section 2.3. Radosevich et al. [10] successfully discriminated colorectal and pancreatic cancer field carcinogenesis from healthy tissues using EBS. Likewise, Backman et al. [65] successfully extracted the nucleus size distribution from malignant and normal intestinal cells *in situ* using Light Scattering Spectroscopy (LSS), as described in the section 2.3. More recently, Qiu et al. [9] used this method to show that the nuclear size distributions can be accurately

estimated in a dysplastic and in a non-dysplastic site in a Barrett's esophagus.

In this study, BSC parametrization, ES, LSS and EBS were used to characterize two bone cancer histological types: chondrosarcoma and osteosarcoma established in rodents. The rat chondrosarcoma model reproduces the histological and aggressivity characteristics of grade II human chondrosarcoma. Chondrosarcoma, prevails as the primary bone sarcoma in adulthood, with an annual diagnosis rate of approximately 2 cases per one million people. Chondrosarcoma can appear as lobules of cells within a cartilage-like matrix [2]. On the other hand, the murine osteosarcoma models used (K7M2 and MOS-J) are representative of conventional metastatic osteosarcoma. Osteosarcoma is the most prevalent type of primary bone tumor, with an estimated incidence of approximately 2 to 3 new cases per one million individuals each year, predominantly affecting adolescents. Osteosarcoma is characterized by the production of an immature bone matrix and is hypercellular [2].

The use of chondrosarcoma and osteosarcoma tumors is motivated by their different microstructures. Characterizing these tumors appears as a way to validate our bimodal method with the aim of establishing a proof-of-concept. Given that the inner mechanisms of our methods probe the tissue microstructure, our approach could potentially be applied to other types of tumors and to healthy tissues.

Optical and ultrasound measurements were carried out on the day of sacrifices. Quantitative parameters were then estimated and compared between different tumor types. Simultaneously, histological analyses were conducted for all tumors. Morphometric measurements of cellular structures, derived from these examinations, were then compared to evaluate the performances of the BSC parametrization and LSS in estimating scatterer parameters related to cells or nuclei.

6.2 Materials and methods

6.2.1 Animal models

Tumor growth and surgical procedures

The experiment was approved by the ethical committee CECCAP (Comité d'éthique en expérimentation animale de la Région Rhône-Alpes, registration number C2EA15, Lyon, France) and by the the ethical committee ACCESS (Comité d'éthique en expérimentation animale commun Centre Léon Bérard - Centre de Recherche en cancérologie de Lyon, CE010, MESR number: #35086). All methods were conducted in agreement with the established guidelines and with the European and French regulations. For all surgical procedures, pre-analgesia was induced by a subcutaneous injection of buprenorphine (0.05mg/kg) (ECUPHAR, Belgique). All tumor implantations were performed on anesthetized animals (isoflurane/oxygen, 2.5%/1.5%, v/v) (Minerve, Esternay, France). Five chondrosarcomas tumors, hereafter referred to as Ch1 to Ch5, were grafted on 25-d-old Sprague–Dawley rats. Tumor fragments (10 mm^3) were transplanted on the right posterior

tibia of the rats after periostal abrasion [151]. The osteosarcoma models were established by injection of 1×10^6 MOS-J (Os1 and Os2) or K7M2 (Os3 and Os4) suspended cells [152]. Tumor progression was monitored twice a week by palpation and caliper measurements until it reached a 500 - 600 mm^3 volume for all tumors. The animals were then euthanized by CO_2 inhalation and the tumors were removed for optical and ultrasound imaging, which were performed the same day.

Histological examination

Then, the tumors were embedded in formalin-fixed paraffin-embedded blocks before undergoing histological analyses. Tumor slices were H&E and Ki67 stained through an automated procedure and scanned to obtain microphotographs. The histological parameters were analyzed using Qupath (software version 0.3.2) to estimate the size distributions of osteosarcoma cells and all nuclei. Osteosarcoma microstructures were measured using H&E images, while chondrosarcoma nucleus sizes were evaluated using Ki67 images. Following segmentation with the automatic detection tool, the radii of cells and nuclei were extracted by assuming the circularity of the detected objects. For chondrosarcoma cells, a Matlab program (software version R2020b) was employed to detect cells within bounding boxes on H&E microphotographs The sizes of the bounding boxes were halved to obtain a characteristic size, considered as the radius. The cell size distribution for each animal was then fitted to a Γ-distribution to extract the mean radius a and the Schulz width factor z. As an approximation, the volume fractions of both the cell and nucleus were assumed equal to the surface fractions [153]. The surface fraction represents the ratio of the mean intercepted areas of the object of interest to the total surface area analyzed. An average volume fraction was considered for each tumor type. Only Ch3 and Ch4 contributed to the estimated cell volume fraction for chondrosarcomas, as the cell detection procedure yielded poor results for other animals.

6.2.2 Quantitative ultrasound

Theoretical scattering models

The Lizzi-Feleppa parameters were extracted from each estimated BSC (*c.f.* subsection 3.2.5). The corresponding linear parameters were then used to discriminate the different tumor types. To obtain ultrasound parameters that can be compared with histological analysis, more sophisticated BSC theoretical models were used. The Fluid-Filled Sphere model (FFSM, Equation 3.14) was applied to extract the effective scatterer radius a. To take into account potential structural effects in the probed tumors, we also used the Polydisperse II model introduced in Han et al. [38] (Equation 3.19). Han et al. provided an expression to model the ultrasound backscattering of polydisperse scatterers in concentrated media based on a Fluid-Filled sphere form factor. The use of this model allowed the estimation of the scatterer mean radius a and corresponding Schulz width factor z

(*i.e.* distribution sharpness). Hereafter, the PII model will refer to this BSC model.

Envelope parameters were also estimated. The Probability Density Function (PDF) of the measured ultrasound envelope was fitted with a Nakagami distribution model to extract the scaling factor Ω_{nak} and the Nakagami parameter α_{nak}. The scaling factor Ω_{nak} is equal to the mean backscattered intensity [44] and α_{nak} can be used to quantify the effective number of scatterers per resolution cell [45].

Implementation of QUS techniques

Each sample was insonified with focused waves using two linear probes (MS250S, LZ400, Vevo LAZR scanner, Fujifilm VisualSonics) centered at 21 MHz and 30 MHz, allowing tissue characterizations over the 13 - 24 MHz and 18 - 38 MHz frequency ranges respectively. The use of a high-frequency probe makes the successful characterization of small objects (i.e. nuclei) more likely since the Mie scattering region is targeted ($ka \sim 1$). A 3D scan was performed and consisted of 10 B-mode images spaced out 0.2 mm away from each other with three focal lengths of 6, 8 and 10 mm for osteosarcomas and 10, 12 and 14 mm for chondrosarcomas. Each scan was composed of 1536 RF lines and imaged the tumor over 15 mm in the lateral direction. Regions of Interest (ROI) were 15λ long in both directions and were located at a relatively shallow depth (1 - 1.5 mm). Our reference phantom was composed of polyamide particles of diameter 5 µm (Orgasol 2001 UD, Arkema) at the relative mass concentration of 0.25% in a gel that contains agarose (2%, Sigma) and water. The number of independent ROIs used or averaged for each technique is shown in Table 6.1. The sample attenuation was estimated using a standard substitution method [110]. The BSC for each ROI was estimated using the reference phantom method [113]. Then, the BSC estimations from each frame were averaged for the MS250S probe and the LZ400 probe. A b-spline fit was then performed to merge the BSC estimations from the two probes to perform BSC inversions over the whole frequency range, as done in Han et al. [38].

Inversions

When applying a linear model to the measured BSCs, linear fits were filtered out based on their resulting Pearson correlation coefficient using a threshold value $R^2_{min} = 0.60$. The fits that did not meet this specification were considered as not representative of the experimental data. This procedure removes less than 5% of the collected data.

The BSC inversion procedure was performed using the Matlab function *fminsearchbnd* by minimizing the squared error between the experimental data and the expected model with the following constraints: $(a, z) \in [0.1\ \mu\text{m}\ , 100\ \mu\text{m}] \times [1, 120]$ for the PII model. The scatterer radius a was also constrained in this range for the inversions using the FFSM. For each inversion, multiple seed values for the parameters of interest were tested. The volume fraction ϕ was either set to the nucleus or the cell volume fractions, using the estimates obtained through histological analyses.

The scaling parameters Ω_{nak} from the Nakagami distribution were obtained using a maximum-likelihood estimator. In this study, envelope parameters have been extracted from the RF data acquired in the 18 MHz - 38 MHz range.

Envelope correction

In this study, the envelope estimates were corrected for the attenuation and the diffraction effects (*c.f.* section 3.3.4). The correction allows the comparisons between envelope parameters from ROI located at different positions. To do so, we introduce two corrective factors that were applied to the Nakagami envelope parameters. These factors were inspired by the κ factor and the χ factor (Equation (8) and (9) respectively in [45]) suggested by Mamou et al. [45].

Nakagami parameter α_{nak} As detailed in the subsection 2.2.2, the Nakagami parameter α_{nak} can represent the number of scatterers per resolution cell to a certain extent. However, the volume of the resolution cell varies across the field of view due to the attenuation and the diffraction effects [45]. Thus, to compare α_{nak} coefficients from ROIs with different locations across the field of view, these estimates can be corrected for the volume spatial variations of the resolution cell. To do so, we can estimate a corrective factor κ for the estimates of α_{nak} in each ROI:

$$\kappa = \frac{\{\Sigma_{min} \; such \; as \; ACF[e_{ref}(x,z)] > 60\%\}}{\{\Sigma_{ROI} \; such \; as \; ACF[e_{ROI,ref}(x,z)] > 60\%\}} \tag{6.1}$$

where Σ_{ROI} is the surface in mm^2 for which the 2D normalized autocorrelation function (ACF) of the reference envelope signal $e_{ROI,ref}(x,z)$ for a given ROI is greater than 60%. The surface Σ_{min} represents the same quantity but is a constant value that represents the smallest Σ_{ROI} across the field of view and serves as a normalization factor. It is noteworthy that all surfaces Σ are estimated according to the position of the ROI in the tumor image using the corresponding RF data in the reference phantom. Consequently, the sample RF data are not necessary to compute κ_{ROI}.

The rationale behind this corrective factor is that the surface Σ_{ROI} is considered inversely proportional to the volume of the resolution cell for a given ROI [154]. In this study, Σ_{min} was estimated at 0.055 mm^2 and corresponds approximately to a ROI located at the shallowest focal distance. As a result, κ takes smaller values for ROIs that are away from the focal points and indicate larger resolution cells. Conversely, κ takes higher values for ROIs that are close to the focal points and indicate smaller resolution cells.

An example of evolution of κ over the imaging depth is shown in Figure 6.1 (a). In this figure, a grid of rectangular non-overlapping ROIs was set across the whole field of view of the scans of the reference phantom. The κ factor was then estimated for each ROI and its mean value was calculated along the Z-axis. The positions of the three focal lengths are shown with vertical dashed lines, along with the position of the deepest ROI used in

this study. The local maxima of κ around 7, 9 and 11 mm corresponds approximately to the positions of the three focals with a constant horizontal shift of 1 mm. This horizontal shift may indicate the actual positions of the focals and could therefore slightly differ from their positions set on the ultrasound scanner, as shown by the dashed lines. Consequently, the coefficient κ could capture the inverse variations of the resolution cell, allowing for potential compensation by multiplication with the corresponding estimate α_{nak}.

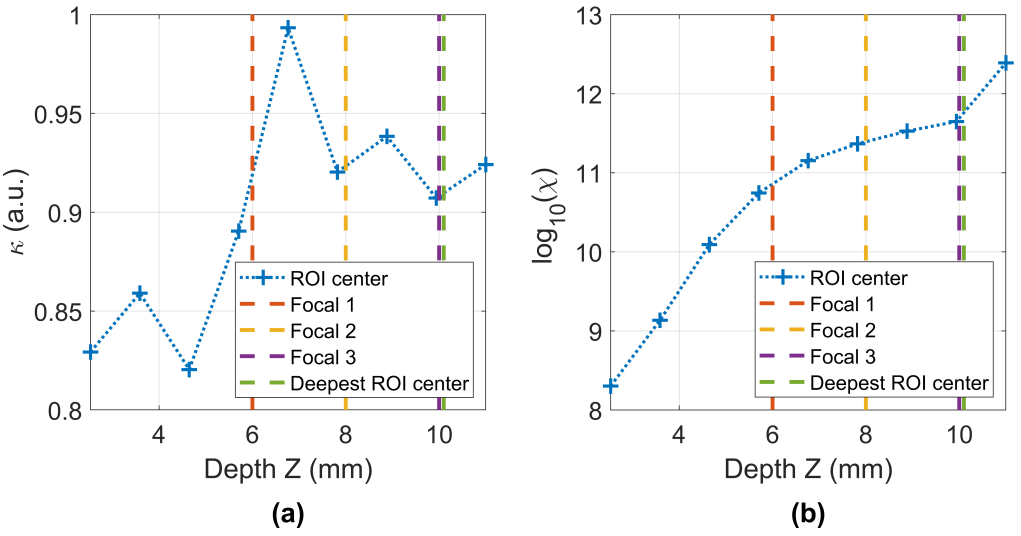

Figure 6.1: (a) Illustrative example of the variations in the corrective factor κ as a function of the imaging depth. (b) Illustrative example of the variations in the corrective factor χ for the scaling parameter Ω_{nak} as a function of the imaging depth.

Scaling parameter Ω_{nak} The scaling parameter Ω_{nak} is sensitive to the attenuation and the diffraction effects as well. Hence, it is important to adjust the estimates Ω_{nak} in order to preserve the fundamental physical interpretation, namely the tissue's mean backscattered intensity, regardless of the acquisition parameters.

For each ROI segmented in the B-mode image of the tumor, we first compute the corresponding power spectra of in reference phantom at its specific location as follows:

$$S_{ROI}^{ref}(f) = \frac{1}{N}\sum_{i=1}^{N}\left|FT[RF_{ref}(t)]\right|^2 \tag{6.2}$$

where N is the number of RF segments $RF_{ref}(t)$ within the ROI in the reference phantom and FT denotes the Fourier transform. We then calculate a virtual spectrum $S^{\Omega}_{ROI}(f)$ for each ROI location as follows:

$$S^{\Omega}_{ROI}(f) = \frac{S^{ref}_{ROI}(f)}{BSC_{theo}(f)} e^{4z_{ROI}(\alpha_{ref}(f)+\alpha_s(f))} \tag{6.3}$$

where α_{ref} is the acoustic attenuation of the reference phantom, α_s is the acoustic attenuation of the sample, z_{ROI} the depth of the center of the ROI and BSC_{theo} is the known theoretical BSC of the reference phantom. The factor $e^{4z_{ROI}(\alpha_{ref}(f)+\alpha_s(f))}$ compensates for both the phantom and the sample attenuation. According to Equation 3.8 of the discrete models detailed in chapter 3, the power spectra $S^{\Omega}_{ROI}(f)$ reflects the pressure field resulting from the diffraction pattern of the single-element transducer that is corrected for the sample attenuation.

A corrective factor χ for the scaling parameter Ω_{nak} can then be estimated by evaluating $S^{\Omega}_{ROI}(f)$ for $f = f_c$, with f_c being the center frequency of the ultrasound probe LZ400 ($f_c = 30MHz$):

$$\chi = S^{\Omega}_{ROI}(f_c) \tag{6.4}$$

An example of the variations of the coefficient χ over the imaging depth is given in Figure 6.1 (b). In this example, the coefficient χ was computed following the same procedure as described for the κ coefficient. The corrective factor χ increases exponentially with the depth and can therefore be used to correct the effects of attenuation and diffraction over the estimates Ω_{nak} through a simple multiplication.

6.2.3 Light Enhanced Backscattering Spectroscopy

Acquisition

Figure 6.2 illustrates the experimental setup used for EBS and LSS. The components used in the previous chapters were used in this study. Differences in the implementation are described in this paragraph. The incident beam was shaped into a circular spot with a diameter of 1.8 mm using an iris diaphragm, ensuring compliance with the Nyquist sampling criterion. The tissue sample was immersed in an aqueous solution of glycerol (mixture of 33% glycerol to 67% deionized water by volume), which has a refractive index similar to that of the assumed tissue refractive index (n = 1.38) [85]. To minimize the presence of speckle noise, a motor was used to rotate the sample gently. The analyzer was parallel to the polarizer to select the co-polarized channel. A Fourier lens (aspherized, achromatic, focal length = 50 mm) focused the light onto a CCD camera. The camera (Thorlabs 340M, not depicted in the diagram) detected the backscattered light filtered at a wavelength of 700 nm (filter FWHM of 10 nm). The camera pixels have dimensions of 7.4×7.4 µm. This configuration allowed an angular resolution of 8×10^{-3} °.

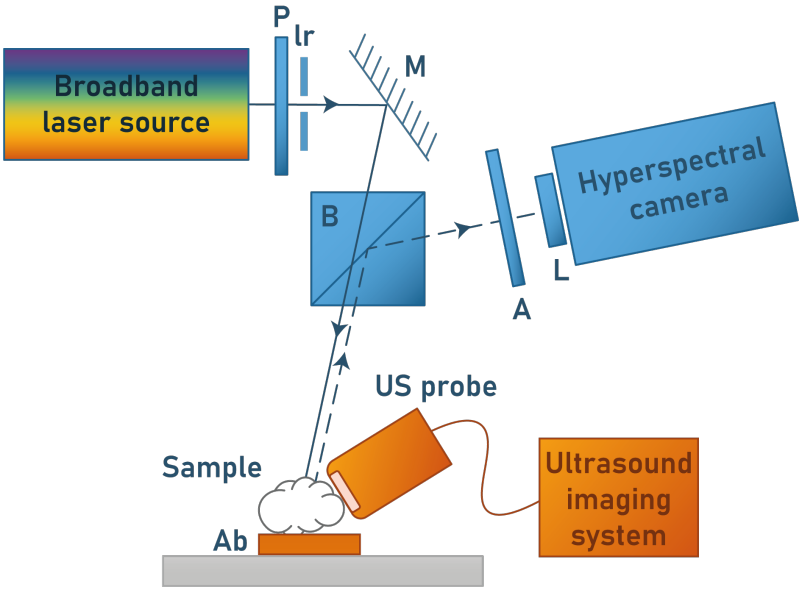

Figure 6.2: Experimental setup used for EBS and LSS; P: polarizer, Ir: iris diaphragm, M: mirror, B: beamsplitter cube, A: analyzer, L: Fourier lens, Ab: absorbing material. The detection block was substituted by a filter wheel and a monochrome camera for EBS. The Fourier lens is integrated in the hyperspectral camera.

Data processing

The outlines of the data processing steps described in the section 4.2.3 were followed. The implementation for this study is similar to the one reported in the previous chapter. Differences are described here. The total unpolarized incoherent intensity was estimated by integrating the intensity in a ring spanning from 0.9° to 1° away from the center. The sample incoherent baseline was estimated in the same ring and fitted to a plane. Then, the plane was subtracted from the sample image. To mitigate the effect of unwanted systematic reflections in a half plane, the sample images were mirrored with respect to the horizontal axis that passes through the intensity peak. The rotational averages of the Hann-windowed 2D Fourier transform images led to the effective reflectance profiles. Mirror measurements allowed the extraction of the sample reflectance profile $p(r)$ by estimating the 1D product of $s(r) \times mtf(r)$ after calculating the radial average of the effective reflectance profile $p_{eff}(r)$. The exit radii were restricted to the range where the reflectance profiles were above the noise level (*i.e.* $p(r_s)$ values for r_s close to the iris diameter [124]). Tumor size allowed us to perform five EBS measurements corresponding to different positions for the chondrosarcoma tumors and one EBS measurement for the osteosarcomas (Table 6.1).

6.2.4 Light Scattering Spectroscopy

Acquisition

The experimental protocol to measure the LSS spectrum $\Delta I(\lambda)$ was detailed in the subsection 4.3.1. In brief, $\Delta I(\lambda)$ is obtained by subtracting the co-polarized signal (A and

P ||, Figure 6.2) with the cross-polarized signal (A and P $\perp$) after background subtraction and white standard normalization [11]. Experimentally, $\Delta I(\lambda)$ was measured over the range 550-700 nm with 32 spectral points using a hyperspectral camera (HERA VIS-NIR, Nireos). However, the relevant information in the LSS spectra is contained within the low frequencies [68]. We confirmed this observation by injecting the size distributions extracted from the histological analyses into the forward LSS model. Similarly to what was done by Fang et al. [68], 16 points were kept to resolve the differential polarization signals across the 550-700 nm range. The resulting spectral resolution was 9.3 nm (Fang et al. [68] used 8.9 nm). Multiple acquisitions were realized to measure the LSS spectra from different positions for each tumor (Table 6.1). During the acquisitions, the samples were submerged in an index-matching solution with the same refractive index as the surrounding medium of the sample.

Data processing

The analytical procedure to extract the scatterer size distribution was detailed in the subsection 4.3.3.

To minimize the coherent signal in each spectral image, the angular intensity was integrated within a ring spanning from 1.0° to 1.5° for each wavelength. This part of the image corresponds to what EBS considers as the incoherent baseline.

Light undergoes depolarization as it is subject to multiple scattering events [11]. To mitigate the effect of multiple scattering, a criterion based on the mean degree of polarization DOP (DOP = $(|I_{\parallel} - I_{\perp}|/|I_{\parallel} + I_{\perp}|)$ is applied. In our configuration (linearly polarized incident light), the DOP values equal zero when the detected light is completely depolarized and equal one when it maintains the initial polarization state. As an approximation, we use the DOP value as an indicator of multiple scattering. We consider that the LSS model in this study is not suited to experimental spectra where multiple scattered light predominates. Consequently, LSS spectra with a mean DOP above 0.35 across the visible range are selected. This threshold lead us to take into account 11 out of 14 measured spectra for chondrosarcomas and 3 out of 7 spectra for osteosarcomas (MOS-J type only). We argue that the tumor heterogeneities may be responsible for the varying DOP values within samples of the same type.

The relative refractive index n_{re} was set to 1.06 to target the nuclei/cytoplasm refractive index variation mismatch [65]. The surrounding medium refractive index was assumed to be 1.38.

Equation 4.42 was solved using a linear least squares algorithm with a non-negativity constraint applied to F. The minimum radius for the size estimation r_{min} was set to 100 nm. While rationales can be found in the literature to justify the r_{min} value and the number of points to reconstruct F, the choices of r_{max} values appear to be predominantly empirical. Yet, this parameter has an important physical meaning since it corresponds to the largest scatterer contribution "allowed" in the differential polarization spectrum.

Method	Independent Measurements	Mean per animal	Mean per tumor group
BSC estimations*, Fig. 6.5		✓	
Linear model* (18 - 38 MHz), Fig. 6.6 (a)	✓		
ES*, (18 - 38 MHz), Fig. 6.6 (b)	✓		
EBS†, Fig. 6.7 (a)		5 per Ch., 1 per Os.	
EBS residuals†, Fig. 6.7 (b)			Ch : 5 ; Os(K7M2) : 2 ; Os(MOS-J) : 2
PII* (13 - 24 MHz), Fig. 6.10		✓	
FFSM* (24 - 38 MHz), Fig. 6.11			Ch : 274 ; Os(K7M2) : 50 ; Os(MOS-J) : 106
PII* (13 - 38 MHz), Fig. 6.12		✓(Os. only)	
LSS†, Fig. 6.13 and 6.14			Ch : 11 ; Os(MOS-J) : 3

Table 6.1: Degree of averaging and number of underlying independent measurements per technique. Independent measurement refers to ROI for ultrasound techniques* and sample position for optical techniques†. Checkmarks refer to the following number of ROIs: 36 (Ch1), 75 (Ch2), 88 (Ch3), 51 (Ch4), 24 (Ch5), 23 (Os1), 27 (Os2), 61 (Os3), 45 (Os4).

Hence, multiple matrices $\tilde{I}(\lambda, r, n_{re})$ with different maximum radii r_{max} were computed. The different r_{max} values were limited to around 17 µm to include the chondrosarcoma cells and to ensure a sufficiently fine radius resolution capable of distinguishing the size distribution of osteosarcoma nuclei from that of chondrosarcoma (about one micron).

This study focused on a single r_{max} values because the estimation of the size distribution F is extracted from the precomputed LSS spectrum matrix $\tilde{I}(\lambda, r, n_{re})$. The implementation of this look-up table approach results in computational times of only a few seconds, thus enabling real-time inversions. Hence, a unique and common $\tilde{I}$ matrix was used to characterize the two tumor types.

Optimized histograms

LSS has been initially developed to probe the nucleus size distribution. However, we make the hypothesis that cells could be involved in the scattering process, particularly in media with abundant extracellular matrix. Indeed, Mie Theory describes the interaction of light of discrete spherical scatterers in a homogeneous surrounding medium. Therefore, cells could be considered as scatterers within the extracellular matrix, analogous to how nuclei scatter the electromagnetic incident plane wave within the cytoplasm. Therefore, we took the LSS analysis one step further using the estimated size distributions. To account for both the nucleus and the cell scattering, linear combinations of the nucleus and the cell histological histograms were computed for different nucleus weight values w_{nuc}, defined such as $w_{nuc} = 1 - w_{cell}$. The optimized nucleus weight was then extracted by minimizing the root mean squared error (RMSE) between the estimated LSS solution F and the newly computed histogram for each tumor type. This procedure led us to the assumption that the relative refractive index between the nuclei and the cytoplasm is equal to the one between cells and the extracellular matrix.

6.3 Results

6.3.1 Animal models

Histological analyses are conducted to serve as references. Morphometric measurements of cellular structures are carried out using the histological slices of tumors to compare the performances of each technique. Chondrosarcoma is characterized by low cell density within an abundant extracellular matrix. One can clearly distinguish extracellular membrane, cell cytoplasm and cell nuclei (Figure 6.3, a). Both osteosarcoma models exhibit high cellular density and a minimal extracellular matrix. Osteosarcoma cells exhibit a different morphology in comparison to chondrosarcoma cells. They are smaller in size and have large nuclei (Figure 6.3, b and c). Hence, histological staining reveals specific morphological features in each bone sarcoma model.

The cell and nucleus size distributions are also estimated using the microphotographs

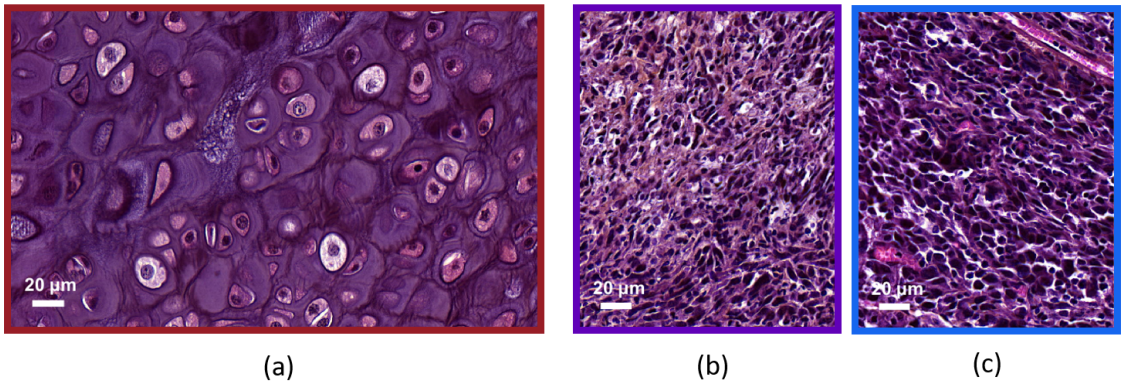

Figure 6.3: Representative histological stainings of chondrosarcoma and osteosarcoma. (a) Chondrosarcoma. HPS staining enables to distinguish cell nuclei, membranes and abundant extracellular matrix. (b) and (c) Osteosarcomas (K7M2 and MOS-J model respectively). HPS staining shows smaller cells with large nuclei in comparison to chondrosarcoma. Osteosarcomas exhibit a higher cellular density. The absence of extracellular matrix is also observed.

of histological slices. Chondrosarcoma cells exhibit radii with a mean value and a standard deviation of 9.5 ± 2.6 µm, while K7M2 osteosarcoma cells have radii of 4.7 ± 0.9 µm and MOS-J osteosarcoma 4.8 ± 1.0 µm. Osteosarcoma cells are about twice as small as chondrosarcoma cells. The size distributions of osteosarcoma cells appear more uniform compared to chondrosarcomas. Chondrosarcoma nuclei exhibit radii with a mean value and a standard deviation of 4.2 ± 0.5 µm, while K7M2 osteosarcoma nuclei have radii of 2.4 ± 0.6 µm and MOS-J osteosarcomas 2.7 ± 0.7 µm. Osteosarcoma nuclei appear approximatively twice as small as chondrosarcoma nuclei. The size distributions of chondrosarcoma nuclei are sharper compared to osteosarcomas. Similar cell sizes can be observed between K7M2 and MOS-J osteosarcomas. However, these two osteosarcoma types exhibit slight variations in the nucleus radii.

The cell volume fraction is estimated at $\phi_{Ch,cell} = 0.23$ and $\phi_{Os,cell} = 0.88$ for the chondrosarcoma and two osteosarcoma types respectively. Osteosarcoma is a hypercellular histological subtype that contains almost no extracellular matrix. The nucleus volume fraction is estimated at $\phi_{Ch,nuc} = 0.03$ for the chondrosarcoma and $\phi_{Os,nuc} = 0.25$ for the osteosarcomas.

6.3.2 Tumor characterization

Quantitative ultrasound

Examples of B-mode images are given in Figure 6.4.

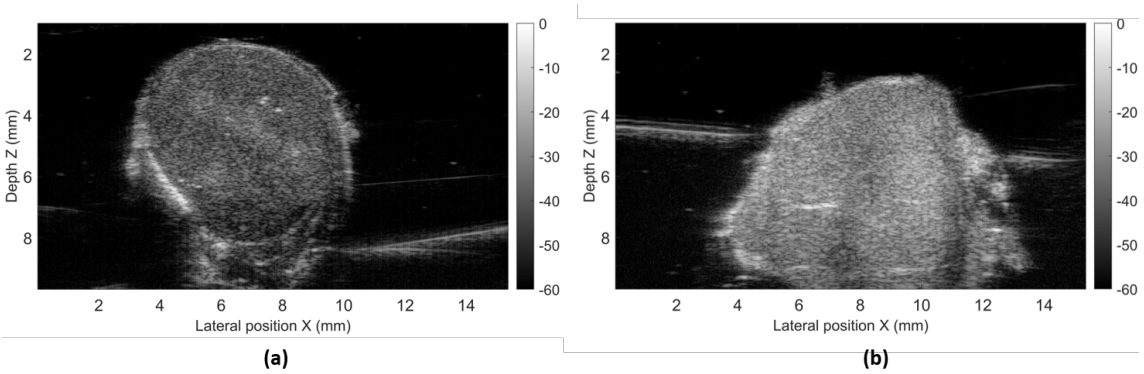

Figure 6.4: Example of B-mode images using the LZ400 probe. (a) Osteosarcoma. (b) Chondrosarcoma. The gray levels indicate the scale in dB. In each case, the tumors are immersed in a PBS solution.

Mean BSCs per animal using the low (13-24 MHz) and the high-frequency probes (restricted to 24-38 MHz) are presented in Figure 6.5 (a). The corresponding b-spline fits in the whole frequency range are shown in Figure 6.5 (b). The BSCs exhibit differences between the tumor types and similar trends among tumors of the same nature. The two different osteosarcoma cell lines (MOS-J and K7M2) lead to highly contrasted BSCs.

The differences within the BSCs per ROI are translated into the Lizzi-Feleppa parameters in the scatter plots shown in Figure 6.6 (a). A Wilcoxon rank sum test conducted at a significance level of 5% reveals statistically significant differences in the intercept values between chondrosarcomas and osteosarcomas. However, there is no evidence indicating significant differences in the slope values between the two tumor types (t-test p-value = 0.73). The ES parameters are shown in Figure 6.6 (b). The scaling parameters Ω_{nak} and the Nakagami parameters α_{nak} underwent compression using a base-10 logarithm due to their extensive value range. The observed α_{nak} values indicate Nakagami-gamma distribution ($\alpha < 0.5$) [4]. Wilcoxon rank sum tests report statistically significant differences in the compressed α_{nak} and Ω_{nak} coefficients at the 5% significance level between chondrosarcomas and osteosarcomas.

The same observations can be made for K7M2 and MOS-J osteosarcomas. Student's t-tests reveal significant differences between the two osteosarcoma types for the intercept

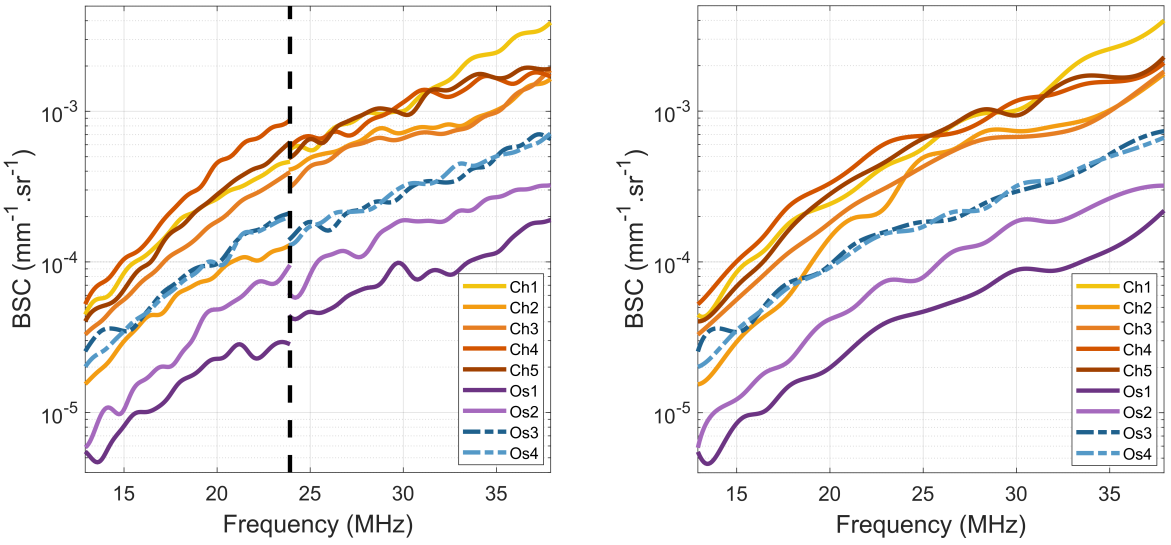

Figure 6.5: (a): Mean estimated BSC with the MS-250S probe (left of the black dotted line) and the LZ-400 probe (right of the black dotted line) per animal. (b): corresponding BSC b-spline fits. 'Ch' stands for chondrosarcomas and 'Os' for osteosarcomas.

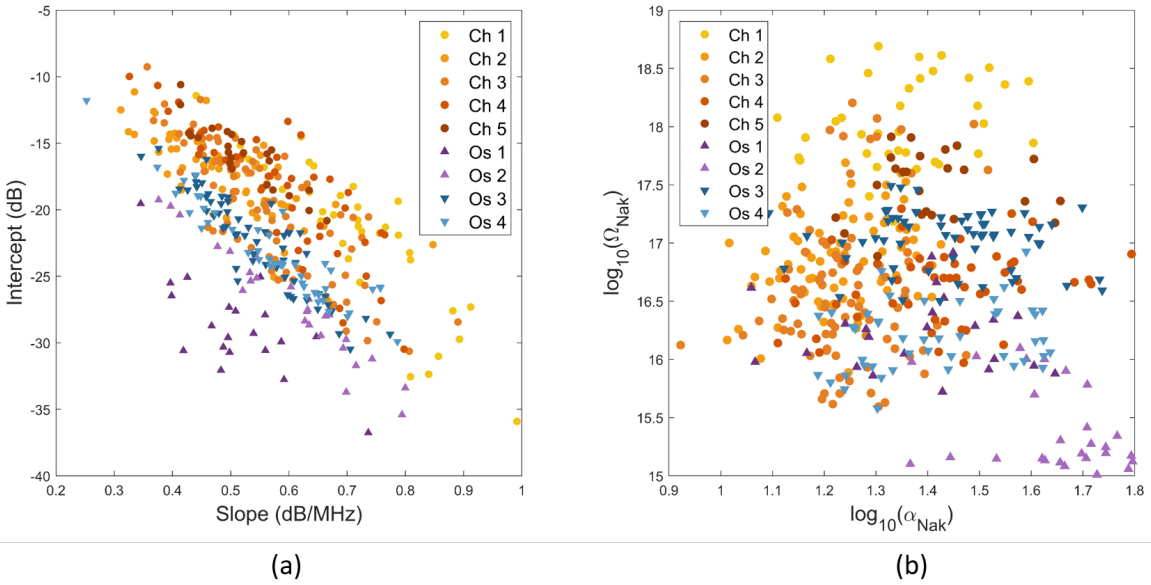

Figure 6.6: Scatter plots by model. Each point represents an independent region of interest (ROI). (a) Intercept versus slope (BSC linear model over the 18-38 MHz frequency range). (b) Nakagami envelope model estimated over the 18-38 MHz frequency range. Up and down arrows represent osteosarcomas from MOS-J and K7M2 cell lines respectively.

values and the Nakagami parameters but not for the slope. The compressed Ω_{nak} coefficients also show significant differences in this case. In summary, the three ultrasound parameters (the intercept, α_{nak} and Ω_{nak}) can discriminate the chondrosarcomas from the osteosarcomas, and the K7M2 from the MOS-J osteosarcomas. The linear slope appears irrelevant for tumor classification in this study.

Light Enhanced Backscattering Spectroscopy

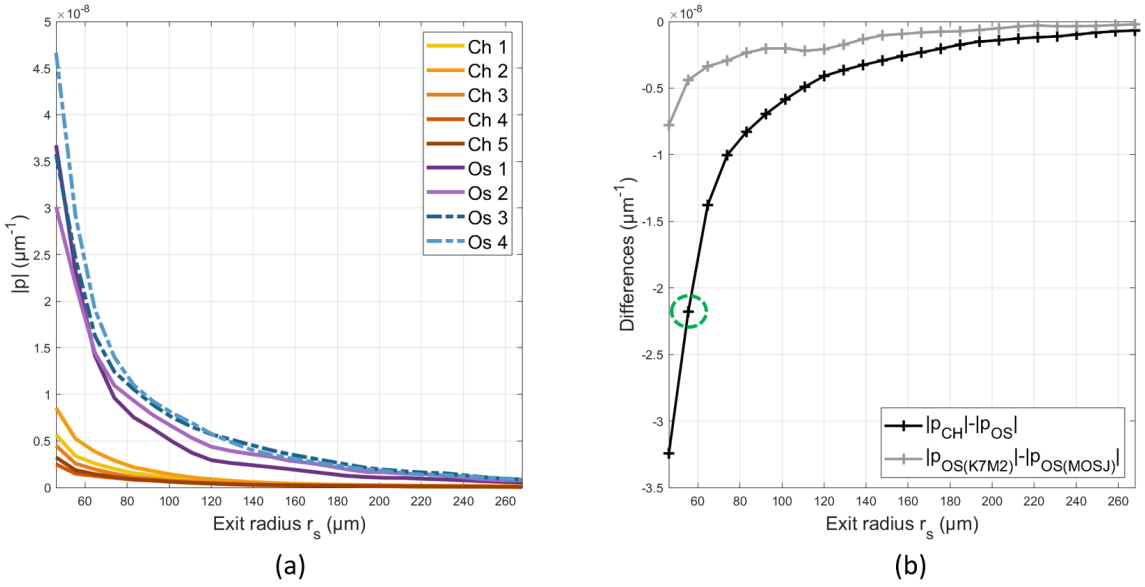

Figure 6.7: (a) Mean reflectance profiles per animal in the co-polarized channel at 700 nm. Statistical significances between chondrosarcomas and osteosarcomas signals were observed using a two-tailed student's t-test at the 5% level in the whole exit radius range. The location with the most significant changes occurred at $r_{s,opt} = 55$ µm with a p-value reaching 3×10^{-6}. No significant statistical differences were found at the 5% level between MOS-J and K7M2 osteosarcomas. (b): Absolute difference of mean reflectance profiles per group. The green dotted circle indicates the $r_{s,opt}$ of the difference curve.

The reflectance profiles measured in the co-polarized channel at 700 nm are plotted in Figure 6.7 (a). The five chondrosarcoma reflectance profiles exhibit fast decay and can be clearly identified from the osteosarcomas. This is highlighted by the differences between the mean reflectance profiles of each group, which increases for small exit radius values (Figure 6.7, b). Statistical significances for each exit radius value were observed using a two-tailed student's t-test at the 5% level. The location with the most significant changes between chondrosarcomas and osteosarcomas occurred at $r_{s,opt} = 55$ µm with a p-value reaching 3×10^{-6}. The K7M2 osteosarcomas (Os1 and Os2) signals exhibit a faster decay compared to the MOS-J osteosarcomas (Os3 and Os4). Similarly, differences in mean reflectance profiles between the two types of osteosarcoma increase at small length scales (Figure 6.7, b) but no significant statistical differences were found at the 5% level.

6.3.3 Scatterer size distribution

Ultrasound BSC parametrization

The BSC fits using the PII model in the low-frequency range (MS250S only) are shown in Figure 6.8 (a). The fitting procedure was performed using the average BSCs per animal ($R^2 > 0.99$). The volume fractions were set to the cell volume fraction based on histological estimations. Illustrative examples of 2D cost functions (base-10 logarithm of Equation 3.29) are shown in Figure 6.9 for a chondrosarcoma and an osteosarcoma. The corresponding inversion results are shown in Figure 6.10.

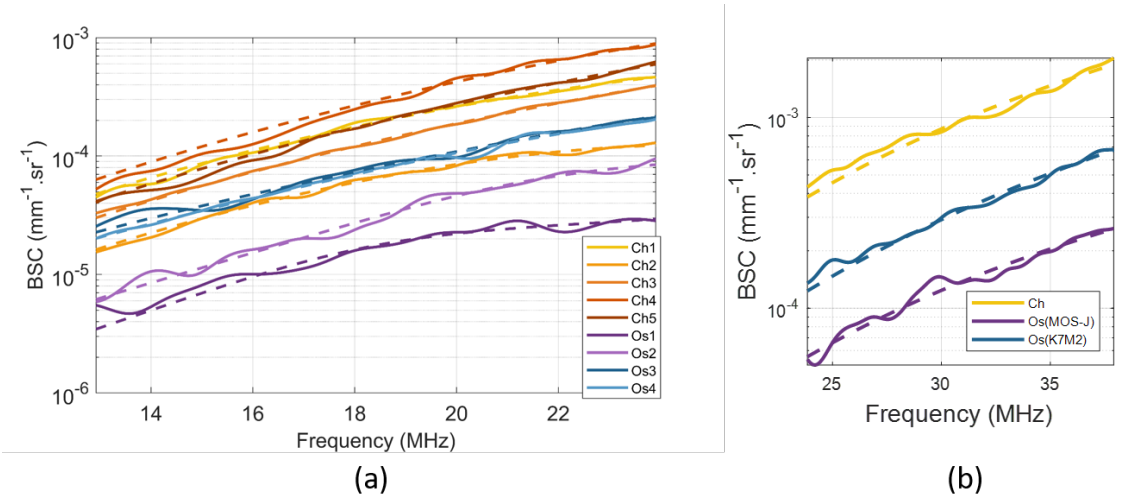

Figure 6.8: BSC fits. The estimated BSCs are shown with solid lines and the corresponding fits are shown with dashed lines of the same color. (a) Inversion results using the Polydisperse II model per animal in the frequency range 13 - 24 MHz (probe MS250S). The cell volume fraction is supposed to be known *a priori* and is set to $\phi_{Ch,cell} = 0.28$ for chondrosarcomas and $\phi_{Os,cell} = 0.88$ for osteosarcomas after histological analyses. (b) Inversion results using the Fluid-filled sphere model per group in the frequency range 24 - 38 MHz (LZ400 probe). The nucleus volume fraction is supposed to be known *a priori* and is set to $\phi_{Ch,nuc} = 0.03$ for chondrosarcomas and $\phi_{Os,nuc} = 0.25$ for osteosarcomas after histological analyses.

The estimated chondrosarcoma mean scatterer sizes correspond with the mean cell sizes extracted from the histological analyses with a mean relative error of 22% (Figure 6.10, a). However, these similarities are not observed for osteosarcomas: the PII model identifies larger scatterers for each tumor (mean relative error > 100%). The Schulz width factors z were extracted with relative errors about 3% for Ch1 and Ch2 and superior to 100% for Ch3 (Figure 6.10, b). The estimated Schulz width factor for other chondrosarcomas reached the upper bound of the inversion constraints. The distribution sharpness is systematically underestimated for the osteosarcomas. The relative acoustic impedance contrasts γ_z obtained after inversions are 0.02, 0.01, 0.02, 0.03, 0.03 for Ch1, Ch2, Ch3, Ch4 and Ch5 respectively. Similarly, for the osteosarcomas, the relative acoustic impedance contrasts γ_z are 0.02, 0.03, 0.06 and 0.05 for Os1, Os2, Os3 and Os4 respectively. The same

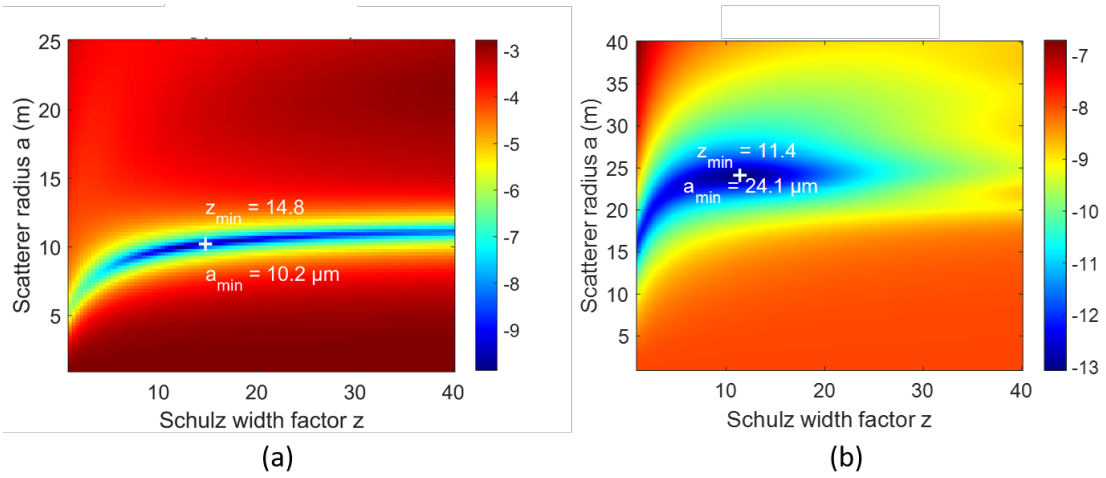

Figure 6.9: Inversion cost functions for the two tumor types. (a) Illustrative example of a 2D cost function (base-10 logarithm of the mean square error) of a chondrosarcoma (Ch1) in the frequency range 13 - 24 MHz. (b) Illustrative example of a 2D cost function (base-10 logarithm of the mean square error) of an osteosarcoma (Os1) in the frequency range 13 - 24 MHz. To plot the cost functions as a function of the mean scatterer radius a and the Schulz width factor z, the relative impedance contrast was set to 0.02. The latter value corresponds to the relative impedance contrasts that was obtained for these two animals after inversions. The detected minima are spotted with white crosses on each graph.

inversions were conducted by setting the volume fraction to the nuclei volume fractions to validate the results. A minimum mean relative error of 65% was found for all estimates.

The BSC fits using the Fluid-filled sphere model (FFSM) in the high-frequency range (LZ400 only) are shown in Figure 6.8 (b). The fitting procedure was performed using the average BSCs per animal ($R^2 > 0.97$). In this case, the volume fractions were set to the nucleus volume fraction after histology analyses ($\phi_{Ch,nuc} = 0.03$ and $\phi_{Os,nuc} = 0.25$). The corresponding inversion results are shown in Figure 6.11. The relative acoustic impedance contrasts γ_z obtained after inversions are 0.12, 0.03 and 0.01 for the chondrosarcomas, the K7M2 and the MOS-J osteosarcomas respectively. The chondrosarcoma scatterer radii estimated by the FFSM correspond to the mean nucleus size extracted in histology with a relative error equal to 9%. The osteosarcomas scattering structures identified by the BSC theoretical model are larger than the histological measurements (relative errors > 33%). The PII model estimated the nucleus radius with relative errors equal to 70%, 15% and 49% for the chondrosarcomas, the K7M2 and the MOS-J osteosarcomas respectively. All the estimations of the Schulz width factor reached the lower bound of the inversion constraint using the PII model. Therefore, we did not further consider these inversion results.

The BSC inversions with the PII model using the BSC b-spline fits (Figure 6.5, b) for the osteosarcomas are shown in Figure 6.12 ($R^2 > 0.97$). Here, the volume fraction was set to the cell volume fraction ($\phi_{Os,cell} = 0.88$). No clear correspondences were observed between the BSC-based parameters and the cell sizes using the whole frequency range

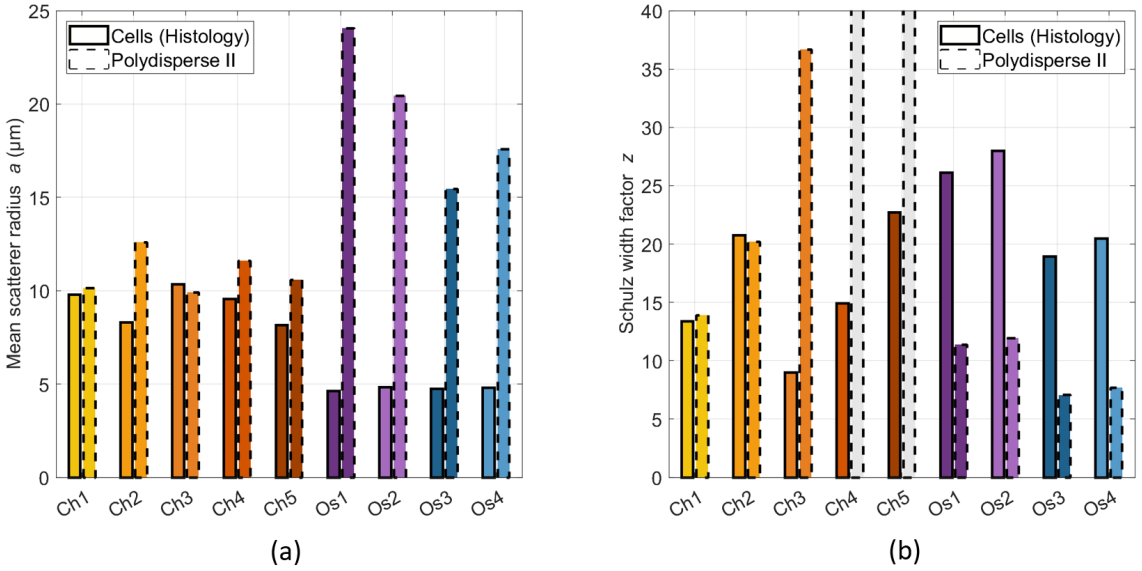

Figure 6.10: Inversion results using the Polydisperse II model per animal. The cell volume fraction is supposed to be known *a priori* and is set to $\phi_{Ch,cell} = 0.28$ for chondrosarcomas and $\phi_{Os,cell} = 0.88$ for osteosarcomas after histological analyses. (a) Mean scatterer radius. (b) Schulz width factor. The estimated Schulz width factor for Ch3 and Ch4 reached the upper bound of the inversion constraints.

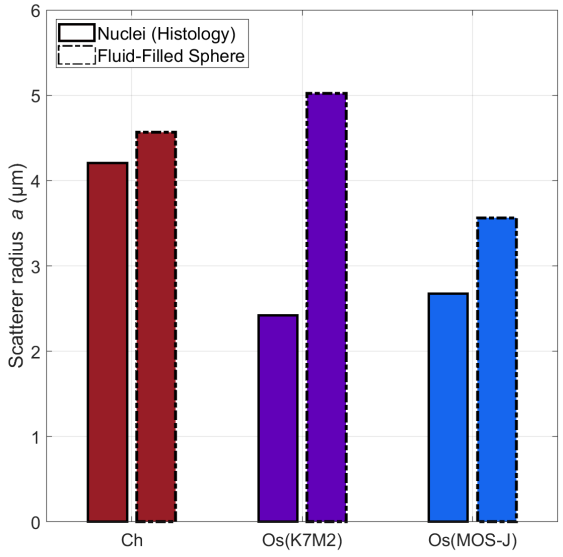

Figure 6.11: Inversion results using the Fluid-filled sphere model (FFSM) per group in the 24-38MHz bandwidth. The nucleus volume fraction is supposed to be known *a priori* and is set to $\phi_{Ch,nuc} = 0.03$ for chondrosarcomas and $\phi_{Os,nuc} = 0.25$ for osteosarcomas. The solid bars show the mean nucleus radii estimated by histological analyses.

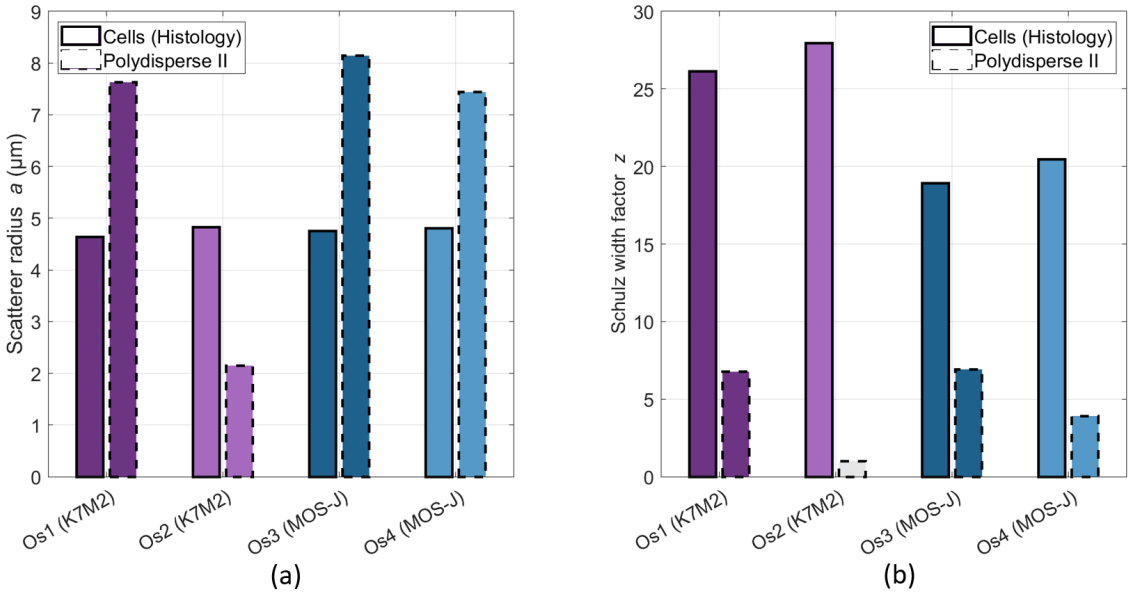

Figure 6.12: Inversion results using the Polydisperse II model for the osteosarcomas using the BSC b-spline fits (13 - 38 MHz bandwidth). The cell volume fraction is supposed to be known *a priori* and is set to $\phi_{Os,cell} = 0.88$ for osteosarcomas. (a) Mean scatterer radius. (b) Schulz width factor. The estimated Schulz width factor for Os2 reached the lower bound of the inversion constraint.

(relative errors superior to 50%, Figure 6.12, a). The Schulz width factors z were poorly extracted (relative errors superior to 50%, Figure 6.12, b). Indeed, the distribution sharpness is underestimated by the PII model. The estimated z coefficient for Os2 reached the lower bound of the inversion constraint. The same inversions were conducted by setting the volume fraction to the nuclei volume fractions to validate the results. The osteosarcoma nuclei were estimated with a relative error of 18%. However, all the estimations of the Schulz width factor reached the lower bound of the inversion constraint. Therefore, we did not further consider these results.

Light Scattering Spectroscopy

Figure 6.13 (a) shows the mean differential polarization signals for each tumor type. The measured LSS spectra exhibit significant differences between the two tumor types. The corresponding estimated size distributions F are shown in Figure 6.13 (b) and (c) for $r_{max} = 16.75\,\mu m$. The integral of each distribution is normalized (*i.e.* cells and nuclei from histological examinations independently analyzed). The shapes of the nucleus size distributions are accurately replicated by LSS. The cell size distributions also appear in the LSS estimations, particularly for the chondrosarcomas.

We hypothesize that cells could be involved in the light scattering process depending on the volume density of the extracellular matrix. In the following procedure, we simply

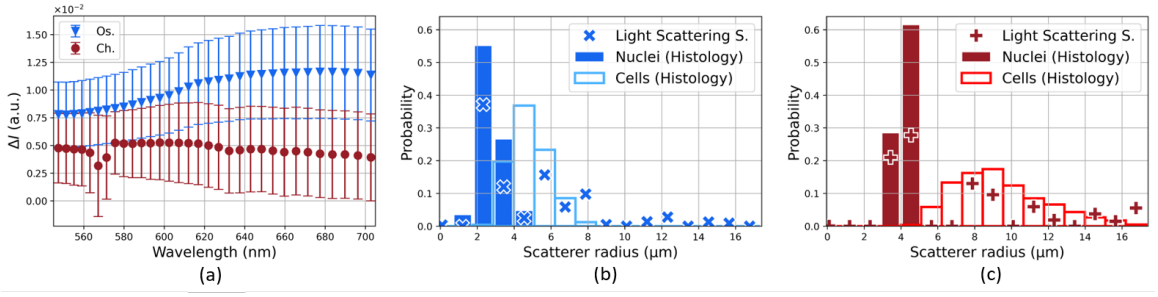

Figure 6.13: (a) Mean differential polarization signals ± standard error for the two tumor types. (b) and (c) Estimated scatterer size distribution for the osteosarcoma and the chondrosarcoma respectively. The nuclear and cellular size distribution estimated from histological analyses are normalized.

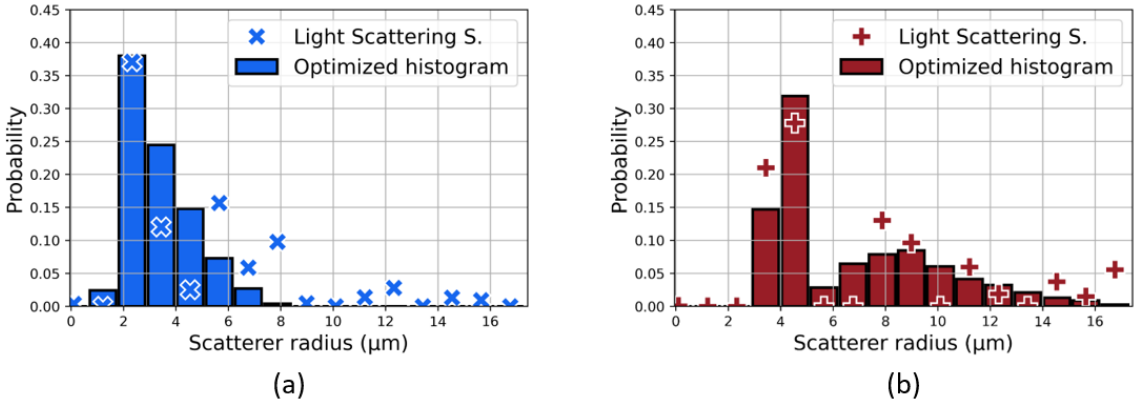

Figure 6.14: (a) Osteosarcoma estimated solution and its optimized linear combination of nucleus and cell size distribution. The nucleus scattering identified in the estimated solution accounts for 69%. (b) Chondrosarcoma estimated solution and its optimized linear combination of nucleus and cell size distribution. The cell scattering identified in the estimated solution accounts for 52%.

assume that cells and nuclei represent two independent populations of potential scatterers with linearly additive contributions. To test this hypothesis, linear combinations of the nucleus and cell histograms obtained from the histological analyses were computed using different nucleus weights w_{nuc} and cell weights w_{cell}. These values were defined such that $w_{nuc} = 1 - w_{cell}$, thus merging the estimated nucleus and cell sizes such as the integral over the scatterer radius equals unity. The optimized nucleus weight was considered as the value that leads to the best fit between the estimated LSS solution F and the newly merged histogram. In other words, this procedure redistributes the probabilities obtained with histological analyses to quantify the contribution of nucleus and cell scattering in the LSS solution F. Figure 6.14 (a) and (b) shows the obtained optimized histograms for each tumor type. The histogram optimization procedure resulted in an estimated nucleus weight of 69% for osteosarcomas and 52% for chondrosarcomas. The coefficient of determination between the estimated size distribution F_{LSS} and the optimized histograms $R^2_{Ch}(F_{LSS}, F_{opt,histo})$ equals 0.80 for chondrosarcomas and $R^2_{Os}(F_{LSS}, F_{opt,histo})$ equals 0.73 for osteosarcomas.

6.4 Discussion

In this study, BSC parametrization, ES, and EBS were performed to discriminate chondrosarcoma and osteosarcoma based on quantitative estimates. Then, BSC parametrization using other models and LSS were conducted to estimate the scatterer size distribution. Results were compared with histological analyses to study the agreement with cell and nucleus size distributions.

6.4.1 Tumor discrimination

Significant differences were observed between chondrosarcomas and osteosarcomas in the Nakagami parameters α_{nak}, the scaling parameter Ω_{nak}, the BSC linear intercept and the light reflectance profile intensity. These results align with the distinct microarchitectures observed in each histological subtype since these scattering parameters reflect the underlying tissue microstructure. Surprisingly, the same three ultrasound parameters show significant variations within the two osteosarcoma cell lines (K7M2 versus MOS-J cell lines). This result was not expected since these cell lines lead to the same tumor model. Indeed, the visual aspects of the histological slices in the microphotographs are not sufficient to identify the specific cell line that induced the osteosarcoma. Moreover, the K7M2 and the MOS-J osteosarcomas exhibit similar volume fractions and mean cell sizes. The observed contrasts between their BSCs could be explained by the differences in their Schulz width factors z. Indeed, in this frequency range, the PII model associates a low BSC amplitude to high z values. We can observe that this parameter is higher for the K7M2 ($z \approx 26 - 28$) compared to the MOS-J ($z \approx 18 - 21$). Interestingly, the

estimated BSCs support this hypothesis. Alternatively, the observed contrasts between their BSCs could also probably be explained by differences in their relative impedance contrasts γ_z, although it is difficult to check this assertion experimentally. This result illustrates the high sensitivity of the BSC parametrization technique to probe fine tissue properties. Likewise, the reflectance profiles showed variations at small exit radii between the osteosarcomas types. However, the limited number of EBS measurements does not provide sufficient evidence to draw conclusions regarding the statistical significance of the observed difference. However, the striking contrasts in EBS signals between chondrosarcomas and osteosarcomas accurately reflect the pronounced differences in their respective microarchitectures. These results are in line with the EBS's philosophy. EBS is applied in biological tissues to probe submicron microarchitectures by analyzing the reflectance profiles at small length scales relative to the light transport mean free path [10]. Indeed, EBS is used to detect early cancerous cells located in the epithelial layers that are invisible to histological biomarkers. In this study, the extreme sensitivity of this tool is reported with the highly contrasted EBS signals between two completely distinct microarchitectures, as well as the finer differences observed at small length scales for microarchitectures that share a similar histological appearance (K7M2 and MOS-J osteosarcomas).

6.4.2 Size estimations of cellular structures

Chondrosarcoma

BSC inversions were conducted to investigate the extent to which cellular structures could be regarded as ultrasound scatterers in chondrosarcomas. The PII model (Figure 6.10, a) successfully identified the mean chondrosarcoma cell size and two Schulz width factors out of five estimated the sharpness of the cell size distribution in the low-frequency range. However, poor correspondences between the Schulz parameters and the histological analyses were observed in other cases, leading to mainly unstable estimations of this parameter. These observations are in line with the ones reported by Han et al. [38]. Indeed, they observed higher relative errors for the estimations of the Schulz width factor z compared to the mean scatterer radius using the PII model in cell pellet biophantoms. To study the sensitivity of the PII model to the scatterer radius and the Schulz width factor, we conducted simulations (Figure 6.15). We illustrate the sensitivity of the PII model by observing the BSCs for varying input parameters around the reference values estimated for Ch1 (10% variations). Simulations reveal that the BSC shape is more sensitive regarding the mean radius (a) than the Schulz parameter z (b) in the PII model. Thus, the estimation of z is more subject to experimental noise, thereby increasing the difficulty of its accurate determination. The mean nucleus radii of the chondrosarcomas were correctly estimated by the FFSM model in the high-frequency range at the expense of the averaging process of all the independent BSC estimations. Conversely, a limited number of independent LSS measurements were sufficient to accurately extract the nucleus size

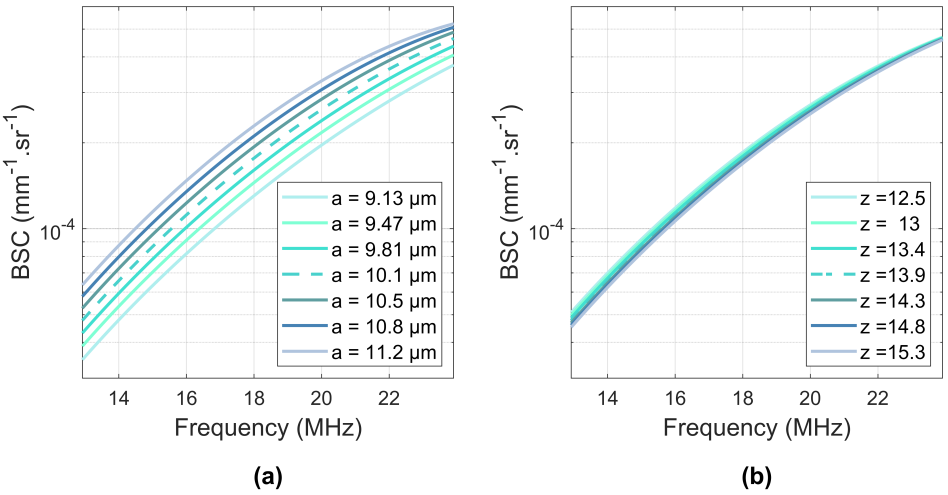

Figure 6.15: Sensitivity of the Polydisperse II model in the 14 - 24 MHz frequency range. (a) BSCs with a 10% variation around the scatterer radius estimated in Ch1. (b) BSCs with a 10% variation around the Schulz width factor estimated in Ch1. In each case, the volume fraction was set to 0.23. The relative impedance contrast was set as the one estimated for Ch1 ($\gamma_z = 0.02$)

distribution. However, the LSS estimation of the cell size distribution was less precise but allowed to quantify the contribution of cell scattering in the observed spectrum. Indeed, approximately half of the chondrosarcoma LSS spectrum can be attributed to cell optical scattering, while the remaining half corresponds to nucleus scattering. These results are coherent with the histological analyses and the simple microarchitecture observed in this tumor type. Indeed, chondrosarcoma tumors are characterized by a low cell density. Moreover, chondrosarcoma cells and nuclei exhibit limited size overlapping, thereby facilitating the clear identification of each structure. Thus, we make the hypothesis that the cells could be considered as discrete optical scatterers surrounded by the abundant extracellular matrix, similar to how nuclei are usually modeled as isolated scatterers surrounded by cytoplasm.

Osteosarcoma

The same protocol was carried out for the osteosarcomas. The BSC parametrization systematically overestimated the osteosarcoma cell radius. To explain this result, our first hypothesis was that the center frequency may not be sufficiently high to induce scattering from the osteosarcoma cells, which are smaller than the chondrosarcoma cells. This led us to carry out another inversion procedure using the b-spline BSCs (Figure 6.12, b) by setting the volume fraction to the cell volume fraction estimated after histology analyses.

The PII model also did not identify the cells as scatterers. Besides, the BSC parametrization successfully identified the chondrosarcoma nuclei, which are approximately as small as the osteosarcoma cells. Thus the insonification frequency was not believed to be too low for osteosarcoma cells. These observations brought us to formulate a second hypothesis which is that the scattering from osteosarcoma cells may not be predominant. The LSS size distribution estimation led us to the same observation and attributed less than 30% to optical cell scattering in the measured spectra. We suggest that these results arise from the hypercellular nature of osteosarcoma tumors. Indeed, this tumor type contains almost no extracellular matrix (Figure 6.3, b) and presents contiguous cells. Thus, competing ultrasound and optical scattering from other structures may potentially mask the scattering signals from cells. Moreover, the significant size overlap among osteosarcoma cells and nuclei further complicates their discrimination, presenting an additional challenge. One should note that the effects of a high concentration of scatterer per unit volume are taken into account in the ultrasound scattering model PII. Thereby, structural effects are also not sufficient to explain the failure of BSC parametrization in estimating the osteosarcoma cell sizes. LSS and BSC inversions were performed to study the degree to which nuclei could be considered as scatterers in the osteosarcomas. LSS successfully extracted the nucleus size distribution and outperformed the FFSM inversion results, which overestimated the nucleus size. This may be explained by the fact that the ultrasound frequency was not high enough for the incident wave to interact with the osteosarcoma nuclei. Indeed, the histological analyses show that they are smaller than the chondrosarcoma nuclei. As a result, the products of wavenumber by scatterer radius are equal to $ka_{Os} = 0.39$ and $ka_{Ch} = 0.65$ at 38 MHz.

Cell mitochondria can also scatter light [155]. However, Ghosh et al. [156] measured mitochondria sizes in sarcoma cells and reported a longest dimension of 161 nm. Given the 700 nm excitation, the ka product can be estimated at $ka = 0.7$ at maximum, indicating scattering at the frontier between the Mie and the Rayleigh scattering regions. The Mie scattering of large mitochondria could appear in the estimated scatterer size distribution (minimum radius of 100 nm) while smaller mitochondria are considered as Rayleigh scatterers and therefore have their influence mitigated through post-processing treatment. Consequently, the scattering of mitochondria is not expected to interfere with the nucleus scattering of interest due to their size smaller in comparison.

In summary, the BSC parametrization and EBS appear as relevant tools for discriminating tumor types. Moreover, these techniques detected signal contrasts even among samples that present similar cellular morphologies. Thus, they might provide biomarkers that are invisible to conventional H&E histological markers. To estimate the microstructure sizes, the BSC parametrization was complementary to LSS for the study of chondrosarcomas. The first technique was more accurate in the estimation of the mean cell sizes while the second method led to a more efficient extraction of the nucleus size distri-

bution. We argue that these results arise from the correspondences between the simple microarchitectural structures of the chondrosarcoma and the basic geometries assumed in the scattering models. Conversely, identifying the cell size in highly cellular media such as osteosarcoma tumors appears more challenging due to their geometrical cell contiguity and the competing scattering from other microstructures. However, in both cases, LSS can provide valuable insights into the cell size distributions and can quantify the scattering contributions of each object.

6.4.3 Limitations

Potential limitations associated with the present study can be discussed. LSS correctly estimated the nucleus size distribution for both tumor types using a certain value of the maximum scatterer radius allowed in the inversion procedure. The numerical stability of the previous solution was investigated by varying the maximum scatterer radius values. The osteosarcoma solutions appeared relatively more robust than the chondrosarcoma solutions. Indeed, any r_{max} values taken within the interval [16.50 µm ,17 µm] lead to satisfying and reproducible estimations of the osteosarcoma nucleus size distribution. The observed amplitude of this interval is ten times smaller for the chondrosarcoma. To understand the observed instability of the chondrosarcoma solution, the LSS spectra shape could be analyzed (Figure 6.13, a). The osteosarcoma spectra appear smoother than the chondrosarcoma spectra, which show a brutal variation around 570 nm. To mitigate the influence of Rayleigh scattering, the LSS spectra are multiplied by λ^4 prior to differentiation with respect to λ. Consequently, the experimental noise in the LSS spectra gets strongly amplified in the signal processing required to estimate the scatterer size distribution. This could explain the poor stability observed for the chondrosarcoma inversions. In brief, the LSS analytical procedure initially described by Fang et al. [68] appears useful to mitigate Rayleigh scattering and to justify the r_{min} value. However, it also introduces a significant increase in experimental noise, particularly at high wavelengths. The precise estimation of the nuclear size distribution using LSS is challenging, and we argue that this tool should be more robust for classification applications. Indeed, the measured LSS spectra exhibit significant variations (Figure 6.13, a). This observation aligns with findings from the latest studies. Recent papers investigated the use of a diagnostic parameter based on the differences between LSS spectra from normal and dysplastic sites [9,69] to detect precancerous lesions. This simple approach led them to outperform the specificity and the sensitivity of recently commercialized optical tools. The inversions of the BSCs led to a good estimation of the cell size diameter for the chondrosarcoma (product $ka \approx 1.0$ at 24 MHz) using the PII model in the low-frequency range. On the other hand, the scatterer radius estimated by the FFSM model in the 24-38 MHz frequency range does reflect the mean nucleus size of the chondrosarcoma ($ka \approx 0.65$ at 38 MHz). This observation suggests that the identified scattering structures depend on the incident frequency. However, because

the *ka* product is lower than unity when estimating the nucleus size, one could discuss this result of the inversion in the high-frequency range.

6.5 Conclusions

6.5.1 Perspectives

The points discussed above brought us directions for future investigations. The contribution of optical scattering by cells and nuclei brought by LSS covers a great potential that deserves further consideration. As observed in this study, the cell scattering percentage may reflect the volume fraction of the extracellular matrix within the tumor. Consequently, LSS and the histogram optimization procedure could have the capacity to estimate the cell density if the cell and the nuclei size distributions are known *a priori* or if a model is applied to describe them. Considering that cellularity is of prime interest to pathologists, this additional capability enhances the value of LSS in diagnostic applications. Moreover, an estimation of the cell volume fraction by LSS would be of great benefit in BSC fitting procedures. Indeed, ultrasound scattering models are parameterized by multiple independent coefficients that can include the volume fractions. In the fitting procedures conducted here, the volume fractions were set to a fixed value considered to be known *a priori*. Using one LSS output as an input for the BSC parametrization could avoid this hypothesis. Hence, this optical method can be beneficial for the spectral-based ultrasound technique, additionally to providing complementary information. This makes our approach a promising bimodal application for tumor characterization.

In this study, the excised tumors that were used exhibited a whitish color. Blood residuals were assumed minimal with a limited impact on the optical absorption, which was therefore neglected. For *in vivo* studies, this assumption may hold to a certain extent for the chondrosarcoma that is poorly vascularized compared to the osteosarcoma. However, blood absorption should be taken into account for *in vivo* spectral analyses that involve osteosarcoma.

6.5.2 Conclusion

In conclusion, the two quantitative ultrasound and the two optical techniques brought complementary parameters that reflect the underlying tissue microstructure for different tumor types. The estimated morphological parameters were found to be sensitive to the cellular and nuclear scales. These promising findings led us to conduct an *ex vivo* animal longitudinal study to assess the sensitivity of this bimodal technique for treatment monitoring applications.

Chapter 7

Therapy monitoring: a longitudinal study

The successful tumor characterization of sarcoma subtypes presented in the previous chapter motivated us to conduct a follow-up experiment. The study reported in this chapter aims to assess the capability of our bimodal technique to monitor the tumor response to an anti-cancer drug treatment. For this purpose, *ex vivo* experiments were carried out. These experiments are part of an *OncoStarter* project from the Cancéropôle Lyon Auvergne Rhône Alpes. Aurélie Dutour and Iveta Fajnorova (Centre Léon Bérard - CRCL) provided the biological materials. Celia Mansilla (graduate student) contributed to the ultrasound experiment.

7.1 Introduction

In the cancer patient care workflow, the selection of treatment options takes place after the diagnosis is made. An interdisciplinary team of medical professionals discusses the best therapeutic choices based on the grade, the stage and the histological subtype of the diagnosed tumor. Chemotherapy is one option that can be combined with other treatments. It involves drug treatment administered in cycles, carefully planned over a specific duration. The number of cycles depends on several factors such as the histological subtype. The drug can be administered to the patient before surgery (neoadjuvant).The tumor reaction to the anticancer agent is the mechanism of interest in this study.

At the cellular scale, increases in tumor cell death at the early stage of treatment and inhibition of proliferation can reflect positive tumor responses [157]. At the macroscale, this phenomenon can manifest as a shrinkage in the tumor size [158]. Common methods for monitoring tumor response include Magnetic Resonance Imaging, Computed Tomography,

Positron Emission Tomography or ultrasound imaging. The tumor response is typically determined after estimating the tumor size from the medical images using the Response Evaluation Criteria in Solid Tumors (RECIST) method [158]. However, the tumor size may be a limited metric to detect the tumor regression as the changes in the tumor size indicating its positive responsiveness may occur 6 to 8 weeks after the first drug administration [24, 159]. Additionally, the agreement between the histological examination and the tumor shrinkage observed in some conventional imaging modalities can be less than 50% [160].

In the cases bone sarcomas, when neoadjuvant chemotherapy is chosen, the treatment plan can typically be established over 8 weeks between the first chemotherapy session and the surgery. During this time, the tumor response is not routinely assessed. The potential cancer regression is only observed at the time of surgery on the resected tumors and the associated histological examination. The lack of tumor response can be a challenging situation for both the patient and the clinicians. In this case, the treatment plan can be reviewed and can result in extra weeks of drug administration which are not without side effects. As time is a crucial parameter in cancer patient care, choosing the best chemotherapeutic drug as early as possible is of prime importance for the patient's outcome. Consequently, a patient may benefit from the early detection of non-responsive treatment as it can guide the healthcare team toward other treatment options that are potentially more effective.

As a potential solution to provide early detection of non-responsive tumors, we applied our bimodal method to osteosarcoma and chondrosarcoma tumor models over weeks, injecting a chemotherapeutic drug into certain rodents and saline solutions into others (control). The amount of injected drug was calibrated to mimic the most realistic tumor responses observed in humans. These tumors can either be responsive or non-responsive. This study aims to assess the capability of ultrasound or optical scatterer parameters to reflect the tumor reactions. As mentioned in subsection 2.2.3, numerous successful studies reported changes in the BSC-related Lizzi Feleppa parameters, in the effective scatter diameter or the acoustic concentration in chemotherapy-response monitoring applications [161]. To my knowledge, no previous study reported the application of EBS or LSS for therapy monitoring. However, these tools show great potential since *in vivo* applications successfully probed fine tissue properties [7, 85].

To observe potential correlations between the ultrasound and the optical measurements with the tumor response, reference values are needed. Firstly, the tumor volume growth is used as a reference indicator. In the case of animal models, treated tumors are expected to exhibit limited growth if they are responsive in comparison to control tumors. The reduction of the tumor size is not expected (*i.e.* tumors are not expected to become smaller). Secondly, the previous chapters showed that the size of nuclei and cells may impact the scattering parameters. To interpret potential differences in the estimated ultrasound and optical parameters as changes in the size of cells or nuclei, histological analyses were also conducted, similarly to the previous chapter.

In clinical settings, high frequency QUS techniques could provide a non-invasive solution for treatment monitoring applications as long as the tumor is located at a shallow depth. One could note that the presence of hard tissues between the lesion and the probe may prevent QUS analyses. The application of EBS and LSS appears more limiting to probe the tumor response if the lesion is not on the surface. Indeed, these modalities exhibit a relatively restricted depth selectivity in comparison to the ultrasound measurements. Alternatively, EBS and LSS could serve to assess the response of excised tumors to newly tested administered drugs. This assessment could hold significant promise, particularly in the context of clinical trials preceding the approval of a novel therapeutic treatment within the medical research domain.

In this study, a total of 22 osteosarcoma and 24 chondrosarcoma tumor models were examined. For each tumor type, the cohort was divided into two groups: a control group and a treated group that received one to two injections of doxorubicin per week. Doxorubicin is a chemotherapeutic drug that can be prescribed for patients with bone sarcomas. Four sessions of ultrasound and optical measurements were conducted for the chondrosarcomas. For the osteosarcomas, four sessions of ultrasound measurements and two sessions of optical measurements were carried out. These sessions were spaced several days apart to observe tumor responses over a period of 16 to 18 days. Rodents from both the control and treated groups were sacrificed for each day of measurement, enabling a direct comparison. A day of measurement involves BSC and ES ultrasound acquisitions followed by LSS and EBS measurements prior to tumor fixation. All these procedures were completed on the same day. Subsequently, histological examinations were conducted on the samples to serve as a reference.

BSC spectral parameters and envelope parameters were extracted from the experimental ultrasound data. The collected optical data led to the estimation of the LSS spectra and the reflectance profiles. Scattering parameters from treated and control rodents were compared in each session to observe potential differences resulting from the treatment.

7.2 Methods

In this section, we describe the animal models used in this study. The implementation of the quantitative ultrasound techniques is then detailed. Similarly, the implementation of LSS and EBS are successively described.

7.2.1 Animal models

Surgical procedures

The description made in the previous chapter (*c.f.* section 6.2.1) remains valid in this study. Thus, only differences are mentioned in this paragraph. Twenty-four chondrosarcomas tumors, hereafter referred to as Ch, were grafted on 25-day-old Sprague–Dawley

rats. The osteosarcoma models, hereafter referred to as Os, were established by injection of 1×10^6 K7M2 suspended cells [152] in the tibia of twenty-two BALB/cByJ mice. Upon establishment of palpable tumors, (*i.e.* 10 days for chondrosarcomas and 9 days for osteosarcomas after tumor implantation, animals were randomly divided into two groups: NaCl, control (100 µL, n = 12 Ch and n = 11 Os); doxorubicin, treated (1mg/kg, n = 12 Ch and 0.75 mg/kg, n = 11 Os). Rats and mice were treated over a period of 3 weeks or till tumors reached 2500 mm^3 or 600 mm^3, respectively. Tumor growth was monitored by regular visual inspection and tumor dimensions were measured with a caliper twice a week to estimate their volume. Animals were euthanized progressively every week and the tumors were removed for ultrasound and optical imaging.

Intraperitoneal injections of chemotherapeutic drug were administered at Day 0, Day

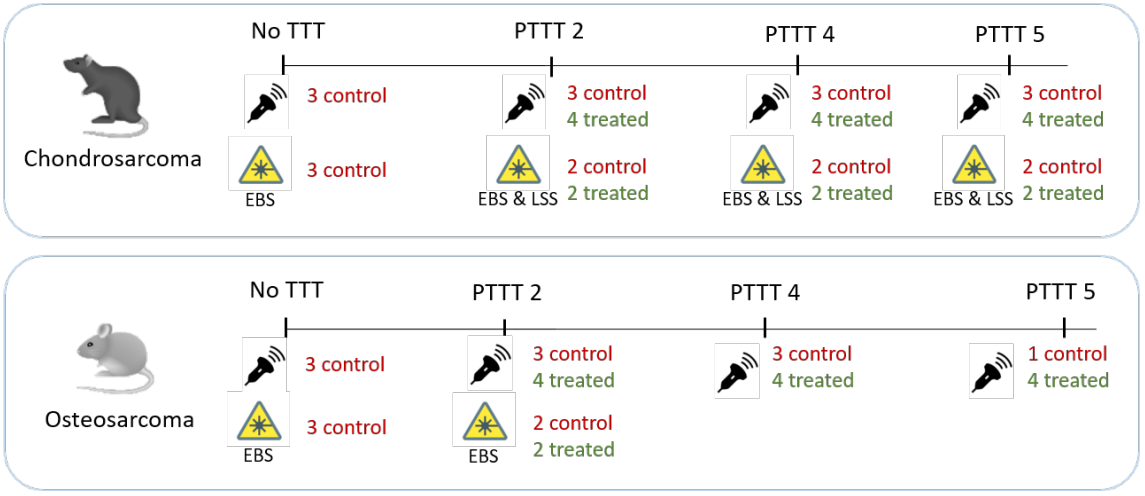

Figure 7.1: Timeline of the therapy monitoring experiment. The ultrasound probe and the laser sign show when ultrasound and optical measurements were performed respectively. LSS was only conducted for the chondrosarcoma in PTTT 2, 4 and 5.

3, Day 7, Day 10 and Day 14 for the chondrosarcomas. The ultrasound and the optical measurements were conducted at Day 0, Day 7, Day 14 and Day 16. For the sake of simplicity, the time points will be denoted based on the number of treatments received: No treatment (No TTT), Post-treatment 2 (PTTT 2), PTTT 4 and PTTT 5. For osteosarcomas, the drug were administered at Day 0, Day 4, Day 7, Day 12 and Day 14. The ultrasound and the optical measurements were conducted at Day 0, Day 6, Day 13 and Day 18. Osteosarcoma control tumors probed on Day 13 were excised on Day 11 because they reached a critical volume. Consequently, animals had to be sacrificed to comply with ethical guidelines. These tumors were immersed in PBS and stored in a refrigerator until Day 13. Similarly, the time points will be referred to as No TTT, PTTT 2, PTTT 4 and PTTT 5. The timeline of experiments is summarized in the diagram given in Figure 7.1.

Histological examination

After the measurements, the samples were immersed in paraformaldehyde for 24 hours for tumor fixation. Then, the tumors were embedded in paraffin blocks before undergoing histological analyses. The paraffin blocks were sliced to obtain 5 µm thick sections. The tumor sections were H&E stained through an automated procedure and scanned to obtain microphotographs. The histological parameters were analyzed using Qupath (software version 0.3.2) to automatically estimate the size distributions of osteosarcoma cells and nuclei. Due to the difficulties encountered in segmenting chondrosarcoma cells with H&E staining using QuPath, the cells and the nuclei of chondrosarcoma were manually segmented. Thus, the number of detected nuclei/cells is much higher using the automatic detection (min 2900 detections/tumor) compared to the manual segmentation (min 100 detections/tumors). In both cases, cell segmentation was performed in areas corresponding to the ROIs (*i.e.* maximum depth = 1 mm). The radii of cells and nuclei were extracted by assuming the circularity of the detected objects. Similarly to the previous chapter, the volume fraction was taken equal to the surface fraction of the cells or the nuclei as an approximation [153].

All the ultrasound and optical measurements had to be conducted within one single day to limit the physiological variations of the tumor cells. Consequently, optical measurements were performed on 4 tumors only (two controls and two treated) each day due to logistical reasons.

Relative Tumor Volume (RTV)

Relative Tumor Volume (RTV) is a common metric used in cancer research that can be used to monitor the tumor size over time in response to a chemotherapeutic drug. In this study, the RTV is used to estimate whether a tumor is responsive or not and serves as a reference. The volume of the tumors V are estimated under the approximation of the cylinder volume formula based on the caliper measurements such as:

$$V = longest\,diameter \times \pi\Big(\frac{shortest\,diameter}{2}\Big)^2 \tag{7.1}$$

Then, the RTV is calculated as the ratio of the tumor volume at a specific time point V_i during the study and the initial tumor volume V_0:

$$RTV = \frac{V_i}{V_0} \tag{7.2}$$

Low RTV values may reflect the positive response of a treated tumor, while high RTV values may indicate non-responsive or control tumors.

7.2.2 Implementation of QUS techniques

Acquisitions

The tumors were insonified with focused waves using a circular single-element transducer (RMV 704 probe, Vevo 770 ultrasound scanner) centered at 40 MHz, allowing tissue characterizations over the 25-55 MHz frequency range. The transducer has a fixed focal distance of 6 mm. A 3D scan was performed and consisted in 10 to 12 B-mode images spaced out 1 mm away from each other. Each scan was composed of 464 RF lines and imaged the tumor over 14.5 mm in the lateral direction thanks to the sweeping movement of the transducer. The tumor was placed onto an absorbing material immersed in a PBS solution for estimating the QUS parameters and onto a reflector for attenuation estimation (Figure 7.2). In the first case, the PBS/tumor interface was placed just above the focal distance. Regions of Interest (ROI) were 15λ long in both directions and were located at a relatively shallow depth (about 1 mm).

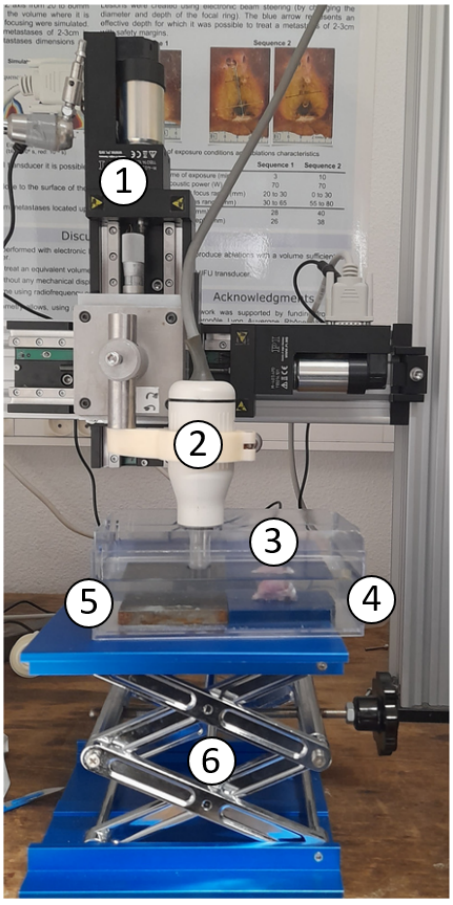

Figure 7.2: Picture of the ultrasound setup used in the therapy monitoring experiment. 1: Motorized platform, 2: RMV704 probe, 3: tumor immersed in PBS, 4: Absorbing material, 5: acoustic reflector, 6: lifting platform.

Similarly to the previous study, the ROIs were chosen with no overlap after manual

segmentation on the B-mode image of each tumor. Although QUS parameters from non-overlapping ROIs might be more subject to noise as opposed to overlapped ROIs, we opted for this configuration to obtain independent QUS estimates. The attenuation coefficients were estimated following standard substitution methods [110] for each tumor. The BSC for each ROI was estimated using the reference phantom method [113]. Our reference phantom was composed of polyamide particles of diameter 5 µm (Orgasol 2001 UD, Arkema) at the relative mass concentration of 0.25% in a gel that contains agarose (2%, Sigma) and water. The BSC of the reference phantom was computed using the Faran theory.

Data management

A signal-to-noise ratio (SNR) criterion is applied to filter out ROI with noisy power spectra due to the important amount of data. To do so, we apply a procedure inspired by the SNR criterion suggested by Mamou et al. [26]. For each ROI segmented in the B-mode image of the tumor, we first compute the corresponding power spectra of the reference phantom at its specific location as follows:

$$S_{ROI}^{ref}(f) = \frac{1}{N}\sum_{i=1}^{N}\left|FT[RF_{ref}(t)]\right|^2 \tag{7.3}$$

where N is the number of RF segments $RF_{ref}(t)$ within the ROI in the reference phantom and FT denotes the Fourier transform. Then, we calculated a virtual spectrum $S_{ROI}^{v}(f)$ that reflects the acoustic intensity at the ROI location as follows:

$$S_{ROI}^{v}(f) = \frac{S_{ROI}^{ref}(f)}{BSC_{theo}(f)} e^{4z_{ROI}(\alpha_{ref}(f)-\alpha_s(f))} \tag{7.4}$$

where α_{ref} is the acoustic attenuation of the reference phantom, α_s is the acoustic attenuation of the sample, z_{ROI} the depth of the center of the ROI and BSC_{theo} is the known theoretical BSC of the reference phantom. The factor $e^{4z_{ROI}(\alpha_{ref}(f)-\alpha_s(f))}$ compensates for the phantom attenuation and "adds" the attenuation that would be obtained in the sample at this specific location. According to Equation 3.8 of the discrete models detailed in chapter 3, the power spectra $S_{ROI}^{v}(f)$ reflects the pressure field resulting from the diffraction pattern of the single-element transducer with the sample attenuation. This quantity was then used to estimate whether a given ROI located in the sample image has a location in the field of view that received "sufficient" acoustic energy relative to the maximum detected power. This estimation was done through the computation of the band ΔF_{ROI} for each ROI in the sample image as follows:

$$\Delta F_{ROI}(f) = \left[f \; such \; that \; 10log\left(\frac{S_{ROI}^{v}(f)}{max_{f,x,z}\left[S^{v}(f)\right]}\right) > -12dB \right] \tag{7.5}$$

where $max_{f,x,z}\left[S^v(f)\right]$ represents the highest detected amplitude in the virtual power spectra $S^v(f)$ within all the ROIs located across the whole field of view and the whole frequency range. It is noteworthy that each power spectrum $S^v_{ROI}(f)$ was estimated following the position of the ROI in the tumor image using the corresponding RF data in the reference phantom. Consequently, the RF data of the tumors are not required to apply this criterion.

The bandwidth δF_{ROI} of each ROI was then computed as:

$$\delta F_{ROI} = max\{\Delta F_{ROI}(f)\} - min\{\Delta F_{ROI}(f)\} \tag{7.6}$$

The ROI was kept if δF_{ROI} is greater than 10 MHz and lower than 30 MHz. The ROIs that did not meet this specification are considered as abnormally short or long and are therefore omitted. The bandwidth of each power spectrum could have been truncated to the frequency values that respected the above criteria, as was done in Mamou et al. [26]. However, to allow direct comparison of the BSCs across the -6 dB bandwidth of the transducer, the power spectra were analyzed in the 25 - 55 MHz frequency range.

This criterion appears useful to select the ROIs that were located in the vicinity of the fixed focal distance of the transducer. The criterion kept most of the ROIs located at the surface of the tumors and rejected the ones that were away from the focal distance. One could note that the factor $BSC_{theo}(f)$ in Equation 7.4 is canceled out when the criterion is applied (Equation 7.5) and therefore does not contribute to the ROI selection. This factor was simply kept for attributing a physical meaning to $S^v_{ROI}(f)$. An average of 240 ROIs and 140 ROIs per tumor met the criterion for the chondrosarcoma and the osteosarcoma respectively.

QUS estimates

A linear model was fitted to the estimated BSC (Lizzi Feleppa approach) to estimate the linear midband fit and the linear slope for all the ROIs that were selected by the SNR criterion. For a given ROI, these spectral parameters were estimated as well as envelope parameters. Envelope parameters from the Nakagami distribution were extracted from the RF data contained in the ROI of the tumors. The correction for the attenuation and the diffraction effects was achieved following the same procedures as in the previous chapter (subsection 6.2.2). The Nakagami parameters α_{nak} were multiplied by the autocorrelation-based corrective factor κ (Equation 6.1) and the scaling parameter Ω_{nak} was multiplied by the χ factor (Equation 6.4).

The comparative analysis was conducted for every session (*i.e.* each day of measurement) to shed the light upon the potential effects of the chemotherapeutic drug over the course of the study.

7.2.3 Optical experimental setup

In this study, the experimental protocol described in the previous chapter for EBS and LSS was repeated with some improvements. All the modifications are detailed in this subsection.

In the study reported in the previous chapter, the camera was changed to switch from LSS to EBS: a hyperspectral camera (HERA) was used in the first case and a monochrome camera (Thorlabs 340M) was used for EBS that was performed at 700 nm only. Switching the camera implied tedious alignments. The white standard, mirror and background measurements had to be repeated for each new configuration. These steps consumed valuable time during the days of measurements, as both ultrasound and optical measurements had to be conducted within a single day.

To limit these time-consuming procedures, we modified the previous experimental setup by designing two independent channels for EBS and LSS. The newly designed benchtop setup is described in Figure 7.3 and a picture is shown in Figure 7.4 (a).

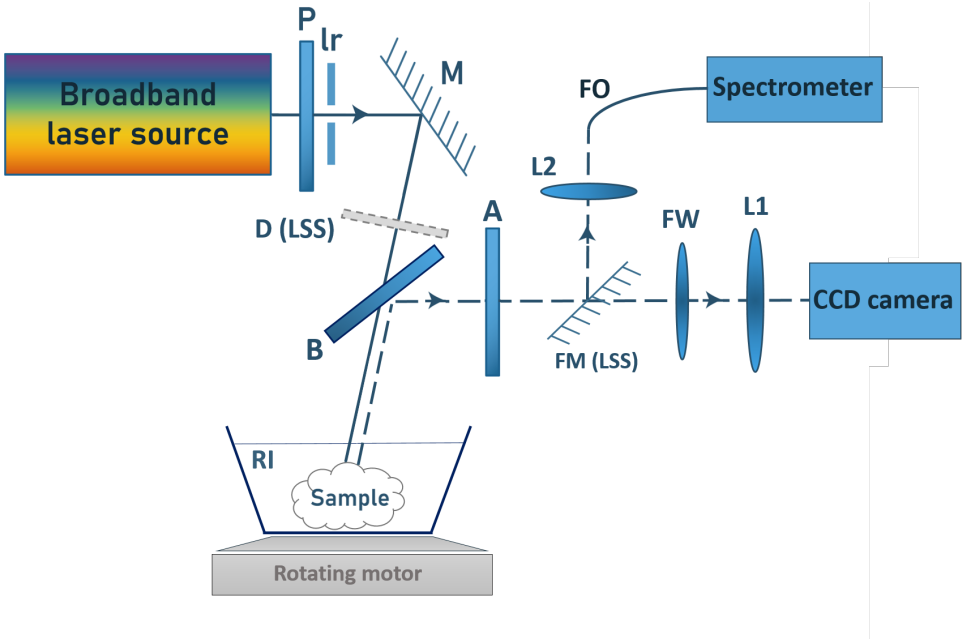

Figure 7.3: Scheme of the optical setup used in the therapy monitoring experiment. P: polarizer, Ir: Iris, M: mirror, D: diffuser used for LSS only, B: beamsplitter plate. A beam dump traps the useless reflected beam on the first interface (not depicted), RI: refractive index matching liquid, A: Analyzer, FM: flip mirror used for LSS only, FW: filter wheel, L1: Fourier lens, L2: focusing lens, FO: fiber optics. The rotating motor was used in EBS only to average the speckle away.

In this setup, switching from EBS to LSS only required adding a diffuser before the beamsplitter B and adding the flip mirror FM after the analyzer A. The modifications are detailed below for each experiment.

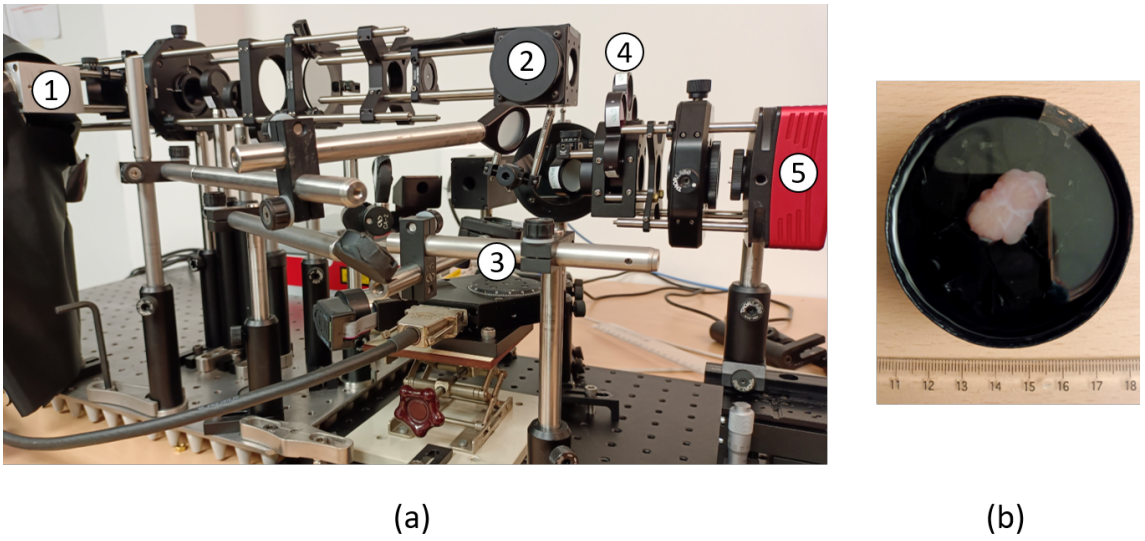

Figure 7.4: (a) Picture of the optical setup used in the therapy monitoring experiment. 1: Broadband laser source, 2: Mirror (M), 3: Rotating platform over which the sample is placed for measurement (80°/sec, EBS only), 4: filter wheel (FW), 5: CCD camera. The spectrometer used in LSS is not visible. (b) Picture of a chondrosarcoma tumor immersed in the refractive index matching liguid (n = 1.38) in the black receptacle that is used for EBS and LSS measurements

Enhanced Backscattering spectroscopy

EBS was performed with a hyperspectral camera in Chapter 5 and with a monochrome camera in Chapter 6 at 702 nm and 700 nm respectively. The configuration with a monochrome camera presented several advantages over the hyperspectral camera which has an integrated Fourier lens. First, choosing a monochrome camera and its Fourier lens allowed us to control the characteristics of the latter. Indeed, it is noteworthy that the focal length of the Fourier lens dictates the angular resolution of the EBS image for a given camera. Similarly to the EBS experiment carried out in the previous chapter, we opted for an aspherized achromatic lens with a focal distance of 50 mm (Edmund Optics, ref #49-665). As a result, an angular resolution of 8×10^{-3} ° is obtained (against 1.0×10^{-2}° in Chapter 5).

A filter wheel that contains narrow band-pass filters (FWHM 10 nm) was inserted before the CCD camera to spectrally resolve the EBS peak. The EBS measurements were performed at twelve visible wavelengths ranging from 550 nm to 700 nm. For each chondrosarcoma, 12 reflectance profiles corresponding to each working wavelength were acquired. For the osteosarcoma, logistical issues conducted us to perform EBS at 700 nm over 3 to 4 positions for the first two sessions (Day 0 and Day 6). Similarly to the previous experiment, the sample was immersed in the refractive index matching liquid (Figure 7.4, b).

The beamsplitter cube was changed to a beamsplitter plate to eliminate the unwanted reflections that were reported in the previous study. The iris diameter was set to 1.8 mm

to respect the Nyquist criteria. The angle above which noise is predominant is taken at 1.2°. The estimation of the incoherent baseline was done in a ring that spans from 1.0° to 1.1°.

One reflectance profile of animals from each tumor group was used to extract the Whittle-Matérn parameters to demonstrate the capability of EBS to probe tissue properties at small length scales. The optical properties of the corresponding tumors were then calculated, as described in section 4.1.4.

Light Scattering Spectroscopy

While EBS aims to analyze a coherent phenomenon, LSS was initially introduced as the study of the incoherent single-scattered light [68]. In the previous study, the incoherent backscattered light was considered as the signal on the periphery of the EBS peak. However, the LSS signal is no longer angularly resolved in the present setup, making it not possible to separate the incoherent backscattered light as was previously achieved. Consequently, we decided to minimize the spatial coherence of the light source as much as possible. To do so, we placed a diffuser before the beamsplitter plate. The diffuser was chosen with a fine grit (1500) to obtain a small diffusion pattern. This component was positioned perpendicular to the incident beam when LSS was performed. The backscattered light is then focused (f' = 25 mm) into a fiber optics (NA = 0.22) connected to a spectrometer (USB 2000, Ocean Optics). The LSS spectra were then computed as was done previously, by orientating the analyzer A parallel or perpendicular to the axis of the polarizer P. The LSS spectra were acquired over three to six different positions for each tumor. White standard measurements were repeated for each session day (SG3051, Sphere Optics).

7.3 Results

In all the boxplots shown in this chapter, the box displays the median as its central mark, while its lower and upper boundaries represent the 25^{th} and 75^{th} percentiles, denoted q_1 and q_3 respectively. The whiskers extend to the most extreme non-outlier data points. Data points are considered as outliers if they fall outside the range $[q_1 - 3/2(q_3 - q_1), q_3 + 3/2(q_3 - q_1)]$. Outliers are individually depicted using '+' symbols. Each box exhibits notches on its center. In a boxplot, when the notches of two boxes do not overlap, it can be concluded that the true medians differ with 95% confidence. The number of treatments received is indicated in the title of each boxplot. The labels of the X-axis give the identification number of each tumor and allow the comparison between the ultrasound and the optical measurements. The red boxes correspond to control tumors (*i.e.* no treatement) and the green boxes to treated tumors.

7.3.1 Chondrosarcoma

Histological analysis

As in the previous chapter, histological analyses are conducted to serve as references. The cell size distributions are shown in Figure 7.5 for each day of measurement. The orange dots indicate the volume fraction of each tumor. The corresponding value can be read on the right Y-axis. Only the chondrosarcoma tumors that underwent ultrasound and optical experiments are shown. Limited changes in the cell size distributions can be observed over the days of measurements for the treated and the control tumors. Additionally, no significant difference appears between the medians of the treated and the control tumors, as the notches of their boxes are overlapping (5% level). The volume fractions of the treated tumors appear similar to the control tumors, except for the treated tumors in PTTT 5, which exhibit higher values compared to the control tumors.

The same observations can be made for the nucleus size distributions (Figure 7.6): the nucleus sizes exhibit limited changes over the days and the treated tumors cannot be discriminated from the control tumors based on the nucleus radius. The nucleus volume fractions are similar, apart in PTTT 5, where the treated tumors exhibit higher values compared to the control tumors.

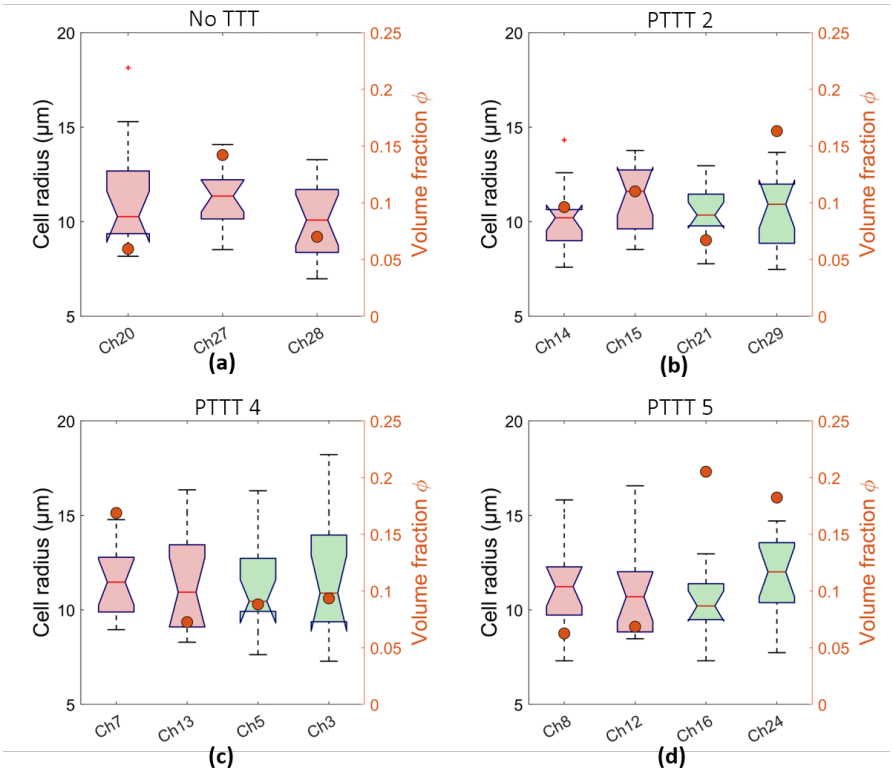

Figure 7.5: Chondrosarcoma: cell size distribution. (a) No treatment (No TTT), (b) Post-treatment 2 (PTTT 2), (c) PTTT 4, (d) PTTT 5. Control tumors and treated tumors are represented in red and green respectively. Orange dots show the volume fraction (right Y-axis).

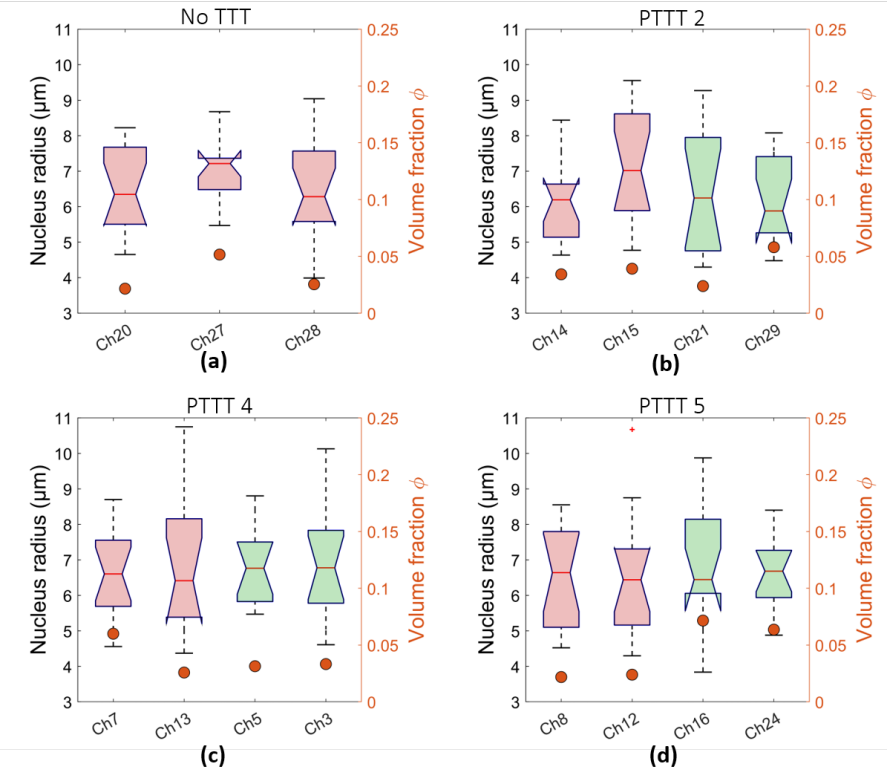

Figure 7.6: Chondrosarcoma: nucleus size distribution. (a) No treatment (No TTT), (b) Post-treatment 2 (PTTT 2), (c) PTTT 4, (d) PTTT 5. Control tumors and treated tumors are represented in red and green respectively. Orange dots show the volume fraction (right Y-axis). Only the tumors of chondrosarcoma that underwent ultrasound and optical measurements are shown.

Ultrasound BSC

The mean BSCs of each chondrosarcoma are shown in Figure 7.7. The RTV of the tumor is given in parenthesis in the legend. The BSCs of control tumors in No TTT are higher than the ones observed for the other days. The BSCs of treated tumors are lower than the control tumors for PTTT 2 and PTTT 4. The BSCs of control and treated tumors are in close proximity in PTTT 5. To conduct a more in-depth analysis of the BSC shapes for each day of measurement, the midband fit values and the slope of the BSC are considered.

Figure 7.8 shows the midband values and the RTV per day of measurement. Before analyzing the midband values, let us focus on the RTV. The RTV is shown with a blue dot for each tumor and its value can be read on the right Y-axis. RTV values are normalized with the volume of first day of measurement (No TTT). Therefore, the RTV values equal 1 for this day.

In PTTT 2, the RTV of the treated tumors are higher than the control tumors in average. In PTTT 4, two treated tumors exhibit important RTV (Ch18 and Ch3). In PTTT 5, the RTV of treated tumors are higher than the ones observed for the control tumors,

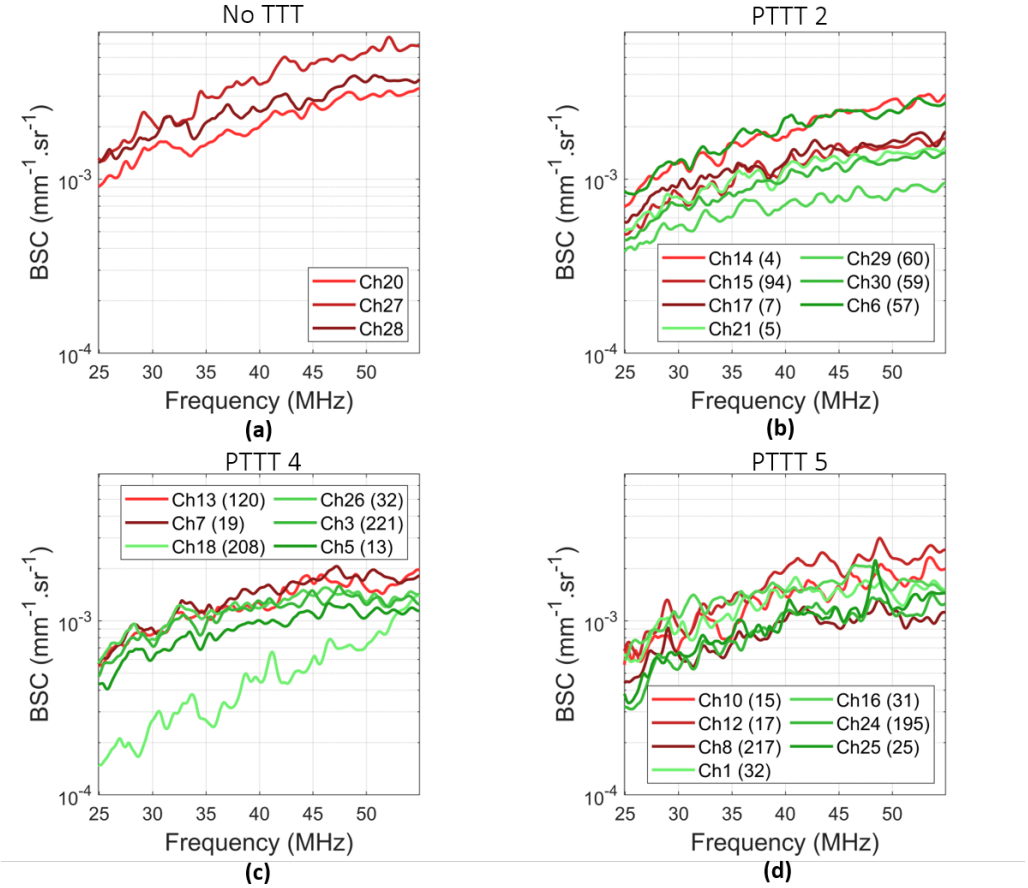

Figure 7.7: Chondrosarcoma: mean BSC per tumor. (a) No treatment (No TTT), (b) Post-treatment 2 (PTTT 2), (c) PTTT 4, (d) PTTT 5. Control tumors and treated tumors are represented in red and green respectively.

except for Ch8. In all day of measurements, an important disparity can be observed within the RTV of tumors that belong to the same group (*i.e.* control or treated). The only RTV of treated tumor that is below the smallest RTV of the corresponding control tumors is Ch5 in PTTT 4.

The midband values for each tumor exhibit limited changes over the days, typically ranging between -5 and 5 dB (Figure 7.8). The higher values can be observed in the tumors with No TTT. The coefficient of determination R^2 between the medians of the midband values and the RTV values of the treated tumors over these three days of measurement (12 data points) equals $R^2 = 0.20$.

In PTTT 2, 4 and 5, no threshold on the midband value can discriminate all the treated tumors from the control tumors. After checking the data normality, non-parametric tests are conducted to shed the light on potential statistical differences between the midband values from control and treated tumors. A Wilcoxon rank sum test conducted at a significance level of 5% reveals statistically significant differences in the midband values between control and treated tumors in PTTT 2 and PTTT 4.

The BSC slopes for each tumor are shown in Figure 7.9. The slopes estimated for

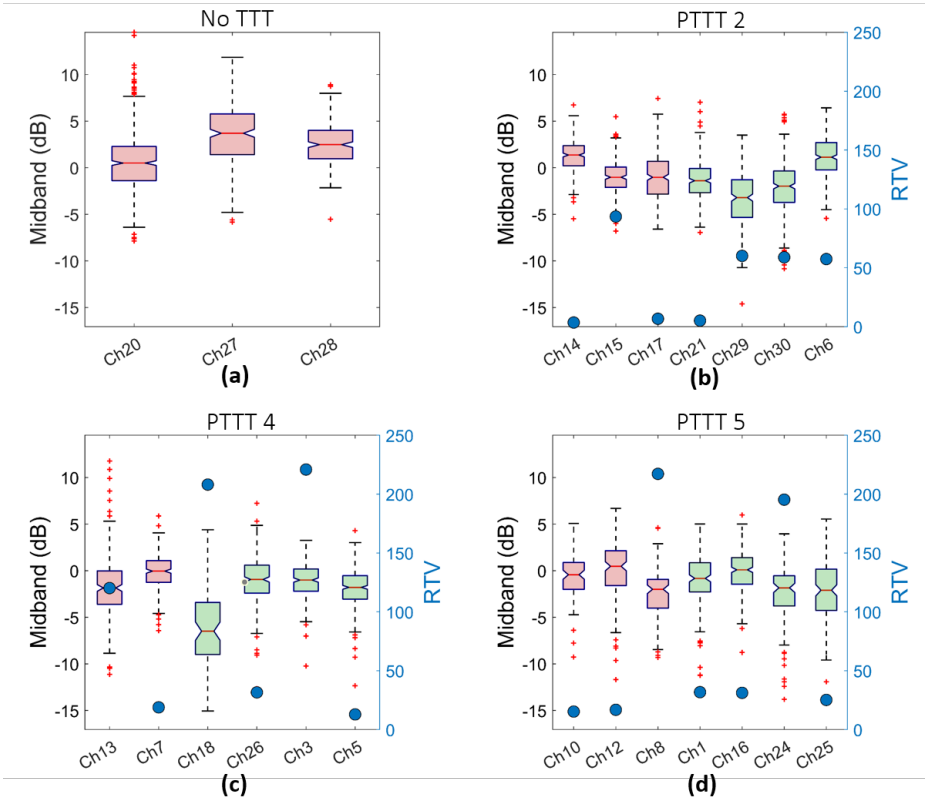

Figure 7.8: Chondrosarcomas: BSC midband fit values per day of measurement. (a) No TTT, (b) PTTT 2, (c) PTTT 4, (d) PTTT 5. Control tumors and treated tumors are represented in red and green respectively. The boxes show the distribution of data points for each tumor. The blue dot indicates the corresponding RTV and its value can be read on the right Y-axis.

No TTT are similar to ones observed for the other day of measurements. Similarly to what was observed for the midband, the slopes of both treated and control tumors exhibit similar distributions over the days. In PTTT 4, the treated tumor Ch18 exhibits a higher slope and a high RTV in comparison to other treated tumors. However, the treated tumor Ch3 shows a similar RTV but with a slope that is close to other treated tumors. In PTTT 5, the slope of the treated tumor Ch24 is the highest and corresponds with the greatest RTV of treated tumors. The coefficient of determination R^2 between the slope of the treated tumors and the RTV equals $R^2 = 0.32$ (12 data points). For each day of measurement, no unique slope value can allow to discriminate all the treated tumors from the control tumors. Significant statistical differences in the slopes are identified at the 5% level between the control and the treated tumors in PTTT 2.

Ultrasound envelope statistics

The distribution of the Nakagami parameters α_{nak} per tumor are shown in Figure 7.10. The values of α_{nak} of tumor with No TTT are lower compared to the ones reported for other days of measurements. Apart from this, limited changes in the distributions of the α_{nak} estimates can be observed over the days for each tumor group. In PTTT 4, the

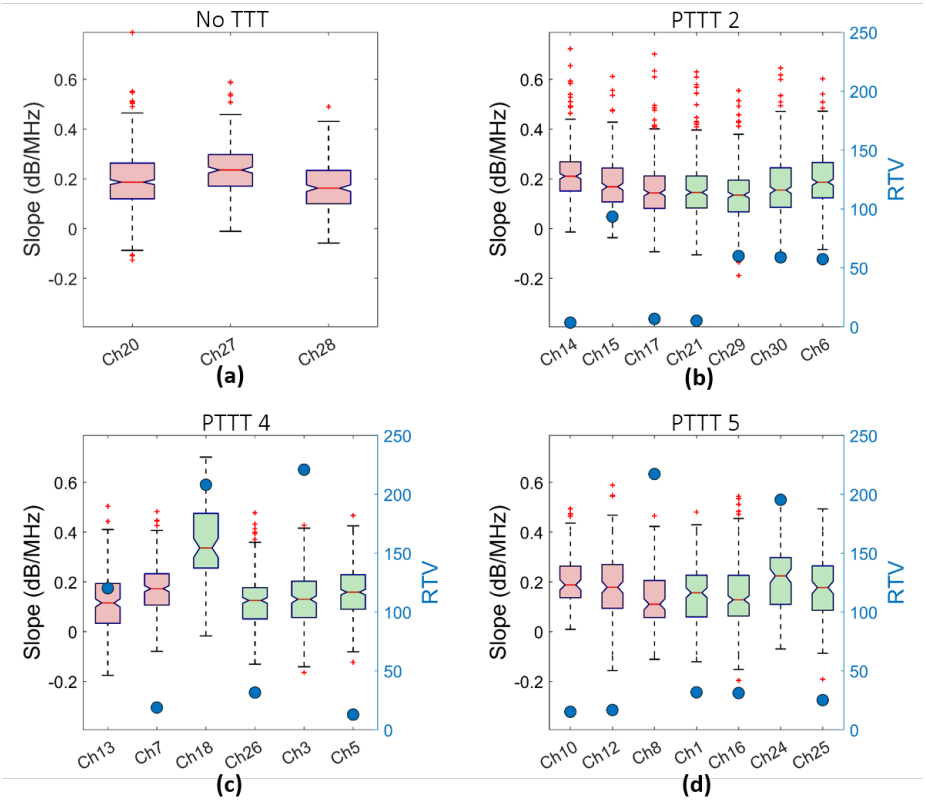

Figure 7.9: Chondrosarcomas: BSC slope per day of measurement. (a) No TTT, (b) PTTT 2, (c) PTTT 4, (d) PTTT 5. Control tumors and treated tumors are represented in red and green respectively. The boxes show the distribution of data points for each tumor. The blue dot indicates the corresponding RTV and its value can be read on the right Y-axis.

treated tumor Ch16 exhibits the lowest α_{nak} value. However, its RTV is similar to the other treated tumor. The coefficient of determination between the α_{nak} values and the RTV of the treated tumors equals $R^2 = 0.13$. No obvious difference in the α_{nak} values can be observed between the control and treated tumors for each day of measurement. Significant statistical differences in the Nakagami parameters α_{nak} are identified at the 5% level between the control and the treated tumors in PTTT 5.

The scaling parameter Ω_{nak} are shown in Figure 7.11. The control tumors with No TTT exhibit similar Ω_{nak} values as the other control tumors. A greater disparity in the median values can be observed for the treated tumors in comparison to the control tumors. The coefficient of determination between the Ω_{nak} values and the RTV of the treated tumors equals $R^2 = 0.11$. Similarly to what was observed for α_{nak}, no threshold based on the Ω_{nak} values can discriminate all the treated tumors from the control tumors for each day of measurement. Significant statistical differences in the scaling parameter Ω_{nak} are identified at the 5% level between the control and the treated tumors in PTTT 4 and PTTT 5.

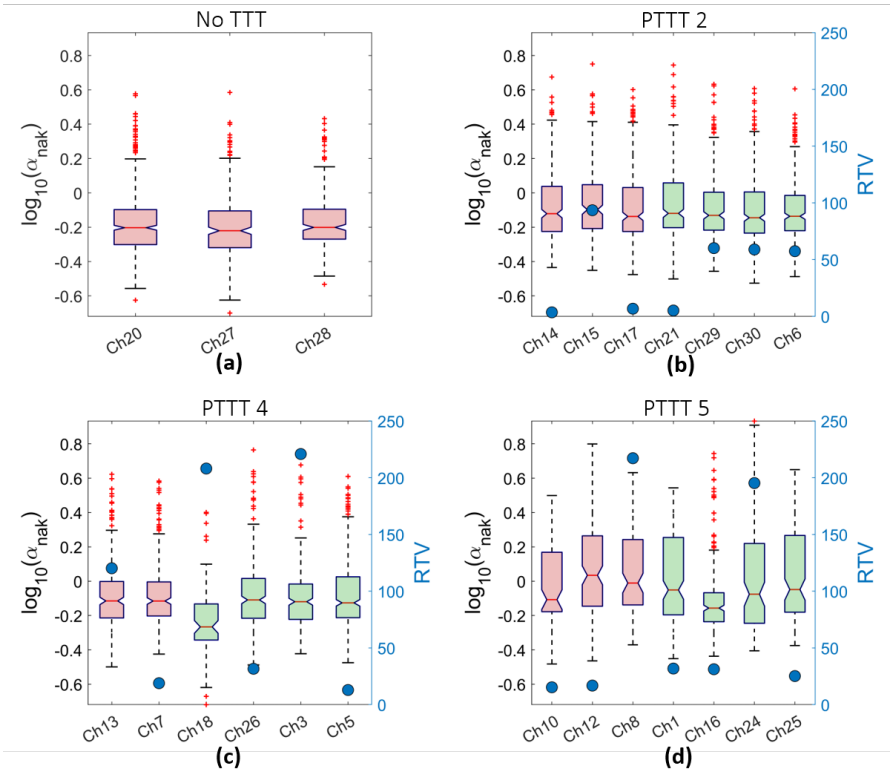

Figure 7.10: Chondrosarcomas: Nakagami parameter α_{nak}. (a) No TTT, (b) PTTT 2, (c) PTTT 4, (d) PTTT 5. Control and treated tumors are in red and green respectively

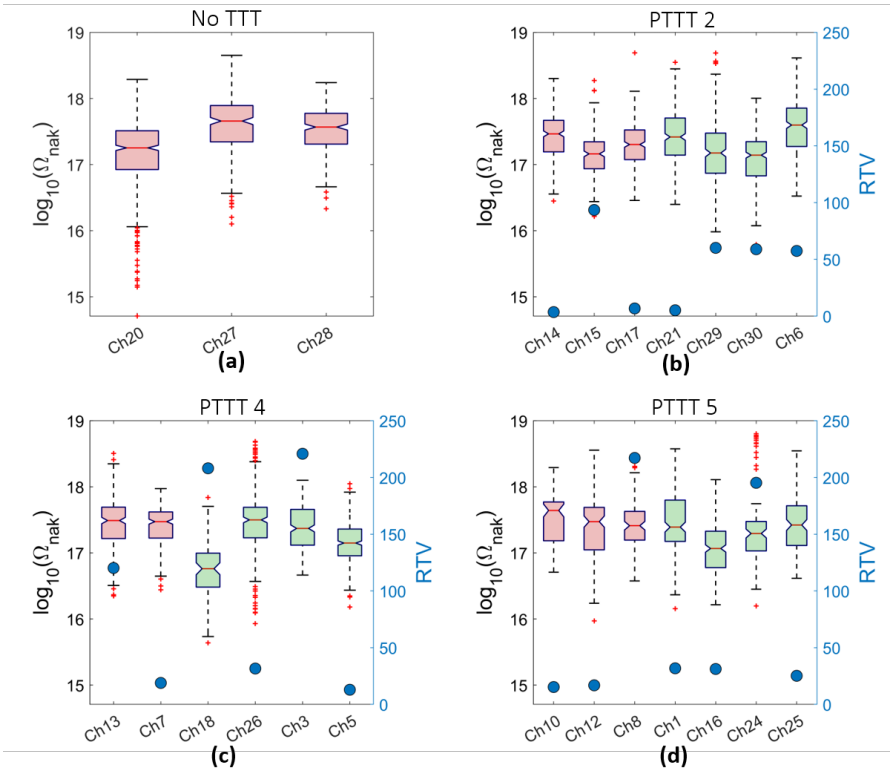

Figure 7.11: Chondrosarcomas: scaling parameter Ω_{nak}. (a) No TTT, (b) PTTT 2, (c) PTTT 4, (d) PTTT 5. Control and treated tumors are in red and green respectively.

Light EBS

Representative examples of reflectance profiles estimated at twelve different visible wavelengths from each tumor group are shown in Figure 7.12. The reflectance profiles of one control tumor is shown with colors spanning from yellow to red (550 to 700 nm) per day. The reflectance profiles of one treated tumor are also shown with colors spanning from blue to green (550 to 700 nm) per day. The reflectance profiles of tumors with No TTT exhibit the sharpest EBS peak in comparison to other days of measurements. The difference in the reflectance profiles of control and treated tumors of PTTT 2 and PTTT 5 are limited compared to PTTT 4. Indeed, the treated tumors in PTTT 4 show reflectance profiles with a faster decay and can therefore be discriminated from the control tumors.

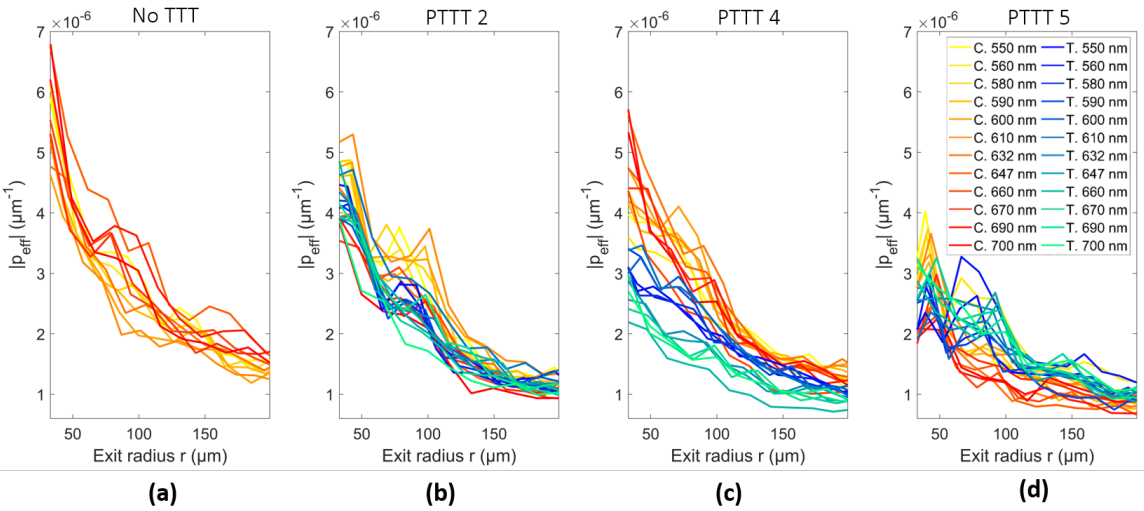

Figure 7.12: Chondrosarcoma: Illustrative examples of effective reflectance profiles in the visible range in the co-polarized channel. Only two tumors of each group per day for clarity. (a) No TTT (Ch20), (b) PTTT 2: control Ch15 (RTV = 94) versus treated Ch21 (RTV = 5). (c) PTTT 4: control Ch7 (RTV = 19) versus treated Ch3 (RTV = 221). PTTT 5: control Ch8 (RTV = 217) versus treated Ch16 (RTV = 31). The legend given in (d) applies to all graphs.

For the sake of clarity, the reflectance profiles of only one tumor of each group were shown per day of measurements. It is noteworthy that the reflectance profiles can be integrated over the exit radius r to obtain the integrated effective reflectance profile I_{eff} for each wavelength. The quantity I_{eff} can then be plotted as a function of the wavelength (Figure 7.13). The tumors with No TTT exhibit irregular EBS spectra, making their analysis challenging. The EBS spectra of the treated tumors in PTTT 4 show similar trends and are lower than the control tumors. The treated tumors exhibit similar shapes despite the important difference in their RTV (13 vs 221 for Ch5 and Ch3 respectively). The integrated reflectance profiles in PTTT 2 and PTTT 5 show similar shapes (*i.e.* decreasing with wavelength) but the discrimination of the treated tumors from the control

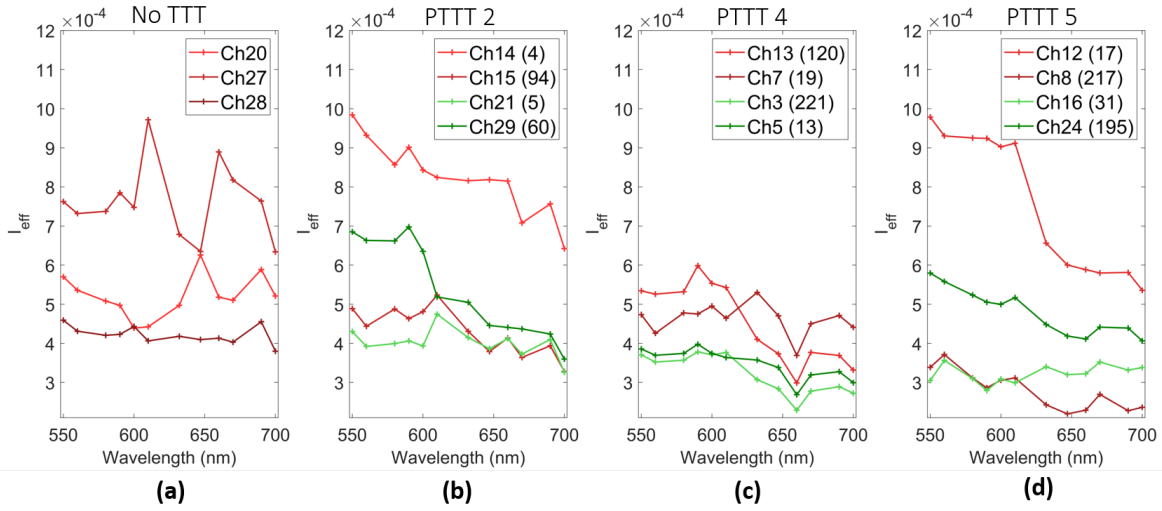

Figure 7.13: Chondrosarcoma: Integrated effective reflectance profiles per day of measurement. (a) No TTT, (b) PTTT 2, (c) PTTT 4, (d) PTTT 5. Control tumors and treated tumors are represented in red and green respectively. Optical measurements were conducted on four tumors in PTTT2, 4 and 5.

tumors based on these spectra is not straightforward.

The effective reflectance profiles at 700 nm of a control (Ch8, RTV = 217) and a treated tumor (Ch3, RTV = 221) are fitted using the Whittle-Matérn model. As a result, the three coefficients that parametrize the refractive index correlation function B_n are extracted. The characteristic length of heterogeneity of refractive index L_n is found equal to L_n = 0.6 µm and L_n = 1.4 µm for the control and the treated chondrosarcoma respectively. The refractive index variance equal $\sigma_n^2 = 3.4 \times 10^{-4}$ and $\sigma_n^2 = 5.4 \times 10^{-4}$ for the control and the treated chondrosarcoma respectively. The shape parameter D equals $D = 2.5$ and $D = 2.1$ for the control and the treated chondrosarcoma respectively.

All these parameters can serve as inputs to generate representations of the variations of the refractive index. Examples of the spatial mappings of the refractive index excesses are shown in Figure 7.14 for these two tumors.

The analysis of the Whittle-Matérn parameters is brought one step further. The refractive index-related parameters are then used to compute the optical properties of the tumors. The reduced scattering coefficient $\mu_s' = 11.0$ cm^{-1} and $\mu_s' = 5.8$ cm^{-1} for the control and the treated chondrosarcoma respectively. The anisotropy coefficient is estimated at $g = 0.83$ and $g = 0.81$ for the control and the treated chondrosarcoma respectively.

Light scattering Spectroscopy

The mean LSS spectra for PTTT 2, 4 and 5 are shown in Figure 7.15. LSS measurements were achieved using the tumors with No TTT following a different implementation compared to other days (no diffuser) and are therefore not directly comparable. Thus, the

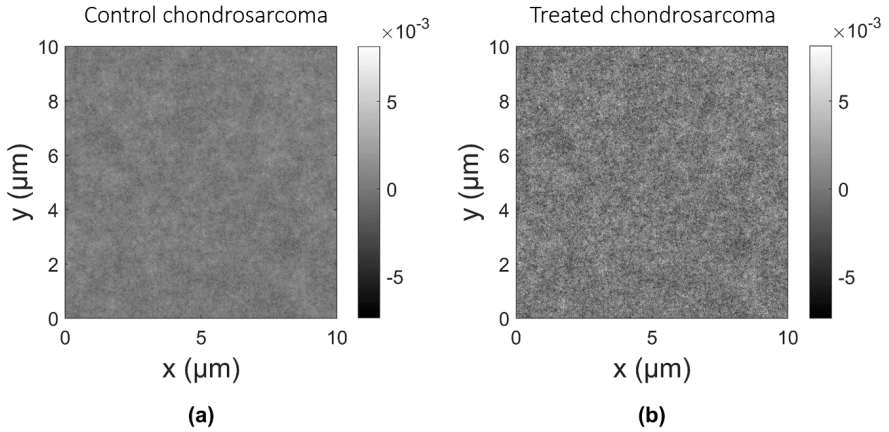

Figure 7.14: Chondrosarcoma: Examples of representation of the spatial variation of the refractive index. The gray levels represent the excess relative refractive index. (a) Control tumor (Ch8, RTV = 217), $L_n = 0.6$ µm, $\sigma_n^2 = 3.4 \times 10^{-4}$, $D = 2.5$, $\mu_s' = 11.0$ cm^{-1}, $g = 0.83$. The fitting quality is estimated by the coefficient of determination $R^2 = 0.78$ and the noise variance $\sigma_{noise}^2 = 4.5 \times 10^{-14}$ µm^{-2} . (b) Treated tumor (Ch3, RTV = 221). $L_n = 1.4$, $\sigma_n^2 = 3.4 \times 10^{-4}$, $D = 2.1$, $\mu_s' = 5.8$ cm^{-1}, $g = 0.81$. The fitting quality is estimated by the coefficient of determination $R^2 = 0.98$ and the noise variance $\sigma_{noise}^2 = 1.0 \times 10^{-14}$ µm^{-2}

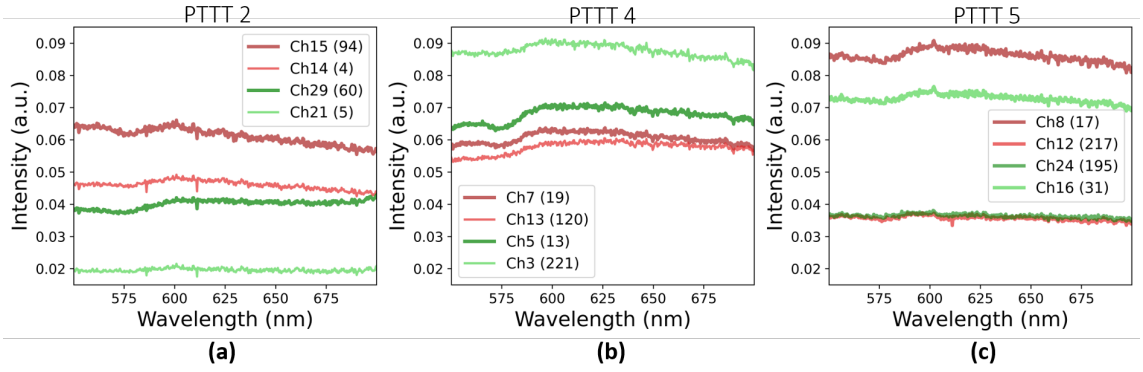

Figure 7.15: Chondrosarcoma: Light Scattering Spectra. (a) PTTT 2, (b) PTTT 4, (c) PTTT 5. Control tumors and treated tumors are represented in red and green respectively. The RTV values are given in parenthesis.

corresponding data are not shown for clarity. The control tumors in PTTT 2 and PTTT 4 exhibit limited variations compared treated tumors. In PTTT 2, LSS spectra of treated tumors are lower than control tumors. Then, they are higher in PTTT 4. Treated tumors can therefore can be distinguished from the control tumors in PTTT 2 and PTTT 4. In PTTT 5, the LSS spectrum of the treated tumor Ch24 exhibits close proximity with the control tumor Ch12. The two other tumors show a different contrast. After describing the relative magnitudes of LSS spectra, their relative shapes can be analyzed. In PTTT

2, treated tumors show a slight increase at high wavelengths while control tumors exhibit the opposite trend. In PTTT 4 and PTTT 5, the LSS spectra show similar shapes.

As the number of tumors per day is relatively low, statistical analyses and correlation between the RTV and the LSS spectra present a limited interest and were not conducted consequently.

7.3.2 Osteosarcoma

In this subsection, the results for osteosarcomas are described following the same order.

Histological analysis

The cell size distributions are shown in Figure 7.16 for each day of measurement. The orange dots indicate the volume fraction of each tumor. The corresponding value can be read on the right Y-axis. Similarly to chondrosarcomas, limited changes in the cell size distributions can be observed over the days of measurements for the treated and the control osteosarcomas.

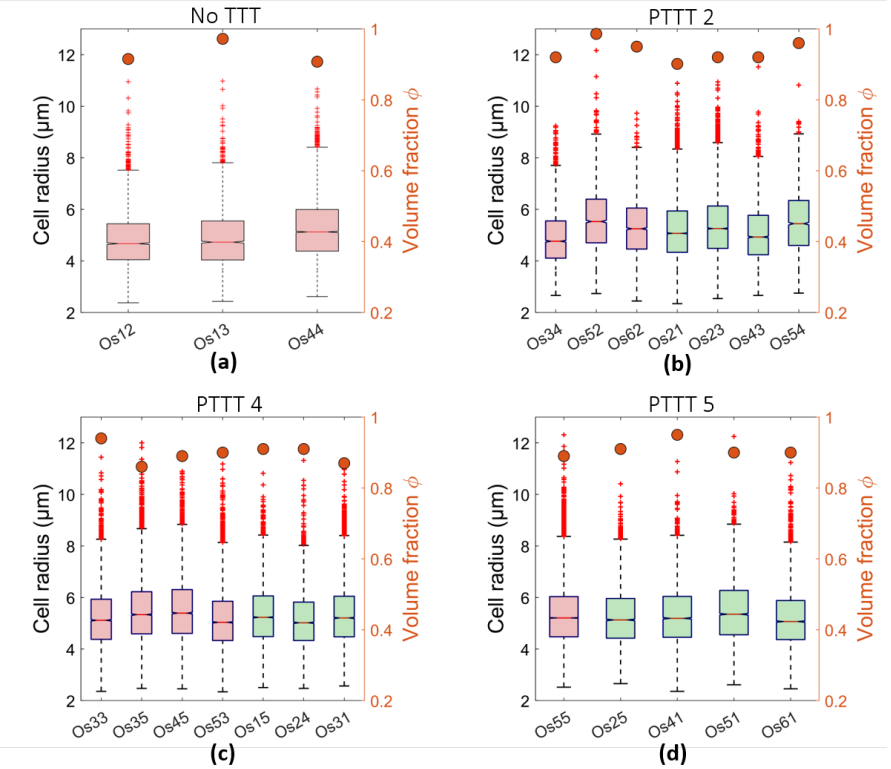

Figure 7.16: Osteosarcoma: cell size distribution. (a) No TTT, (b) PTTT 2, (c) PTTT 4, (d) PTTT 5. Control tumors and treated tumors are in red and green respectively. Orange dots show the volume fraction (right Y-axis).

Additionally, the control and the treated tumors exhibit similar nucleus sizes. The volume fractions of the treated tumors appear similar to the control tumors.

The same observations can be made for the nucleus size distributions (Figure 7.17):

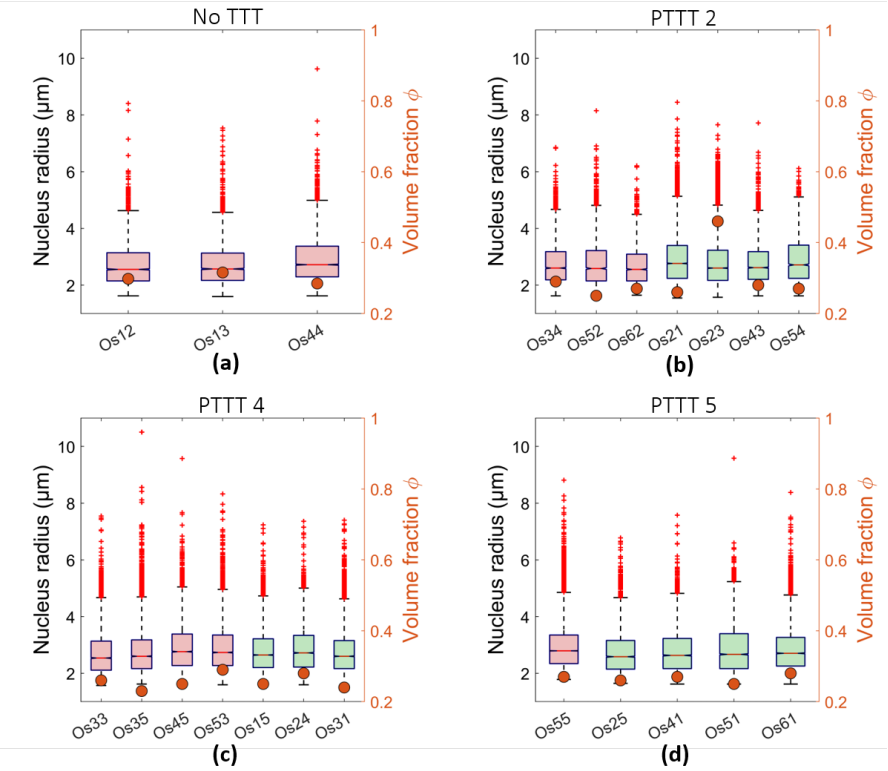

Figure 7.17: Osteosarcoma: nucleus size distribution. (a) No TTT, (b) PTTT 2, (c) PTTT 4, (d) PTTT 5. Control tumors and treated tumors are in red and green respectively. Orange dots show the volume fraction (right Y-axis).

the nucleus sizes exhibit limited changes over the days and the treated tumors cannot be discriminated from the control tumors based on the nucleus radius. The nucleus volume fractions are similar, apart in PTTT 2, where the treated tumor Ch3 exhibits a higher value compared to other tumors.

Ultrasound BSC

The mean BSCs of each osteosarcoma are shown in Figure 7.18. The RTV are given in parenthesis in the legend. The BSCs of control tumors with No TTT are higher in average than the ones observed for the other days. The BSCs of treated tumors are lower than the control tumors for PTTT 2 and PTTT 4 in average. This difference is more important in PTTT 4. The contrasts in the BSCs between the control and the treated tumors is less pronounced in PTTT 5. The analysis of the BSC trends for each day of measurement can be made more easily using the midband value and the slope (Figure 7.19 and 7.20):

Before analyzing the midband values for the osteosarcomas, let us focus on the RTV shown in Figure 7.19. The RTV values of the treated tumors are higher in average compared to the control tumors in PTTT 2 but they remain within the same order of magnitudes. The mean RTV of the treated tumors (7.2) is approximately equal to the mean RTV of control tumors (7.1). However, a greater disparity of RTV can be observed in PTTT 4 within the tumors of the same group. In PTTT 4, only one treated tumor (Os25)

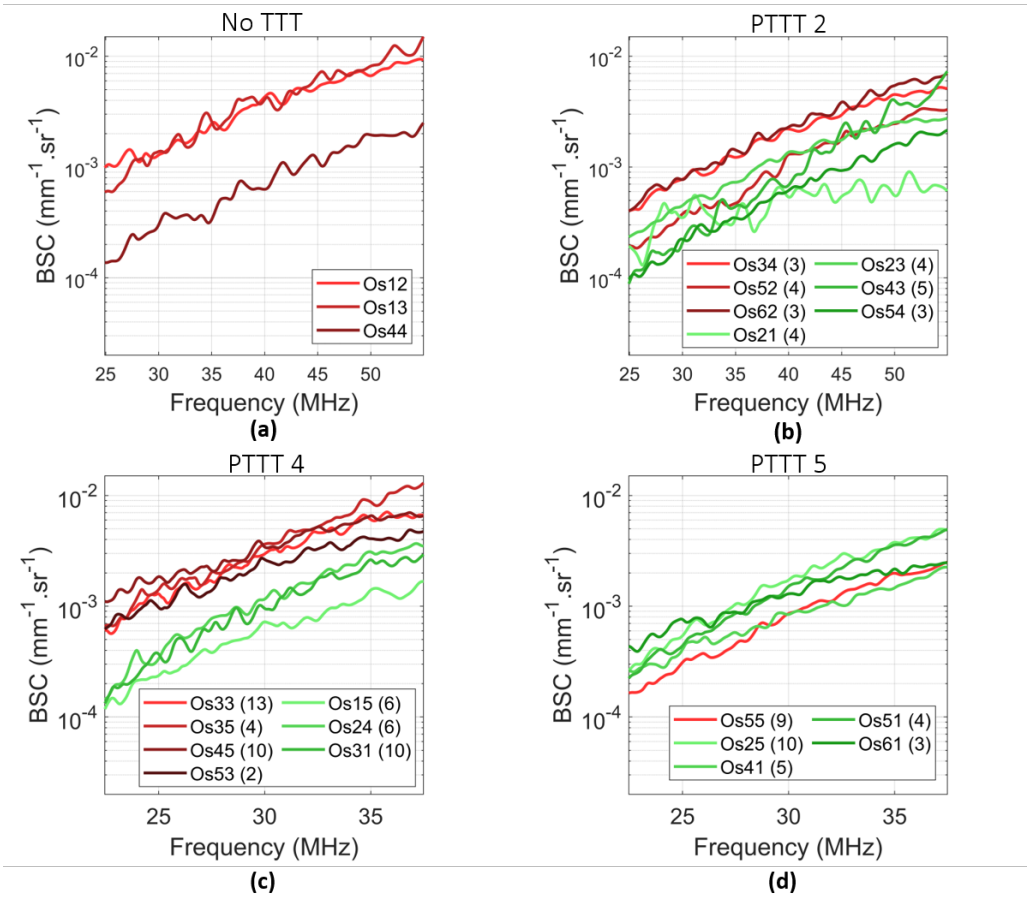

Figure 7.18: Osteosarcoma: mean BSC per tumor per day of measurements. (a) No TTT, (b) PTTT 2, (c) PTTT 4, (d) PTTT 5. Control tumors and treated tumors are represented in red and green respectively.

presents a RTV greater than the RTV of the control tumor (Ch55).

In PTTT 4, the midband values of treated tumors are lower than the control tumors. The lowest notch of the control tumor (Os53) does not overlap with the highest notch of the treated tumors (Os24). As a result, it can be concluded that their true medians do differ at the 5% level. Consequently, the treated tumors can be discriminated from the control tumors based on their midband values. The treated tumors exhibit midband medians in the range 0 - 5 dB over the last three days of measurement while the midband values of control tumors show a greater disparity, specifically in PTTT 2.

The coefficient of determination R^2 between the medians of the midband values and the RTV values of the treated tumors over the last three days of measurements (11 data points) equals $R^2 = 0.04$. A Wilcoxon rank sum test conducted at a significance level of 5% reveals statistically significant differences in the midband values between control and treated tumors in PTTT 2, PTTT 4 and PTTT 5.

The BSC slopes for each osteosarcoma are shown in Figure 7.20. The slopes estimated with No TTT are similar to the ones observed for the control tumors in the the other day of measurements. Similar distributions are reported for the control tumors over the days. The same observation can be made for the treated tumors in PTTT 4 and PTTT

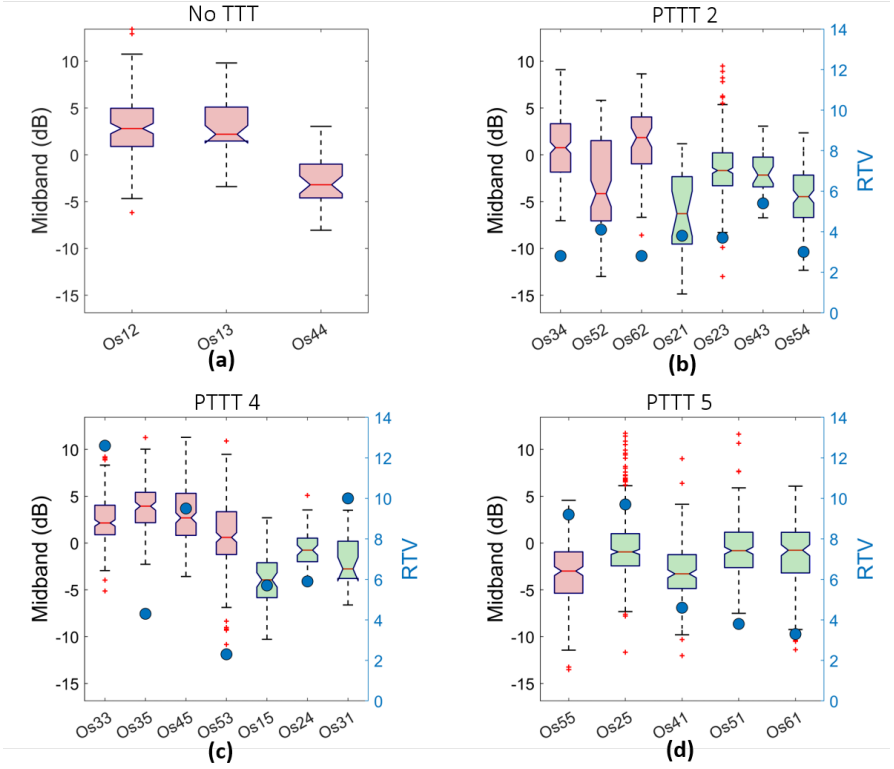

Figure 7.19: Osteosarcoma: BSC midband values. (a) No TTT, (b) PTTT 2, (c) PTTT 4, (d) PTTT 5. Control and treated tumors are in red and green respectively.

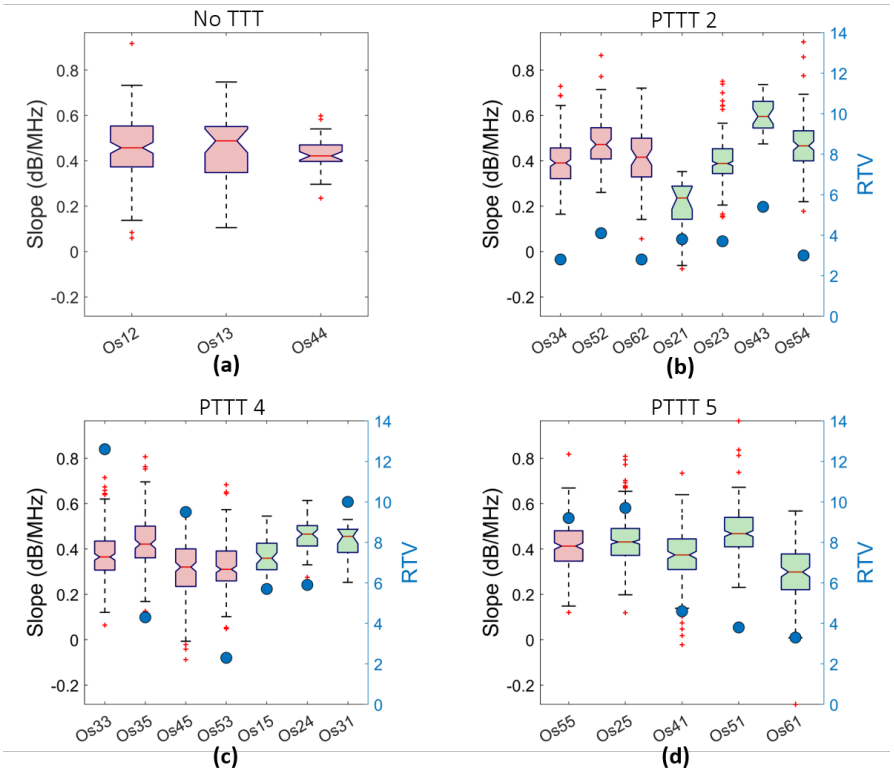

Figure 7.20: Osteosarcoma: BSC slope. (a) No TTT, (b) PTTT 2, (c) PTTT 4, (d) PTTT 5. Control and treated tumors are in red and green respectively.

5. A greater disparity appears within the treated tumors in PTTT 2. The coefficient of determination R^2 between the slope of the treated tumors and the corresponding RTV equals $R^2 = 0.08$ (11 data points). For each day of measurement. No threshold can be set to discriminate all treated tumors from the control tumor. Significant statistical differences in the slope are identified at the 5% level between the control and the treated tumors in PTTT 4.

Ultrasound envelope statistics

The distribution of the Nakagami parameters α_{nak} per osteosarcoma are shown in Figure 7.21. The values of α_{nak} of tumors with No TTT are similar compared to the control tumors in other days of measurements. Overall, limited changes in the distributions of the α_{nak} estimates can be observed over the days for each tumor group. The coefficient of determination R^2 between the α_{nak} values and the RTV of the treated tumors is less than 0.01. No threshold can discriminate the control tumors from the treated tumors for each day of measurement. Significant statistical differences in the Nakagami parameters α_{nak} are identified at the 5% level between the control and the treated tumors in PTTT 4.

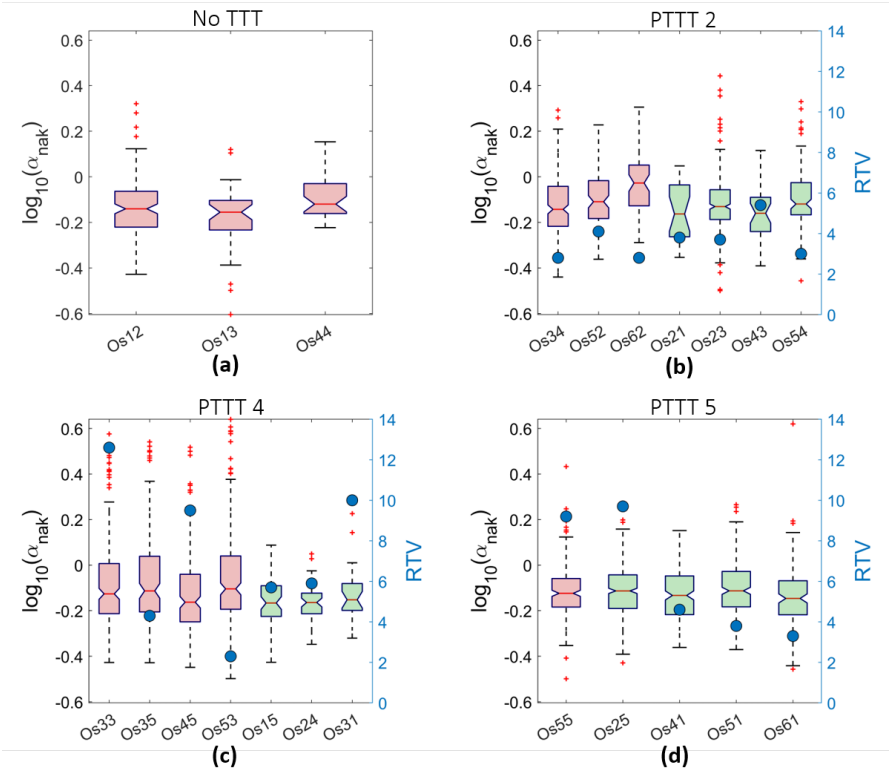

Figure 7.21: Osteosarcoma: Nakagami parameters α_{nak}. (a) No TTT, (b) PTTT 2, (c) PTTT 4, (d) PTTT 5. Control and treated tumors are in red and green respectively.

The scaling parameter Ω_{nak} are shown in Figure 7.22. The control tumors with No TTT exhibit similar Ω_{nak} values as the other control tumors. The coefficient of determination between the Ω_{nak} values and the RTV of the treated tumors equals $R^2 = 0.11$.

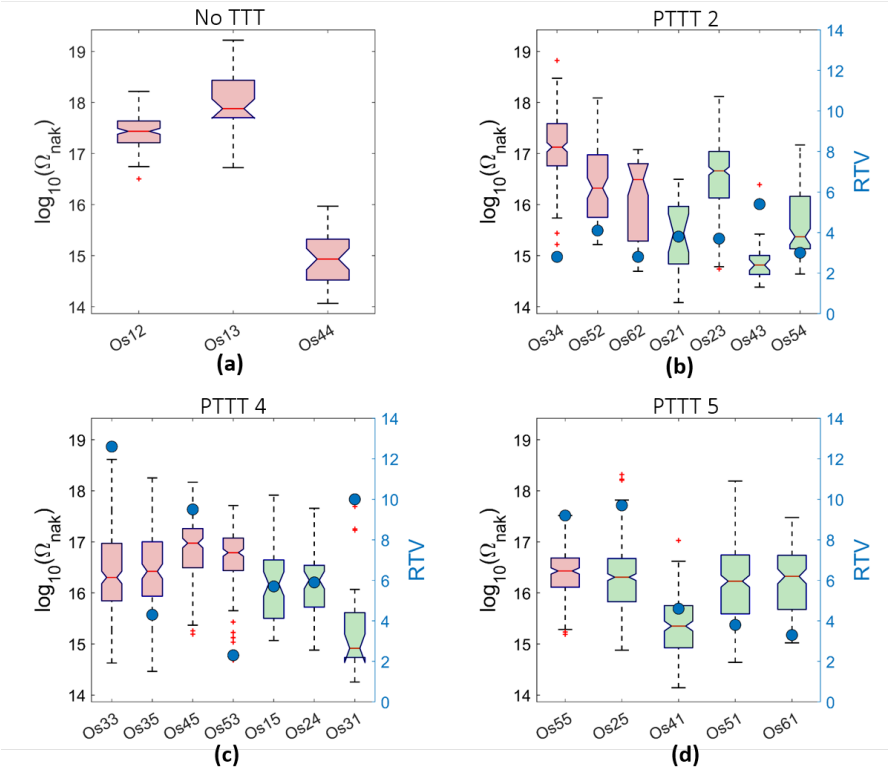

Figure 7.22: Osteosarcoma: Scaling parameters Ω_{nak}. (a) No TTT, (b) PTTT 2, (c) PTTT 4, (d) PTTT 5. Control and treated tumors are in red and green respectively.

Similarly to what was observed for α_{nak}, no threshold based on the Ω_{nak} values can discriminate all the treated tumors from the control tumors for each day of measurement. Significant statistical differences in the scaling parameter Ω_{nak} are identified at the 5% level between the control and the treated tumors in PTTT2, PTTT 4 and PTTT 5.

Light EBS

Reflectance profiles at 700 nm are shown in Figure 7.23. The reflectance profiles of control tumors with No TTT exhibit similar shapes. The same observation can be made in PTTT 2. The treated tumor Os54 is represented by a lower reflectance profile compared to the treated tumor Os21. These two tumors present similar RTV. The effective reflectance profiles at 700 nm of a control (Os42, RTV = 2) and a treated tumor (Os54, RTV = 3) are fitted using the Whittle-Matérn model. As a result, the three coefficients that parametrize the refractive index correlation function B_n are extracted. The characteristic length of heterogeneity of refractive index L_n is found equal to $L_n = 1.2$ µm and $L_n = 1.4$ µm for the control and the treated osteosarcoma respectively. The refractive index variance equals $\sigma_n^2 = 2.6 \times 10^{-4}$ and $\sigma_n^2 = 6.5 \times 10^{-4}$ for the control and the treated osteosarcoma respectively. The shape parameter D equals $D = 2.2$ and $D = 2.1$ for the control and the treated osteosarcoma respectively.

Similar to what was done for the chondrosarcomas, examples of the spatial mappings

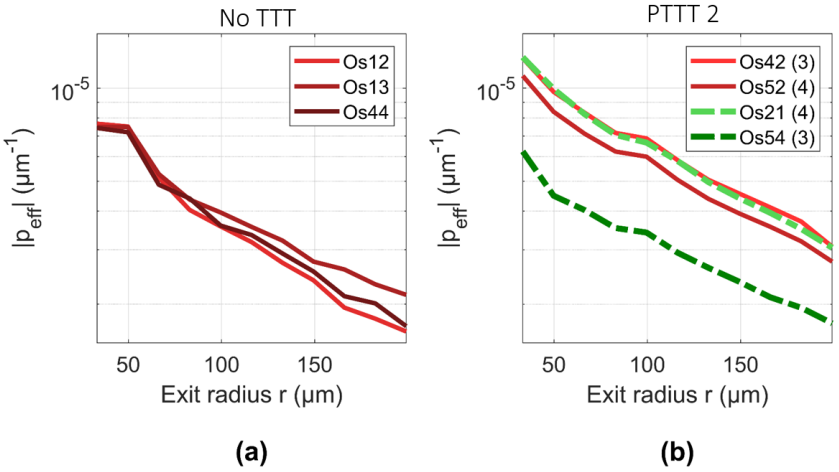

Figure 7.23: Osteosarcoma: Reflectance profiles at 700 nm in the co-polarized channel. (a) No TTT, (b) PTTT 2. The RTV are given in parenthesis in the legend.

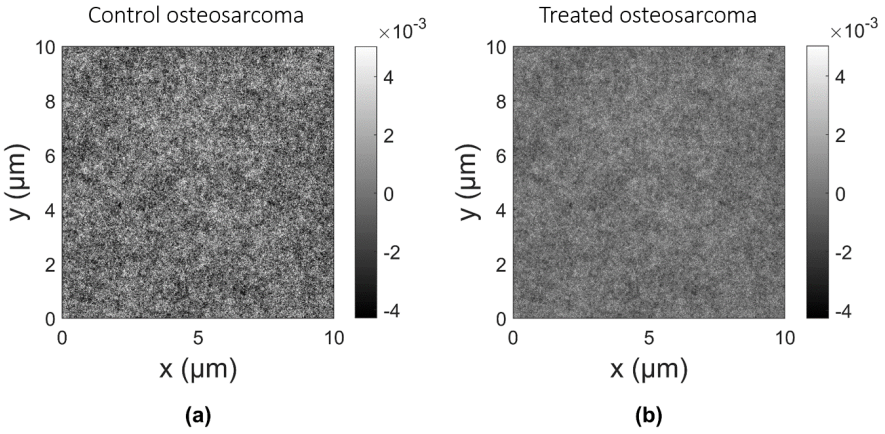

Figure 7.24: Osteosarcoma: Examples of representation of the spatial variation of the refractive index. The gray levels represent the excess relative refractive index. (a) Control tumor (Os42, RTV = 2), $L_n = 1.2$ µm, $\sigma_n^2 = 2.6 \times 10^{-4}$, $D = 2.2$, $\mu_s' = 4.0$ cm^{-1}, $g = 0.83$. The fitting quality is estimated by the coefficient of determination $R^2 = 0.97$ and the noise variance $\sigma_{noise}^2 = 1.4 \times 10^{-13}$ µm^{-2} . (b) Treated tumor (Os54, RTV = 3). $L_n = 1.4$, $\sigma_n^2 = 6.5 \times 10^{-4}$, $D = 2.1$, $\mu_s' = 6.1$ cm^{-1}, $g = 0.80$. The fitting quality is estimated by the coefficient of determination $R^2 = 0.99$ and the noise variance $\sigma_{noise}^2 = 9.1 \times 10^{-14}$ µm^{-2}

of the refractive index excesses are shown in Figure 7.24 for these two tumors.

The refractive index-related parameters are then used to compute the optical properties

of the tumors. The reduced scattering coefficient $\mu'_s = 4.0$ cm^{-1} and $\mu'_s = 6.1$ cm^{-1} for the control and the treated osteosarcoma respectively. The anisotropy coefficient is estimated at $g = 0.83$ and $g = 0.80$ for the control and the treated osteosarcoma respectively.

7.4 Discussion

In this study, BSC-related parameters, envelope parameters, EBS-related parameters and LSS spectra were measured on two types of bone tumor models. For each tumor subtype, ultrasound and optical measurements were conducted over four days of measurements on two populations: control animals with PBS injections and rodents that have received a chemotherapeutic drug. Only control tumors were probed the first day (No TTT). The treated animals had received 2 injections of anti-cancer treatment on the first day of measurement (PTTT 2), 4 injections on the second day (PTTT 4) and 5 injections on the last day (PTTT 5). This study aims to investigate the potential correlation between QUS or optical parameters with the tumor response to the administered drug. The RTV of each tumor was estimated as an indicator of the tumor response. Small RTV values may reflect a positive tumor response. Histological analyses were also conducted to measure potential changes in the cell and the nucleus sizes of the tumors during the treatment period.

The slope, the midband, the Nakagami parameter α_{nak} and the scaling parameters Ω_{nak} showed poor correlations with the RTV of the treated chondrosarcomas and osteosarcomas ($R^2 < 0.33$). Interestingly, multiple significant statistical differences were observed when comparing the estimates from independent ROIs of the control and the treated tumors. Indeed, for the chondrosarcomas, the slope and the midband values reflected notable disparities in PTTT2. In PTTT 4, the midband values and the scaling parameters Ω_{nak} indicated substantial differences. The same observation was found with the Nakagami parameter α_{nak} and the scaling parameters Ω_{nak} in PTTT 5. For the osteosarcomas, the midband values and the scaling parameters Ω_{nak} reported significant discrepancies between the control and the treated tumors in PTTT 2, 4 and 5. Additionally, the slopes and the Nakagami parameters α_{nak} reflected significant differences in PTTT 4. Consequently, the QUS estimates are sensitive to the effects of injections of chemotherapeutic drug but do not reflect the RTV.

In order to draw conclusions regarding the efficiency of QUS estimates in this therapy monitoring application, one can legitimately question the appropriate criterion for defining positive responders. Indeed, notable disparities in the RTV were observed within the control tumors of the chondrosarcomas and the osteosarcomas. Therefore, defining a threshold based on the RTV over which tumors would be considered as non-responders is not straightforward. Surprisingly, an important number of treated tumors exhibited greater RTV compared to the control tumors (*e.g.* chondrosarcomas in PTTT 2 or osteosarcomas in PTTT 4). Strictly speaking, only the treated chondrosarcoma Ch5 (RTV = 13) exhibits a lower RTV than the smallest RTV reported for a control tumor on this day

(Ch7, RTV = 19). Therefore, it could be hypothesized that most of the chondrosarcomas and osteosarcomas tumors used in this study were non-responsive to the chemotherapeutic drug.

The chondrosarcomas are known for their chemoresistance [162,163]. This phenomenon can manifest over time as the ability of the tumor cells to adapt to and to survive to external factors, such as treatments. A hypothesis is that the different ultrasound and optical parameters observed could be related to this mechanism. First, figure 7.7 showed that the mean BSC of treated tumors tends to be lower than the control tumors in PTTT 2 and PTTT 4. In PTTT 5, 16 days after the first injection, this contrast is less pronounced. This phenomenon of convergence in PTTT 5 can also be observed in the reflectance profiles. In PTTT 4, the integrated reflectance profiles of treated tumors are lower than the control tumors (Figure 7.13). No clear distinction between them can be observed in PTTT 5. The LSS spectra (Figure 7.15) also showed discrepancies between these two populations in PTTT 2 and PTTT 4. One treated and one control tumor led to similar magnitudes of LSS spectra in PTTT 5. Additionally, similar shapes of LSS spectra were observed in PTTT 5. Thus, the disappearance of differences in PTTT 5 may reflect the adaptations of the treated tumors to the administered treatment, making them similar to the control tumors.

Osteosarcomas may also develop chemoresistance over time [164, 165]. Remarkably, similar observations regarding the evolution of contrasts over days between control and treated osteosarcomas can be made. Indeed, the differences between these two populations can be observed in their mean BSCs per tumor (Figure 7.18) in PTTT2. This contrast is even more pronounced in PTTT 4, and also manifests through clear separations in the midband values (Figure 7.19) and the scaling parameters Ω_{nak} (Figure 7.22). In PTTT 5, none of these ultrasound parameters allow direct discrimination of the treated tumors from the control osteosarcomas. Once again, the cellular and molecular mechanisms of chemoresistance may be reflected through a convergence of the scattering parameters over time.

In summary, the RTV of the treated chondrosarcomas and the osteosarcomas show that approximately all tumors could be considered as non-responders. Several scattering parameters appeared sensitive to the effects of injections of treatment during the first days of treatment. Convergences were then observed between treated and control tumors after the final treatment. Consequently, scattering parameters may have reflected the mechanism of chemotherapy resistance. To confirm this hypothesis, RNA sequencing is currently conducted on the tumor genetic materials. This procedure will quantify the expression of chemoresistance genes within each tumor. No conclusion can be made regarding the efficiency of our bimodal approach to detect non-responsive tumors.

7.4.1 Physical interpretation

A physical interpretation of the ultrasound and optical parameters can be made thanks to the histological analyses. The cell and the nucleus size distributions and the volume fractions exhibit limited changes over the days. Additionally, the visual aspects of the histological slices do not show specific evolution in the spatial arrangement of cells either. Thus, it can be assumed that the scatterer size and organization may exhibit limited changes. Consequently, the notable differences between the treated and the control tumors could originate from the variations in the relative impedance contrasts γ_z in ultrasound. The difference in the scattering amplitude between the treated and the control tumors is consistent with the variations reported in the scaling parameter Ω_{nak}, which represents the mean backscattered intensity, specifically for the osteosarcomas. In optics, variations in the refractive indices may contribute to the changes observed in the magnitude of the LSS spectra as well as in the reflectance profiles between treated and control tumors. Examples of spatial mappings of the excesses refractive index are given for control and treated tumors (Figure 7.14 and 7.24) under the approximation of random media. To confirm this hypothesis concerning the scattering amplitude in ultrasound and in optics, additional histological analyses are in progress with collagen markers to study the extracellular matrix composition of control and treated tumors.

The similarities between the shape of the LSS spectra of treated tumors with control tumors obtained for PTTT 4 and 5 are consistent with the histological analyses. Indeed, LSS aims to extract the scatterer diameters based on the "slow" oscillations of the LSS spectra (*c.f.* section 6.2.4). Since no difference in the cell and the nucleus size was reported for the chondrosarcomas over the days, it is coherent to observe limited contrasts in the corresponding LSS spectra. However, the LSS spectra of the treated tumors in PTTT 2 do differ from the control tumors. The inversion procedure described in the preceding chapter has the potential to translate this distinction into variations in the scatterer size distribution. Since the histological analyses did not reveal significant differences in the cell and nucleus size distributions between the tumors, we did not investigate the inversions of LSS spectra as a priority.

Necrotic areas were observed in the center (*i.e.* several millimeters deep) of some tumors on histological slices. Cell death can affect the scattering parameters and its effects could have been used to interpret the observed differences between the estimates. However, given that both the ultrasound and the optical techniques probed the shallow surface of the tumor, we can reasonably assume that necrosis had a minimal impact.

7.4.2 Optical measurements

The EBS and the LSS measurements were conducted on a limited number of tumors, making the correlation of the resulting optical parameters with the RTV challenging to establish in the case of chondrosarcomas (Figure 7.13 and 7.23). Indeed, the inversions of the reflectance profile using the Whittle-Matérn model were conducted on the measured

reflectance profile at 700 nm on one control and one treated tumor for each subtype. This procedure resulted in the extraction of the refractive-index related parameters (L_n, σ_n^2 and D). These results should be considered as illustrative examples of the extreme sensitivity of EBS to estimate the tissue properties at small length scales. The inversions of other reflectance profiles mostly led to poor fitting qualities and/or irrelevant optical properties that differed by several orders of magnitude from those typically found in biological tissues [146]. The optimization parameters of the inversion algorithm (*e.g.* seed values, cost functions and termination tolerances) may impact the inversion results. Their effects deserve further investigation.

7.4.3 Limitations

In this study, the use of the RTV as a reference to decide whether a tumor is responsive or not is questionable for chondrosarcoma. Indeed, the evolution of the tumor size may not reflect the positive response of chondrosarcomas to chemotherapeutic drugs. This sarcoma subtype is characterized by the production of a cartilage matrix that remains after cell death. Thus, a tumor may exhibit an increasing cell death, which is a good prognostic at the early stage of chemotherapy, and limited changes in its size. As a result, the RTV can remain relatively high despite a positive response from the tumor. To address this problem, other response indicators could be observed. Indeed, future studies could also analyze the expression of chemoresistance genes in the tumors to serve as references. Other perspectives are suggested in the following paragraph.

The osteosarcoma Os55 is the only control tumor in PTTT 5. Other control animals did not survive as long as Os55. Therefore, the statistical tests of QUS parameters between the treated tumors and this only tumor should be considered with caution.

7.4.4 Perspectives

Future studies could be conducted *in vivo* to study the prediction of treatment outcome. In this case, ultrasound could be performed day after day to investigate the potential correlation between scattering parameters and the responsive tumors. Optical measurements could also be achieved for other types of tumors that may be located at a shallow depth using fiber optics [9, 78].

To optimize the probability of analyzing non-responders along with positive responders, a similar longitudinal study could be performed with a third group composed of animals that received higher doses of cancer treatment. Thus, a control tumor group, a treated tumor group with a low dose and another one with an important dose of chemotherapeutic drug could be analyzed for each day of measurement. A low dose of anti-cancer is likely to lead to non-responders while the higher doses should lead to more responsive tumors.

7.4.5 Conclusion

To conclude, no correlation was observed between the ultrasound and the optical scattering parameters with the RTV. However, all tumors in this study are likely to be non-responsive given their observed RTV. The BSC-related parameters, envelope parameters, EBS-related parameters and LSS spectra were sensitive to the injections of treatment. More importantly, they could have reflected the process of tumor adaptation over time. Additional analyses are in progress to confirm this hypothesis.

In this study, combining ultrasound and light provided different sources of contrast at different days of measurements (*e.g.* EBS and LSS spectra in PTTT 4 separated treated chondrosarcomas from the control tumors contrary to the corresponding QUS estimates). Thus, our bimodal approach represents a promising direction for pursuing this research, as multiplying the quantitative estimates may reflect more accurately the plurality of complex cellular mechanisms.

Chapter 8

Structural effects on ultrasound scattering: a phantom investigation

The study reported in this chapter aims to investigate the structural effects of ultrasound scattering. The physical interpretations of QUS parameters mentioned in the previous chapters were investigated and unified in the framework of a novel phantom approach.

As a visiting Ph.D. student, I had the privilege to conduct ultrasound experiments under the guidance of Jonathan Mamou, Ph.D., at the Department of Radiology, Weill Cornell Medicine, located in New York City. This collaborative research work spanned three months during the summer of 2022.

Unlike my previous contributions, this chapter focuses on ultrasound scattering and does not encompass contributions related to optics. This decision stems from logistical constraints, such as the fact that the optical bench-top experimental setup developed in Lyon was bulky and could not be relocated.

8.1 Introduction

Quantitative ultrasound studies aim to characterize tissues to extract diagnostic information. Indeed, the estimated QUS parameters reflect the scatterer properties. Interestingly, certain QUS parameters can be doted of a physical meaning, such as the effective scatterer radius, under specific conditions (*e.g.* sparse media in the Spherical Gaussian model [26]). Given that the scattering structures are identified, the QUS parameters can give insight into the tissue underlying microstructure and may reveal specific pathology.

The scatterer concentration is of prime importance in the correct modeling of the backscattering signals. For instance, applying incoherent BSC models in dense media can lead to a misleading physical interpretation of the corresponding QUS parameters. Indeed when the scatterers are not randomly spatially distributed, structural effects affect the ultrasound backscattering. In structured media, both the spectral content and the envelope of the backscattered signals are impacted. The BSC is no longer the incoherent sum of the contributions of each scatterer and a structure factor should be taken into account. As a result, BSC-related parameters exhibit changes. Similarly, the envelope parameters are affected by the coherent signals that rise from any periodic spacing among the scatterers (*i.e.* structure) [42].

Most of the BSC theoretical models and envelope distributions were initially introduced to describe the scattering of media with randomly distributed scatterers. However, cells or nuclei in biological tissues can be associated with moderate to high volume fractions (typically more than 0.05). It can be assumed that the scatterer position correlation increases with their concentration [38]. Hence, to successfully characterize biological samples through QUS parameters, it is important to study to what extent their physical interpretation can hold, as the degree of structure can be important. The present work investigates the meaning of multiple QUS parameters using a tissue-mimicking phantom composed of particles that can exhibit different levels of spatial organization.

Saha et al. [42] studied the effects of different scatterer spatial organizations on the BSC and the ES. They simulated four different media, composed of identical scatterers with a decreasing spatial organization that spans from a perfect lattice structure to a random distribution. They introduced a theoretical model to simulate the BSC and the signal envelope. They restricted the study of the signal envelope to the Rayleigh and the Nakagami distributions. They concluded that the scatterer spatial organization affects the BSC linear slope, the integrated BSC and the envelope parameters. However, they did not investigate the extent to which the physical meaning of the parameters could justify the observed variations. Additionally, this study was restricted to simulations and did not include an experimental phantom validation.

Han et al. [38] carried out a cell pellet phantom study in which they isolated the spectral structural effects using dense phantoms and sparse phantoms containing the same cell lines. After estimating the incoherent BSCs and the total BSCs on each sample, they extracted the structure factors for each cell line by computing their ratio. The estimated structure factors were successfully described by their theoretical models. This study reported an experimental demonstration of the spectral effects of the scatterer spatial correlation in dense media. One could note that the structural effects resulted from the high concentrations.

In the present study, a novel experimental method to control the spatial organization of magnetic particles using a magnetic field is introduced. The variations in the BSC linear slope and intercept (Lizzi-Feleppa parameters) were investigated as the degree structure was increasing. Similarly, we analyzed the evolutions of Nakagami and Homodyned-K

envelope parameters, as they can carry a physical interpretation. The physical meanings of the QUS parameters and their concordance were investigated. To do so, QUS parameters were estimated as the magnetic field intensity was varied over time, strength and directions in three distinct experiments.

8.2 Method

8.2.1 Superparamagnetic beads

In this study, a phantom composed of superparamagnetic beads was used. The microspheres are highly monodisperse (coefficient of variation 1.1%) with a diameter of 10 µm (Sigma-Aldrich, ref. 49664) and are suspended in water with a volume fraction equal to 0.028. The particles consist of a polystyrene polymer matrix in which nanometric iron oxide particles are homogeneously incorporated ($> 20\%$), which gives them magnetic properties. The beads were assumed to be weak acoustic scatterers such as multiple scattering is negligible.

Expected bead dynamics

The magnetic beads show no specific interaction when no surrounding magnetic field is applied. However, when the beads are placed in a magnetic field $\vec{B}$, they behave like magnetic dipoles and exhibit a magnetic moment $\vec{M}$. This phenomenon is known as paramagnetism. The magnetic dipoles are then subject to a magnetic force $\vec{F}$ that can be expressed as:

$$\vec{F} = \overrightarrow{grad}(\vec{M}.\vec{B}) \tag{8.1}$$

where $\overrightarrow{grad}$ represents the gradient operator. As a result, the magnetic force $\vec{F}$ tends to align the magnetic dipoles along magnetic field lines of $\vec{B}$. A secondary induced magnetic field is then exhibited by every bead, as depicted in Figure 8.1. Consequently, the beads act as secondary magnets and could therefore be modeled as individual pairs of north and south poles. Because the north and south poles of two different beads are attracted, the beads form chains along the surrounding magnetic field lines.

The chains exhibit equidistant spacing in the direction perpendicular to the surrounding magnetic field $\vec{B}$ due to their repelling line fields. This distance is characteristic of the magnetic repulsion.

The hysteresis is the delayed response of ferromagnetic materials to changing magnetic fields. The superparamagnetic beads exhibit a limited magnetic hysteresis in comparison to paramagnetic beads. Thus, the superparamagnetic beads can find their initial magnetization state more quickly after a first aimantation compared to paramagnetic beads, which can exhibit a longer "memory". Consequently, superparamagnetic beads were chosen in order to enhance the reproducibility of the experiments over time.

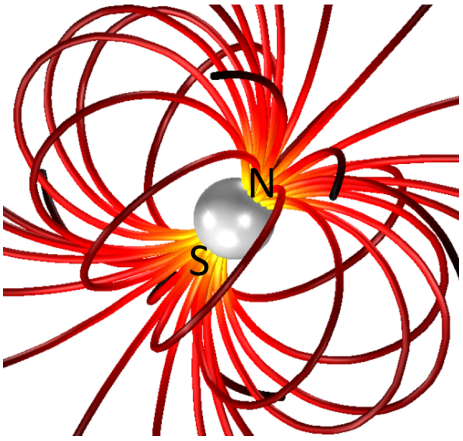

Figure 8.1: Magnetic field lines from a single magnetic bead. Blackness indicates lower intensities. N and S stand for the north and the south poles respectively. Adapted from Wittbracht et al. [166].

In summary, the beads behave like normal plastic beads when no surrounding field is applied. When a homogeneous stationary surrounding magnetic field $\vec{B}$ is present, the superparamagnetic beads are expected to arrange themselves into parallel stationary chains along the orientation of the magnetic field as depicted in Figure 8.2 (a, b). The distance of the chains in the normal direction of the magnetic field reflects a characteristic repulsive distance.

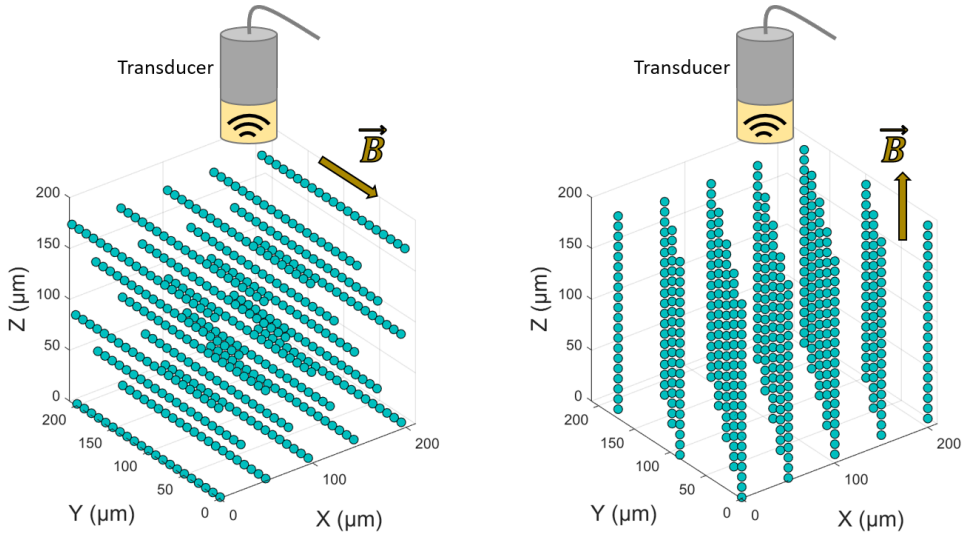

Figure 8.2: Bead alignment in the presence of a homogeneous stationary magnetic field. (a) Horizontal configuration used in the horizontal time and the horizontal steady-state experiment. (b) Vertical configuration used in the vertical steady time experiment. For each configuration, the ultrasound transducer and its agar-gel block were depicted (not on scale) to clarify the directions.

Light microscopy measurements

Light microscopy measurements were achieved to verify the theoretical bead dynamics mentioned in the previous paragraph. To do so, droplets of the phantom solution were put on glass slides. Firstly, the bead dynamic was observed over time under a microscope when the magnetic field intensity instantaneously increases from 0 mT to 4 mT. To create a homogeneous horizontal stationary magnetic field, two neodymium block magnets (N52) of dimension 40 x 40 x 20 mm were manually quickly placed across the glass slide at $t = 3$ s, where t represents the time. The distance between the two permanent magnets was 19.6 cm and was set such that the magnetic field intensity at the droplet location equals 4 mT. The spacing between the magnets was measured with a caliper. The intensity was checked with a teslameter (Naroote). A CCD camera captured the bead dynamics over 9 seconds. Secondly, the CCD camera captured snapshots of droplets of the phantom solution at $t = 9$ s under a magnetic field intensity of 19 mT by reducing the magnet spacing to 15.7 cm.

8.2.2 General method

This paragraph describes the common components of the setups and the general method that were used in the three experiments.

A circular mono-element transducer (PI-50-T2, Panametrics) with a focal distance of 19 mm and an aperture of 6.3 mm scanned the phantom solution with a motorized platform. Its bandwidth spans from 11 MHz to 41 MHz with a center frequency of 26 MHz. The transducer was excited by a Panametrics 5900 pulser/receiver unit (Olympus NDT, Waltham, MA, USA) used with an energy setting of 32 µJ. The wave propagation direction was set to the vertical of the laboratory (*i.e.* Z-axis). All the following orientations mentioned in this chapter are defined relative to this reference direction. According to the formulas given in subsection 3.1.5 in Chapter II, the axial resolution R_{ax} and the lateral resolution R_{lat} were estimated to $R_{ax} = 26$ µm and $R_{lat} = 173$ µm.

To mitigate the effect of the phantom attenuation prior to the focal point of the transducer, a low-attenuating block of agar gel was placed between the transducer and the phantom solution. The agar-gel block was mostly composed of water and had an agar concentration of 0.7%. The dimension of this block was chosen to position the focal point of the transducer immediately following the interface between the agar and phantom solution.

The BSC was estimated using the reference phantom method [113] with a reference phantom composed of glass beads with a 4.5 µm diameter suspended in a gel that acoustically behaves like water. The volume fraction was equal to 0.011 and the density of the glass bead was taken equal to 2.5. The Poisson coefficient was set to 0.2 and the glass bead sound speed to 5640 m/s. The Faran model [101] is chosen to compute the theoretical reference BSC. The magnetic solution attenuation was estimated using a standard substitution method [110] in each configuration to take into account potential anisotropic effects.

In this study the probability density function of each ROI was fitted to Nakagami and Homodyned-K distributions. The scaling parameters Ω_{nak} and the Nakagami parameter α_{nak} were obtained using a maximum-likelihood estimator. The scatterer clustering parameter μ_{hk} and the ratio of the coherent to the diffuse signal k_{hk} from the Homodyned-K distribution were obtained using the XU estimator [122]. The physical interpretation of each parameter is detailed in the subsection 8.2.6.

8.2.3 Horizontal time experiment

The first experiment investigates the QUS parameter variations when the chains of beads are horizontal (*i.e.* normal to the ultrasound propagation direction, Figure 8.2, a). This experiment is referred to as the horizontal time experiment and is described in Figure 8.3. The phantom solution was gently manually stirred prior to data acquisition. In the first three seconds, the magnetic beads were randomly located, as no surrounding magnetic field was applied. To create a homogeneous horizontal stationary magnetic field, the two permanent magnets were placed across the phantom solution at $t = 3$ s, similarly to what is done in the time light microscopy experiment. The distance between the two permanent magnets was set such that the magnetic field intensity at the phantom location was equal to 4 mT.

In this experiment, the single-element transducer scanned the same phantom position along the direction of the magnetic field, therefore generating a 2D scan every second. QUS parameters were then extracted for each 2D scan from a ROI with dimensions equal to 15.6λ and 116λ in the axial and the lateral direction respectively. The width of the ROI was taken as large as the lateral displacement of the transducer to increase the robustness of the corresponding estimates, given that the sample was a phantom that could exhibit limited heterogeneities. The horizontal time experiment was repeated six times (*i.e.* 6 independent data points for each second). Between the experiments, the phantom was stirred in the absence of a surrounding magnetic field to redistribute the beads in their initial random spatial distribution. The last measurements occurred 6 seconds after the magnets were placed.

8.2.4 Horizontal steady-state experiment

The second experiment also investigates the QUS parameter variations when the chains of beads are horizontal (Figure 8.2). This experiment is referred to as the horizontal steady-state experiment and necessitates the same experimental setup as in the horizontal time experience (Figure 8.3, a). The magnets were placed across the phantom and the 1D scan along the Y-axis occurs 6 seconds after the placement of the magnets. Six magnetic field intensities were obtained by varying the spacing between the two magnets. QUS parameters were then extracted for each scan from a ROI with dimensions equal to 15.6λ and 196λ in the axial and the lateral direction respectively. This experiment was repeated 10 times (*i.e.* 10 independent data points per intensity). Similarly, the phantom solution

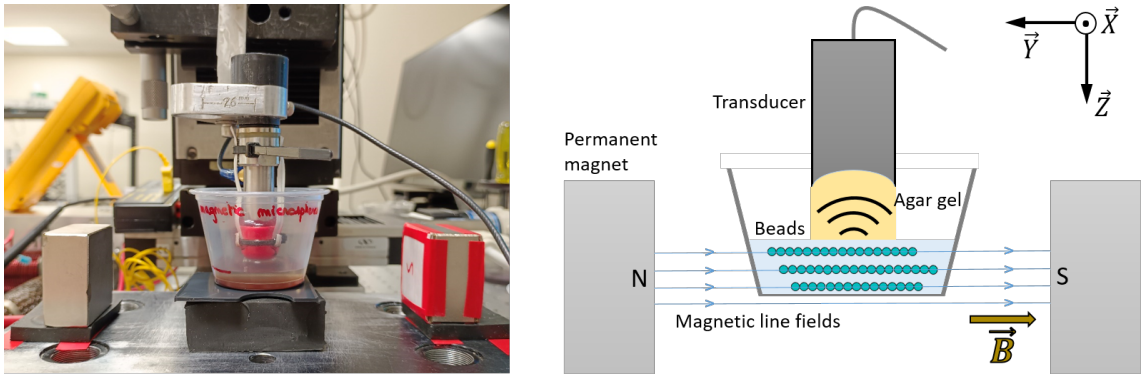

Figure 8.3: Horizontal configuration. (a) Picture of the experimental setup. (b) Explanatory scheme. N and S stand for the north and the south poles respectively. This configuration was used in the horizontal time and the horizontal steady-state experiment.

was stirred between the different acquisitions.

8.2.5 Vertical steady-state experiment

Coil

The third experiment studies the QUS parameter variations when the chains are vertical (Figure 8.2, b). This experiment is referred to as the vertical steady-state experiment and is described in Figure 8.4. The phantom solution was placed in a coil that generated a homogeneous stationary vertical magnetic field when it carried a continuous current I. The coil was specifically designed for this experiment and had 55 spires. The coil's length is 13 cm and its inner diameter is 4 cm. The coil was put in series with a 24 V power supply and an adjustable resistance that can reach a few ohms (down to 0.1 Ohm). The resistor used is suitable for high-power applications (up to 300 W). As the resistance decreases, both the current and magnetic field intensity increase. A 1D scan along the Y-axis was acquired 6 seconds after the power supply was turned on. Four different magnetic field intensities were obtained by varying the current intensity I from 7.2 A to 34.6 A. This experiment was repeated 3 times (i.e. 3 independent 1D scans per intensity). Similarly, the phantom solution was stirred between the acquisitions.

To obtain more estimates than the number of scans, QUS parameters were then extracted from ROIs that were 15.6λ long in the axial direction and 17λ long in the lateral direction with an overlapping equal to 50%. As a result, 39 data points were obtained for each magnetic field intensity for each parameter. The choice of working with smaller ROIs in the lateral direction results from the lower number of 2D scans obtained for this experiment.

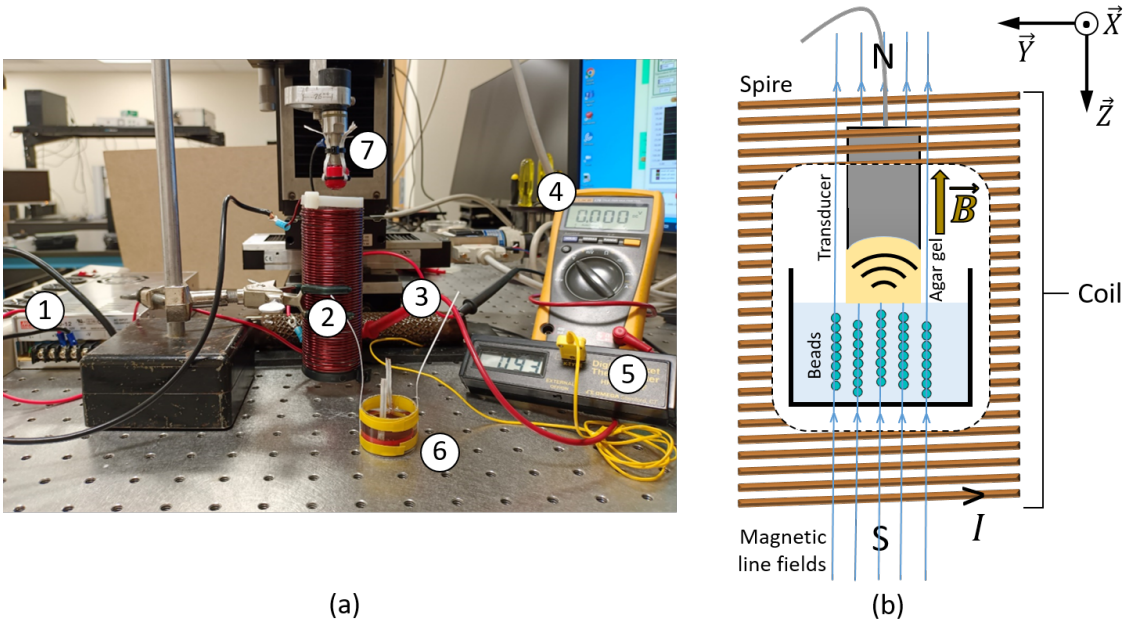

Figure 8.4: Vertical configuration. (a) Picture of the experimental setup. The power supply (1) is in series with the coil (2) and the adjustable resistor (3). A voltmeter (4) in parallel to the resistor measures the intensity I that flows through the coil. A thermometer checks the temperature to avoid overheating. The phantom solution (6) is placed inside the coil when the transducer (7) performs a 1D scan. (b) Explanatory scheme of the coil. N and S stand for the north and the south poles respectively. This configuration was used in the vertical steady-state experiment.

.

8.2.6 Physical interpretations and predictions of QUS parameters

Based on the physical meaning of QUS parameters reported in the literature, preliminary predictions regarding their responses to an increasing magnetic field can be formulated, assuming that the beads follow the theoretical dynamics mentioned in the previous subsection. The physical interpretation of each QUS parameter is revisited below in the framework of this study. Predictions of their variations within an increasing magnetic field intensity are also given.

The coherent-to-diffuse signal ratio

The k_{hk} coefficient reflects the structure in the probed media. This can be seen as the degree of the scatterer's spatial arrangement. Considering the transition of beads from a random distribution to a highly organized pattern, it is reasonable to anticipate that the coherent-to-diffuse signal ratio k_{hk} will exhibit an increase with rising magnetic field intensity.

The Nakagami parameter and the scatterer clustering parameters

The envelope-related coefficients α_{nak} and μ_{hk} can reflect the number of scatterers per resolution cell (*i.e.* the scatterer density) to a certain extent. In a simulation and a phantom study, Cristea et al. [44] reported a monotonic increase of α_{nak} and μ_{hk} as the number of scatterers per resolution cell increases up to 40 at 22 MHz. These estimates and the scatterer density were no longer correlated beyond this limit. Simulations revealed that the scatterer clustering parameters μ_{hk} were more sensitive than the Nakagami parameter α_{nak} to the scatterer number density after it reaches 10 scatterers per resolution cell. Given the bead concentration and the volume of the resolution cell reported in this study, the number of scatterers per resolution cell was estimated to equal 32 at 26 MHz. Hence, the estimations of α_{nak} and μ_{hk} are expected to correlate with the density of scatterers, with μ_{hk} exhibiting a higher sensitivity.

The slope

The slopes of the BSCs are not expected to vary with the magnetic field. Firstly, the coherent backscattering signals may not affect this parameter. Indeed, the sharp periodic peaks in the structure factor could decrease the goodness of the linear fit but they should have a limited impact on the general trend of the BSCs, making their slope potentially unaffected. Secondly, the shape of the incoherent BSC may also be constant under a varying magnetic field. Indeed, the slope can be correlated to the effective scatterer diameter (ESD) to a certain extent [28]. Given that the maximum frequency of the transducer is sufficiently high ($ka = 0.84$ at 40 MHz), the ESD could potentially represent the bead diameter which remains unchanged as the magnetic field intensity increases, making the slope unaffected as well.

The intercept and the scaling parameter

The intercept and the scaling parameter Ω_{nak}, which represents the mean backscattered intensity [167], could also reflect the incoherent BSC signals. Indeed, the coherent signal may not notably impact the overall BSC trend nor the envelope amplitude through constructive and destructive interferences. The incoherent BSCs linearly increase with the scatterer density. However, predicting the evolution of the scatterer density in the horizontal and the vertical configuration is not straightforward. Assuming that the resolution cell continues to populate or depopulate as the chains form, a monotonic trend in the intercept and Ω_{nak} could only be expected as the magnetic field intensity increases.

8.3 Results

The results of each experiment are described in this section. First, light microscopy measurements are described. Second the variations of QUS parameters versus time are presented. Then, the effect of the magnetic field intensity is analyzed in the configurations of a horizontal and a vertical magnetic field.

Light microscopy measurements

Four successive microphotographs are shown at different times in Figure 8.5: with no magnetic field (a), one second after the placement of the magnets (b), two seconds after (c), and 6 seconds after (d). The magnetic field intensity equals 4 mT for these images. At $t = 2$ s, the suspended beads are motionless and behave like normal microspheres without specific interaction. One second after the placement of the magnets, the chain formation can be observed along the direction of the magnetic field. A repulsive distance of about two times the bead diameter can be observed along the X-axis. The beads move until $t = 5$ s. At this time, longer and more distant chains appear in comparison to what can be observed at $t = 4$ s. The beads have reached their final positions or exhibit limited displacements after $t = 5$ s.

The microphotograph of magnetic beads at $t = 9$ s under a 19 mT magnetic field (Figure 8.5, e) reveals the existence of chains that are longer along the Y-axis and more distant along the X-axis in comparison to the chains observed in (d) for 4 mT at the same time.

8.3.1 Horizontal time experiment

Spectral analysis

Similar to the previous chapter, in all the boxplots, the box displays the median as its central mark, while its lower and upper boundaries represent the 25^{th} and 75^{th} percentiles, denoted q_1 and q_3 respectively. The continuous line connects the medians. The whiskers extend to the most extreme non-outlier data points. Data points are considered as outliers if they fall outside the range $[q_1 - 3/2(q_3 - q_1), q_3 + 3/2(q_3 - q_1)]$. Outliers are individually depicted using circular symbols.

Two Lizzi-Feleppa (LF) parameters were computed from each BSC estimation: the slope and the intercept (Figure 8.6 (a) and (b) respectively). The magnets are placed around the phantom solution at the time $t = 3$ s such as the magnetic field intensity equals 4 mT. The slope slightly increases when the magnets are placed. A quick decay is then observed at $t = 5$ s before stabilizing around relatively low slope values. The intercept shows a continuous increase from $t = 3$ s to $t = 6$ s and then reaches a plateau. The goodness of fit R^2 is shown in Figure 8.6 (c). The same fitting quality is reported for

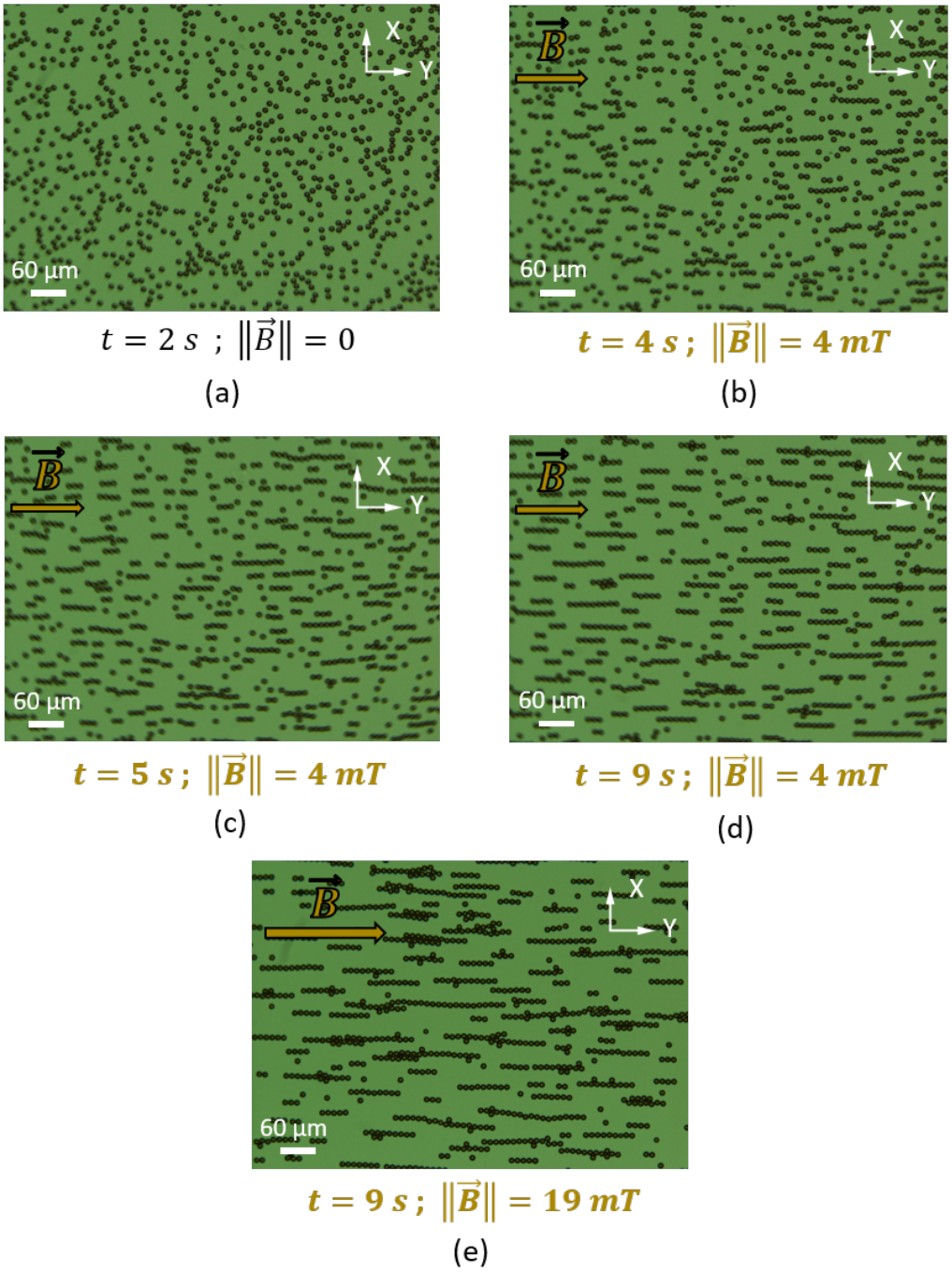

Figure 8.5: Microphotographs of superparamagnetic beads captured with no magnetic field (a), one second after the placement of the magnets (b), 2 seconds after (c) and 6 seconds after (d). The magnetic field intensity equals 4 mT. Images (a),(b), (c) and (d) were acquired successively. Image (e) represents the magnetic beads 6 seconds after the placement of the magnets with a magnetic field intensity equal to 19 mT.

each time (approximately $R^2_{LF} = 0.95$).

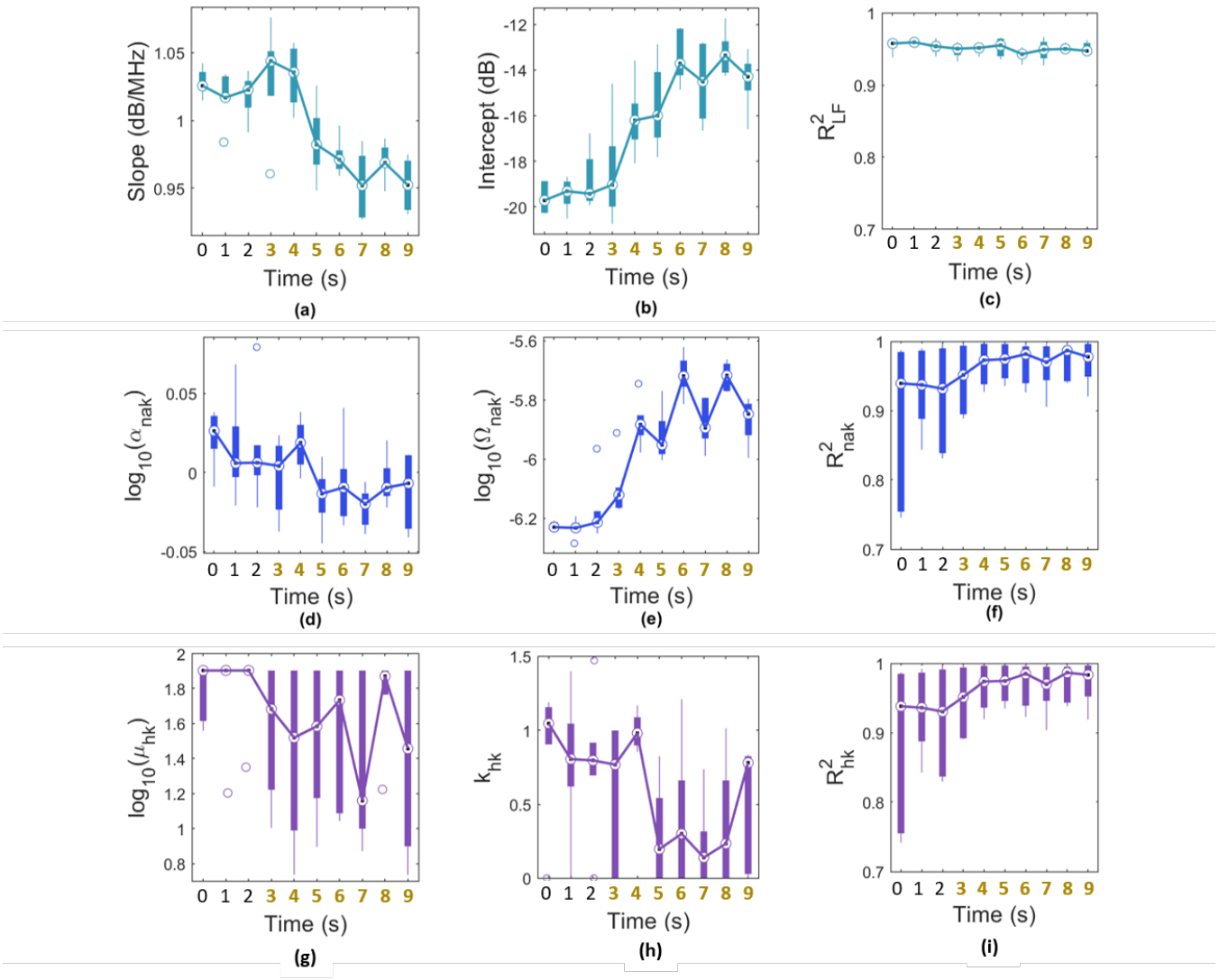

Figure 8.6: Horizontal time experiment results. The first row shows the Lizzi-Feleppa parameters versus time, the second row shows the Nakagami parameters and the third row the Homodyned-K parameters. No magnetic fields were present between $t = 0$ and $t = 2$ s. Bold time values indicate times where the magnetic field equals 4 mT. (a) BSC slope (b) BSC intercept. (c) Goodness of the BSC linear fit. (d) Nakagami parameters α_{nak}. (e) Scaling factors Ω_{nak}. (f) The goodness of fit R^2_{nak} for Nakagami distributions. (g) Scatterer clustering parameter μ_{hk}. (h) Coherent to diffuse signal ratio k_{hk}. (i) The goodness of fit R^2_{hk} for Homodyned-K distributions. The coefficients α_{nak}, Ω_{nak} and μ_{hk} underwent compression using a base-10 logarithm due to their extensive value range.

Envelope analysis

The envelope parameters are shown in the last two rows of Figure 8.6. The second row shows the Nakagami parameters and the third row displays the Homodyned-K parameters. The scaling parameters Ω_{nak}, the Nakagami parameters α_{nak} and the scatterer clustering parameter μ_{nak} underwent compression using a base-10 logarithm due to their extensive value range. The Nakagami parameters α_{nak} show a quick relative increase when the

magnets are placed around the phantom solution (Figure 8.6, d). The coefficient α_{nak} immediately decreases at $t = 5$ s and stabilizes afterward. The scaling parameter Ω_{nak} exhibits an increase when the magnets are placed (Figure 8.6, e) before reaching a plateau at $t = 5$ s.

Figure 8.6 (g) shows the variation of the scatterer clustering parameter μ_{hk}. The estimations for the first three seconds show the presence of data points that have reached the upper bound of the inversion constraint ($\mu_{hk} = 80$). The boxes at other times show extensive ranges of values, making their analysis also limited.

The coherent-to-diffuse signal-to-noise ratio k_{hk} increases when the magnets are placed around the phantom (Figure 8.6, h), followed by a fast decay at $t = 5$ s. The coefficients k_{hk} then stabilize until $t = 8$ s.

The goodness of fits of the Nakagami and the Homodyned-K distributions show similar trends (Figure 8.6, f, i). The R^2 coefficients without the magnetic fields (*i.e.* the first three seconds) exhibit lower values and a broader range in comparison to the other fits. Specifically, the very first measurements at $t = 0$ s led to the poorest quality of fits.

8.3.2 Horizontal steady-state experiment

Spectral analysis

Similarly to the previous experience, the slope and the intercept were extracted following the Lizzi-Feleppa approach on each BSC estimation (Figure 8.7 (a) and (b) respectively). The slope decreases until 15 mT and exhibits a plateau after. The intercept shows a continuous increase up to 15 mT and also presents a plateau after. The goodness of fit R^2 is shown in Figure 8.7 (c). The same fitting quality is reported for each intensity (approximately $R^2_{LF} = 0.94$).

Envelope analysis

The envelope parameters are shown in Figure 8.7. The Nakagami parameter α_{nak} decreases as $\|\vec{B}\|$ increases (Figure 8.7, d). The scaling parameter Ω_{nak} exhibits an increase for the first four magnetic field intensities (Figure 8.6, e). The coefficient Ω_{nak} reaches a plateau at 15 mT.

Figure 8.7 (g) shows the variation of the scatterer clustering parameter μ_{hk}. The estimations for the first three magnetic field intensities show the presence of data points that have reached the upper bound of the inversion constraint. A decrease is observed from after $\|\vec{B}\| = 8$ mT.

The coherent-to-diffuse signal-to-noise ratio k_{hk} slightly decreases up to 11 mT and exhibits a fast decay at 15 mT (Figure 8.7, h). The coefficient k_{hk} reaches near-zero values and stabilizes afterward.

The goodness of fits of the Nakagami and the Homodyned-K distributions show similar

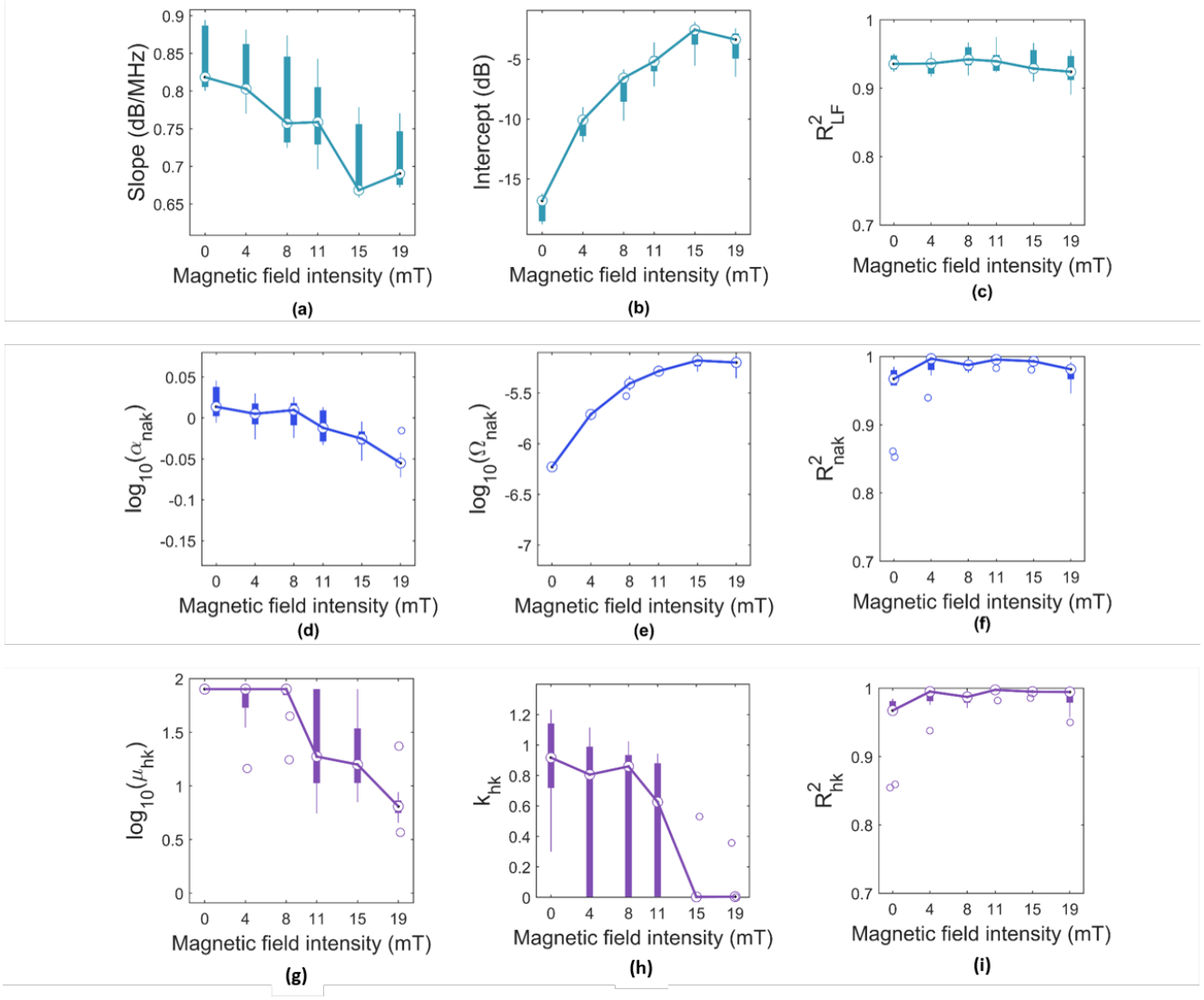

Figure 8.7: Horizontal steady-state experiment results. The first row shows the Lizzi-Feleppa parameters versus magnetic field intensity, the second row shows the Nakagami parameters and the third row the Homodyned-K parameters. (a) BSC slope (b) BSC intercept. (c) Goodness of the BSC linear fit. (d) Nakagami parameters α_{nak}. (e) Scaling factors Ω_{nak}. (f) The goodness of fit R^2_{nak} for Nakagami distributions. (g) Scatterer clustering parameter μ_{hk}. (h) Coherent to diffuse signal ratio k_{hk}. (i) The goodness of fit R^2_{hk} for Homodyned-K distributions. The coefficients α_{nak}, Ω_{nak} and μ_{hk} underwent compression using a base-10 logarithm due to their extensive value range.

trends (Figure 8.7, f, i): the R^2 coefficients are about $R^2 = 0.98$.

8.3.3 Vertical steady-state experiment

Spectral analysis

The slope and the intercept were extracted following the same procedure as in the previous experiences (Figure 8.8 (a) and (b) respectively). The slope increases with the

magnetic field intensity except for $\|\vec{B}\| = 8$ mT, where a drop can be observed. The intercept decreases except for $\|\vec{B}\| = 8$ mT. The goodness of fit R^2 is shown in Figure 8.8 (c). The R^2_{LF} coefficients for $\|\vec{B}\| = 8$ mT exhibit lower values in comparison to the other fits (about $R^2_{LF} = 0.86$ versus $R^2_{LF} = 0.92$).

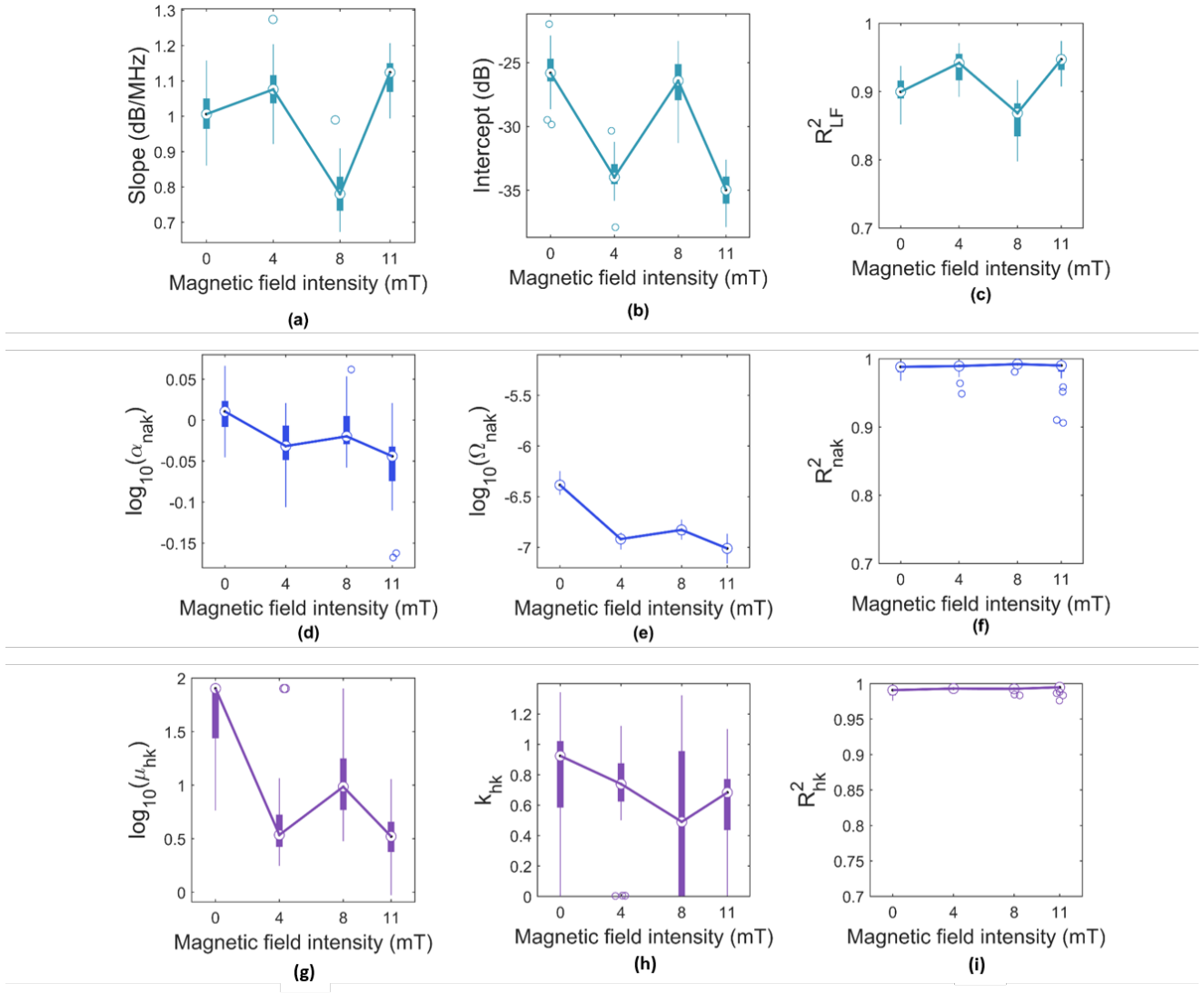

Figure 8.8: Vertical steady-state experiment results. The first row shows the Lizzi-Feleppa parameters versus magnetic field intensity, the second row shows the Nakagami parameters and the third row the Homodyned-K parameters. (a) BSC slope (b) BSC intercept. (c) Goodness of the BSC linear fit. (d) Nakagami parameters α_{nak}. (e) Scaling factors Ω_{nak}. (f) The goodness of fit R^2_{nak} for Nakagami distributions. (g) Scatterer clustering parameter μ_{hk}. (h) Coherent to diffuse signal ratio k_{hk}. (i) The goodness of fit R^2_{hk} for Homodyned-K distributions. The coefficients α_{nak}, Ω_{nak} and μ_{hk} underwent compression using a base-10 logarithm due to their extensive value range.

Envelope analysis

The envelope parameters are shown in Figure 8.8. The Nakagami parameter α_{nak} tends to decrease with the vertical magnetic field intensity (Figure 8.8, d). The scaling parameter Ω_{nak} exhibits a decrease as $\|\vec{B}\|$ increases except for = 8 mT (Figure 8.8, e).

Figure 8.8 (g) shows the variation of the scatterer clustering parameter μ_{hk}. The estimations with no magnetic field show the presence of data points that have reached the upper bound of the inversion constraint. The same trends as described for the Nakagami parameter α_{nak} can be observed. However, the relative variations between estimates are greater in this case. The coherent-to-diffuse ratio k_{hk} shows a broad range of values for each magnitude of the vector field $\|\vec{B}\|$ (Figure 8.8, g). As a result, no clear trend can be identified.

The goodness of fits of the Nakagami and the Homodyned-K distributions show similar trends (Figure 8.8, f, i) and approximately equal $R^2 = 0.99$.

8.4 Discussion

This study aims to investigate and combine the physical interpretations of QUS parameters experimentally by introducing a new phantom method. This approach takes benefits from the spatial arrangement of superparamagnetic beads when a surrounding magnetic field is applied to isolate the effects of the coherent scattering signals.

To do so, BSC-related and envelope parameters were estimated in a phantom solution composed of superparamagnetic beads in different magnetic field configurations. The magnetic field intensity was varied over time, strength and orientation in three distinct experiments.

Firstly, in the horizontal time experiment, the magnetic field was horizontal (Y-axis) and induced by the placement of two solid magnets across the phantom solution. The beads were instantaneously exposed to a 4 mT magnetic field. The orientation of the chains was normal to the ultrasound wave propagation (Z-axis). Secondly, the horizontal steady-state experiment also studied the QUS parameter variations in a horizontal magnetic field. This experiment probed the steady state of the horizontally aligned beads for different magnetic field intensities. Thirdly, in the vertical steady-state experiment, the phantom was placed in a vertical coil that generated a magnetic field. The magnetic field was parallel to the ultrasound wave propagation. This experiment probed the steady state of the vertically aligned beads for different magnetic field intensities.

8.4.1 Actual beads dynamics and QUS parameter variations

The observed bead dynamics and the QUS estimate variations are related to previous predictions (subsection 8.2.6). The actual bead dynamics and the physical meaning of each parameter are discussed in the light of the three experiments.

Bead dynamics

The microphotographs captured at different times revealed the existence of a 2-second transitional regime when the beads are instantaneously exposed to a magnetic field. In this first regime, the beads are moving and organizing themselves into chains. Then, the establishment of a steady state was observed, characterized by nearly immobile beads. In this permanent state, the spatial pattern drawn by the beads does not correspond to the ideal long equidistant chains that were initially expected since discontinuous chains of variable length appear.

The coherent-to-diffuse ratio

The coherent-to-diffuse ratio k_{hk} shows an increase during the transitional regime in the horizontal time experiment (Figure 8.6, h), probably reflecting the increasing degree of structure inside the phantom solution. In the scalar approximation where the scattering is restricted to the Z-axis, the coherent signal could emanate from the periodicity of the spatial positions of the short chains, resulting from a regular repulsive distance. Interestingly, this hypothesis is supported by the microphotograph at $t = 4$ s (Figure 8.5, b) where repulsive distances about two times the bead diameter can be observed. As the beads transition into the steady state, a decrease in the coherent-to-diffuse ratio k_{hk} was reported. To explain this phenomenon, a hypothesis is formulated below, in the light of the horizontal steady-state experiment.

In the horizontal steady state experiment, the coherent-to-diffuse ratio k_{hk} exhibit a slight decrease as the magnetic field increases and show a striking drop to near-zero values after 15 mT (Figure 8.7, h). This could be explained by the chain depopulation for a given resolution cell. Indeed, in a 2D approximation, the resolution cells is a rectangle that is about 26 µm along the Z axis, and 173 µm along the lateral direction. In the experiment of the QUS estimates varying over time and horizontal magnetic intensity, the chains are horizontal. Thus, a given resolution cell could encompass a single chain at maximum if the repulsive distance is greater than 26 µm (Figure 8.9, a). Interestingly, the steady-state microphotograph at 19 mT (Figure 8.5, e) supports this hypothesis by showing repulsive distances higher than 26 µm. As a result, in a scalar approximation where the scattering is strictly limited to occur along the Z axis, the large scatterers exhibit the same spatial positions along the Z axis and are therefore unable to generate interferences because of periodic spacings in this direction. In brief, only incoherent backscattering signals could emanate from an isolated horizontal chain in this configuration. Consequently, the coherent-to-diffuse ratio k_{hk} could exhibit an important decrease as the repulsive distances exceed the height of the resolution cell.

This hypothesis could also be applied to explain the steady-state decrease in k_{hk} men-

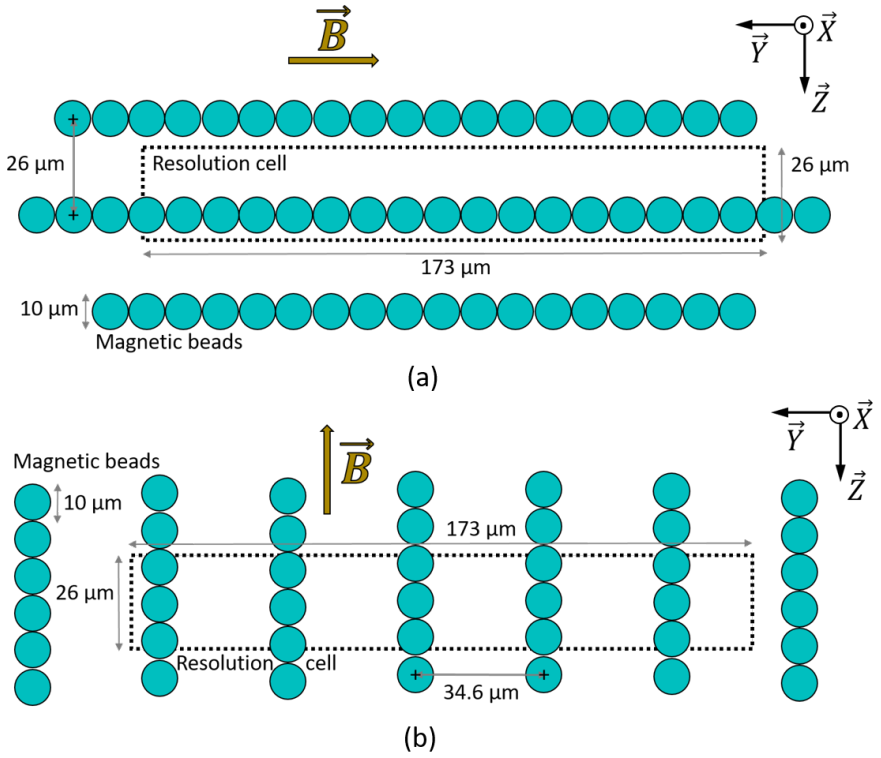

Figure 8.9: 2D geometrical considerations. (a) Horizontal configurations. As the repulsive distances exceed the height of the resolution cell, the resolution cell may encompass one chain at maximum. (b) Vertical configuration. As the distance between the chains exceeds a critical repulsive distance (173/5 = 34.6 µm), the number of beads per resolution at maximum could not be greater than the one in the horizontal configuration. In both schemes, the scaling is maintained.

tioned in the first paragraph, in the time experience. Interestingly, the repulsive distances increase as a function of the time for a given magnetic field intensity, as revealed by the microphotographs at $t = 4$ s and $t = 9$ s (Figure 8.5, b and d). As the chains depopulate the resolution cell, incoherent scattering could become predominant, thus justifying the time variations of k_{hk}.

In the vertical steady-state experiment, a broad range of k_{hk} values was observed for each magnitude of the vector field $\|\vec{B}\|$ (Figure 8.8, h). This variability in data distribution complicates the analysis of its evolution. However, no increase can be observed as it was predicted. This result could show that the scalar approximation in which the scattering is restricted to the Z-axis may be limited in this vertical configuration. Indeed, a coherent signal emanating from the periodic spacing (*i.e.* one bead diameter) of the microspheres along the Z-axis was expected. Incoherent competing scattering signals originating from other directions may attenuate this coherent component, therefore preventing a frank increase in the coherent-to-diffuse signal ratio k_{hk}.

In summary, in the horizontal configurations, the effects of regular repulsive distances could be reported in the transitional regime only. The steady states potentially showed that

the resolution cells tend to encompass individual chains, making the incoherent scattering predominant in this regime. Under these hypotheses that are supported by microphotographs, the coherent-to-diffuse signal ratio accurately reflected the spatial organization of the scatterers.

The Nakagami and the scatterer clustering parameters

In the horizontal time experiment, the Nakagami parameter α_{nak} exhibits an increase during the transitional regime (Figure 8.6 ,d), probably indicating an increasing number of scatterers per resolution cell and the early chain formations. However, the Nakagami parameter α_{nak} subsequently decreases and reaches a level lower than that observed at the beginning, suggesting a lower number of scatterers per the resolution cell. To justify this observation, we can hypothesize that the contiguous microspheres act as larger scatterers in the steady state. In other words, the scattering of beads from the same chain could be modeled by chains of grouped beads. As a result, the effective scatterer number density would decrease while the actual bead number density would remain mostly unchanged. This hypothesis could justify the observed decrease in the Nakagami parameter α_{nak}. If the previous assertion is true, this phenomenon is also expected to manifest as changes in the effective scatterer diameters (ESD). Interestingly, this hypothesis is supported by the observed slope variations, which can be correlated to the ESD. Indeed, the slope showed an important decrease as the beads transitioned into their steady state (Figure 8.6, a), probably indicating a notable change in the ESD values.

In the horizontal steady-state experiment, the Nakagami parameter α_{nak} decreases (Figure 8.7, d) with an increasing magnetic field. Similarly, the scatterer clustering parameter μ_{hk} variations follow the same trend for the three strongest magnetic intensities (Figure 8.7, g). Interestingly, this could be explained following the same hypothesis mentioned above: the effective scatterers are larger but fewer for a given resolution cell. Indeed, the microphotographs at $\|\vec{B}\| = 4$ mT and $\|\vec{B}\| = 19$ mT (Figure 8.5, d, e) show that longer chains appear when $\|\vec{B}\|$ increases. As a result, the short chains that potentially represent the smallest ESD may become less numerous, therefore increasing the ESD values. Similarly to what was observed before, the decrease in the slopes reported in the horizontal steady-state experiments may also support this assumption.

In the vertical steady state experiment, the Nakagami parameter α_{nak} and the scatterer clustering parameter μ_{hk} decrease (Figure 8.8, d, g) with an increasing magnetic field. However, the slope increases as the magnetic field increases, therefore exhibiting an opposite trend to the ones previously observed. Since we assumed that the previous decreases in slope values reflected an increase in the ESD values, the slight increase reported here cannot support the same conclusion regarding the ESD values. Thus, the hypothesis of larger but fewer scatterers per resolution cell cannot be made here. Alternatively, this phenomenon could be explained by the scatterer (*i.e.* bead) depopulation within a given resolution cell due to the repulsive distances between the chains. In this

experiment, a given resolution cell "sees" fragments (*i.e.* 3 magnetic beads at maximum) of parallel vertical chains, as opposed to the horizontal configurations, where a resolution cell can encompass longer horizontal chains (17 magnetic beads at maximum). Figure 8.9 (b) illustrates these geometrical considerations in a 2D approximation. Given that 3 beads per chain are included in the resolution cell, the number of beads per resolution cell at maximum cannot be greater than the one in the horizontal configuration if the distance between the chains exceeds the critical repulsive distance of $173/5 = 34.6$ µm. Indeed, $3 \times 5 = 15$ beads at maximum would be encompassed in a 2D resolution cell in the vertical configuration for this specific repulsive distance. The number of beads at maximum then decreases as the repulsive distance increases. Interestingly, the microphotograph of magnetic beads at $t = 9$ s under 4 mT magnetic field intensity (Figure 8.5, d) reveals the presence of repulsive distances higher than 30 µm. The repulsive distances are likely to increase as the magnetic field intensity increases given the higher spacings observed in the microphotograph at 19 mT (Figure 8.5, e). Thus, the critical repulsive distance may be exceeded as $\|\vec{B}\|$ exceeds 4 mT. In brief, in this vertical configuration, the scatterer depopulation due the the bead alignment may be more pronounced as the magnetic field increases above a certain threshold, in comparison to the horizontal configurations.

In summary, the beads aligned within one horizontal chain could act as larger but less numerous scatterers in comparison to individual beads randomly located. In the vertical configuration, the beads could depopulate a given resolution cell by forming distant vertical chains. Under these hypotheses supported by microphotographs and geometrical considerations, the estimated Nakagami parameters α_{nak} and the scatterer clustering parameters μ_{hk} effectively described the scatterer number density.

The intercept and the scaling parameters

In the horizontal time experiment, the observed increases in the intercepts and the scaling parameters Ω_{nak} (Figure 8.6, b, e) could potentially reflect an increase in the incoherent BSC since the coherent signals vanish in the steady state. The incoherent BSC is defined as the product of the scatterer number density with the differential backscattering cross-section σ_b. To explain the increase in the incoherent BSC, the increasing scatterer density due to contiguous beads could have been a plausible hypothesis. However, the variations in the Nakagami and the clustering parameters mentioned previously showed the opposite phenomenon. Alternatively, the increase in the incoherent BSC could be explained by the increase in the effective differential backscattering cross-section σ_b. Indeed, when the beads are aligned, the effective scatterers are likely to exhibit a strong geometrical anisotropy. Specifically, in this horizontal configuration, the effective scattering cross-sections could reflect the numerous contiguous beads from the same chain. Thus, we hypothesize that the effects of the increasing differential backscattering cross-section are predominant and overcompensate for the scatterer depopulation for a given resolution cell.

In the horizontal steady-state experiment, the intercept and the scaling parameter Ω_{nak} increase as the magnetic field intensity increases (Figure 8.7, b, e). Similarly, this phenomenon could reflect an increase in the incoherent BSC since the coherent signals vanish in the steady state. As detailed in the previous paragraph, the effective differential backscattering cross-section may be higher when the beads are horizontally aligned in comparison to when the beads are randomly located.

Interestingly, the Ω_{nak} and the intercept continuously increased as the magnetic field intensity increased. However, horizontal chains were already observed in the steady state for a low magnetic field intensity (Figure 8.5, d). Thus, the previous hypothesis may be insufficient to justify this observation. An additional mechanism could justify the continuous increase in the incoherent BSC when the beads are already aligned horizontally. To understand this phenomenon, we can hypothesize that the magnetic cohesion among the beads from the same chain could also contribute to the increases in the differential backscattering cross-section. In other words, the magnetic forces that maintain the scatterer's position in the steady state may increase the backscattering signal when the scatterer faces a disturbance (*i.e.* an incident wave). We hypothesize that this effect could manifest as an increase in the relative impedance contrast γ_z.

One should note that the increase in the effective scattering cross section due to the horizontal geometrical alignment and the increase in the effective relative impedance contrast could be concomitant. Similarly, we infer that the resulting increase in the incoherent BSC overcompensates for the scatterer depopulation in this experiment.

In the vertical steady-state experiment, the scaling parameter Ω_{nak} decreases as the magnetic field increases (Figure 8.8, e). The intercept denoted a decrease between extreme magnetic field intensity values (Figure 8.8, b). The hypothesis formulated above to justify the variations of the Nakagami parameters in the vertical configuration could be applied here. In this case, the intercept and Ω_{nak} would then reflect the decrease in the incoherent BSC and more specifically the scatterer depopulation within a given resolution cell. The increase in the effective relative impedance contrast due to the magnetic cohesion of the beads within one chain may also be present. However, this mechanism could manifest minor effects in comparison. Indeed, both the Nakagami parameters α_{nak} and the scatterer clustering parameter μ_{kh} exhibit a stronger decay at 11 mT in the vertical steady-state experiment in comparison to one observed in the horizontal steady-state experiment. This observation may suggest a more pronounced scatterer depopulation.

In summary, in the horizontal configuration, the intercept and the scaling parameters could reflect the variations in the incoherent BSC and more specifically the increase in the effective differential backscattering cross-section. The horizontal time experiment showed that the geometrical horizontal alignment of the beads may contribute to this effect while the horizontal steady-state experiment potentially revealed the existence of a magnetic cohesion that could impact the effective relative impedance contrast. The vertical steady-state experiment may have shown a stronger scatterer depopulation when the beads are aligned vertically in comparison to horizontal chains.

8.4.2 Limitations

This study presents some limitations that are discussed below:

Firstly, the microphotographs depicted the two-dimensional dynamics of the beads, as they were in motion within a droplet of solution applied to a microscope slide. As a result, the 3D bead dynamics may not have been fully captured. As an approximation, the microphotographs served as references to assume the scatterer's behavior in 3D. Thus, the QUS estimates may have reflected mechanisms that were not observed under the microscope and that could have been omitted as a result.

Secondly, the scattering was reduced to occur along the vertical axis as part of a scalar approximation in some of the physical interpretations suggested. This assumption may have oversimplified the vectorial nature of scattering, specifically in the vertical steady-state experiment where the expected coherent signal was not observed. A vectorial simulation tool could be developed to overcome these limitations.

Thirdly, the fast mechanical displacement of the mono-element transducer may have impacted the bead spatial organization and could have affected the bead scattering as a result. The beads exhibited a slow uniform vertical movement that resembles sedimentation (typically after 10 s) because the magnetic fields were not perfectly homogeneous. Therefore, the scanning speed was set to an in-between to allow gentle displacement that mitigates the effect of magnetic field heterogeneities. The use of a multi-element probe may overcome these limitations.

Fourthly, the strict applicability of the Born approximation for the superparamagnetic beads could be further investigated. For instance, the impact of potential multiple scattering effects could be assessed by repeating the estimation of QUS parameters within ROIs of increasing sizes in both axial and lateral directions. This procedure would be equivalent to varying the duration of the time gating window. If multiple scattering can be safely disregarded, the QUS estimates should exhibit minimal fluctuations. Conversely, significant variations in the QUS estimates could suggest addressing the effects of multiple scattering. However, this solution is not straightforward to implement due to the concomitant impact of acoustic attenuation over the QUS estimates. To mitigate the potential effects of multiple scattering, one approach could be to increase the mass density and the sound speed of the surrounding medium, effectively reducing the relative impedance contrast. In practice, this could be achieved by adding glycerol to the aqueous solution containing the beads. However, one could note that this may impact the dynamics of the beads due to changes in viscosity.

8.5 Conclusions

8.5.1 Conclusion

In conclusion, the Nakagami parameter and the coherent-to-diffuse signal ratio showed variations in agreement with the theoretical predictions in the transitional regime, there-

fore confirming their physical interpretation reported in the literature. The steady state of the magnetic beads revealed actual spatial patterns that differed from what was initially expected. However, hypotheses supported by reference microphotographs were formulated to describe the variations of each quantitative estimate according to their physical interpretation in the distinct configurations. One could note that the different hypotheses are concordant. Consequently, we successfully combined the physical interpretations of multiple envelope and spectral parameters by analyzing a magnetic media over time, magnetic field strength and structural orientation. The meaning of each QUS parameter was validated in the framework of this study.

8.5.2 Perspectives

Geometrical considerations involving the beads and the resolution cell also supported our understanding of the observed changes in some QUS parameters. These considerations could be confirmed by changing the transducer geometry or the center frequency to modify the geometry of the resolution cell.

To our knowledge, no quantitative ultrasound study has previously leveraged the properties of superparamagnetic beads to analyze the ultrasound coherent scattering. We believe that this work paves the way toward a novel type of phantom study. This approach could be of prime interest to validate theoretical scattering models in structured media. Additionally, it is noteworthy that the magnetic components are inexpensive and widely available (*e.g.* magnets or coil), therefore making our setup easily reproducible.

This study was limited to a uniform magnetic field. However, one could note that numerous magnetic field patterns could be achieved using different magnet configurations (c.f. Halbach arrays). As a result, a great variety of scatterer spatial organization could be obtained, therefore showing that any specific type of structure could be studied. Thus, this approach could be adapted to different applications.

Chapter 9

Conclusions

9.1 Conclusion

This thesis aimed to investigate a bimodal approach for cancer characterization. To illustrate the complementarities between ultrasound and optical techniques, we selected four promising methods associated with recent successful applications for characterizing cancerous tissues. To our knowledge, combining these techniques on the same sample had not been investigated before.

First, BSC parametrization and EBS were combined to characterize three tissue-mimicking phantoms, that were designed to obtain realistic ultrasound and optical scattering properties. This study served as a preliminary validation of the experimental protocol carried out for each method. Our bimodal approach was then applied with ES and LSS to two bone tumor types from animal models. The ultrasound and the optical signatures of each tumor subtype revealed significant differences, allowing their discrimination. The cell and the nucleus size distributions were successfully estimated for the two types of sarcomas. A follow-up study was conducted to assess the sensitivity of our bimodal approach in identifying non-responsive bone tumors during chemotherapy treatment. Certain scattering parameters appeared sensitive to the effects of drug injections. The time evolution of scattering parameters may have reflected the mechanisms of chemotherapy resistance. Finally, a new type of phantom study was introduced for analyzing the structural effects on ultrasound scattering. QUS parameters were estimated on superparamagnetic beads suspended in water by varying the magnetic field intensity over time and magnitude. This study aimed to unify the physical interpretation of ultrasound scattering parameters.

Our bimodal approach has proved its worth in:

- Applications with relative considerations. In Chapter 6, the chondrosarcoma and osteosarcoma tumors exhibited significant differences in their reflectance profiles and in their QUS parameters. These results were in line with the frank differences in the microarchitecture revealed by the histological slices. Interestingly, pronounced contrasts were also found within the two types of osteosarcoma cell lines that were used, despite their similar microstructures observed in the histological slices. In Chapter 7, multiple significant differences were identified in the QUS parameters between control and treated tumors at different times during the course of the chemotherapy treatment. Notable contrasts at other times were observed in the EBS and the LSS spectra for the chondrosarcomas. In this study, histological analyses did not reveal microarchitectural differences between the control and the treated tumors.
  Consequently, our bimodal method identified differences in the ultrasound and optical signatures in two distinct populations of samples. These results were based on quantitative estimates which do not carry a straightforward physical meaning. Thus, the absolute value of the scattering parameters was not of prime interest. Our bimodal approach has also the power to shed the light on differences between tissue samples where conventional histological examinations do not reveal specific contrast.

- Applications where absolute values matter. In Chapter 5, the tissue-mimicking phantoms were composed of microspheres of different sizes. This forward study showed good agreement with the expected theoretical scattering models and experimental data. EBS performed well for one phantom while BSC parametrization led to a better discrimination for the other two phantoms. This result paved the way for the size estimation of cellular components using biological samples through inversion procedures. In Chapter 6, the cell size and the nucleus size of chondrosarcomas were successfully estimated by the BSC theoretical models. The nucleus sizes of chondrosarcomas and osteosarcomas were successfully extracted using LSS, therefore validating and completing the size characterization provided by the ultrasound approach. The cell size distribution estimated by LSS allowed to quantify the part of cell and nucleus scattering. Interestingly, these estimations reflected the portion of the extracellular matrix in the two tumor types.

All the results reported in this thesis illustrate experimentally the complementarity of ultrasound and light scattering. Combining these modalities provided diverse sources of contrast along with physically meaningful estimates, leading to a comprehensive assessment of tissue microstructure. Therefore, we can conclude that the association of QUS and light backscattering techniques is valuable for cancer characterization. Promising results could be obtained in future studies.

9.2 Perspectives

Before reaching the clinics, the benchtop setup designed in this study would need to be integrated into a portable device, combining an ultrasound transducer and fiber optics. The probes used for photo-acoustic applications can typically integrate those two components and may present an interesting starting solution to which collection fibers and polarizers could be added for light detection. Similarly, an integrated system compatible with commercialized endoscopes would allow a broad range of applications, as what was designed by Qiu et al. [9] for conducting LSS in the esophagus. One could note that a benchtop version of the setup may still serve as a medical research tool, therefore allowing *ex vivo* studies, as discussed in the conclusion of Chapter 7.

Once a portable tool is developed, one of the most "immediate" clinical applications for our bimodal approach could be intra-operative margin assessment. In this context, the primary goal is the discrimination between healthy and cancerous tissues. Clinical trials can help validate appropriate thresholds, enabling the classification of samples based on estimated values of specific scattering parameters. Applications where relative considerations between two populations of samples need to be made are more likely to succeed compared to the ones where the absolute values of the estimates need to be accurate. This is primarily because assigning a meaningful physical interpretation to scattering parameters is a complex task that demands dedicated research efforts for each specific application.

Additionally, some general guidelines concerning the theoretical scattering models may be discussed.

The quantitative ultrasound community would greatly benefit from an open-source platform for sharing programs optimized for estimating spectral and envelope parameters. Providing these codes, along with guidelines for designing a reference phantom, is likely to foster enhanced uniformity and wider adoption.

Additionally, the use of ultrasound scattering models in structured media such as tumors should be pushed forward. Indeed, relatively few papers reported the use of the Polydisperse II structure factor [38] with a fluid-filled form factor. Yet, this model appears as one of the most realistic scattering models in ultrasound since it takes into account the scatterer size polydispersity that can be found in dense media such as tumors.

In biomedical optics, the Whittle-Matérn family of autocorrelation functions appears as a versatile model that may cover a great variety of biological tissues. A. Radosevich provided the Matlab programs to perform inversion procedures with the Whittle-Matérn model with nearly analytical speed [85, 139]. However, relatively few papers reported the use of this model for tissue diagnosis. Yet, this model can lead to a valuable representation of the probed sample through the spatial variations of its refractive index. This representation carries an interesting physical meaning that may open multiple interpretations at the biological level. Thus, this approach also deserves further investigation.

The quantitative ultrasound and the optical communities that study scattering for

tissue diagnosis are distinct and tend to evolve independently. However, the numerous analogies between light and ultrasound scattering should feed mutual interests. An example is suggested below:

The Spherical Gaussian model in ultrasound considers continuous variations of the relative impedance contrast that follow a Gaussian decay where the spheres are located. To our knowledge, other models also imply a spherical geometry but with discrete scatterers that are represented by a discontinuous variation of acoustic impedance from the surrounding medium. Given the true complexity of biological tissues and the diversity of cellular components, modeling the samples as continuous random media appears legitimate, at high ultrasound frequencies at least. By analogy with the Whittle-Matérn model in optics, one could imagine that the BSC fitting procedure with a similar model could result in three acoustic impedance-related parameters: a characteristic length of heterogeneity L_n, a variance σ_n^2 and a shape parameter D. In this case, no assumption regarding the scatterer geometry would need to be made. By employing a bimodal approach, as outlined in this thesis, the random representation of the variations of the acoustic impedance could be obtained and compared to the stochastic representation of refractive index variations.

Appendix

Appendix A

Structure factor

This appendix gives additional details related to the analytical computation of the structure factors used in the framework of BSC parametrization (*c.f.* section 3.2.3).

A.1 Monodiperse scatterers

In the case of hard monodisperse scatterers that are randomly distributed, the total correlation function $h(\vec{r}) = g(\vec{r}) - 1$ can be computed using the equations formed by the Ornstein-Zernike integral equation and the Percus-Yevick approximation [38, 39]. The structure factor can then be expressed as:

$$S(k) = \frac{1}{1 - nC(k)} \tag{A.1}$$

where $C(k)$ is the Fourier transform of the direct correlation function and can be written as:

$$C(k) = -32\pi a^3 \int_0^1 s^2 \frac{sin(4kau)}{4kau}(\alpha + \beta u + \gamma u^3)du \tag{A.2}$$

where a is the scatterer radius, ϕ the volume faction and with

$$\alpha = \frac{(1+2\phi)^2}{(1-\phi)^4}, \beta = -\frac{6\phi(1+\phi/2)^2}{(1-\phi)^4}, \gamma = \frac{\phi(1+2\phi)^2}{2(1-\phi)^4} \tag{A.3}$$

where u is the mathematical variable of integration.

A.2 Poydisperse scatterers

In the Polydisperse II model [38], the scatterers are polydisperse in both size and scattering amplitude. Given that the scatterers are hard and randomly distributed, the

corresponding structure factor can then be written:

$$S_{PII}(k) = 1 + \frac{\int_0^\infty \int_0^\infty S_i'(k) S_m'(k) H_{im}(k) D_z(x_i) D_z(x_m) dx_i dx_m}{\int_0^\infty S_m'(k) D_z(x_m) dx_m} \tag{A.4}$$

where $H_{im}(k)$ is a partial structure function given by Blum and Stell [168], D_z is the probability density function of the Γ-distribution, $S_i'(k)$ is the scattering amplitude based on the fluid-filled sphere form factor. The full expression of $S_{PII}(k)$ is given in Appendix B in Han et al. [38], who took the model from Griffith et al. [169].

Appendix B

Résumé en français

B.1 Introduction et contexte

Le développement du cancer se décline en différents stades et affecte les tissus à diverses échelles spatiales et temporelles. À un stade précoce, des altérations morphologiques induites, connues sous le nom de dysplasie, peuvent se produire à l'échelle cellulaire et nucléaire. Au fur et à mesure que le cancer progresse, les tissus malins peuvent présenter des cellules atypiques pouvant présenter une organisation spatiale anormale. À un stade ultérieur, la nécrose, ou mort cellulaire, peut être observée. Ce phénomène se manifeste par la rupture de la membrane cellulaire et la libération de débris cellulaires. Dans le cas où la chimiothérapie est choisie comme traitement, la nécrose peut être induite par l'exposition à l'agent anti-cancer. En effet, les médicaments chimiothérapeutiques ont pour objectif d'inhiber la progression du cancer. Cependant, les tumeurs peuvent ne pas répondre positivement à la chimiothérapie et peuvent ainsi développer des formes de résistances. Tous ces mécanismes liés au cancer sont sources de changements de la microstructure tissulaire, pouvant résulter de processus complexes aux échelles génétiques et moléculaires.

En milieu clinique, la caractérisation du cancer vise à identifier les traits caractéristiques du cancer mentionnés précédemment afin d'établir le diagnostic du patient. Le diagnostic initial est établi après des examens histologiques. À ce stade, la caractérisation du cancer implique la détermination du type de cancer et de ses principales caractéristiques, telles que le grade. Le grade reflète l'agressivité de la tumeur primaire et est attribué sur la base de différents critères, incluant la morphologie des cellules et de leur noyau. La justesse du diagnostic est d'une importance cruciale pour l'avenir du patient. En effet, les options de traitement sont choisies en conséquence par un panel de cliniciens. La caractérisation du cancer peut se faire à d'autres stades en utilisant des modalités d'imagerie conventionnelles, allant du dépistage du cancer à la surveillance continue de l'efficacité de la thérapie. Pour ces deux applications spécifiques, la détection précoce du cancer et la détection rapide de l'inefficacité d'un traitement sont respectivement d'une grande importance. En effet, le temps joue un rôle essentiel dans le pronostique du patient.

L'imagerie ultrasonore conventionnelle fournit principalement des informations anatomiques par le biais d'images en niveaux de gris, appelées images B-mode. Cependant, le diagnostic appuyé sur les images B-mode peut être sujet à des variations inter-observateurs et intra-observateurs. Pour améliorer la reproductibilité du diagnostic, l'utilisation d'estimations quantitatives est une solution pertinente. Les techniques d'échographie ultrasonore quantitative (QUS) visent à fournir des estimations quantifiées pouvant être utilisées à des fins de diagnostic. En effet, des informations pertinentes concernant les microstructures du tissu sous-jacent peuvent être obtenues en analysant le contenu spectral et les statistiques de l'enveloppe des signaux de radiofréquence (RF) utilisés pour générer des échographies. Ces deux approches sont appelées paramétrisation du coefficient de rétrodiffusion (BSC) et statistiques de l'enveloppe (ES). Il est intéressant de noter que la paramétrisation du BSC et ES peuvent être effectuées sur les mêmes signaux RF. Ils peuvent fournir différents paramètres de diffusion des ultrasons reflétant la microstructure des tissus. En effet, les ondes ultrasonores sont diffusées si elles subissent des variations de contraste d'impédance. Par exemple, les cellules ou les noyaux peuvent être considérés comme des diffuseurs d'ultrasons entourés respectivement de matrice extracellulaire et de cytoplasme. Le diamètre du diffuseur peut être estimé en effectuant une paramétrisation du BSC sur un échantillon de tissu par exemple. Tous les changements induits par le développement du cancer mentionnés dans le premier paragraphe peuvent avoir un impact sur les paramètres de diffusion des ultrasons.

Il est intéressant de noter que les ondes lumineuses peuvent également être diffusées si elles rencontrent des variations de l'indice de réfraction. De même, l'analyse spectrale de la lumière rétrodiffusée peut conduire à des paramètres de diffusion qui contiennent des informations sur la microstructure du tissu. La spectroscopie de rétrodiffusion augmentée (EBS) et la spectroscopie de diffusion de la lumière (LSS) sont deux techniques optiques qui peuvent être réalisées à l'aide d'un dispositif expérimental similaire afin de caractériser les tissus biologiques par des estimations quantitatives. Il est intéressant de noter que LSS peut également impliquer l'estimation du diamètre du diffuseur. Des articles récents ont fait état d'applications réussies pour la caractérisation du cancer. Les longueurs d'onde de la lumière visible sont environ cent fois plus petites que les longueurs d'onde des ultrasons utilisés pour l'imagerie médicale. Par conséquent, le processus de diffusion pourrait provenir de différentes structures cellulaires de tailles variables, étant donné les différents ordres de grandeur associés à chaque modalité. Ainsi, l'analyse des ondes ultrasonores et optiques rétrodiffusées peut fournir des informations complémentaires sur la microstructure des tissus. Cette association peut potentiellement conduire à une évaluation plus approfondie des tissus. Les travaux de recherche présentés dans cette thèse se concentrent sur une approche bimodale motivée par cette hypothèse.

La combinaison des ultrasons et de la lumière à travers la paramétrisation du BSC, ES, EBS et LSS offre de multiples avantages. En effet, l'association résultante peut rester: relativement peu invasive (comparé à la biopsie), non-ionisante (lumière visible), point-of-care (les composants nécessaires peuvent être intégrés dans un chariot), relativement peu coûteux (par rapport à certains outils d'imagerie conventionnels tels que l'imagerie par résonance magnétique ou la tomodensitométrie), temps réel (compatibles avec les applications intra-opératoires)

Étant donné que les mécanismes internes de nos méthodes sondent les altérations microstructurelles qui sont des caractéristiques des tissus cancéreux, notre approche bimodale

pourrait potentiellement être appliquée à d'autres types de cancers.
L'association de techniques ultrasonores quantitatives et de rétrodiffusion de la lumière est motivée par toutes les raisons mentionnées ci-dessus. Cette thèse vise à investiguer une approche bimodale pour la caractérisation du cancer.

Il est important de noter que notre objectif n'est pas de surpasser ou de remplacer les méthodes de référence établies dans les procédures cliniques. Notre intention est de développer les prémisses d'un outil qui pourrait aider le clinicien à la prise de décisions en fournissant des informations complémentaires aux méthodes conventionnelles. Un outil bimodal qui combine toutes les qualités mentionnées ci-dessus a également le potentiel d'apporter des informations diagnostiques dans des applications médicales où aucun outil n'est actuellement utilisé de manière routinière (*e.g.* dans certains cas de suivi de la thérapie).

B.2 Ultrasons quantitatifs: méthodes

Le BSC quantifie la capacité du tissu à rétrodiffuser l'énergie acoustique en fonction de la fréquence de l'onde incidente d'excitation. Le BSC reflète la microstructure sous-jacente du tissu et peut être considéré comme la signature acoustique de l'échantillon sondé. Dans les applications de caractérisation des tissus, le principal défi consiste à estimer avec précision la BSC. L'étape suivante est sa paramétrisation et permet d'extraire les paramètres de diffusion par des procédures d'inversion. Pour ce faire, des modèles analytiques sont appliqués aux BSC mesurées. Plusieurs modèles théoriques ont été développés pour modéliser la diffusion des ultrasons dans les tissus biologiques.

Le modèle Gaussien et le modèle de sphères fluides sont paramétrés par le diamètre effectif du diffuseur (ESD). De nombreux articles ont rapporté des correspondances entre ESD et taille de composants cellulaires suite à application de ces modèles adaptés aux milieux dilués. Dans les milieux comportant une concentration élevée de diffuseurs, les modèles à facteur de structure ont permis de meilleurs résultats dans l'estimation des tailles de cellules. D'autres paramètres ultrasonores comportant des interprétations physiques peuvent être estimés suite à la paramétrisation du BSC. La fraction volumique des diffuseurs et le contraste d'impédance acoustiques en sont des exemples.

Alors que la paramétrisation du BSC extrait des paramètres basés sur le contenu spectral des signaux radiofréquences, ES implique l'estimation des attributs de la distribution statistique d'enveloppe de ces signaux. Cette procédure permet d'obtenir des paramètres de diffusion supplémentaires qui caractérise également la microstructure du tissu sous-jacent. La fonction de densité de probabilité de l'enveloppe mesurée peut être modélisée par des distributions statistiques connues. Dans cette thèse, nous nous concentrerons sur les deux distributions d'enveloppe les plus courantes dans les études QUS : les distributions de Nakagami et de Homodyned-K.

La distribution de Nakagami peut être utilisée pour extraire le facteur d'échelle Ω_{nak} et le paramètre de Nakagami α_{nak}. Le facteur d'échelle Ω_{nak} est équivalent à l'intensité rétrodiffusée moyenne et α_{nak} peut être utilisé pour quantifier le nombre effectif de diffuseurs par cellule de résolution. La distribution Homodyned-K peut être utilisée pour extraire μ_{hk}, qui est en quelque sorte l'analogue du paramètre de Nakagami α_{nak}. En ef-

fet, le nombre effectif de diffuseurs par cellule de résolution peut également être reflété par le paramètre μ_{hk}. Cette distribution peut aussi extraire le ratio signal cohérent / signal incohérent k_{hk}, qui peut décrire le degré de structure de la position spatiale du diffuseur dans la zone d'intérêt considérée. Des articles récents ont rapportés l'utilité de ces paramètres d'enveloppe pour caractériser des tissus cancéreux. Dans cette thèse, nous nous proposons donc d'associer la paramétrisation du BSC et ES pour sonder la microstructure tissulaire grâce aux ultrasons.

B.3 Spectroscopie optique de rétrodiffusion: méthodes

La spectroscopie de rétrodiffusion augmentée (EBS) consiste à extraire le profil de réflectance de l'échantillon. Cette quantité est également connue sous le nom de fonction d'étalement radial (PSF). Ce profil de réflectance peut être considéré comme une signature optique du tissu. En effet, ce dernier est extrêmement sensible à la fonction de phase de diffusion. La fonction de phase est paramétrée par des coefficients reflétant les propriétés optiques des tissus. Plusieurs modèles peuvent être choisis pour décrire cette fonction. La fonction de phase de Mie décrit la diffusion d'une sphère par une onde plane et est notamment caractérisée par le rayon de la sphère. Egalement, la fonction de phase de Whittle Matérn est paramétrée par des coefficients liés aux fluctuations continues de l'indice de réfraction. Une fois le profil de réflectance mesuré, les paramètres de la fonction de phase choisie peuvent être extrait grâce à des procédures d'inversions. En effet, le profil de réflectance théorique peut être obtenu par des simulations de Monte Carlo pour différentes fonctions de phase.

La spectroscopie de diffusion de la lumière (LSS) est une autre technique qui vise à analyser les photons ayant subi un seul évènement de diffusion de manière élastique afin d'extraire des informations sur la microstructure du tissu sous-jacent. La distribution de la taille des diffuseurs peut être estimée à l'aide de la théorie de Mie en analysant la lumière rétrodiffusée. Cette analyse repose sur une techniques d'isolement de la composante d'intérêt exploitant la polarisation. Contrairement à l'EBS, qui repose sur des mesures angulairement et spectralement résolues, la méthode LSS ne nécessite que des mesures spectralement résolues. Il est intéressant de noter que ces mesures peuvent être effectuées à l'aide d'un instrument similaire à celui nécessaire pour EBS. Egalement, la nature similaire du signal analysé et des paramètres extraits fait de LSS l'équivalent optique de la technique de paramétrisation ultrasonore BSC dans le cas incohérent.

Des articles récents ont rapportés les performances de EBS et LSS pour caractériser des tissus cancéreux. Dans cette thèse, nous nous proposons donc d'associer ces techniques pour sonder la microstructure tissulaire grâce à la lumière visible. Elles seront combinées aux deux autres techniques ultrasonores mentionnées plus haut avec l'objectif d'obtenir des paramètres complémentaires.

B.4 Etude sur fantôme

Ce chapitre constitue une validation préliminaire de notre méthode bimodale sur des fantômes imitant les tissus. La complémentarité de la paramétrisation du BSC et de EBS est y étudiée expérimentalement. La sensibilité des paramètres de diffusion à la taille du

diffuseur est étudiée pour chaque technique en utilisant trois fantômes avec différentes tailles de microparticules: 10 µm, 20 µm et 60 µm.

Dans un premier temps, les trois fantômes sont conçus avec des composants et des concentrations choisis pour obtenir les propriétés de diffusion ultrasonore et optique les plus réalistes.

Un modèle à facteur de structure (SFM) est utilisé pour cette étude. Le SFM a modélisé avec succès les BSC des fantômes 10 et 20 µm. Un bon accord global a également été observé entre les profils de réflectance estimés et attendus pour ces deux fantômes. Cependant, les profils de réflectance simulés des fantômes 10 µm et 20 µm présentent la même tendance et sont fortement corrélés ($R^2 = 0{,}99$). Dans le cadre d'une étude d'inversion où le rayon du diffuseur serait extrait à l'aide d'un algorithme d'inversion, il est raisonnable de penser que l'inversion précise de ces profils de réflectance serait difficile en raison de leur haut degré de ressemblance. Il est intéressant de noter que le contraste entre les BSC des fantômes de 10 et 20 µm a permis une distinction nette dans les hautes fréquences. Par conséquent, le succès de leur inversion pourrait être plus probable. Cela conduirait à une estimation précise du rayon du diffuseur.

La simulation de Monte Carlo a fourni les meilleures prédictions des variations du profil de réflectance du fantôme de 60 µm ($R^2 = 0,97$). Son profil de réflectance a présenté une corrélation plus faible avec les autres profils de réflectance simulés ($R^2 = 0{,}95$ dans les deux cas). Par conséquent, le succès de son inversion pourrait être potentiellement plus probable puisque le fantôme de 60 µm présente un profil de réflectance singulier. De même, cela pourrait conduire à une estimation correcte du rayon du diffuseur.

La BSC du fantôme de 60 µm a montré une correspondance faible avec le modèle de diffusion théorique. Cependant, cette estimation du BSC doit être considérée avec prudence, en particulier dans la région des hautes fréquences. En effet, les coefficients d'atténuation α_0 des trois fantômes ont été estimés dans les mêmes conditions. Cependant, la mise en œuvre de la méthode de substitution dans cette étude n'a pas permis d'estimer α_0 pour le fantôme de 60 µm, en raison de sa forte atténuation acoustique. Ce coefficient α_0 a été fixé empiriquement pour pallier ce problème. Par conséquent, la correction de l'atténuation peut être limitée pour le fantôme de 60 µm. Il est intéressant de noter que la faible performance de l'approche ultrasonore rapportée dans cette étude pour le fantôme de 60 µm pourrait être considérée pour discuter de la complémentarité avec EBS. En effet, comme mentionné ci-dessus, la théorie de Mie a décrit avec succès le profil de réflectance du fantôme de 60 µm. Par conséquent, EBS pourrait être une solution plus efficace pour caractériser les milieux qui présentent une forte atténuation acoustique.

En conclusion, la combinaison de la paramétrisation du BSC et de EBS a permis de caractériser chaque fantôme avec succès. Ce résultat intéressant a motivé une étude *ex vivo* sur des échantillons biologiques.

B.5 Caractérisation de sous-types de sarcomes : une étude *ex vivo* sur des modèles animaux

Une étude *ex vivo* sur des modèles animaux a été réalisée après l'étude sur fantôme. En plus de la paramétrisation du BSC et de EBS, ES et LSS ont été combinées pour caractériser deux sous-types de sarcomes : le chondrosarcome et l'ostéosarcome. Deux types de lignée cellulaire ont été utilisées pour générer les ostéosarcomes : MOS-J et K7M2. Des analyses histologiques ont été réalisées pour servir de référence.

L'utilisation de tumeurs de chondrosarcome et d'ostéosarcome est motivée par leurs microstructures différentes. La caractérisation de ces tumeurs apparaît comme un moyen de valider notre méthode bimodale dans le but d'établir une preuve de concept sur un type de tumeur particulier. Etant donné que les mécanismes internes de nos méthodes sondent la microstructure des tissus, notre approche pourrait potentiellement être appliquée à d'autres types de tumeurs ainsi qu'à des tissus sains.

Les mesures optiques et ultrasonores ont été réalisées le jour des sacrifices. Les paramètres quantitatifs ont ensuite été estimés et comparés entre les différents types de tumeurs. Des analyses histologiques ont été réalisées pour chaque tumeurs. Des mesures morphométriques des structures cellulaires, dérivées de ces examens, ont ensuite été comparées pour évaluer les performances de la paramétrisation du BSC et de LSS dans l'estimation des tailles de cellules ou de noyaux.

Trois paramètres ultrasonores et les profils de réflectance ont montré des différences significatives entre les chondrosarcomes et les ostéosarcomes avec un intervalle de confiance de 95%. De même, des variations des mêmes biomarqueurs ont été rapportées pour les deux types d'ostéosarcome (MOS-J et K7M2), malgré leur morphologie cellulaire similaire observée. Ces observations montrent la sensibilité de nos techniques à des propriétés tissulaires invisibles au marquage conventionnel H&E. La paramétrisation du BSC a permis d'identifier la taille moyenne des cellules et des noyaux des chondrosarcomes avec des erreurs relatives d'environ 22% et 9% respectivement. LSS a correctement estimé les distributions de taille des noyaux et des cellules pour les chondrosarcomes et les ostéosarcomes ($R^2 = 0{,}80$ et $R^2 = 0{,}73$ respectivement).

La paramétrisation du BSC et EBS sont apparus comme des outils pertinents pour discriminer les types de tumeurs. En outre, ces techniques ont permis de détecter des contrastes de signaux même parmi des échantillons présentant des morphologies cellulaires similaires. Pour estimer la taille des microstructures, la paramétrisation du BSC fut complémentaire de LSS pour l'étude des chondrosarcomes. La première technique s'est avérée plus précise dans l'estimation de la taille moyenne des cellules, tandis que la seconde méthode a permis une extraction plus efficace de la distribution de la taille des noyaux. Il est possible que ces résultats découlent de la correspondance entre les structures microarchitecturales simples du chondrosarcome et les géométries simples supposées dans les modèles de diffusion ultrasonore ou la théorie de Mie (*i.e.* sphères contenus dans un milieu environnant). À l'inverse, l'identification de la taille des cellules dans des milieux hautement cellulaires tels que les tumeurs d'ostéosarcome pourraient être plus difficile en raison de la contiguïté géométrique des cellules et de la diffusion concurrente d'autres microstructures.

En conclusion, les deux techniques quantitatives ultrasonores et les deux techniques optiques ont apporté des paramètres complémentaires qui reflètent la microstructure tissulaire sous-jacente pour différents types de tumeurs. Les paramètres morphologiques

estimés se sont révélés sensibles aux échelles cellulaire et nucléaire. Ces résultats prometteurs nous ont amèné à mener une étude longitudinale animale *ex vivo* afin d'évaluer la sensibilité de cette technique bimodale pour des applications de suivi de traitement.

B.6 Suivi de thérapie : une étude longitudinale

Dans ce chapitre, nous avons étudié les performances de notre approche bimodale pour évaluer la réponse d'une tumeur au fil du temps lorsque des traitements chimiothérapeutiques sont administrés. Pour ce faire, nous avons appliqué les quatre techniques mentionnées ci-dessus aux mêmes sous-types de sarcomes pendant plusieurs semaines, en injectant un médicament chimiothérapeutique deux fois par semaine à certains rongeurs et une la solution saline à d'autres (animaux témoins). Les volumes tumoraux relatifs (RTV) ont été estimés au fil des semaines et ont été considérés comme indicateurs de références de réponse au traitement. Les RTV ont révélé que toutes les tumeurs étaient susceptibles d'être non répondeuses.

Des corrélations faibles ont été observée entre les paramètres de diffusion ultrasonore et optique et la RTV. Plusieurs paramètres ultrasonores et optiques sont apparus sensibles aux effets des injections de traitement pendant les premiers jours de traitement. Des convergences ont ensuite été observées entre les tumeurs traitées et témoins après le traitement final. Par conséquent, ces paramètres de diffusion pourraient avoir reflété le mécanisme de résistance à la chimiothérapie.

Dans cette étude, la combinaison des ultrasons et de la lumière a aussi permis d'obtenir différentes sources de contraste à différents jours de mesure. Par exemple, pour le chondrosarcome, les spectres EBS et LSS (après 4 traitements) ont permis de séparer les tumeurs traitées des tumeurs de contrôle, contrairement aux estimations ultrasonores correspondantes. La multiplication des estimations quantitatives pourrait refléter plus précisément la pluralité des mécanismes cellulaires intervenant dans le développement du cancer ainsi que la réaction aux agents anti-cancer. En somme, notre approche bimodale représente une solution intéressante pour la poursuite de cette recherche.

De futures études pourraient être menées *in vivo* pour étudier la prédiction des résultats du traitement. Dans ce cas, les mesures d'ultrasons quantitatifs pourraient être réalisées jour après jour pour étudier les corrélations potentielles entre les paramètres de diffusion et les RTV faibles des tumeurs répondeuses. Des mesures optiques pourraient également être réalisées pour d'autres types de tumeurs qui peuvent être situées à une faible profondeur en utilisant une fibre optique.

Pour optimiser la probabilité d'analyser les tumeurs non-répondeuses en même temps que les répondeuses, une étude longitudinale similaire pourrait être réalisée avec un troisième groupe composé d'animaux ayant reçu des doses plus élevées de traitement anticancéreux. Ainsi, des tumeurs témoins, des tumeurs traitées avec une faible dose et d'autres avec une dose importante de traitement chimiothérapeutique pourraient être analysées pour chaque jour de mesure. En effet, une faible dose de traitement anti-cancer est susceptible de conduire à des tumeurs non-répondeuses alors que les doses plus élevées ont plus de chance de conduire à des tumeurs répondeuses.

B.7 Effets structurels sur la diffusion des ultrasons : une étude sur fantôme

Ce chapitre introduit une nouvelle méthode d'étude des paramètres QUS sur fantôme. De plus, la concordance des interprétations physiques de multiples paramètres QUS est étudiée.

Les cellules des tissus biologiques peuvent être associés à des fractions volumiques modérées ou élevées (généralement supérieures à 0,05). Or, la concentration des diffuseurs dans un milieu donné est un paramètre essentiel pour modéliser correctement la diffusion des ondes ultrasonores. En effet, on peut raisonnablement supposer que la corrélation de la position des diffuseurs augmente avec leur concentration. Lorsque les diffuseurs ne sont pas répartis de manière aléatoire dans l'espace, des effets structurels affectent la rétrodiffusion des ultrasons. Dans les milieux structurés ou concentrés, le BSC n'est plus la somme incohérente des contributions de chaque diffuseur. Le BSC total comporte alors une composante cohérente. De même, l'enveloppe des signaux RF est affectée par l'espacement périodique entre les diffuseurs.

Dans ce chapitre, ces effets structurels sur la diffusion ultrasonore ont été étudiés dans le cadre d'une analyse sur fantôme. Pour ce faire, une nouvelle approche expérimentale a été introduite. Le fantôme utilisé ici est composé de particules magnétiques dont l'organisation spatiale a été modifiée par un champ magnétique environnant. Les significations physiques des paramètres ultrasonores et leur concordance ont été constatées dans trois expériences distinctes.

Ls billes se comportent comme des billes de polystyrène normales lorsqu'aucun champ magnétique environnant n'est appliqué. En présence d'un champ homogène et stationnaire, les billes superparamagnétiques sont censées se disposer en chaînes immobiles et parallèles selon l'orientation du champ magnétique. La distance entre les chaînes dans la direction normale du champ magnétique doit reflèter une distance répulsive caractéristique.

Les paramètres liés au BSC et à l'enveloppe ont été estimés dans cette solution dans différentes configurations de champ magnétique. L'intensité du champ magnétique a été modifiée en fonction du temps, de son amplitude et de l'orientation spatiale dans trois expériences distinctes.

Tout d'abord, dans l'expérience temporelle horizontale, dénommée expérience 1, le champ magnétique est horizontal (axe Y) et est induit par le placement de deux aimants solides de part et d'autre de la solution fantôme. Les billes ont été instantanément exposées à un champ magnétique de 4 mT. L'orientation des chaînes est normale à la propagation des ondes ultrasonores (axe Z). Deuxièmement, l'expérience en régime permanent horizontal, dénommée expérience 2, étudie aussi les variations des paramètres QUS dans un champ magnétique horizontal. Cependant, cette expérience permet de sonder l'état d'équilibre des billes alignées horizontalement pour différentes intensités de champ magnétique. Troisièmement, dans l'expérience verticale en régime permanent, dénommée expérience 3, le fantôme est placé dans une bobine verticale qui génére un champ magnétique. Le champ magnétique est parallèle à la propagation de l'onde ultrasonore. Cette expérience a permis de sonder l'état d'équilibre des billes alignées verticalement pour différentes intensités de champ magnétique.

Lorsque la solution est soumise à un champ magnétique instantanée, les billes magnétiques montrent un régime transitoire de l'ordre de 2s dans lequel elles commencent à s'organiser. Passé ce délai, les billes forment des chaînes quasiment immobiles présentant des discontinuités. Plus le champ est intense, plus les chaînes sont longues et les distances de répulsion entre les chaînes tendent à augmenter également.

Le ratio du signal cohérent et diffus k_{hk} reflète la présence d'un régime transitoire, il augmente lorsque les billes commencent à s'organiser puis diminue en régime permanent car la cellule de résolution du transducteur ne pourrait contenir qu'une seule chaîne (*i.e.* un diffuseur effectif). Cette hypothèse est cohérente avec des considérations géométriques. Dans l'expérience 3, son évolution n'est pas concluante.

Le paramètre de Nakagami α_{nak} et le paramètre d'aggrégation des diffuseurs μ_{hk} suivent les mêmes évolutions. Dans les expériences 1 et 2, ces paramètres augmentent pendant le régime transitoire puis diminuent pendant le régime permanent. L'augmentation temporaire traduirait le début d'organisation des billes. La diminution pourrait s'expliquer par une dépopulation des diffuseurs. En chaînes, les billes pourrait former des diffuseurs effectifs "plus larges" mais moins nombreux. Cette hypothèse est supportée par la diminution de la pente du BSC linéaire, qui peut indiquer une augmentation du diamètre effectif des diffuseurs. Dans l'expérience 3, α_{nak} et μ_{hk} diminue avec la pente du BSC linéaire. Dans ce cas, il pourrait s'agir d'une dépopulation des diffuseurs. Cette hypothèse est cohérente avec des considérations géométriques.

L'ordonnée à l'origine du BSC linéaire et le facteur d'échelle Ω_{nak} suivent les mêmes évolutions. Ces coefficients augmentent avec le champ magnétique dans les expériences 2 et 3. Or d'après les variations de k_{hk}, le signal incohérent prédomine dans ces configurations. La densité du nombre de diffuseurs n diminue d'après les variations de α_{nak}. Ainsi, la surface efficace de rétrodiffusion différentiel σ_b pourrait augmenter et compenser la diminution de n. Cela peut s'expliquer par une augmentation du contraste relatif d'impédance acoustique γ_z ou par des considérations géométriques. Dans l'expérience 3, l'ordonnée à l'origine du BSC linéaire et Ω_{nak} diminue, traduisant potentiellement la dépopulation de diffuseurs plus prononcée dans la configuration verticale. La chute plus importante observée pour α_{nak} et μ_{hk} par rapport aux configurations horizontales soutient cette hypothèse.

Des hypothèses étayées par des microphotographies de référence ont été formulées pour décrire les variations de chaque estimation quantitative conformément à leur interprétation physique dans les différentes configurations. On peut noter que les différentes hypothèses sont concordantes. Par conséquent, les interprétations physiques de multiples paramètres d'enveloppe et spectraux ont été combinés avec succès en analysant un fantôme magnétique en fonction du temps, de l'intensité du champ magnétique et de l'orientation structurelle. La signification de chaque paramètre ultrasonore a été validée dans le cadre de cette étude.

B.8 Conclusion

Les résultats présentés dans cette thèse illustrent expérimentalement la complémentarité des paramètres de diffusion ultrasonores et optiques. La combinaison de ces modalités a fourni diverses sources de contraste entre les populations d'échantillons sondés. Des estimations représentant la taille de certains composants cellulaires ont également été obtenues, conduisant à une évaluation approfondie de la microstructure des tissus. Nous pouvons donc conclure que l'association des techniques ultrasonores quantitatives et de rétrodiffusion de la lumière est pertinente pour la caractérisation du cancer. Des résultats

prometteurs pourraient être obtenus dans de futures études.

List of Figures

List of Tables

Bibliography

[1] C. Fletcher, J. A. Bridge, P. C. W. Hogendoorn, F. Mertens, *et al.*, *WHO classification of tumours of soft tissue and bone: WHO classification of tumours, vol. 5.* World Health Organization, 2013.

[2] E. S. for Medical Oncology, "Bone sarcomas: a guide for patients - information based on esmo clinical practice guidelines," no. v1, 2016.

[3] J. Baak, "The principles and advances of quantitative pathology.," *Analytical and quantitative cytology and histology*, vol. 9, no. 2, pp. 89–95, 1987.

[4] M. L. Oelze and J. Mamou, "Review of Quantitative Ultrasound: Envelope Statistics and Backscatter Coefficient Imaging and Contributions to Diagnostic Ultrasound," *IEEE Transactions on Ultrasonics, Ferroelectrics, and Frequency Control*, vol. 63, no. 2, pp. 336–351, 2016.

[5] P. Muleki-Seya, R. Guillermin, J. Guglielmi, J. Chen, T. Pourcher, E. Konofagou, and E. Franceschini, "High-Frequency Quantitative Ultrasound Spectroscopy of Excised Canine Livers and Mouse Tumors Using the Structure Factor Model," *IEEE Transactions on Ultrasonics, Ferroelectrics, and Frequency Control*, vol. 63, no. 9, pp. 1335–1350, 2016.

[6] V. Turzhitsky, J. D. Rogers, N. N. Mutyal, H. K. Roy, and V. Backman, "Characterization of light transport in scattering media at subdiffusion length scales with low-coherence enhanced backscattering," *IEEE Journal on Selected Topics in Quantum Electronics*, vol. 16, no. 3, pp. 619–626, 2010.

[7] L. T. Perelman, "Optical diagnostic technology based on light scattering spectroscopy for early cancer detection," *Expert Review of Medical Devices*, vol. 3, no. 6, pp. 787–803, 2006.

[8] L. Qiu, D. K. Pleskow, R. Chuttani, E. Vitkin, J. Leyden, N. Ozden, S. Itani, L. Guo, A. Sacks, J. D. Goldsmith, M. D. Modell, E. B. Hanlon, I. Itzkan, and L. T. Perelman, "Multispectral scanning during endoscopy guides biopsy of dysplasia in Barrett's esophagus," *Nature Medicine*, vol. 16, no. 5, pp. 603–606, 2010.

[9] L. Qiu, R. Chuttani, D. K. Pleskow, V. Turzhitsky, U. Khan, Y. N. Zakharov, L. Zhang, T. M. Berzin, E. U. Yee, M. S. Sawhney, Y. Li, E. Vitkin, J. D. Goldsmith, I. Itzkan, and L. T. Perelman, "Multispectral light scattering endoscopic imaging of esophageal precancer," *Light: Science and Applications*, vol. 7, no. 4, pp. 17110–17174, 2018.

[10] A. J. Radosevich, N. N. Mutyal, J. Yi, Y. Stypula-Cyrus, J. D. Rogers, M. J. Goldberg, L. K. Bianchi, S. Bajaj, H. K. Roy, and V. Backman, "Ultrastructural alterations in field carcinogenesis measured by enhanced backscattering spectroscopy," *Journal of Biomedical Optics*, vol. 18, no. 9, p. 097002, 2013.

[11] Y. Liu, Y. L. Kim, R. K. Wali, H. K. Roy, M. J. Goldberg, A. K. Kromine, K. Chen, and V. Backman, "Simultaneous measurement of angular and spectral properties of light scattering for early cancer detection," *OSA Trends in Optics and Photonics Series*, vol. 88, no. 2, pp. 98–99, 2003.

[12] L. Gorski, "Dysplasia," 2023. url: www.mypathologyreport.ca/wp-content/uploads/2020/01/picture-dysplasia_edited.jpg ;Accessed: August 9th 2023.

[13] L. Gorski, "Grade," 2023. url: url: www.mypathologyreport.ca/wp-content/uploads/2020/01/Grade-1_edited.jpg; Accessed: August 9th 2023.

[14] J. A. Kim, D. J. Wales, and G.-Z. Yang, "Optical spectroscopy for in vivo medical diagnosis—a review of the state of the art and future perspectives," *Progress in Biomedical Engineering*, vol. 2, p. 042001, aug 2020.

[15] M. Basij, Y. Yan, S. S. Alshahrani, H. Helmi, T. K. Burton, J. W. Burmeister, M. M. Dominello, I. S. Winer, and M. Mehrmohammadi, "Miniaturized phased-array ultrasound and photoacoustic endoscopic imaging system," *Photoacoustics*, vol. 15, p. 100139, 2019.

[16] L. Qiu, D. K. Pleskow, R. Chuttani, E. Vitkin, J. Leyden, N. Ozden, S. Itani, L. Guo, A. Sacks, J. D. Goldsmith, M. D. Modell, E. B. Hanlon, I. Itzkan, and L. T. Perelman, "Multispectral scanning during endoscopy guides biopsy of dysplasia in Barrett's esophagus," *Nature Medicine*, vol. 16, no. 5, pp. 603–606, 2010.

[17] H. K. Roy, Y. Liu, R. K. Wali, Y. L. Kim, A. K. Kromine, M. J. Goldberg, and V. Backman, "Four-Dimensional Elastic Light-Scattering Fingerprints as Preneoplastic Markers in the Rat Model of Colon Carcinogenesis," *Gastroenterology*, vol. 126, no. 4, pp. 1071–1081, 2004.

[18] N. N. Mutyal, A. Radosevich, A. K. Tiwari, Y. Stypula, R. Wali, D. Kunte, H. K. Roy, and V. Backman, "Biological Mechanisms Underlying Structural Changes Induced by Colorectal Field Carcinogenesis Measured with Low-Coherence Enhanced Backscattering (LEBS) Spectroscopy," *PLoS ONE*, vol. 8, no. 2, pp. 12–13, 2013.

[19] S. C. Lester, *Manual of Surgical Pathology: Expert Consult-Online and print*. Elsevier Health Sciences, 2010.

[20] G. T. Kennedy, O. T. Okusanya, J. J. Keating, D. F. Heitjan, C. Deshpande, L. A. Litzky, S. M. Albelda, J. A. Drebin, S. Nie, P. S. Low, *et al.*, "The optical biopsy: a novel technique for rapid intraoperative diagnosis of primary pulmonary adenocarcinomas," *Annals of surgery*, vol. 262, no. 4, pp. 602–609, 2015.

[21] B. W. Maloney, D. M. McClatchy, B. W. Pogue, K. D. Paulsen, W. A. Wells, and R. J. Barth Jr, "Review of methods for intraoperative margin detection for breast conserving surgery," *Journal of biomedical optics*, vol. 23, no. 10, pp. 100901–100901, 2018.

[22] M. Leiloglou, V. Chalau, M. S. Kedrzycki, P. Thiruchelvam, A. Darzi, D. R. Leff, and D. S. Elson, "Tissue texture extraction in indocyanine green fluorescence imaging for breast-conserving surgery," *Journal of Physics D: Applied Physics*, vol. 54, p. 194005, feb 2021.

[23] A. Dutour, V. Josserand, D. Jury, S. Guillermet, A. V. Decouvelaere, F. Chotel, T. Pointecouteau, P. Rizo, J. L. Coll, and J. Y. Blay, "Targeted imaging of $\alpha v\beta 3$ expressing sarcoma tumor cells in vivo in pre-operative setting using near infrared: A potential tool to reduce incomplete surgical resection," *Bone*, vol. 62, pp. 71–78, 2014.

[24] J. Mamou and M. L. Oelze, *Quantitative ultrasound in soft tissues*. 2013.

[25] F. L. Lizzi, M. Greenebaum, E. J. Feleppa, M. Elbaum, and D. J. Coleman, "Theoretical framework for spectrum analysis in ultrasonic tissue characterization," *The Journal of the Acoustical Society of America*, vol. 73, pp. 1366–1373, 04 1983.

[26] J. Mamou, A. Coron, M. Hata, J. Machi, E. Yanagihara, P. Laugier, and E. J. Feleppa, "Three-Dimensional High-Frequency Characterization of Cancerous Lymph Nodes," *Ultrasound in Medicine and Biology*, vol. 36, no. 3, pp. 361–375, 2010.

[27] F. L. Lizzi, M. Ostromogilsky, E. J. Feleppa, M. C. Rorke, and M. M. Yaremko, "Relationship of ultrasonic spectral parameters to features of tissue microstructure," *IEEE transactions on ultrasonics, ferroelectrics, and frequency control*, vol. 34, no. 3, pp. 319–329, 1987.

[28] P. Muleki-Seya, A. Han, M. P. Andre, J. W. Erdman Jr, and W. D. O'Brien Jr, "Analysis of two quantitative ultrasound approaches," *Ultrasonic imaging*, vol. 40, no. 2, pp. 84–96, 2018.

[29] E. Franceschini, J. M. Escoffre, A. Novell, L. Auboire, V. Mendes, Y. M. Benane, A. Bouakaz, and O. Basset, "Quantitative Ultrasound in Ex Vivo Fibrotic Rabbit Livers," *Ultrasound in Medicine and Biology*, vol. 45, no. 7, pp. 1777–1786, 2019.

[30] M. F. Insana, J. G. Wood, and T. J. Hall, "Identifying acoustic scattering sources in normal renal parenchyma in vitro by varying arterial and ureteral pressures," *Ultrasound in Medicine & Biology*, vol. 18, no. 6, pp. 587–599, 1992.

[31] M. L. Oelze, W. D. O'Brien, J. P. Blue, and J. F. Zachary, "Differentiation and characterization of rat mammary fibroadenomas and 4T1 mouse carcinomas using quantitative ultrasound imaging," *IEEE Transactions on Medical Imaging*, vol. 23, no. 6, pp. 764–771, 2004.

[32] R. Bracewell, *The Fourier Transform and Its Applications, 2nd editions*. McGraw-Hill Book Company, 1978.

[33] M. L. Oelze and W. D. O'Brien Jr, "Application of three scattering models to characterization of solid tumors in mice," *Ultrasonic imaging*, vol. 28, no. 2, pp. 83–96, 2006.

[34] E. Franceschini, *Modèle de facteur de structure pour l'estimation ultrasonore des structures cellulaires*. Habilitation à diriger des recherches, Aix-Marseille Universite, Oct. 2015.

[35] J. McNew, R. Lavarello, and W. D. O'Brien, "Sound scattering from two concentric fluid spheres," *The Journal of the Acoustical Society of America*, vol. 125, no. 1, pp. 1–4, 2009.

[36] M. Teisseire, A. Han, R. Abuhabsah, J. P. Blue, S. Sarwate, and W. D. O'Brien, "Ultrasonic backscatter coefficient quantitative estimates from Chinese hamster ovary cell pellet biophantoms," *The Journal of the Acoustical Society of America*, vol. 128, no. 5, pp. 3175–3180, 2010.

[37] A. Han, R. Abuhabsah, J. P. Blue, S. Sarwate, and W. D. O'Brien, "Ultrasonic backscatter coefficient quantitative estimates from high-concentration Chinese hamster ovary cell pellet biophantoms," *The Journal of the Acoustical Society of America*, vol. 130, no. 6, pp. 4139–4147, 2011.

[38] A. Han and W. O'Brien, "Structure function for high-concentration biophantoms of polydisperse scatterer sizes," *IEEE Transactions on Ultrasonics, Ferroelectrics, and Frequency Control*, vol. 62, no. 2, pp. 303–318, 2015.

[39] E. Franceschini and R. Guillermin, "Experimental assessment of four ultrasound scattering models for characterizing concentrated tissue-mimicking phantoms," *The Journal of the Acoustical Society of America*, vol. 132, no. 6, pp. 3735–3747, 2012.

[40] E. Franceschini, R. Guillermin, F. Tourniaire, S. Roffino, E. Lamy, and J.-F. Landrier, "Structure factor model for understanding the measured backscatter coefficients from concentrated cell pellet biophantoms," *The Journal of the Acoustical Society of America*, vol. 135, pp. 3620–3631, 06 2014.

[41] E. Franceschini, R. D. Monchy, and J. Mamou, "Quantitative Characterization of Tissue Microstructure in Concentrated Cell Pellet Biophantoms Based on the Structure Factor Model," *IEEE Transactions on Ultrasonics, Ferroelectrics, and Frequency Control*, vol. 63, no. 9, pp. 1321–1334, 2016.

[42] R. K. Saha and M. C. Kolios, "Effects of cell spatial organization and size distribution on ultrasound backscattering," *IEEE Transactions on Ultrasonics, Ferroelectrics, and Frequency Control*, vol. 58, no. 10, pp. 2118–2131, 2011.

[43] F. Destrempes and G. Cloutier, "A critical review and uniformized representation of statistical distributions modeling the ultrasound echo envelope," *Ultrasound in Medicine and Biology*, vol. 36, no. 7, pp. 1037–1051, 2010.

[44] A. Cristea, N. Collier, E. Franceschini, J. Mamou, C. Cachard, and O. Basset, "Quantitative assessment of media concentration using the homodyned k distribution," *Ultrasonics*, vol. 101, p. 105986, 2020.

[45] J. Mamou, A. Coron, M. L. Oelze, E. Saegusa-Beecroft, M. Hata, P. Lee, J. Machi, E. Yanagihara, P. Laugier, and E. J. Feleppa, "Three-dimensional high-frequency backscatter and envelope quantification of cancerous human lymph nodes," *Ultrasound in Medicine and Biology*, vol. 37, no. 3, pp. 345–357, 2011.

[46] Z. Zhou, J. Fang, A. Cristea, Y. H. Lin, Y. W. Tsai, Y. L. Wan, K. M. Yeow, M. C. Ho, and P. H. Tsui, "Value of homodyned K distribution in ultrasound parametric imaging of hepatic steatosis: An animal study," *Ultrasonics*, vol. 101, no. August 2019, p. 106001, 2020.

[47] E. Feleppa, F. Lizzi, D. Coleman, and M. Yaremko, "Diagnostic spectrum analysis in ophthalmology: a physical perspective," *Ultrasound in medicine & biology*, vol. 12, no. 8, pp. 623–631, 1986.

[48] M. L. Oelze, "Quantitative ultrasound techniques and improvements to diagnostic ultrasonic imaging," *IEEE International Ultrasonics Symposium, IUS*, pp. 232–239, 2012.

[49] R. J. Lavarello, W. R. Ridgway, S. S. Sarwate, and M. L. Oelze, "Characterization of thyroid cancer in mouse models using high-frequency quantitative ultrasound techniques," *Ultrasound in Medicine & Biology*, vol. 39, no. 12, pp. 2333–2341, 2013.

[50] J. Mamou, E. Saegusa-Beecroft, A. Coron, M. L. Oelze, T. Yamaguchi, M. Hata, J. Machi, E. Yanagihara, P. Laugier, and E. J. Feleppa, "Lymph explorer: A new gui using 3d high-frequency quantitative ultrasound methods to guide pathologists towards metastatic regions in human lymph nodes," in *2012 IEEE International Ultrasonics Symposium*, pp. 2340–2343, IEEE, 2012.

[51] C. Hoerig, K. Wallace, M. Wu, and J. Mamou, "Classification of metastatic lymph nodes in vivo using quantitative ultrasound at clinical frequencies," *Ultrasound in Medicine & Biology*, vol. 49, no. 3, pp. 787–801, 2023.

[52] G. Czarnota, M. Kolios, J. Abraham, M. Portnoy, F. Ottensmeyer, J. Hunt, and M. Sherar, "Ultrasound imaging of apoptosis: high-resolution non-invasive monitoring of programmed cell death in vitro, in situ and in vivo," *British journal of cancer*, vol. 81, no. 3, pp. 520–527, 1999.

[53] M. Kolios, G. Czarnota, M. Lee, J. Hunt, and M. Sherar, "Ultrasonic spectral parameter characterization of apoptosis," *Ultrasound in medicine & biology*, vol. 28, no. 5, pp. 589–597, 2002.

[54] B. Banihashemi, R. Vlad, B. Debeljevic, A. Giles, M. C. Kolios, and G. J. Czarnota, "Ultrasound imaging of apoptosis in tumor response: novel preclinical monitoring of photodynamic therapy effects," *Cancer research*, vol. 68, no. 20, pp. 8590–8596, 2008.

[55] L. Sannachi, H. Tadayyon, A. Sadeghi-Naini, W. Tran, S. Gandhi, F. Wright, M. Oelze, and G. Czarnota, "Non-invasive evaluation of breast cancer response to chemotherapy using quantitative ultrasonic backscatter parameters," *Medical image analysis*, vol. 20, no. 1, pp. 224–236, 2015.

[56] T. N. Nguyen, A. S. Podkowa, T. H. Park, R. J. Miller, M. N. Do, and M. L. Oelze, "Use of a convolutional neural network and quantitative ultrasound for diagnosis of fatty liver," *Ultrasound in medicine & biology*, vol. 47, no. 3, pp. 556–568, 2021.

[57] H. Taleghamar, H. Moghadas-Dastjerdi, G. J. Czarnota, and A. Sadeghi-Naini, "Characterizing intra-tumor regions on quantitative ultrasound parametric images to predict breast cancer response to chemotherapy at pre-treatment," *Scientific Reports*, vol. 11, no. 1, pp. 1–13, 2021.

[58] H. Taleghamar, S. A. Jalalifar, G. J. Czarnota, and A. Sadeghi-Naini, "Deep learning of quantitative ultrasound multi-parametric images at pre-treatment to predict breast cancer response to chemotherapy," *Scientific reports*, vol. 12, no. 1, p. 2244, 2022.

[59] B. Beauvoit and B. Chance, "Time-resolved spectroscopy of mitochondria, cells and tissues under normal and pathological conditions," *Bioenergetics of the Cell: Quantitative Aspects*, pp. 445–455, 1998.

[60] A. H. Hielscher, J. R. Mourant, and I. J. Bigio, "Influence of particle size and concentration on the diffuse backscattering of polarized light from tissue phantoms and biological cell suspensions," *Applied optics*, vol. 36, no. 1, pp. 125–135, 1997.

[61] J. R. Mourant, J. P. Freyer, A. H. Hielscher, A. A. Eick, D. Shen, and T. M. Johnson, "Mechanisms of light scattering from biological cells relevant to noninvasive optical-tissue diagnostics," *Applied Optics*, vol. 37, no. 16, p. 3586, 1998.

[62] P. Sloot and C. G. Figdor, "Elastic light scattering from nucleated blood cells: rapid numerical analysis," *Applied Optics*, vol. 25, no. 19, pp. 3559–3565, 1986.

[63] V. Backman, *Early diagnosis of cancer using light scattering spectroscopy.* PhD thesis, Massachusetts Institute of Technology, 2001.

[64] L. T. Perelman, V. Backman, M. Wallace, G. Zonios, R. Manoharan, A. Nusrat, S. Shields, M. Seiler, C. Lima, T. Hamano, I. Itzkan, J. Van Dam, J. M. Crawford, and M. S. Feld, "Observation of periodic fine structure in reflectance from biological tissue: A new technique for measuring nuclear size distribution," *Physical Review Letters*, vol. 80, no. 3, pp. 627–630, 1998.

[65] V. Backman, R. Gurjar, K. Badizadegan, I. Itzkan, R. R. Dasari, L. T. Perelman, and M. S. Feld, "Polarized light scattering spectroscopy for quantitative measurement of epithelial cellular structures in situ," *IEEE Journal on Selected Topics in Quantum Electronics*, vol. 5, no. 4, pp. 1019–1026, 1999.

[66] M. B. Wallace, L. T. Perelman, V. Backman, J. M. Crawford, M. Fitzmaurice, M. Seiler, K. Badizadegan, S. J. Shields, I. Itzkan, R. R. Dasari, J. Van Dam, and M. S. Feld, "Endoscopic detection of dysplasia in patients with Barrett's esophagus using light-scattering spectroscopy," *Gastroenterology*, vol. 119, no. 3, pp. 677–682, 2000.

[67] V. Backman, R. S. Gurjar, L. T. Perelman, V. Gopal, M. Kalashnikov, K. Badizadegan, A. Wax, I. Georgakoudi, M. G. Mueller, C. W. Boone, I. Itzkan, R. R. Dasari, and M. S. Feld, "Imaging and measurement of cell structure and organization with submicron accuracy using light scattering spectroscopy," *Optical Biopsy IV*, vol. 4613, no. May 2002, pp. 101–110, 2002.

[68] H. Fang, M. Ollero, E. Vitkin, L. M. Kimerer, P. B. Cipolloni, M. M. Zaman, S. D. Freedman, I. J. Bigio, I. Itzkan, E. B. Hanlon, and L. T. Perelman, "Noninvasive sizing of subcellular organelles with light scattering spectroscopy," *IEEE Journal on Selected Topics in Quantum Electronics*, vol. 9, no. 2, pp. 267–276, 2003.

[69] D. K. Pleskow, M. S. Sawhney, P. K. Upputuri, T. M. Berzin, M. F. Coughlan, U. Khan, M. Glyavina, X. Zhang, L. Chen, C. J. Sheil, J. M. Cohen, E. Vitkin, Y. N. Zakharov, I. Itzkan, L. Zhang, L. Qiu, and L. T. Perelman, "In vivo detection of bile duct pre-cancer with endoscopic light scattering spectroscopy," *Nature Communications*, vol. 14, no. 1, 2023.

[70] L. Fang, Qiu, V. Turzhitsky, E. Vitkin, L. Guo, E. B. Hanlon, I. Itzkan, and L. T. Perelman, "Coherent confocal light absorption and scattering spectroscopic microscopy," *Biomedical Optics, BIOMED 2012*, 2007.

[71] I. Itzkan, L. Qiu, H. Fang, M. M. Zaman, E. Vitkin, I. C. Ghiran, S. Salahuddin, M. Modell, C. Andersson, L. M. Kimerer, P. B. Cipolloni, K. H. Lim, S. D. Freedman, I. Bigio, B. P. Sachs, E. B. Hanlon, and L. T. Perelman, "Confocal light absorption and scattering spectroscopic microscopy monitors organelles in live cells with no exogenous labels," *Proceedings of the National Academy of Sciences of the United States of America*, vol. 104, no. 44, pp. 17255–17260, 2007.

[72] L. Qiu, V. Turzhitsky, E. Vitkin, L. Guo, E. B. Hanlon, I. Itzkan, and L. T. Perelman, "Coherent confocal light absorption and scattering spectroscopic microscopy," *Biomedical Optics, BIOMED 2012*, 2012.

[73] D. K. Pleskow, L. Zhang, V. Turzhitsky, M. F. Coughlan, U. Khan, X. Zhang, C. J. Sheil, M. Glyavina, L. Chen, S. Shinagare, Y. N. Zakharov, E. Vitkin, I. Itzkan, L. T. Perelman, and L. Qiu, "Coherent confocal light scattering spectroscopic microscopy evaluates cancer progression and aggressiveness in live cells and tissue," *ACS Photonics*, vol. 8, no. 7, pp. 2050–2059, 2021.

[74] Y. L. Kim, Y. Liu, R. K. Wali, H. K. Roy, and V. Backman, "Low-coherent backscattering spectroscopy for tissue characterization," *Applied Optics*, vol. 44, no. 3, pp. 366–377, 2005.

[75] Y. Kuga and A. Ishimaru, "Retroreflectance from a dense distribution of spherical particles," *JOSA A*, vol. 1, no. 8, pp. 831–835, 1984.

[76] Y. L. Kim, V. M. Turzhitsky, Y. Liu, H. K. Roy, R. K. Wali, H. Subramanian, P. Pradhan, and V. Backman, "Low-coherence enhanced backscattering: review of principles and applications for colon cancer screening," *Journal of Biomedical Optics*, vol. 11, no. 4, p. 041125, 2006.

[77] J. D. Rogers, V. Stoyneva, and V. Turzhitsky, "Alternate formulation of enhanced backscattering as phase conjugation and diffraction : derivation and experimental observation," vol. 19, no. 13, pp. 1000–1005, 2011.

[78] N. N. Mutyal, A. Radosevich, B. Gould, J. D. Rogers, A. Gomes, V. Turzhitsky, and V. Backman, "A fiber optic probe design to measure depth- limited optical properties in-vivo with Low- coherence Enhanced Backscattering (LEBS) Spectroscopy," vol. 20, no. 18, pp. 1087–1089, 2012.

[79] H. K. Roy, V. Turzhitsky, Y. Kim, M. J. Goldberg, P. Watson, J. D. Rogers, A. J. Gomes, A. Kromine, R. E. Brand, M. Jameel, A. Bogovejic, P. Pradhan, and V. Backman, "Association between rectal optical signatures and colonic neoplasia: Potential applications for screening," *Cancer Research*, vol. 69, no. 10, pp. 4476–4483, 2009.

[80] V. Turzhitsky, A. J. Radosevich, J. D. Rogers, N. N. Mutyal, and V. Backman, "Measurement of optical scattering properties with low-coherence enhanced backscattering spectroscopy," *Journal of Biomedical Optics*, vol. 16, no. 6, p. 067007, 2011.

[81] A. J. Radosevich, N. N. Mutyal, V. Turzhitsky, J. D. Rogers, J. Yi, A. Taflove, and V. Backman, "Measurement of the spatial backscattering impulse-response at short length scales with polarized enhanced backscattering," vol. 36, no. 24, pp. 4737–4739, 2011.

[82] A. J. Radosevich, V. M. Turzhitsky, N. N. Mutyal, J. D. Rogers, V. Stoyneva, A. K. Tiwari, M. De La Cruz, D. P. Kunte, R. K. Wali, H. K. Roy, and V. Backman, "Depth-resolved measurement of mucosal microvascular blood content using low-coherence enhanced backscattering spectroscopy," *Biomedical Optics Express*, vol. 1, no. 4, p. 1196, 2010.

[83] A. J. Radosevich, J. Yi, J. D. Rogers, and V. Backman, "Structural length-scale sensitivities of reflectance measurements in continuous random media under the Born approximation," *Optics Letters*, vol. 37, no. 24, p. 5220, 2012.

[84] A. J. Radosevich, J. D. Rogers, R. Çapoğlu, N. N. Mutyal, P. Pradhan, and V. Backman, "Open source software for electric field Monte Carlo simulation of coherent backscattering in biological media containing birefringence," *Journal of Biomedical Optics*, vol. 17, no. 11, p. 115001, 2012.

[85] A. J. Radosevich, A. Eshein, T.-Q. Nguyen, and V. Backman, "Subdiffusion reflectance spectroscopy to measure tissue ultrastructure and microvasculature: model and inverse algorithm," *Journal of biomedical optics*, vol. 20, no. 9, pp. 097002–097002, 2015.

[86] M. A. Pinkert, Z. J. Simmons, R. C. Niemeier, B. Dai, L. B. Woods, T. J. Hall, P. J. Campagnola, J. D. Rogers, and K. W. Eliceiri, "Platform for quantitative multiscale imaging of tissue composition," *Biomedical Optics Express*, vol. 11, no. 4, p. 1927, 2020.

[87] K. P. E. Mercado, *Developing high-frequency quantitative ultrasound techniques to characterize three-dimensional engineered tissues.* University of Rochester, 2015.

[88] R. S. Cobbold, *Foundations of biomedical ultrasound.* Oxford university press, 2006.

[89] P. Narayana, J. Ophir, and N. Maklad, "The attenuation of ultrasound in biological fluids," *The Journal of the Acoustical Society of America*, vol. 76, no. 1, pp. 1–4, 1984.

[90] J.-y. Lu, H. Zou, and J. F. Greenleaf, "Biomedical ultrasound beam forming," *Ultrasound in medicine & biology*, vol. 20, no. 5, pp. 403–428, 1994.

[91] A. Jain, M. Mittal, H. Verma, A. Rai, and H. Verma, "Traffic density measurement based on-road traffic control using ultrasonic sensors and gsm technology," 2013.

[92] D. Garcia, "Simus: an open-source simulator for medical ultrasound imaging. part i: theory & examples," *Computer Methods and Programs in Biomedicine*, vol. 218, p. 106726, 2022.

[93] F. Varray, O. Basset, P. Tortoli, and C. Cachard, "Creanuis: a non-linear radiofrequency ultrasound image simulator," *Ultrasound in medicine & biology*, vol. 39, no. 10, pp. 1915–1924, 2013.

[94] J. Park, J. B. Kang, J. H. Chang, and Y. Yoo, "Speckle reduction techniques in medical ultrasound imaging," *Biomedical Engineering Letters*, vol. 4, pp. 32–40, 2014.

[95] L. Zhu, C.-W. Fu, M. S. Brown, and P.-A. Heng, "A non-local low-rank framework for ultrasound speckle reduction," in *Proceedings of the IEEE conference on computer vision and pattern recognition*, pp. 5650–5658, 2017.

[96] L. Zhao, Y. C. Lam, and C. Q. Lai, "Interaction of ultrasound with microporous polyethylene scaffolds," *Applied Acoustics*, vol. 153, pp. 102–109, 2019.

[97] R. d. Monchy, *Développement et évaluation d'une théorie de milieu effectif combinée à un facteur de structure polydisperse pour la caractérisation ultrasonore de l'agrégation érythrocytaire*. PhD thesis, Aix-Marseille, 2016.

[98] T. H. Lye, R. Roshankhah, Y. Karbalaeisadegh, S. A. Montgomery, T. M. Egan, M. Muller, and J. Mamou, "In vivo assessment of pulmonary fibrosis and edema in rodents using the backscatter coefficient and envelope statistics," *The Journal of the Acoustical Society of America*, vol. 150, no. 1, pp. 183–192, 2021.

[99] R. Huang, L. W. Schmerr, and A. Sedov, "Improving the Born approximation for the scattering of ultrasound in elastic solids," *Ultrasonics*, vol. 44, no. SUPPL., 2006.

[100] J. Garcia-Duitama, B. Chayer, A. Han, D. Garcia, M. L. Oelze, and G. Cloutier, "Experimental Application of Ultrafast Imaging to Spectral Tissue Characterization," *Ultrasound in Medicine and Biology*, vol. 41, no. 9, pp. 2506–2519, 2015.

[101] J. J. Faran Jr, "Sound scattering by solid cylinders and spheres," *The Journal of the acoustical society of America*, vol. 23, no. 4, pp. 405–418, 1951.

[102] M. F. Insana, R. F. Wagner, D. G. Brown, and T. J. Hall, "Describing small-scale structure in random media using pulse-echo ultrasound," *The Journal of the Acoustical Society of America*, vol. 87, no. 1, pp. 179–192, 1990.

[103] S. G. Kanzler and M. L. Oelze, "Improved scatterer size estimation using backscatter coefficient measurements with coded excitation and pulse compression," *The Journal of the Acoustical Society of America*, vol. 123, no. 6, pp. 4599–4607, 2008.

[104] J. R. Sanchez, D. Pocci, and M. L. Oelze, "A novel coded excitation scheme to improve spatial and contrast resolution of quantitative ultrasound imaging," *IEEE transactions on ultrasonics, ferroelectrics, and frequency control*, vol. 56, no. 10, pp. 2111–2123, 2009.

[105] M. Tanter and M. Fink, "Ultrafast imaging in biomedical ultrasound," *IEEE Transactions on Ultrasonics, Ferroelectrics, and Frequency Control*, vol. 61, no. 1, pp. 102–119, 2014.

[106] S. Salles, H. Liebgott, O. Basset, C. Cachard, D. Vray, and R. Lavarello, "Experimental evaluation of spectral-based quantitative ultrasound imaging using plane wave compounding," *IEEE Transactions on Ultrasonics, Ferroelectrics, and Frequency Control*, vol. 61, no. 11, pp. 1824–1834, 2014.

[107] F. L. Lizzi, S. K. Alam, S. Mikaelian, P. Lee, and E. J. Feleppa, "On the statistics of ultrasonic spectral parameters," *Ultrasound in medicine & biology*, vol. 32, no. 11, pp. 1671–1685, 2006.

[108] A. Han, J. W. Erdman, D. G. Simpson, M. P. Andre, and W. D. O'Brien, "Early detection of fatty liver disease in mice via quantitative ultrasound," *IEEE International Ultrasonics Symposium, IUS*, vol. 1, no. Fig 1, pp. 2363–2366, 2014.

[109] M. L. Oelze and W. D. O'Brien Jr, "Defining optimal axial and lateral resolution for estimating scatterer properties from volumes using ultrasound backscatter," *The Journal of the Acoustical Society of America*, vol. 115, no. 6, pp. 3226–3234, 2004.

[110] R. Kuc and M. Schwartz, "Estimating the acoustic attenuation coefficient slope for liver from reflected ultrasound signals," *IEEE Transactions on Sonics and Ultrasonics*, vol. 26, no. 5, pp. 353–361, 1979.

[111] D. Rohrbach and J. Mamou, "Autoregressive Signal Processing Applied to High-Frequency Acoustic Microscopy of Soft Tissues," *IEEE Transactions on Ultrasonics, Ferroelectrics, and Frequency Control*, vol. 65, no. 11, pp. 2054–2072, 2018.

[112] X. Chen, D. Phillips, K. Q. Schwarz, J. G. Mottley, and K. J. Parker, "The measurement of backscatter coefficient from a broadband pulse-echo system: A new formulation," *IEEE transactions on ultrasonics, ferroelectrics, and frequency control*, vol. 44, no. 2, pp. 515–525, 1997.

[113] L. X. Yao, J. A. Zagzebski, and E. L. Madsen, "Backscatter Coefficient Measurements Using a Reference Phantom to Extract Depth-Dependent Instrumentation Factors," *Ultrasonic Imaging*, vol. 12, no. 1, pp. 58–70, 1990.

[114] M. L. Oelze, J. F. Zachary, and W. D. O'Brien, "Characterization of tissue microstructure using ultrasonic backscatter: Theory and technique for optimization using a Gaussian form factor," *The Journal of the Acoustical Society of America*, vol. 112, no. 3, pp. 1202–1211, 2002.

[115] M. L. Oelze and W. D. O'Brien Jr, "Method of improved scatterer size estimation and application to parametric imaging using ultrasound," *The Journal of the Acoustical Society of America*, vol. 112, no. 6, pp. 3053–3063, 2002.

[116] R. Lavarello and M. Oelze, "Quantitative ultrasound estimates from populations of scatterers with continuous size distributions: Effects of the size estimator algorithm," *IEEE transactions on ultrasonics, ferroelectrics, and frequency control*, vol. 59, no. 9, pp. 2066–2076, 2012.

[117] K. A. Wear, T. A. Stiles, G. R. Frank, E. L. Madsen, F. Cheng, E. J. Feleppa, C. S. Hall, B. S. Kim, P. Lee, W. D. O'Brien Jr, *et al.*, "Interlaboratory comparison of ultrasonic backscatter coefficient measurements from 2 to 9 mhz," *Journal of ultrasound in medicine*, vol. 24, no. 9, pp. 1235–1250, 2005.

[118] M. L. Oelze, "Quantitative ultrasound successes: past, present and future," in *Medical Imaging 2020: Ultrasonic Imaging and Tomography*, vol. 11319, pp. 183–188, SPIE, 2020.

[119] T. N. Nguyen, A. J. Tam, M. N. Do, and M. L. Oelze, "Estimation of backscatter coefficients using an in situ calibration source," *IEEE transactions on ultrasonics, ferroelectrics, and frequency control*, vol. 67, no. 2, pp. 308–317, 2019.

[120] A. Cristea, *ULTRASOUND TISSUE CHARACTERIZATION USING SPECKLE STATISTICS*. Theses, Universite Claude Bernard Lyon 1, Dec. 2015.

[121] C. Malinet, P. Muleki-Seya, A. Dutour, I. Fajnorova, H. Liebgott, and B. Montcel, "Toward cancer characterization using light backscattering spectroscopy and quantitative ultrasound," in *Photons Plus Ultrasound: Imaging and Sensing 2023*, vol. 12379, pp. 39–46, SPIE, 2023.

[122] F. Destrempes, J. Porée, and G. Cloutier, "Estimation method of the homodyned k-distribution based on the mean intensity and two log-moments," *SIAM journal on imaging sciences*, vol. 6, no. 3, pp. 1499–1530, 2013.

[123] A. Pierangelo, A. Benali, M.-R. Antonelli, T. Novikova, P. Validire, B. Gayet, and A. De Martino, "Ex-vivo characterization of human colon cancer by mueller polarimetric imaging," *Optics express*, vol. 19, no. 2, pp. 1582–1593, 2011.

[124] A. J. Radosevich, N. N. Mutyal, J. Yi, H. K. Roy, and V. Backman, "Targeting the ultrastructural origins of field carcinogenesis using low coherence enhanced backscattering," 2014.

[125] J. D. Rogers, A. J. Radosevich, J. Yi, and V. Backman, "Modeling light scattering in tissue as continuous random media using a versatile refractive index correlation function," *IEEE Journal on Selected Topics in Quantum Electronics*, vol. 20, no. 2, 2014.

[126] S. A. P. Steven L. Jacques, "miepython." url: https://miepython.readthedocs.io/en/latest/index.html ; Accessed: October 20th 2023.

[127] A. J. Radosevich, J. D. Rogers, V. Turzhitsky, N. N. Mutyal, J. Yi, H. K. Roy, and V. Backman, "Polarized enhanced backscattering spectroscopy for characterization of biological tissues at subdiffusion length scales," *IEEE Journal on Selected Topics in Quantum Electronics*, vol. 18, no. 4, pp. 1313–1325, 2012.

[128] J. D. Rogers, N. Mutyal, A. Radosevich, V. Turzhitsky, H. Roy, and V. Backman, "Biomedical applications of enhanced backscattering spectroscopy," *Optics InfoBase Conference Papers*, pp. 5–6, 2011.

[129] A. Radosevich, "User manual, operation of ebs instrumentation and matching with monte carlo simulation," 2015.

[130] E. Akkermans, P. Wolf, and R. Maynard, "Coherent backscattering of light by disordered media: Analysis of the peak line shape," *Physical review letters*, vol. 56, no. 14, p. 1471, 1986.

[131] K. Ishii and T. Iwai, "Double-scattering approximation theory of enhanced backscatterings of light produced from aggregated particles," *Japanese journal of applied physics*, vol. 41, no. 8R, p. 5155, 2002.

[132] G. Zonios and A. Dimou, "Modeling diffuse reflectance from semi-infinite turbid media: application to the study of skin optical properties," *Optics Express*, vol. 14, no. 19, p. 8661, 2006.

[133] G. Mie, "Beiträge zur optik trüber medien, speziell kolloidaler metallösungen," *Annalen der Physik*, vol. 330, no. 3, pp. 377–445, 1908.

[134] L. Qiu, V. Turzhitsky, R. Chuttani, D. K. Pleskow, J. D. Goldsmith, L. Guo, E. Vitkin, I. Itzkan, E. B. Hanlon, and L. T. Perelman, "Spectral imaging with scattered light: From early cancer detection to cell biology," *IEEE Journal on Selected Topics in Quantum Electronics*, vol. 18, no. 3, pp. 1073–1083, 2012.

[135] G. Pettinato, M. F. Coughlan, X. Zhang, L. Chen, U. Khan, M. Glyavina, C. J. Sheil, P. K. Upputuri, Y. N. Zakharov, E. Vitkin, A. B. D'Assoro, R. A. Fisher, I. Itzkan, L. Zhang, L. Qiu, and L. T. Perelman, "Spectroscopic label-free microscopy of changes in live cell chromatin and biochemical composition in transplantable organoids," *Science Advances*, vol. 7, no. 34, p. eabj2800, 2021.

[136] D. K. Pleskow, L. Zhang, V. Turzhitsky, M. F. Coughlan, U. Khan, X. Zhang, C. J. Sheil, M. Glyavina, L. Chen, S. Shinagare, Y. N. Zakharov, E. Vitkin, I. Itzkan, L. T. Perelman, and L. Qiu, "Coherent confocal light scattering spectroscopic microscopy evaluates cancer progression and aggressiveness in live cells and tissue," *ACS Photonics*, vol. 8, no. 7, pp. 2050–2059, 2021.

[137] C. Malinet, B. Montcel, A. Dutour, H. Liebgott, and P. Muleki-Seya, "Combined ultrasound and light backscattering spectroscopy for cancer characterization: a proof of concept," in *2022 IEEE International Ultrasonics Symposium (IUS)*, pp. 1–4, IEEE, 2022.

[138] C. Malinet, B. Montcel, H. Liebgott, and P. Muleki-Seya, "Caractérisation du cancer par associations de techniques acoustiques et optiques de rétrodiffusion," in *16ème Congrès Français d'Acoustique, CFA2022*, 2022.

[139] A. J. Radosevich, "Monte carlo codes, other codes." url: https://arad-c09ed.firebaseapp.com/ ; Accessed: September 12th 2023.

[140] S. C. Lester, S. Bose, Y.-Y. Chen, J. L. Connolly, M. E. de Baca, P. L. Fitzgibbons, D. F. Hayes, C. Kleer, F. P. O'Malley, D. L. Page, *et al.*, "Protocol for the examination of specimens from patients with invasive carcinoma of the breast," *Archives of pathology & laboratory medicine*, vol. 133, no. 10, pp. 1515–1538, 2009.

[141] J. A. Sebastian, M. J. Moore, E. S. Berndl, and M. C. Kolios, "An image-based flow cytometric approach to the assessment of the nucleus-to-cytoplasm ratio," *PLoS One*, vol. 16, no. 6, p. e0253439, 2021.

[142] Arkema, "Orgasol." url: www.azelis.com/sites/default/files/uploads/OrgasolAccessed: September 11th 2023.

[143] I. Pala Rosas, J. L. Contreras, J. Salmones, C. Tapia, B. Zeifert, J. Navarrete, T. Vázquez, and D. C. García, "Catalytic dehydration of glycerol to acrolein over a catalyst of pd/lay zeolite and comparison with the chemical equilibrium," *Catalysts*, vol. 7, no. 3, p. 73, 2017.

[144] B. Beauvoit, T. Kitai, and B. Chance, "Contribution of the mitochondrial compartment to the optical properties of the rat liver: a theoretical and practical approach," *Biophysical Journal*, vol. 67, no. 6, pp. 2501–2510, 1994.

[145] E. Franceschini, B. Metzger, and G. Cloutier, "Forward problem study of an effective medium model for ultrasound blood characterization," *IEEE transactions on ultrasonics, ferroelectrics, and frequency control*, vol. 58, no. 12, pp. 2668–2679, 2011.

[146] S. L. Jacques, "Erratum: Optical properties of biological tissues: A review (Physics in Medicine and Biology (2013) 58)," *Physics in Medicine and Biology*, vol. 58, no. 14, pp. 5007–5008, 2013.

[147] C. Mätzler, "Matlab functions for mie scattering and absorption, version 2," 2002.

[148] R. Chivers and C. Hill, "Ultrasonic attenuation in human tissue," *Ultrasound in medicine & biology*, vol. 2, no. 1, pp. 25–29, 1975.

[149] O. Lombard, J. Rouyer, E. Debieu, F. Blanc, and E. Franceschini, "Ultrasonic backscattering and microstructure in sheared concentrated suspensions," *The Journal of the Acoustical Society of America*, vol. 147, no. 3, pp. 1359–1367, 2020.

[150] C. Malinet, B. Montcel, A. Dutour, I. Fajnorova, H. Liebgott, and P. Muleki-Seya, "Cancer characterization using light backscattering spectroscopy and quantitative ultrasound: an ex vivo study on sarcoma subtypes," *Scientific Reports*, vol. 13, no. 1, p. 16650, 2023.

[151] J. Perez, A. V. Decouvelaere, T. Pointecouteau, D. Pissaloux, J. P. Michot, A. Besse, J. Y. Blay, and A. Dutour, "Inhibition of chondrosarcoma growth by mtor inhibitor in an in vivo syngeneic rat model," *PLoS One*, vol. 7, no. 6, p. e32458, 2012.

[152] B. Gobin, G. Moriceau, B. Ory, C. Charrier, R. Brion, F. Blanchard, F. Redini, and D. Heymann, "Imatinib mesylate exerts anti-proliferative effects on osteosarcoma cells and inhibits the tumour growth in immunocompetent murine models," *PLoS One*, vol. 9, no. 3, p. e90795, 2014.

[153] Y. Liu, A. G. Schwartz, Y. Hong, X. Peng, F. Xu, S. Thomopoulos, and G. M. Genin, "Correction of bias in the estimation of cell volume fraction from histology sections," *Journal of biomechanics*, vol. 104, p. 109705, 2020.

[154] H. Liebgott, O. Bernard, C. Cachard, and D. Friboulet, "Field simulation parameters design for realistic statistical parameters of Radio - Frequency ultrasound images," *Proceedings - IEEE Ultrasonics Symposium*, pp. 2247–2250, 2007.

[155] G. S. Gotterer, T. E. Thompson, and A. L. Lehninger, "Angular light-scattering studies on isolated mitochondria," *The Journal of Cell Biology*, vol. 10, no. 1, pp. 15–21, 1961.

[156] A. Ghosh, S. Bera, S. Ray, T. Banerjee, and M. Ray, "Methylglyoxal induces mitochondria-dependent apoptosis in sarcoma," *Biochemistry (Moscow)*, vol. 76, pp. 1164–1171, 2011.

[157] C. Gkogkou, K. Frangia, M. W. Saif, R. Trigidou, and K. Syrigos, "Necrosis and apoptotic index as prognostic factors in non-small cell lung carcinoma: a review," *Springerplus*, vol. 3, no. 1, pp. 1–5, 2014.

[158] E. A. Eisenhauer, P. Therasse, J. Bogaerts, L. H. Schwartz, D. Sargent, R. Ford, J. Dancey, S. Arbuck, S. Gwyther, M. Mooney, *et al.*, "New response evaluation criteria in solid tumours: revised recist guideline (version 1.1)," *European journal of cancer*, vol. 45, no. 2, pp. 228–247, 2009.

[159] L. C. Michaelis and M. J. Ratain, "Measuring response in a post-recist world: from black and white to shades of grey," *Nature Reviews Cancer*, vol. 6, no. 5, pp. 409–414, 2006.

[160] E. Yeh, P. Slanetz, D. B. Kopans, E. Rafferty, D. Georgian-Smith, L. Moy, E. Halpern, R. Moore, I. Kuter, and A. Taghian, "Prospective comparison of mammography, sonography, and mri in patients undergoing neoadjuvant chemotherapy for palpable breast cancer," *American Journal of Roentgenology*, vol. 184, no. 3, pp. 868–877, 2005.

[161] D. Sharma, L. O. Osapoetra, and G. J. Czarnota, "Implementation of non-invasive quantitative ultrasound in clinical cancer imaging," *Cancers*, vol. 14, no. 24, p. 6217, 2022.

[162] Y. de Jong, D. Monderer, E. Brandinelli, M. Monchanin, B. E. van den Akker, J. G. van Oosterwijk, J. Y. Blay, A. Dutour, and J. V. Bovée, "Bcl-xl as the most promising bcl-2 family member in targeted treatment of chondrosarcoma," *Oncogenesis*, vol. 7, no. 9, p. 74, 2018.

[163] S. Miwa, N. Yamamoto, K. Hayashi, A. Takeuchi, K. Igarashi, and H. Tsuchiya, "Therapeutic targets and emerging treatments in advanced chondrosarcoma," *International Journal of Molecular Sciences*, vol. 23, no. 3, p. 1096, 2022.

[164] J. A. Crasto, M. S. Fourman, A. Morales-Restrepo, A. Mahjoub, J. B. Mandell, K. Ramnath, J. C. Tebbets, R. J. Watters, and K. R. Weiss, "Disulfiram reduces metastatic osteosarcoma tumor burden in an immunocompetent balb/c or-thotopic mouse model," *Oncotarget*, vol. 9, no. 53, p. 30163, 2018.

[165] K. Rejniak, M. Lloyd, D. Reed, and M. Bui, "Diagnostic assessment of osteosarcoma chemoresistance based on virtual clinical trials," *Medical Hypotheses*, vol. 85, no. 3, pp. 348–354, 2015.

[166] F. Wittbracht, A. Weddemann, A. Auge, and A. Hütten, "Flow Guidance of Magnetic Particles by Dipolar Particle Interaction," vol. 1, no. 2, pp. 102–106, 2010.

[167] J. Mamou, A. Coron, M. L. Oelze, E. Saegusa-Beecroft, M. Hata, P. Lee, J. Machi, E. Yanagihara, P. Laugier, and E. J. Feleppa, "Three-dimensional high-frequency backscatter and envelope quantification of cancerous human lymph nodes," *Ultrasound in Medicine and Biology*, vol. 37, no. 3, pp. 345–357, 2011.

[168] L. Blum and G. Stell, "Polydisperse systems. i. scattering function for polydisperse fluids of hard or permeable spheres," *The Journal of Chemical Physics*, vol. 71, no. 1, pp. 42–46, 1979.

[169] W. Griffith, R. Triolo, and A. Compere, "Analytical scattering function of a polydisperse percus-yevick fluid with schulz-(γ-) distributed diameters," *Physical Review A*, vol. 35, no. 5, p. 2200, 1987.